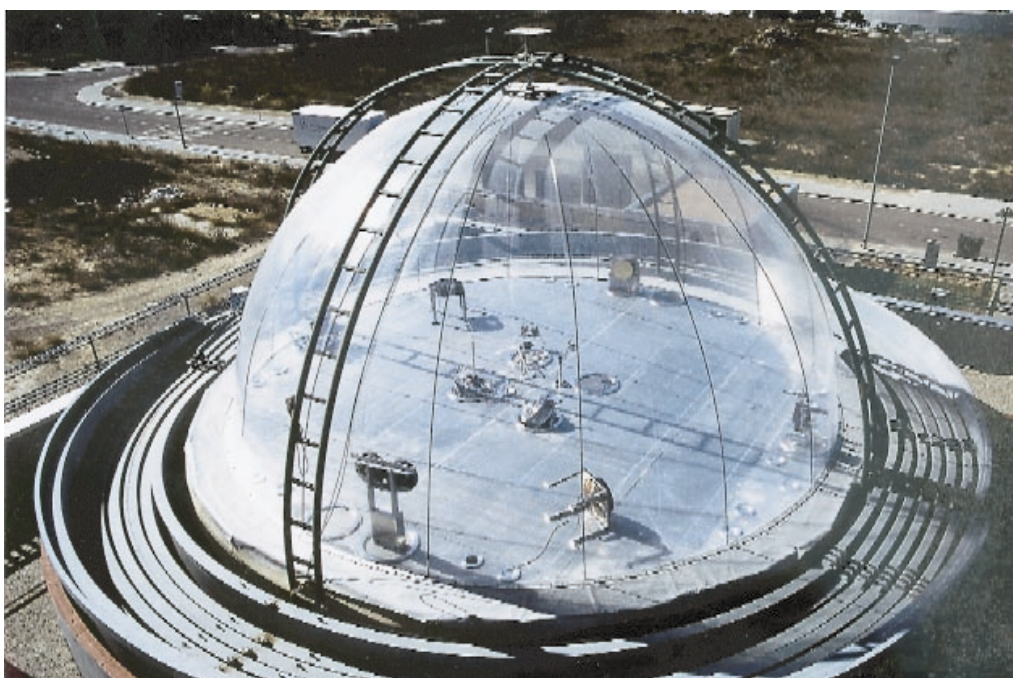


A DOAS Study on the Oxidation Mechanism of Aromatic Hydrocarbons under Simulated Atmospheric Conditions



by
Rainer Volkamer

INAUGURAL - DISSERTATION
zur
Erlangung der Doktorwürde
der
Naturwissenschaftlichen - Mathematischen
Gesamtfakultät
der
Ruprecht - Karls - Universität
Heidelberg

vorgelegt von
Dipl. Phys. Rainer Volkamer
aus Freiburg

Tag der mündlichen Prüfung: 16.07.2001

A DOAS Study on the Oxidation Mechanism of Aromatic Hydrocarbons under Simulated Atmospheric Conditions

Gutachter: Prof. Dr. Ulrich Platt
Prof. Dr. Paul Crutzen

DISSERTATION
submitted to the
Combined Faculties for the Natural Sciences and for Mathematics
of the Rupertus Carola University of
Heidelberg, Germany
for the degree of
Doctor of Natural Sciences

**A DOAS Study on the Oxidation Mechanism of Aromatic
Hydrocarbons under Simulated Atmospheric Conditions**

presented by
Diplom-Physicist: Rainer Volkamer
born in: Freiburg

Heidelberg, 16.07.2001

Referees: Prof. Dr. Ulrich Platt
Prof. Dr. Paul Crutzen

Abstract

The aim of this work was to improve the understanding of the OH-radical initiated oxidation of aromatic hydrocarbons (benzene, toluene, p-xylene (BTX) and 1,3,5-trimethylbenzene (TMB)). These mechanisms are considered a major uncertainty in state-of-the-art photochemical models as they are used to predict photooxidant formation from urban air. Differential Optical Absorption Spectroscopy (DOAS) was employed in a systematic outdoor smog-chamber study at the European Photo Reactor (EUPHORE) located at the CEAM-Institute, Valencia/Spain. The available DOAS system was improved for this purpose. The yields of ring-retaining products (phenol from benzene, phenol-type and aldehyde-type compounds from p-xylene and TMB) and glyoxal (from BTX) were investigated. The phenol yield ($\Phi_{PHEN} = 53\%$) was found more than two times higher than presently available literature values. Further, the bicycloalkyl-radical pathway was identified as a major pathway from BTX. It was demonstrated that the results of this study are representative for the atmosphere. Deviations from the the degradation pathways of BTX and TMB were further observed under conditions of high NO_x (e.g. several ppm). The results of this work indicate that the representations of aromatics in photochemical models need to be updated. The results indicate that the contribution of aromatic hydrocarbons to the formation of photooxidants (i.e. ozone) is underestimated today.

Zusammenfassung

Das Ziel dieser Arbeit war es das Verständnis der OH-Radikal initiierten Oxidation aromatischer Kohlenwasserstoffe (Benzol, Toluol, p-Xylol (BTX) und 1,3,5-Trimethylbenzol (TMB)) zu verbessern. Diese Mechanismen gelten als Hauptunsicherheitsfaktoren in Chemie-Modellen zur Erfassung der Photooxidantienbildung aus Stadtluft. Differentielle Optische Absorptions Spektroskopie (DOAS) wurde in einer systematischen Smog-Kammer Studie am Europäischen Photoreaktor (EUPHORE), CEAM-Institute, Valencia/Spain angewandt. Das vorhandene DOAS-System wurde hierzu weiterentwickelt. Die Verzweungsverhältnisse (Yields) der ringerhaltenden Produkte (Phenol von Benzol, Phenole und Aldehyde von p-Xylol und TMB) sowie Glyoxal (von BTX) wurden bestimmt. Der Phenol-Yield aus Benzol ($\Phi_{PHEN} = 53\%$) wurde zu mehr als dem doppelten des Literaturwertes bestimmt. Weiterhin wurde der Ringspaltungsmechanismus über das Bicycloalkyl-Radikal als einer der Hauptwege in der Oxidation von BTX identifiziert. Es wurde gezeigt, daß die Ergebnisse dieser Arbeit repräsentativ sind für die Atmosphäre. Abweichungen von den atmosphärisch relevanten Reaktionswegen von BTX und TMB wurden in Anwesenheit von hohen NO_x -Konzentrationen (einige ppm) beobachtet. Die Resultate dieser Arbeit werden von heute verwendeten Aromat-Mechanismen in Chemie Modellen nur unzureichend beschrieben. Die Ergebnisse zeigen, daß der Beitrag von Aromaten zur Bildung von Photooxidantien (z.B. Ozon) bislang unterschätzt wird.

Contents

1	Introduction	1
1.1	Guide to this work	5
1.2	Collaborations	6
2	State of knowledge	7
2.1	Proposed pathways for phenol formation	7
2.2	Further proposed intermediate compounds	10
2.3	Assessment of the state of knowledge	13
3	Experimental	15
3.1	The EUPHORE facility	15
3.2	Differential Optical Absorption Spectroscopy	16
3.2.1	The measurement principle	18
3.2.2	The analysis procedure	22
3.2.3	The DOAS system	25
3.2.4	Improvements to the DOAS system	28
3.2.5	Detection limits of selected trace gases	30
3.3	Further analytical instruments employed	30
3.4	Experimental conditions	34
3.4.1	Calibration experiments	34
3.4.2	Kinetic studies	35
3.4.3	Product studies	36
3.4.4	Employed OH-radical-sources	36
3.4.5	Employed NO ₃ -radical-sources	38
3.5	Evaluation procedures	39
3.5.1	The kinetic data used in the evaluation	39
3.5.2	Calibration experiments	39
3.5.3	The relative-rate method	41

3.5.4	Monoexponential loss-processes	41
3.5.5	Employed methods to derive product yields	42
3.5.6	Employed methods to trace the OH-concentration	45
3.5.7	Employed methods to trace the NO ₃ -concentration	47
4	Results	49
4.1	Calibration	49
4.1.1	Phenol absorption cross-section	49
4.1.2	Glyoxal absorption cross-section	49
4.2	Kinetic studies	51
4.2.1	The influence of the chamber-walls	51
4.2.2	Reaction rate-constants towards the OH-radical	54
4.2.3	Reaction rate-constants towards the NO ₃ -radical	57
4.2.4	Photolysis of aromatic aldehydes	59
4.3	The phenol yield from benzene	61
4.3.1	Dependence on the NO _x -concentration	64
4.3.2	The average phenol yield	67
4.3.3	Dependence on the oxygen concentration	68
4.3.4	Dependence on the temperature	68
4.3.5	The formation mechanism of phenol	70
4.3.6	Error considerations	71
4.4	The ring-retaining yields from p-xylene	75
4.4.1	Dependence on the NO _x concentration	77
4.4.2	Dependence on the temperature	78
4.5	The ring-retaining yields from 1,3,5-TMB	80
4.6	The glyoxal yields from BTX	82
4.6.1	The primary glyoxal yields	84
4.6.2	The overall glyoxal yields	86
4.6.3	The negligible formation of secondary glyoxal	88
4.6.4	Identification of the bicycloalkyl-radical intermediate	88
4.6.5	Dependence on the NO _x concentration	90
4.7	The overall formaldehyde yields from toluene	92
4.8	Secondary Organic Aerosol formation	95
4.8.1	The NO ₃ -radical balance	95
4.8.2	The NO _x -balance	99
4.8.3	The temporal coincidence of NO ₃ and SOA formation	100

5	Discussion	101
5.1	Calibration	101
5.1.1	Comparison of the σ (phenol) with literature values	101
5.1.2	Comparison of the σ (glyoxal) with literature values	104
5.2	Kinetic studies	106
5.2.1	Comparison with literature values	106
5.2.2	Influence of the walls in the dark and sun-lit reactor	109
5.3	The phenol yield from benzene	112
5.3.1	Comparison with literature values	112
5.3.2	The high NO_x -concentration range	114
5.3.3	The formation mechanism of phenol	115
5.3.4	Additional support	116
5.3.5	The influence of O_2 -concentration and temperature	117
5.4	The ring-retaining yields from alkylbenzenes	118
5.4.1	Comparison with literature values	118
5.4.2	Comparison to the results from benzene	121
5.4.3	Differences under NO_x -free conditions	126
5.5	The glyoxal yields from BTX	128
5.5.1	Precursors for the formation of glyoxal	128
5.5.2	Photolytic processes	132
5.5.3	Comparison with literature values	134
5.5.4	Differences under NO_x -free conditions	138
5.6	The formaldehyde formation from toluene	139
5.6.1	Evidence for short lived stable intermediates	139
5.7	Secondary Organic Aerosol formation	143
6	Summary and conclusions	147
7	Atmospheric Implications	153
	Glossary	157
	References	159
A	Annex	173
	Acknowledgements	181

Chapter 1

Introduction

The formation of photooxidants like ozone and their associated impact on human health is a major environmental issue worldwide today. High ozone levels are one aspect of the phenomenon which is commonly known as photochemical smog (or summer-smog). The term "photochemical" reflects the essential role that solar radiation plays in driving the chemistry of volatile organic compounds (VOCs) in the presence of NO_x (sum of $\text{NO} + \text{NO}_2$). The degradation of the VOCs leads to the formation of ozone, a variety of further oxidizing species (in sum called photooxidants) and particles that form different aspects of the photosmog. Due to its first observation in the Los Angeles basin in the mid-fourties photosmog is alternatively referred to as Los Angeles smog [*Finlayson-Pitts and Pitts, Jr.* 2000].

The importance of aromatic hydrocarbons in this context was recognized back in the sixties [*Altshuller et al.* 1962] after the discovery that hydrocarbons/ NO_x /light-mixtures are actually responsible for the formation of ozone [*Haagen-Smit and Fox* 1956]. The first atmospheric measurements of aromatic concentrations were carried out by the end of the sixties [*Lonnemann et al.* 1968]. At that time, the primary oxidizing agent was assumed to be ozone. The importance of the OH-radical for the photochemical degradation of airborne hydrocarbons was proposed in the late sixties/early seventies [*Weinstock* 1969; *Levy II* 1971]. It coincided with evidence from laboratory studies that indicated that the oxidation of aromatic hydrocarbons may be triggered by an electrophilic reactant [*Glasson and Tuesday* 1970]. However, it was not until the mid-seventies that this electrophilic reactant was unambiguously identified as OH-radical [*Doyle et al.* 1975; *Perry et al.* 1977] and not ozone [*Nojima et al.* 1974]. In addition, the OH-substituted phenol-type compounds were found to react rapidly

Table 1.1: Hydrocarbons in presently used fuels and the urban atmosphere.

Class	mixing ratio [% (w./w.)] ^a			mixing ratio [% (ppbC)] ^b		
	Normal leaded	Normal unleaded	SUPER unleaded	Leipzig urban air	Wuppertal	Wuppertal traffic tunnel
Alkanes	72.1	61.1	56.7	51	42	37
Alkenes	9.2	11.5	7.5	7	14	16
Aromatics	18.8	26.9	35.8	42	44	47

^a fuel composition from [Patyk and Höpfner 1995]

^b data from [Knobloch and Engewald 1997; Kurtenbach et al. 2001]

with NO₃-radicals [Carter et al. 1981]. Today it is known that the degradation of most aromatic hydrocarbons (i.e. benzene, toluene, xylene-isomers etc.) is initiated exclusively by the reaction with OH-radicals [Atkinson 1994].

Aromatic hydrocarbons are emitted into the urban atmosphere as part of automobile exhaust. Further emissions are primarily linked with anthropogenic activity such as solvent use, gasoline evaporation and spillage, industrial processing, the use of household chemicals and coal-heating [Piccot et al. 1992; Legett 1996]. In rural areas, monocyclic aromatic hydrocarbons can also contribute about 10 % of the Non Methane Hydrocarbons (NMHCs) [Nutmagul and Cronn 1985]. Here, an important contribution to the aromatic budget is transport from polluted and industrialized regions. However, some natural emission also occurs from biomass burning [Blake et al. 1994; Eyde and Richards 1991] and volcanic eruptions [Isidorov et al. 1990]. Further natural sources include the biogenic production in sediments [Hunt et al. 1980], seawater and lakes [Juettner and Henatsch 1986]. Aromatic hydrocarbons may further be emitted from plants under conditions of environmental stress [Heiden et al. 1999].

In Europe, the importance of aromatic compounds in urban air started to increase in the mid-eighties when the portion of aromatics in gasoline was increased as a substitute for lead. The aromatic portion of presently used unleaded SUPER fuels typically accounts for about 40 % (% by weight: w./w.) (see Table 1.1) and ranges between 35 % and 55 % (w./w.) [Patyk and Höpfner 1995]. Thereby, the sum of benzene, toluene and xylene-isomers - the so-called BTX aromatics - ac-

counts for the major part of about 75 % of all monocyclic aromatic hydrocarbons [Patyk and Höpfner 1995; Kurtenbach *et al.* 2001]. Considerable reductions in hydrocarbon emissions (i.e. including aromatics) were achieved by the introduction of three-way catalysts. In fact, the emissions of petrol cars equipped with a three-way catalyst are reduced as compared to those of non-equipped cars by about a factor of ten [Sigsby *et al.* 1987; Fontaine 2000]. In Germany, the overall hydrocarbon emissions were estimated to have been reduced by a factor of two from 1417 kt (1985) to 742 kt (1994) [Umweltbundesamt 1998]. Despite this trend in hydrocarbon emissions in Germany, considerable scatter exists among the absolute numbers in the emission inventories. Thus, the overall VOC-emissions for the former Bundesländer were estimated at 2667 kt - about twice as high - with aromatic compounds contributing about 306 kt [Piccot *et al.* 1992].

Recent field measurements have shown that the high aromatic content in presently used gasolines is also reflected in the relative abundance of aromatic compounds compared to alkanes and alkenes in urban air (see Table 1.1). For instance, the fraction of aromatic hydrocarbons in the city air of Wuppertal in Germany accounted for about 47 %_{ppbC} of all volatile organic compounds (VOCs) [Ackermann 2000]. Due to their relative importance in urban air aromatic hydrocarbons substantially contribute to urban air pollution. They are assumed to be responsible for a significant fraction of the photooxidants formed in the industrialized countries. Even though the oxidation mechanisms of aromatics are not understood as-yet, model calculations indicate that the daytime oxidation of aromatics leads to the formation of up to 40 % of the photooxidants formed from VOCs [Derwent *et al.* 1996]. In comparison to the alkanes and alkenes, aromatic hydrocarbons are among those species that are ascribed Photochemical Ozone Creation Potential (POCP) [Derwent *et al.* 1996]. Though the assigned POCP-values vary considerably among different aromatics, species like the xylene-isomers and trimethylbenzenes (TMB) are ascribed high POCP-values, comparable to and even above the values of alkenes. Another aspect of the impact of aromatic hydrocarbons on the atmospheric environment is their effect on health. Benzene, for example, is carcinogenic and its use is therefore strictly controlled [Kelly *et al.* 1994]. In addition, the photooxidation products of aromatic hydrocarbons are known to show both toxic and mutagenic effects, in contrast to the products of most smaller alkanes and alkenes [Bufalini 1989]. Finally, photochemical degradation products from aromatic hydrocarbons are a source of secondary organic aerosol (SOA) in urban air [Odum *et al.* 1997].

Despite their importance, however, our knowledge of the atmospheric degradation mechanisms of aromatic hydrocarbons, in particular of benzene, is still poor. In the past, most experimental studies focused on the more reactive aromatic hydrocarbons like toluene and the xylene isomers [*Bandow and Washida* 1985; *Yu et al.* 1997] whilst studies on benzene were comparably scarce. In general considerable uncertainty still exists on the principal oxidation steps in the degradation of aromatic compounds.

The general aim of this work was to obtain a better understanding of the oxidation pathways of monocyclic aromatic hydrocarbons, i.e. benzene, toluene, p-xylene (hereafter referred to as BTX) and 1,3,5-trimethylbenzene (TMB). More than 150 experiments were performed under simulated atmospheric conditions at the outdoor simulation chamber EUPHORE, located at CEAM-Institute in Valencia/Spain. DOAS (Differential Optical Absorption Spectroscopy) was applied to investigate the ring-retaining and ring-cleavage pathways in the degradation of aromatic compounds.

1.1 Guide to this work

After this introduction, the present state-of-knowledge on the aromatic degradation pathways is summarized and assessed in Chapter 2. Chapter 3 introduces the experimental techniques as well as the experimental conditions and evaluation procedures that have been employed to derive the results of this study.

In Chapter 4 the results are presented. The calibration results obtained from the UV-spectra that have been recorded of phenol and glyoxal are presented first (Section 4.1), followed by the characterization of the wall-influence as a sink for gas-phase compounds (Section 4.2.1). These results and the OH- and NO₃ rate-constants of selected aromatic aldehydes and phenols (Section 4.2.2 and 4.2.3) as well as photolysis-frequencies of aromatic aldehydes (Section 4.2.4) represent essential preliminary information for the further investigation of the three major parts of this study. The first part includes the results on the ring-retaining pathways of benzene (Section 4.3), p-xylene (Section 4.4) and 1,3,5-trimethylbenzene (Section 4.5). The second part is dedicated to the ring-cleavage pathways of benzene, toluene and p-xylene (BTX). By investigating the glyoxal formation from BTX the identification of a major ring-cleavage pathway of BTX has been possible (Section 4.6). Further insight into this ring-cleavage pathway is described in the Section 4.7 from the results on the formaldehyde (HCHO) formation from toluene. The third part is devoted to the role of NO₃-radicals in the context of the formation of Secondary Organic Aerosol (SOA) in an exemplary study on p-xylene (Section 4.8).

In Chapter 5 the results are discussed in the context of available literature values (all Sections). As a result of the discussion some further insight into the mechanism of aromatic oxidation is obtained in spots. These further results concern the phenol yields from benzene in the high-NO_x-range (see Section 5.3.2), similar results for toluene and p-xylene (see Section 5.4.2), the dominant influence of photolysis in the aromatic oxidation (see Section 5.5.2) as well as the evidence for highly reactive stable intermediate compounds from toluene (see Section 5.6.1).

Chapter 6 briefly summarizes the most important results and concludes how they contribute to a better understanding of the mechanism of aromatic oxidation. Finally, in Chapter 7, the outcome of this work is discussed in terms of the atmospheric relevance of the results.

The abbreviations used for compounds, groups of compounds, names and symbols are compiled in a glossary at the end of the text.

1.2 Collaborations

This PhD-thesis is largely based on data obtained within the scope of a Marie Curie Fellowship granted by the Commission of the European Communities. During the funding period of two years, the Fellowship was hosted by CEAM-Institute in Valencia/Spain. Further data was obtained after the end of the funding period in a collaboration between Prof. Dr. U. Platt, University of Heidelberg who supervised this PhD-thesis over the whole time-span and Dr. Klaus Wirtz, CEAM-Institute who supervised the Marie Curie grant.

Ten experiments on the phenol yields from benzene were performed in collaboration with Dr. Björn Klotz from the group of Prof. Dr. K.H. Becker, BUGH Wuppertal, Germany. The cooperation with Dr. Klotz continued during his post-doctoral stay in the group of Prof. Dr. N. Washida, NIES, Tsukuba Japan.

The data obtained from these collaborations will be published in joint articles that are presently in preparation.

Chapter 2

State of knowledge

Despite many years of research on aromatic hydrocarbons our knowledge on the oxidation mechanism in the atmosphere is still limited to the principal oxidation steps. It is well established that most aromatic compounds exclusively react with OH-radicals. Reactions with NO₃-radicals are further important for the OH-substituted (phenol-type) compounds. The reaction with ozone and photolysis is essentially unimportant under the conditions that prevail in the atmosphere. Figure 2.1 illustrates the initial oxidation steps in the OH-reaction with benzene and includes the different mechanisms currently proposed for the formation of phenol. Despite the fact that unlike alkylated aromatic hydrocarbons, benzene reacts exclusively through the OH-addition pathway to the aromatic ring, the initial steps of benzene oxidation are fundamental also for the understanding of other aromatics.

2.1 Proposed pathways for phenol formation

It is well established that the reaction of the OH-radical with benzene **1** proceeds by addition to the aromatic ring giving a hydroxy cyclohexadienyl-radical **2**, also termed benzene-OH adduct **2** (reaction (1) in Figure 2.1). Under atmospheric conditions the benzene-OH adduct **2** (aro-OH) only slowly decomposes back to reactants (-1) and primarily reacts with molecular oxygen [Knispel *et al.* 1990]. Recent progress on the products of this reaction gave final evidence for the reversible formation of the hydroxycyclohexadienyl-peroxy-radical **3** (aro-OH-O₂), see reaction (2) [Bohn and Zetzsch 1999]. With $k_2 \approx 2 \cdot 10^{-15} \text{ cm}^3 \cdot (\text{molec} \cdot \text{s})^{-1}$ and $k_{-2} \approx 8 \cdot 10^3 \text{ s}^{-1}$ [Bohn and Zetzsch 1999], this second equilibrium between **2** and **3** is rapidly attained (<1 ms), and it was not yet possible to differentiate between the two compounds with respect to the further loss-processes. The equilibrium constant

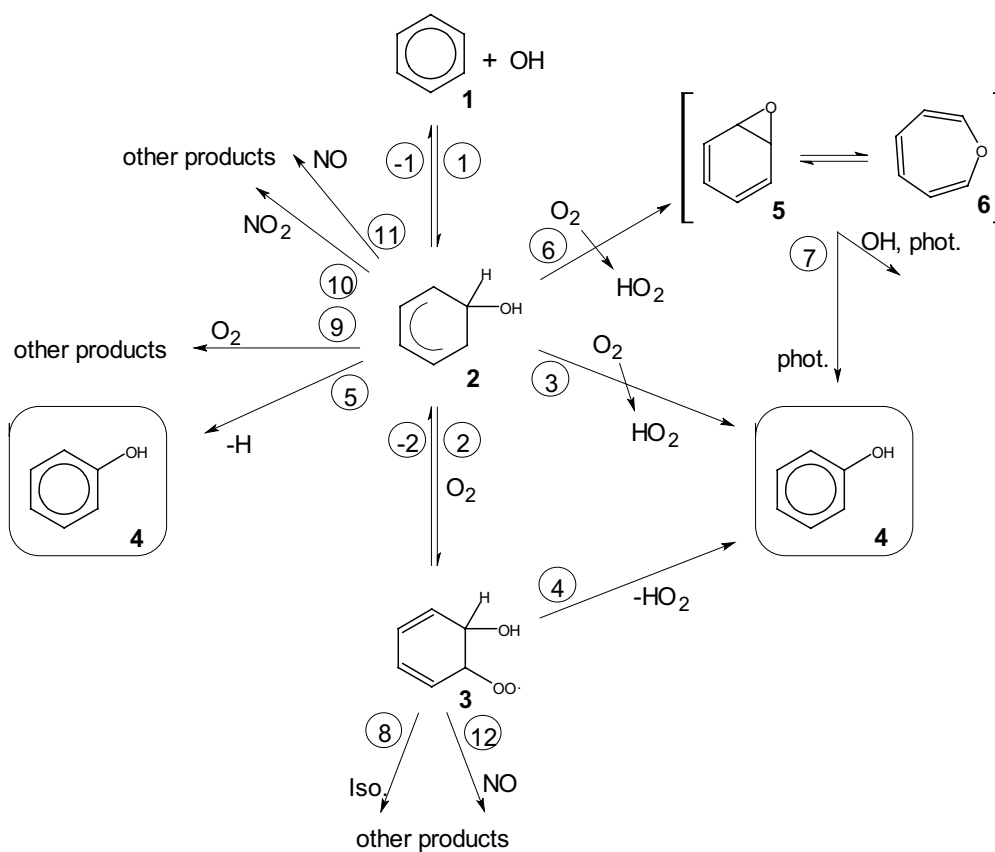


Figure 2.1: The initial steps in the OH initiated oxidation of benzene **1**. Currently proposed loss-processes of the aromatic-OH adduct **2** and the peroxy-radical **3** (which are in rapidly established equilibrium) that lead in part to the formation of phenol **4**. Intermediate species are marked in bold numbers. The reaction pathways are indicated by numbers in circles. Corresponding rate-constants, if available, are given in the text. Similar schemes for the phenol forming pathways can also be drawn for the alkyl-substituted aromatics.

was determined $K_{eq} = k_2/k_{-2} = 2.7 \cdot 10^{-19} \text{ cm}^3$ at $T = 296 \text{ K}$ [Bohn and Zetzsch 1999] indicating that **2** and **3** are present at roughly equal concentration in air of one atmosphere. Both compounds **2/3** may form in chemically activated states [Lay et al. 1996]. For reasons of simplicity these are not explicitly shown in Figure 2.1.

With respect to the formation of phenol-type compounds **4** (and its methylated derivatives) from **2/3** the explicit formation mechanism is subject to an ongoing debate. At present the different pathways (3) to (6) shown in Figure 2.1 have been proposed. Channel (3) forms HO_2 from the hydrogen abstraction reaction of **2** with molecular oxygen. Channel (4) yields the same products through the direct elimination of HO_2 from **3** [Lay et al. 1996]. An alternative phenol formation pathway have been proposed to proceed without the involvement of O_2 directly from the replacement of a ring-bound H atom from **2**, see reaction (5) [Bjergbakke et al. 1996]. However, this pathway is controversially discussed in the literature [Koch 1997; Pagsberg 1997; Bohn and Zetzsch 1999; Berndt et al. 1999]. Finally, pathway (6) was postulated by Klotz et al. [1997]. Reaction of aro-OH **2** with O_2 could yield a HO_2 -radical and benzene oxide **5**, which is in rapid equilibrium with its monocyclic isomer oxepin **6**. Mixtures of benzene oxide/oxepin **5/6** (also termed areneoxides) have been shown to yield phenol on photolysis with sunlight, reaction (7) in Figure 2.1, while its OH initiated oxidation gives ring-opening products [Klotz et al. 1997]. Despite the mechanistic controversy, considerable progress was recently made on the overall branching ratio of the phenols formed from the different pathways in the toluene system [Smith et al. 1998; Klotz et al. 1998]. At present, toluene can be regarded as the only compound where the yields of the cresol-isomers are known under conditions that are representative for the atmosphere.

Reactions (8) to (12) have been proposed as further loss-processes of the species **2/3**. Of these, channels (8) and (9) are thought to dominate under atmospheric conditions (see Figure 2.2). Channel (10), the reaction of **2** with NO_2 , can be important under (smog-chamber) conditions with high NO_2 concentrations. Channel (11), the reaction with NO , on the other hand will be essentially negligible under most conditions [Zetzsch 1997]. Finally, channel (12) indicates the reaction of intermediate **3** with NO . This process is found negligible under atmospheric NO concentrations [Bohn and Zetzsch 1999] but it may become an important loss-process from the equilibrium **2/3** under simulated atmospheric conditions if NO concentrations are considerably higher.

2.2 Further proposed intermediate compounds

In Figure 2.2, the initial oxidation steps were somewhat simplified and are shown for toluene **1**. For reasons of simplicity, those compounds which are similar in structure to the compounds drawn in Figure 2.1 have been assigned the same numbers. For toluene and the further alkyl-substituted aromatics (e.g. p-xylene), a minor fraction of the initial attack of the OH-radical will proceed via the abstraction reaction of a H-atom from the side-chain ($\leq 10\%$). This reaction pathway is comparably well known and in the presence of NO forms benzaldehyde **9** (BALD) [Finlayson-Pitts and Pitts, Jr. 2000]. However, the major OH-reaction with toluene **1** proceeds via the addition to the aromatic ring ($\geq 90\%$). The formation of aro-OH- O_2 **3**, phenolic compounds **4** and areneoxides **5/6** has been discussed above.

Further products from the reaction of aro-OH **2** with oxygen (pathways (8) or (9) in Figure 2.1) could be the bicycloalkyl-radical **7** and an epoxide-alkoxy-radical **8** [Bartolotti and Edney 1995]. Up to date little is known about the branching ratio for the formation of the different intermediates (if, indeed, all of them are formed). With the exception of the phenols **4** (discussed above) the branching ratio of the highly reactive intermediates **3,5/6,7,8** is presently unknown. This is partly due to difficulties in the direct observation of the highly reactive intermediates in the experiment [Klotz *et al.* 1997; Atkinson 2000]. An indirect identification of these intermediates through observable stable products has been extensively studied [Darnall *et al.* 1979; Becker and Klein 1987; Bierbach *et al.* 1994; Kwok *et al.* 1997; Yu and Jeffries 1997; Yu *et al.* 1997] and in fact the presently available product data is consistent with all the proposed intermediates **3,5/6,7,8** [Atkinson 2000]. Nevertheless, the quantitative identification of these intermediate compounds from this product data is not straightforward since - in principle - a given product may be formed through different pathways. Even for a compound like glyoxal **10**, which is known to be a significant ring-cleavage product from the OH-reaction of aromatic compounds [Bandow *et al.* 1985; Tuazon *et al.* 1986; Becker and Klein 1987; Bierbach *et al.* 1994; Smith *et al.* 1999] no definite formation pathways could be established. The several possible formation pathways of glyoxal **10** from the intermediates **3,5/6,7,8** are discussed in Section 5.5.1.

Experimental indications for fast ring-cleavage involving the homologous bicycloalkyl-radical **7** formed from o-xylene have up-to-now been derived from two studies [Darnall *et al.* 1979; Kwok *et al.* 1997]. Both studies investigate the formation of biacetyl, a C_4 - α -dicarbonyl that is formed only from o-xylene and not

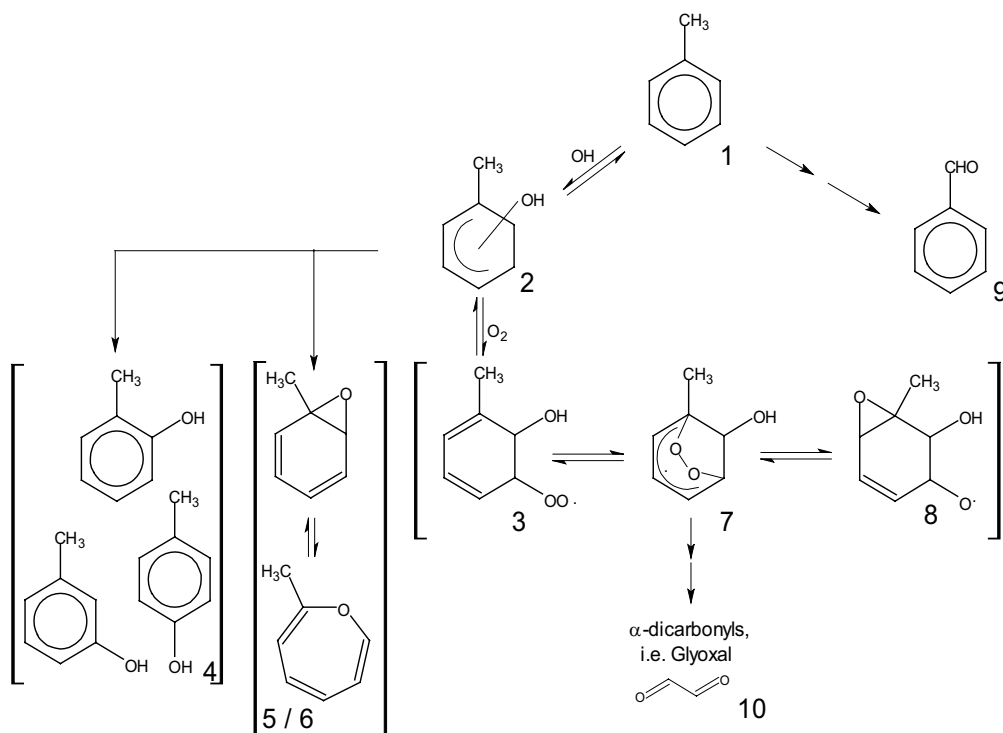


Figure 2.2: Simplified scheme for the initial steps in the OH-radical initiated oxidation of toluene **1**. The OH-radical may either abstract an H-atom from the side-chain or add to the aromatic ring. The aromatic-OH adduct **2** formed in the latter case can react with molecular oxygen to yield one of the five proposed intermediate compounds **3-8**. Analogous intermediates are proposed for benzene and other alkyl-substituted aromatic compounds.

from other aromatic compounds [Atkinson 1994]. Darnall *et al.* [1979] observed the biacetyl with a time-resolution of 30 minutes and postulated the formation of the homologous bicycloalkyl-radical intermediate **7** to explain the observed concentration-time-profile of biacetyl. Nevertheless, primary products observed at sampling rates of tens of minutes may be difficult to distinguish from secondary products formed from highly reactive stable intermediate species, and these measurements cannot rule out the involvement of such intermediates [Atkinson 2000]. Even though time-resolution is not a limitation with the API-MS (Atmospheric Pressure Ionisation Mass Spectrometry) measurements of Kwok *et al.* [1997] the reported data is only qualitative. Furthermore, the API-MS technique is limited to observing biacetyl as the only α -dicarbonyl compound due to problems of the technique with the detection of low molecular weight molecules [Kwok *et al.* 1997]. The API-MS technique is hence restricted to the investigation of the o-xylene system.

The highly time-resolved, simultaneous DOAS detection of ring-retaining products **4,9** and glyoxal **10** eliminates these limitations since glyoxal is formed from almost any aromatic system, i.e. benzene, toluene and p-xylene. Furthermore, limited information is presently available about the dependence of product yields on temperature and oxygen concentration as well as the NO and NO₂ concentration (which if discussed at all are treated as NO_x). The influence of these parameters is investigated explicitly in this work.

2.3 Assessment of the state of knowledge

As described in the previous Section, the understanding of the oxidation mechanism of aromatic hydrocarbons is far from complete. The uncertainties in the principal oxidation steps of aromatic compounds are primarily related to the OH-addition channel. They concern the branching ratios and explicit formation mechanism of ring-retaining (phenol-type) products as well as the explicit mechanisms that lead to the ring-cleavage of aromatic compounds. Further important questions are related to the NO_x -losses that are observed in smog-chamber studies on the OH-radical initiated oxidation of aromatic compounds [Killus and Whitten 1982; Martín-Reviejo *et al.* 1996] as well as the formation of Secondary Organic Aerosol (SOA) [Stern *et al.* 1987; Odum *et al.* 1997].

The uncertainties related to the aromatic degradation schemes affect the results obtained from photochemical models that describe the formation of photooxidants (e.g. ozone) from urban air. In fact, aromatics are considered a major source of uncertainty in these models [Derwent and Jenkin 1991; Carter 1995]. In an attempt to minimize these uncertainties most models use so-called adjusted oxidation schemes for the representation of aromatic degradation. These mechanisms were adjusted to fit the concentration-time-profiles of ozone and NO_x derived from smog-chamber runs on aromatic oxidation [Atkinson *et al.* 1980; Killus and Whitten 1982; Leone *et al.* 1985; Carter 1995]. In most of these smog chamber runs the initial concentrations of reactants and NO_x were increased (typically by several orders of magnitude) as compared to those concentrations that prevail in the polluted and semi-rural atmosphere where the aromatics are mostly oxidized. Furthermore, the model-code typically reduced the complexity of the system to a few parameters and (unless for selected products like glyoxal and methylglyoxal) widely ignored secondary reactions of the products. The interpolation of the thus derived oxidation schemes to the atmosphere is therefore highly speculative.

Improving our understanding of the oxidation of aromatic hydrocarbons is therefore indispensable in order to allow realistic estimates of the product distribution from these models (including photooxidants, hazardous air pollutants and SOA) as they are a prerequisite for the development of effective abatement strategies that reduce the environmental impact of urban air pollution. It especially needs to be demonstrated that the adjustable model-parameters (e.g. product yields, photolysis-frequencies etc.) are actually representative for the atmosphere.

Chapter 3

Experimental

This chapter briefly describes the outdoor simulation chamber EUPHORE (European Photo Reactor) where the experiments presented in this work were carried out (Section 3.1). Further, Differential Optical Absorption Spectroscopy (DOAS) is described and the improvements to the DOAS-system that were implemented over the time-scale of this work are presented (Section 3.2). In Section 3.3 the further analytical instruments of relevance to this work are presented. Section 3.4 gives an overview about the procedures followed to set-up the experimental conditions for the kinetic and product studies. Finally, Section 3.5 describes the employed evaluation procedures.

3.1 The EUPHORE facility

The EUPHORE installations, located at the Centro de Estudios Ambientales del Mediterraneo (CEAM) in Valencia/Spain, consist of two large-volume (approximate volume of $\approx 187 \text{ m}^3$) outdoor simulation chambers. The two hemispherical chambers (designated chamber A and B) are made of $120 \mu\text{m}$ thick fluorine-ethene-propene (FEP) foil which is highly transmittive for visible as well as UV light (transmittance in the visible is approximately 85-90 %, at 290 nm still about 75 %). A top view of the chamber used in this study is shown in Figure 3.1. The flat aluminium floor panels of the chamber, covered by FEP sheet, can be water cooled to avoid heating of the chamber by sun light during the experimental runs, maintaining realistic atmospheric temperature conditions during the course of an experiment. Two mixing fans (see Figure 3.1) of $67 \text{ m}^3 \cdot \text{min}^{-1}$ throughput of air are mounted inside the chamber to provide homogeneous mixing of the volume. An air-purification-and-drying-system provides NO_y -, NMHC-free and dry air allowing the background con-

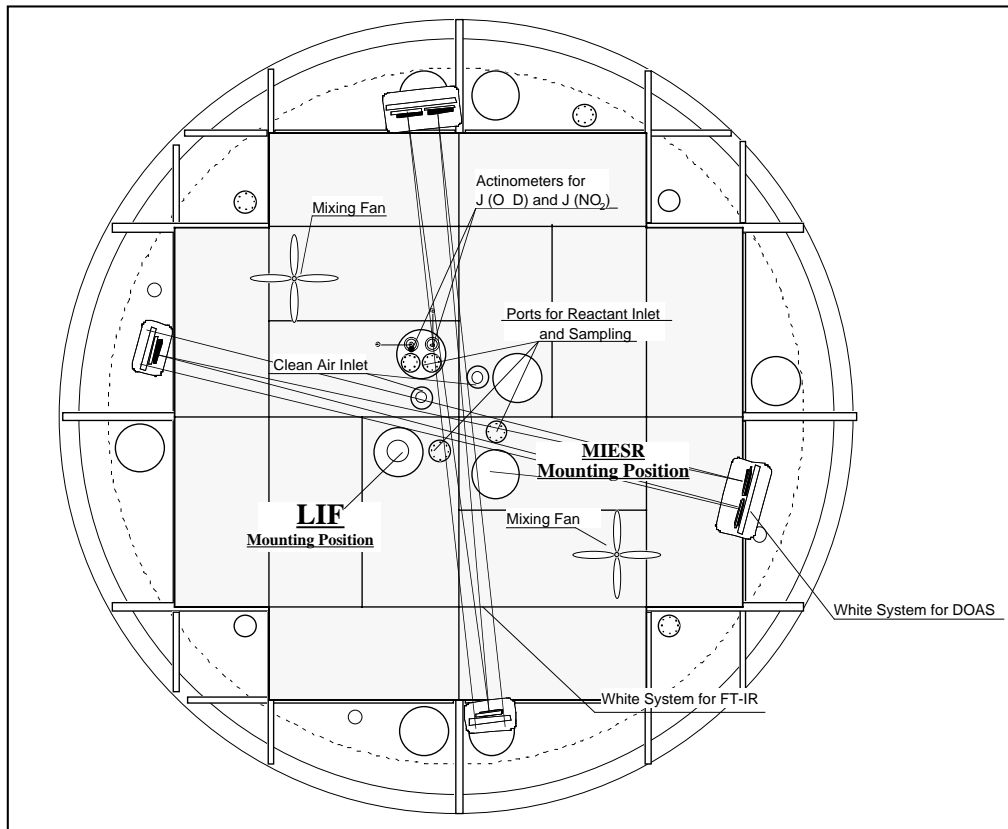


Figure 3.1: Top view of the EUPHORE chamber A that was used in this study.

centration of NMHC species to be as low as $0.3 \text{ mg}\cdot\text{m}^{-3}$. A hydraulically controlled steel housing allows to protect the chamber from sunlight and weather [Becker 1996].

Inside this chamber two White-type multireflection cells are mounted, one coupled to an FTIR interferometer, one to the DOAS spectrometer. The FTIR-system and additional equipment used in this work is presented in Section 3.3. This study was mainly focused on experiments using the DOAS system, which in the following is therefore described in more detail below.

3.2 Differential Optical Absorption Spectroscopy

Since the first remote sensing measurements of ozone in the earth's atmosphere by *Dobson and Harrison* [1926] spectroscopic techniques have become an increasingly important branch in the measurement of atmospheric trace gases. In 1975 and 1979, *Noxon* [1975] [*Noxon et al.* 1979] and *Platt et al.* [1979] introduced a new method

to measure atmospheric trace gas concentrations, Differential Optical Absorption Spectroscopy (DOAS). Since then, DOAS has been applied to measure trace-gas concentrations in the troposphere and stratosphere [Platt 1994; Solomon *et al.* 1987] as well as under simulated atmospheric conditions [Etzkorn 1998]. In fact, several important atmospheric trace gases were measured for the first time using DOAS, e.g. HONO [Perner and Platt 1979; Platt and Perner 1980], OH [Perner *et al.* 1976], NO₃ [Platt *et al.* 1980], BrO [Hausmann and Platt 1994] and IO [Alicke *et al.* 1999] in the troposphere, and OClO and BrO [Sanders *et al.* 1988] in the stratosphere. A large number of other molecules absorbing light in the UV and the visible wavelength region, e.g. NO₂, NO, NH₃, ClO, IO, O₃, SO₂, CS₂, HCHO can also be detected [Platt 1978; Platt 1994] (see also Section 3.2.5).

A further interesting application of the DOAS technique is the measurement of absolute concentrations of aromatic hydrocarbons. Most aromatic hydrocarbons show a characteristic and well structured absorption in the wavelength range below 300 nm. However, the DOAS detection of aromatics suffers the spectral overlap from absorptions of atmospheric oxygen in the Herzberg-bands. For most atmospheric applications the oxygen absorptions will be the dominant spectral structure in the measured spectra [Trost 1997; Volkamer *et al.* 1998]. Since more recently, the problems due to interfering oxygen absorption in the wavelength range between 243 nm and 290 nm could be overcome [Volkamer *et al.* 1998] this interesting spectral range is available for the DOAS detection of a variety of aromatic hydrocarbons. In recent years, the absorption cross-sections of a variety of aromatics like benzene, toluene, o-, m-, p-xylene, TMBs, phenol, cresol-isomers, DMP-isomers, aromatic aldehydes and further aromatic compounds have been determined [Trost 1997; Etzkorn *et al.* 1999] and were applied to the DOAS measurement of aromatic compounds in the atmosphere [Volkamer *et al.* 1998; Ackermann 2000].

The major advantages of the DOAS technique is its ability to measure absolute trace gas concentrations of different isomers (i.e. m-xylene and p-xylene are easily separated) at a good time-resolution in the absence of wall-reactions. DOAS is therefore especially useful in the measurement of highly reactive species, such as the free radicals OH, NO₃, halogenoxides or NO₂ as well as polar compounds, i.e. aromatic aldehyde- and phenol-type compounds. The simultaneous determination of the concentration of several trace gases, by analyzing the sum of their absorptions in one wavelength interval, reduces measurement time and gives well time-resolved insight about the average chemical composition of the observed air mass.

3.2.1 The measurement principle

In Figure 3.2 the components of a simplified DOAS instrument, set-up to measure tropospheric trace gases, is shown. Light, with an initial intensity $I_0(\lambda, L)$, emitted by a suitable source passes through the observed air mass and is collected by a telescope. Extinction of light on the lightpath, due to absorption processes by different trace gases and scattering by air molecules and aerosol particles, reduces the initial intensity. After the light has traveled a pathlength L , the $I_0(\lambda, L)$ is reduced to $I(\lambda, L)$ as is expressed from Equation 3.1 using Lambert-Beer's law:

$$I(\lambda, L) = I_0(\lambda, L) \cdot \exp^{\int_{l=0}^{l=L} -(\sum_j \sigma_j(\lambda, p, T) \cdot c_j(l) + \varepsilon_R(\lambda, l) + \varepsilon_M(\lambda, l)) dl} + N(\lambda) \quad (3.1)$$

where for each trace species j the parameters $\sigma_j(\lambda, p, T)$ is the absorption cross-section which depends on the wavelength λ , the pressure p and the temperature T , $c_j(l)$ its number density at the position l along the light path of length L . The Rayleigh-extinction and Mie-extinction coefficients are here described by ε_R and ε_M . $N(\lambda)$ is the photon noise dependent on $I(\lambda, L)$. In Figure 3.2a the spectrum of $I(\lambda, L)$ that arises from light that passed the atmosphere with one absorber (formaldehyde: HCHO) is shown. In most DOAS instruments, the light is focused on the entrance slit of a grating spectrograph, with a detector system recording the spectrum. Due to the limited resolution of the spectrograph the shape of spectrum $I(\lambda, L)$ changes. The mathematical description of this process is a convolution of $I(\lambda, L)$ with the instrument function H of the spectrograph. Figure 3.2b shows the spectrum $I^*(\lambda, L)$ after a convolution with a typical instrument function H as it is projected by the spectrograph on the detector. During the recording by the detector the wavelength range is mapped into n discrete pixels, numbered by i , each integrating the light in a wavelength interval from $\lambda(i)$ to $\lambda(i+1)$. This interval is given by the wavelength-pixel-mapping Γ_I of the instrument. In the case of a linear dispersion ($\Gamma_I: \lambda(i) = \lambda(0) + \gamma \cdot i$) the spectral width of a pixel ($\Delta\lambda(i) = \lambda(i+1) - \lambda(i) = \gamma_0$) is constant. The signal $I'(i)$ seen by a pixel i (omitting any instrumental factors, i.e. the response of individual pixels) is given by:

$$I'(i) = \int_{\lambda(i)}^{\lambda(i+1)} I^*(\lambda', L) d\lambda' \quad (3.2)$$

In general the wavelength-pixel-mapping Γ_I of the instrument can be approximated by a polynomial:

$$\Gamma_I : \lambda(i) = \sum_{k=0}^q \gamma_k \cdot i^k \quad (3.3)$$

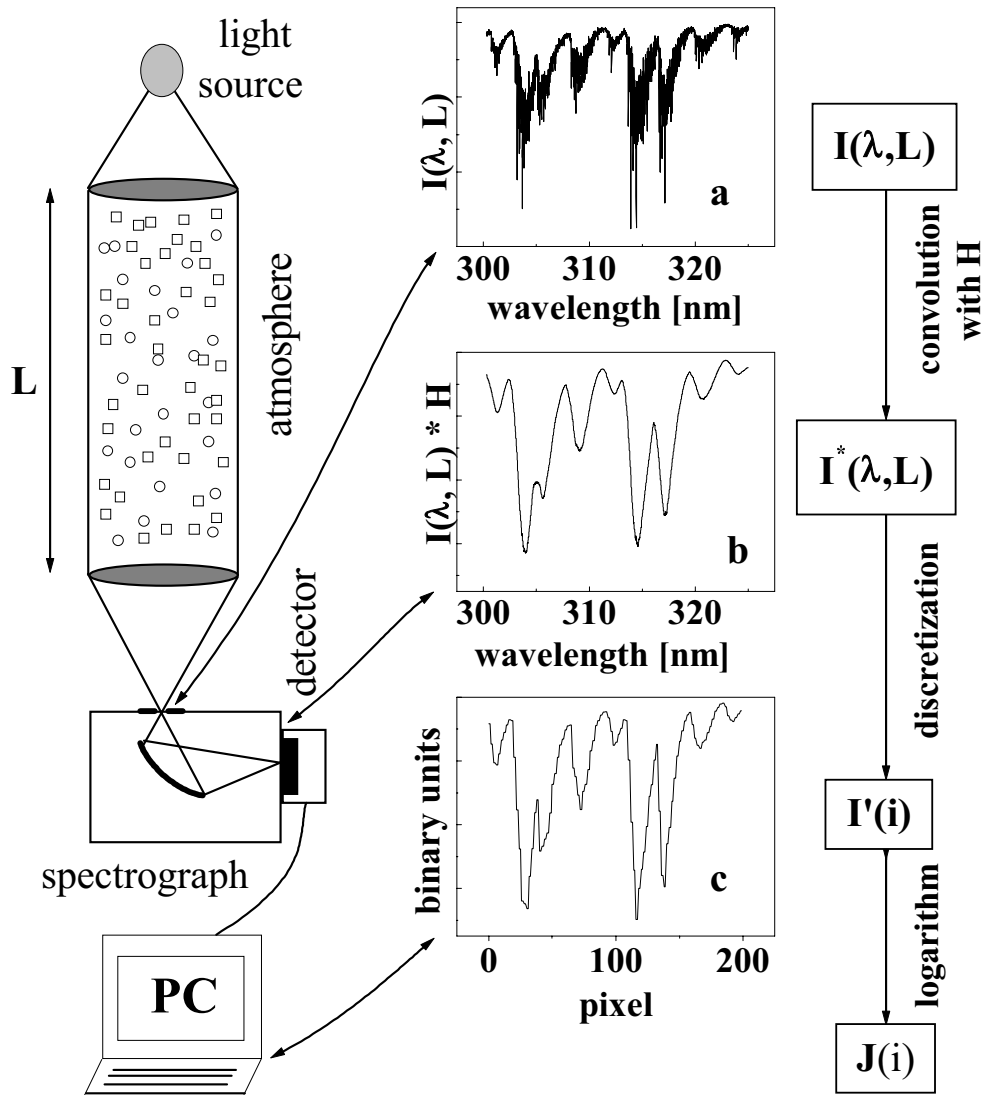


Figure 3.2: The components of a simplified DOAS set-up. Collimated light undergoes absorption processes on its way through the observed air mass. (a): an example-spectrum of this light entering the spectrophotometer is shown, assuming only formaldehyde (HCHO) to be present in the observed air mass. This absorption spectrum shows the ro-vibronic structure of HCHO. (b): the same spectrum convoluted by the spectrophotometer's instrumental function reaches the detector. (c): the spectrum after it was mapped by the detector to discrete pixels as it is actually stored to the hard-disk of a PC and can be analysed numerically.

The parameter vector (γ_k) determines the mapping of pixel i to the wavelength $\lambda(i)$. A change in parameter γ_0 describes a spectral shift of the spectrum. Changing γ_1 squeezes or stretches the spectrum linearly. Parameters γ_k with higher k describe a distortion of the wavelength scale of higher order. Changes in the parameter vector γ_k can be caused by different measurement conditions of the spectra, as grating spectrometers usually show a temperature drift of 1/10 of a pixel per K. It is therefore necessary to correct these effects in the analysis procedure. Figure 3.2c shows the discrete spectrum $I'(i)$ as it is recorded and stored in a computer.

The DOAS technique was originally designed to match the needs of absorption spectroscopy in the atmosphere [Platt 1994]. In contrary to the laboratory, the absolute absorption signal of an observed trace gas in the atmosphere can not be accessed due to the lack of information about the measurement-light intensity in the absence of the atmosphere. The basic concept behind DOAS allows to bypass this lack of information separating the cross section σ_j into two terms:

$$\sigma_j = \sigma_j^b + \sigma_j' \quad (3.4)$$

where for a trace gas j the σ_j^b represents broad spectral features and σ_j' the differential cross-section which represents narrow spectral structures. Considering only σ_j' in the spectra evaluation process avoids interferences from Rayleigh- and Mie-extinction. The separation of the absorption cross-section is illustrated in Figure 3.3 for ozone.

The logarithm of $I'(i)$ (see Figure 3.2c), $J(i) = \ln(I'(i))$, can be described by:

$$J(i) = J_0(i) + \sum_{j=1}^m a'_j \cdot S'_j(i) + B'(i) + R'(i) + A'(i) + N'(i) \quad (3.5)$$

where for each trace gas species j , $S'_j(i)$ indicates the differential absorption structure ($S'_j(\lambda) = \ln(\exp(-\sigma'_j(\lambda)) \star H)$ corresponds to the convolution of the differential cross-section of the trace gas j with the same instrument function H), $B'(i)$ the broad absorption, $R'(i)$ the sum of extinction by Mie- and Rayleigh scattering, $A'(i)$ summarises any variations in the spectral sensitivity of detector or spectrograph and $N'(i) = \ln(N(\lambda))$ is caused by the detector noise and photon statistics. The scaling factors $a'_j = \bar{c}_j \cdot L$ are then the product of the average number densities over the path-length L .

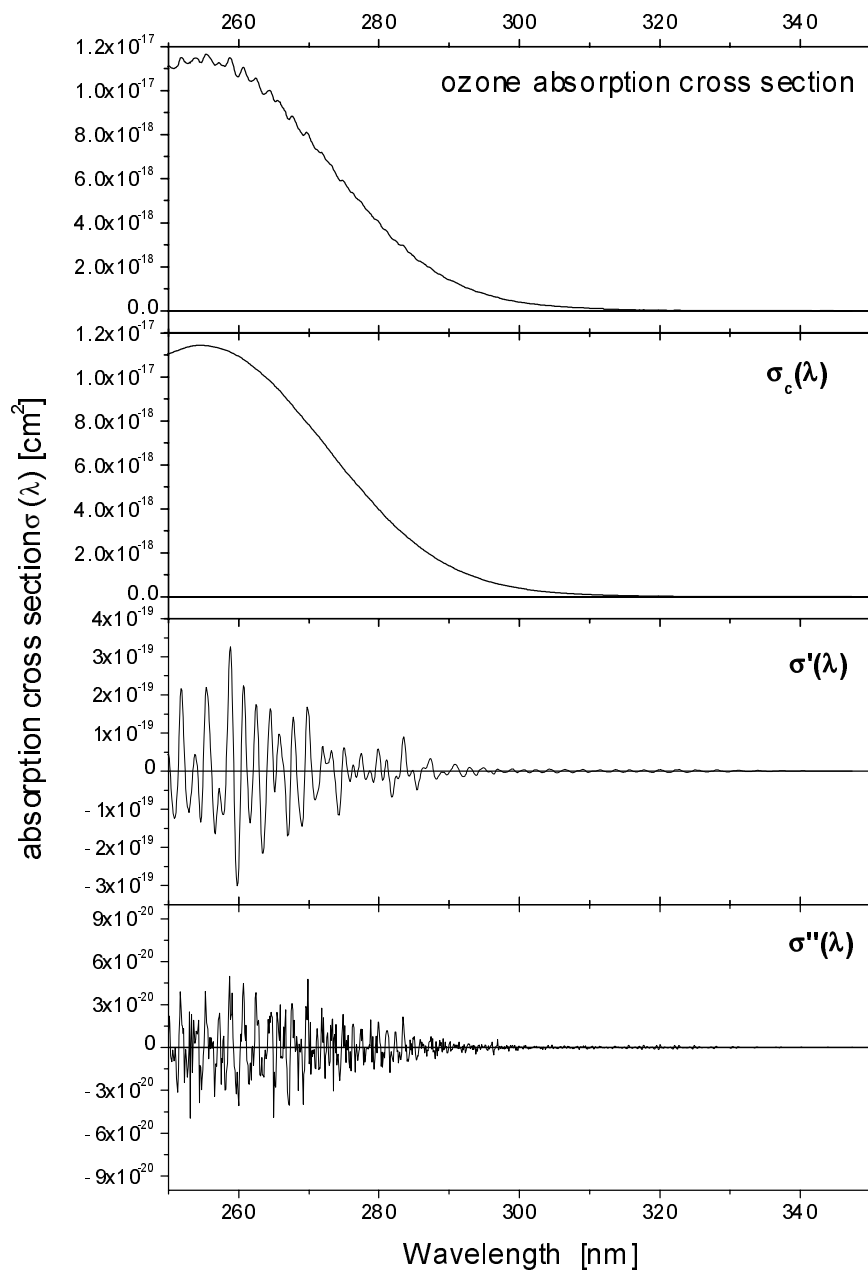


Figure 3.3: The fundamental DOAS principle is the separation of the absorption cross-section (in this example of ozone, upper part) into 'slowly' varying (broad band, second from top), 'rapidly' varying (narrow band, third from top), and high frequency parts (bottom graph) by applying a numerical band pass filter in the evaluation procedure.

The overlaying absorption structures of several trace gases are represented by the sum in Equation 3.5. In practice the number of absorbers m can be limited to those trace gases with their absorption structures are sufficiently strong to be detectable with the respectively used DOAS instrument. As the strength of the absorption structures varies with wavelength, the number of trace gases to be included in Equation 3.5 varies with the observed wavelength interval and the trace gas composition of the probed airmass. Typically $m = 2$ to 10 trace gas absorptions can be identified in a single atmospheric DOAS spectrum [Platt 1994]. The concentrations of these trace gases can, therefore, be measured simultaneously. To retrieve the concentrations, the superimposed absorption structures have to be separated numerically. The task of the evaluation procedure is: (1) to retrieve the parameters a'_j (Equation 3.5) and thus the concentration of the trace gases taking into account all the atmospheric and instrumental effects. (2) to estimate the error $\Delta a'_j$ of the parameters a'_j and therefore of the measured trace gas concentrations. Both tasks can be solved with linear least-squares methods if no instrumental effects are encountered [Stutz and Platt 1996].

3.2.2 The analysis procedure

The evaluation procedure is based on a model that describes the physical behavior of DOAS spectra according to Equation 3.5. The logarithm of the discrete measured intensity, $J(i)$, is modeled by a function $F(i)$:

$$F(i) = P_r(i) + \sum_{j=1}^m a_j \cdot S_j(d_{j,0}, d_{j,1}, \dots)(i) \quad (3.6)$$

where the absorption structures of the trace gases S_j , e.g. measured in the laboratory are input data to the procedure. The polynomial $P_r(i)$ describes the broad spectral structures caused by the characteristics of the lamp $I_0(i)$, the scattering processes $R'(i)$ the spectral sensitivity $A'(i)$, the broad absorptions by the trace gases $B'(i)$ and can be expressed as:

$$P_r(i) = \sum_{h=0}^r c_h \cdot (i - i_c)^h \quad (3.7)$$

where the parameter $i_c = \text{int}(n/2)$ represents the center pixel of the spectral region used for the evaluation. The polynomial refers to i_c to maximize the influence of the nonlinear terms. The scaling parameters a_j (Equation 3.6) and the polynomial coefficients c_h (Equation 3.7) are found by linearly fitting F to J . The scaling factors

a_j are in the further used to calculate the average concentration of the respective trace gases:

$$\bar{c}_j = \frac{a_j}{\sigma'_j \cdot L} \quad (3.8)$$

where σ'_j denotes the differential absorption cross-section of trace gas j , L the absorption path-length.

The analysis procedure aligns the reference spectra $S'_j(i)$ (wavelength-pixel-mapping Γ_j) to the spectrum $J(i)$ (wavelength-pixel-mapping Γ_J). The procedure therefore has to recalculate the reference spectrum $S_j^*(i)$ with the wavelength-pixel-mapping Γ_J . This can be seen as 'shifting and stretching/squeezing' the reference spectrum in wavelength. As Γ_j (identical to Γ_I in Equation 3.3) is a strong monotonous function, its inverse also can be described by a polynomial:

$$\Gamma_j^{-1} : x(\lambda) = \sum_{k=0}^q \beta_k \cdot \lambda^k \quad (3.9)$$

where $x(\lambda)$ represents the non integer 'pixel number' that results from this inverse transformation. $S_j(\lambda)$ can now be calculated from the continuous spectrum $S_j(x)$. This spectrum has to be approximated using a cubic spline interpolation on the discrete spectrum $S_j(i)$.

$S_j^*(i)$ with the wavelength-pixel-mapping Γ_J can be calculated by deriving $S_j(\lambda)$ with Γ_j^{-1} from $S_j(x)$, which is approximated by a interpolation on $S_j(i)$, and then applying Γ_J :

$$S_j(i) \xrightarrow{\text{interpolation}} S_j(x) \xrightarrow{\Gamma_j^{-1}} S_j(\lambda) \xrightarrow{\Gamma_J} S_j^*(i) \quad (3.10)$$

It is possible to refrain from calculating $S_j(\lambda)$ and combine Γ_j^{-1} and Γ_J to a formula, which links i to x using a polynomial with parameters δ_k :

$$x(i) = x(\lambda(i)) = \sum_{k=0}^{q_s \cdot q_l} \delta_k \cdot i^k \quad (3.11)$$

In the analysis procedure a slightly modified equation equivalent to 3.11 is used, which has the advantage that their spectral alignment parameters $d_{j,k}$, determining the transformation, are zero if the wavelength-pixel-mappings of J and S_j are equal:

$$x = i + f_j(i) \quad \text{with} \quad f_j(i) = \sum_{k=0}^{P_j} d_{j,k} \cdot (i - i_c)^k \quad (3.12)$$

The spectrum $S_j(d_{j,0}, d_{j,1}, \dots)(i) = S_j^*(i)$ has now the wavelength-pixel-mapping Γ_j , which was calculated with the parameters $d_{j,k}$ following Equations 3.10 and 3.12 and a cubic spline interpolation on $S_j(i)$. The parameters $d_{j,k}$ are derived by performing a nonlinear fit of the model F to the spectrum J with fixed parameters a_j and c_h . If $p_j = 0$ the spectrum S_j is shifted by $d_{j,0}$ pixels, if $p_j = 1$ the spectrum is additionally linearly squeezed or stretched according to parameter $d_{j,1}$. Higher values of p_j represents a squeeze or stretch of higher order. To achieve the best physical description of the spectra, it is possible to select the degree of the squeeze process p_j for every reference spectrum S_j . It is also possible to use one set of parameters $d_{j,k}$ for two or more reference spectra if the wavelength calibration is identical for these spectra. The analysis procedure is a combination of the well-known nonlinear Levenberg-Marquardt-Method [Levenberg 1944; Marquardt 1963] determining $d_{j,k}$ and a standard linear least-squares fit [Albritton *et al.* 1976; Bevington 1969] to derive the a_j and the c_k . Both methods minimize χ^2 between F and J:

$$\chi^2 = \sum_{i=0}^n (J(i) - F(i))^2 \quad (3.13)$$

The procedure begins with the calculation of the linear fit with starting values $d_{j,k}$. The results of this fit, the parameters a_j and c_k , are used as input data in the following call of the nonlinear Levenberg-Marquardt fit. Only one step of this nonlinear iterative method is then performed. The resulting parameters $d_{j,k}$ are used in the next call of the linear fit. This results are used in the next call of the nonlinear fit. The procedure then invokes the two methods alternating, always using the result of the last call of one method as values for the other fit method. This procedure is repeated until one of several stopping conditions for the nonlinear fit is fulfilled. Normally the fit is aborted, when the relative changes of χ^2 in the last step is smaller than a given value (usually 10^{-6}) and thus the fit has converged. The fit also stops if a number of repetitions of the iteration, determined by the user, is exceeded or if the nonlinear method becomes unstable [Gomer *et al.* 1993; Stutz and Platt 1996].

In Figure 3.4 a sample evaluation is shown for the spectral range between 432 nm and 463.5 nm as it was used to derive the concentration of glyoxal and NO_2 . The spectrum shown in the upper part (indicated A) was recorded in experiment PX24 (see also Figure 4.15) at 11:45 GMT. The spectrum was corrected for offsets and divided by a background spectrum recorded in the clean chamber. In addition to the reference spectra of NO_2 (Part B)) and glyoxal (Part C)) spectral features of the lamp need to be corrected in this spectral range. This was done by simultaneously

fitting two independent reference spectra of the lamp which are added and shown in the part indicated D). In the lower most part E) the residual structure that remained after subtracting all the shown reference spectra is shown. Note that part E) is expanded by a factor of five as compared to parts A)-D).

3.2.3 The DOAS system

The components of the DOAS-system are described in more detail elsewhere [Etzkorn *et al.* 1996; Etzkorn 1998]. The basic components of the DOAS-system are briefly summarized here: light source, White-system, spectrograph-detection unit as well as a PC for data-storage. As light-source, a 500 W high-pressure Xenon short-arc lamp was used (PLI HSAX5002). The White-system is described in more detail below. The spectrograph-detection-unit consists of a UV-transmittive quartz-fiber (AS UV...Vis, $\varnothing_{optical} = 200\mu\text{m}$) equipped with a mode-mixer [Stutz and Platt 1997] coupled to an ACTON Spectra Pro 500. This f/6.9-spectrograph has a focal length of 500 mm and is equipped with three plane diffraction gratings (grating #1: 1200 grooves/mm, blaze: 300 nm, dispersion: 0.03894 nm/pixel (around 272 nm central wavelength), spectral resolution: FWHM = 0.2 nm; grating #2: 600 grooves/mm, blaze: 500 nm, dispersion: 0.07645 nm/pixel (around 643 nm central wavelength), spectral resolution: FWHM = 0.4 nm; grating #3: 300 grooves/mm, blaze: 300 nm, dispersion: 0.16199 nm/pixel (around 329 nm central wavelength), spectral resolution: FWHM = 0.84 nm) interchangeable upon computer control. It was thermostated to a temperature of $T = (301 \pm 0.2)$ K. For recording of the spectra, a 1024-pixel photodiode-array detector (Hoffmann Messtechnik, photodiode array: Hamamatsu S3904-1024N, cooled to a temperature of $T = (253 \pm 0.2)$ K) is mounted in the focal plane of the spectrograph. A more detailed description of the basic components of the DOAS-system is found in Etzkorn [1998].

The White-System

The White-system coupled to the DOAS system is based on the design first presented by [White 1942; White 1976] and further developed by Ritz [1992]. It was incorporated into the EUPHORE-facility by Etzkorn [1998] and further improved within this work, as described in Section 3.2.4.

In the following, the components of the White-system are listed and their function is briefly addressed:

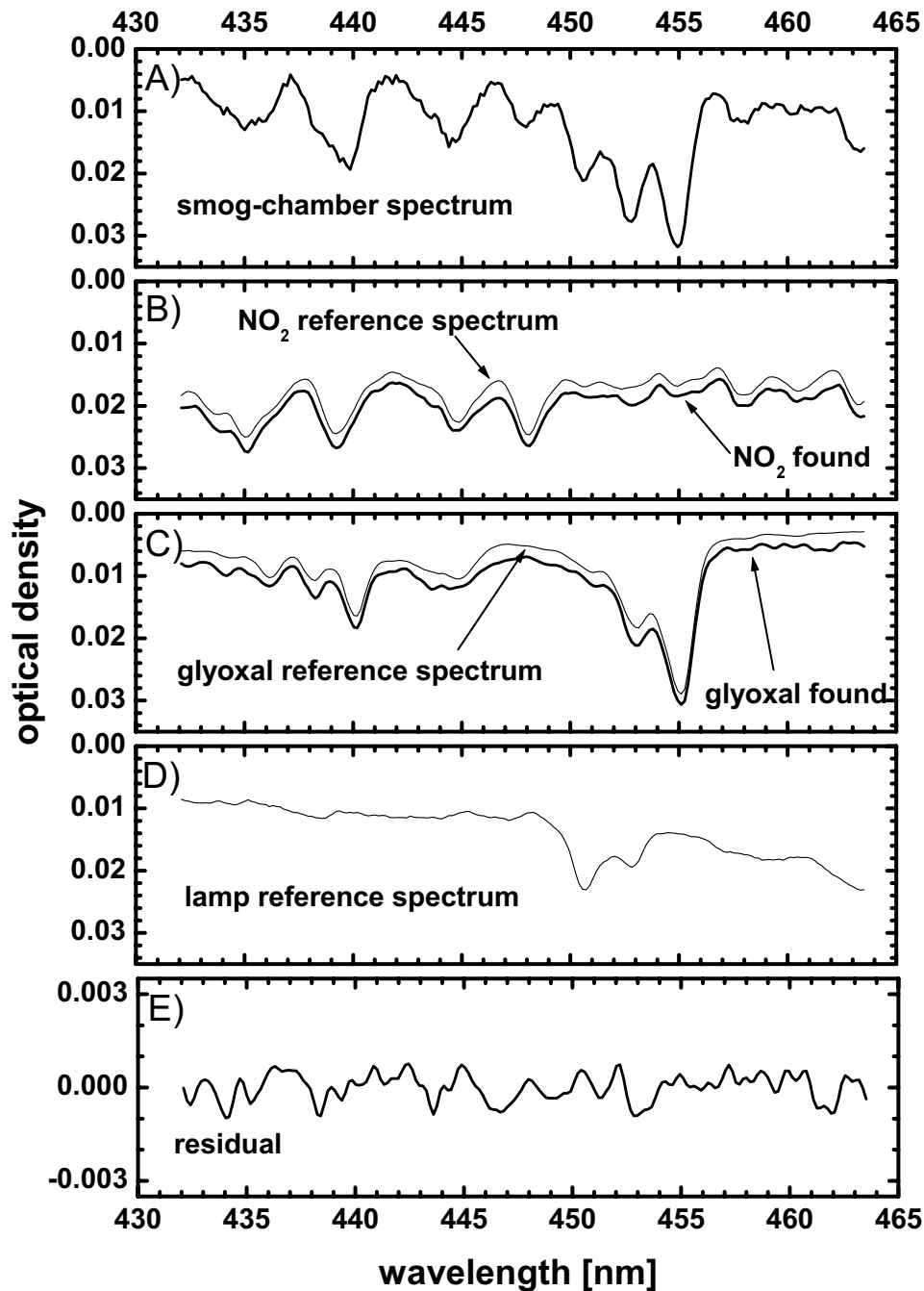


Figure 3.4: Sample evaluation of a spectrum measured in the p-xylene oxidation experiment PX24 at 11:45 GMT. Part A): the measured smog-chamber spectrum; Part B): (thin line) scaled reference spectrum of NO₂ ($\approx 7.6 \cdot 10^{11}$ molec·cm³ or ≈ 30 ppb), (thick line) reference spectrum with added residual; Part C) (thin line) scaled reference spectrum of glyoxal ($\approx 1.6 \cdot 10^{12}$ molec·cm³ or ≈ 63 ppb), (thick line) reference spectrum with added residual; Part D) scaled lamp reference spectrum (see text); Part E) residual (here: $1.7 \cdot 10^{-3}$ peak to peak, shown on an expanded scale).

- The **transfer-optics** consists of two Newton-telescopes. Each Newton-telescope consists of one plane-mirror, elliptical in shape and one spherical-mirror. The transfer optics matches the f-numbers of the White-system (F53) to that of the in- and out-coming light-beam (F6.9).
- the **field-mirror** consists of a round spherical objective-mirror (diameter $\varnothing_{\text{optical}} = 25$ cm; focal length $f = 4$ m) mounted inside an aluminum-frame which further supports a round-shaped diaphragm (in-coming light beam). The field-mirror is cut on one side to allow the mounting of the quartz-prisms (see below). The manual adjustment of the field mirror is possible in two degrees-of-freedom.
- three **quartz-prisms**, different in shape, are mounted on the aluminum-support of the field-mirror. The adjustment of each of the three prisms is possible independently in three-dimensions.
- the two **objective-mirrors** consist of a round spherical-mirrors each (diameter $\varnothing_{\text{optical}} = 15$ cm; focal length $f = 4$ m) which are mounted inside of commercially available cardan-type mirror-holders. The two degrees-of-freedom of each mirror-holder are coupled to four stepper-motors which allow to change the relative orientation of the objective-mirrors relative to the field mirror. These stepper motors are controlled from the automated laser-alignment (see Section 3.2.4).

The field-mirror and objective-mirrors are mounted in a distance of approximately (8 ± 0.15) m facing each other (the exact distance varies slightly with the employed set of mirrors). The light from the light-source enters the White-system via the diaphragm near the field-mirror. It is projected without amplification by one of the objective-mirrors back to the field-mirror where an image of the diaphragm is generated in the plane of the field-mirror. This image serves as object for the second projection etc. From this set-up two rows of light-dots are generated on the field-mirror. At that place where the light-beam misses to hit the field-mirror the first of the three prisms is mounted. The function of each prism is twofold. First, each prism shifts the object-light-dot by a few centimeters. With each traversal of a prism this generates for each existing light-dot a neighboring light-dot in the distance of the shift in the light-beam. Each prism thereby doubles the light-path. Second, the light-beam is back-reflected into the direction that the light-beam entered the prism thereby compensating small de-adjustments in the White-system (e.g. caused

from density fluctuations along the light-beam which deviate the light-beam, de-adjustment of the objective-mirrors). This way of stabilizing the White-system is limited to small de-adjustments that do not cause the light-beam to miss one of the prisms. The number of traverses inside the White-system can be varied at EU-PHORE between 16, 48, 80, 112 and 144 traverses. The minimum and maximal achievable path-lengths are 130 m and 1154 m, respectively.

For further details on the White-system see [Ritz 1992; Volkamer 1996; Etzkorn 1998; Ackermann 2000; Aliche 2000].

3.2.4 Improvements to the DOAS system

The original set-up of the DOAS-system as described by *Etzkorn* [1998] has been subject to changes in order to increase the absorption path length, up-to-then limited to 130 m in the open chamber [Etzkorn 1998], to a maximum achievable path length (1154 m). The effects that had to be overcome are characterized in detail in two diploma-thesis that were carried out at the University of Heidelberg in cooperation with the CEAM Institute [Utz 1997; Ücker 1999]. In brief, dis-alignment of the White-system caused a reduction of the light intensity available for the DOAS-measurements. The dis-alignment could become that large, that the light beam missed the prisms located near the main mirror and no light reached the detector at all. Three effects were identified responsible for the dis-alignment and are summarized as follows:

- Upon opening of the chamber the movement of the heavy steel housing (approximate weight of 20 t) caused bending of the aluminum floor panels that support the mirror of the White-system and dis-align the mirror system.
- Similarly, thermal heating of the floor panels upon exposure to sun-light transfer into a change of the relative orientation of the field mirror towards the objective mirrors.
- The chamber is exposed to a slight overpressure (≈ 0.05 mbar) in order to keep it inflated. Given the large surface of the chamber, considerable forces act via the teflon foil and lift up the panels that support the mirrors of the White system.

For a quantitative description of these effects see *Utz* [1997]. The following changes were applied to the original set-up:

- The measurement platform below the chamber, where the transfer optics is located, was changed. The main mirror inside the chamber was mechanically dis-coupled from the floor panels and coupled to the measurement platform where the transfer optics is located [Utz 1997].
- An automatic laser-alignment system [Geyer 1997] was incorporated into the chamber that actively compensates the dis-adjustments of one objective mirror and maintains it in a fix relative position to the field mirror [Utz 1997]. The alignment of the second mirror at that stage was performed from optimizing the light intensity that reached the detector from the measurement software package Mfc [Gomer et al. 1993] as described earlier [Etzkorn 1998].
- The laser-alignment electronics was improved [Ücker 1999] in order to actively align also the second objective mirror. The thus dis-coupled alignment of the White-system from the measurement software allowed to improve the time-resolution of the DOAS measurements.
- The detector of the second laser-alignment was mounted on a stepper-motor allowing to move it horizontally in the plane of the field mirror. In this set-up, a change of the pathlength (number of traverses) is realized from moving the stepper motor (controlled from the software package Mfc). The thus moving detector forces the objective mirror to follow it via the laser alignment until the desired position is reached. An optimized software package was developed (see annex) that sequentially controls both laser-alignments at a sufficiently high frequency in order to allow changes of the pathlength within few seconds. Any desired pathlength in this setup corresponds to a fix absolute position of the stepper motor.
- All components of the actively aligned White-system were equipped with a shade made of teflon to avoid direct heating of the lasers and optics from sunlight.
- An optimized design for a quartz-fiber bundle was developed. Preliminary tests have been performed which are not further described here. An improvement of the light-balance of the White-system by a factor of five to ten is likely.

3.2.5 Detection limits of selected trace gases

The improved DOAS set-up allows the detection of various trace-gases at an increased pathlength. In Table 3.1 typical detection limits are given for the respectively specified spectrometer settings, using different mirror sets and pathlengths for the detection of selected compounds.

In Figure 3.5 the differential absorption cross-sections $\sigma'(\lambda)$ of selected trace gases are shown (left axis). For these species, typical detection limits are indicated on the right axis for the respectively indicated absorption pathlengths.

3.3 Further analytical instruments employed

In addition to the data obtained from the DOAS-system, the data from the following equipment is relevant to the results of this work:

- FTIR (Fourier Transform InfraRed spectroscopy): the second White-system (see Figure 3.1) is coupled to an IR-interferometer. It is equipped with gold-coated mirrors and was operated at 40 traverses, corresponding to an absorption path length of 326.8 m. The FTIR interferometer, a NICOLET Magna 550 equipped with a liquid-N₂-cooled MCT detector, was operated to yield spectra of the spectral range between 400 cm⁻¹ and 4000 cm⁻¹ at 1 cm⁻¹ spectral resolution. Typically, 280 to 550 scans were co-added yielding a time-resolution of 5 to 15 minutes.
- GC-FID (gas chromatography, flame-ionisation-detection): a Hewlet Packard 6890 equipped with a HP-5 column (crosslinked 5% PHME silicone 30 m x 0.32 mm x 0.25 μm) was operated at a constant temperature to follow the decay of aromatic educt (e.g. benzene: T = 40°C). Sampling was performed via a teflon-tube directly connected to the chamber. Gas samples were injected onto the column from the sampling loop typically every 4 minutes.
- J_{NO₂} filter radiometers: photolysis-frequencies of NO₂ were measured by 2 filter radiometers which covered a 180° field of view each. One of the radiometers was pointed upwards to measure the UV-flux from the upper hemisphere, the other one was pointed towards the floor to measure the flux reflected by the floor panels. Maximum daytime values for the sum of both channels were J_{NO₂} ≈ 9·10⁻³ s⁻¹.

Table 3.1: Detection limits of the DOAS set-up at EUPHORE.

Compound	Calibration	Spectrometer Settings ^a	Mirror-set ^b	Path-length [m]	Detection Limit ^c [ppt]
Ozone	[<i>Bass and Paur</i> 1985]	#1, 272 nm	Alu	386	3000
SO ₂	[<i>Vandaele et al.</i> 1994]	#1, 290 nm	Alu	386	260
NO ₂	[<i>Harder et al.</i> 1997]	#1, 350 nm	Diel	1154	800
		#1, 450 nm	Diel	1154	500 ^d
NO ₃	[<i>Wayne et al.</i> 1991]	#2, 643 nm	Ag	1154	20
HONO	[<i>Stutz et al.</i> 1999]	#2, 350 nm	Diel	1154	500
HCHO	[<i>Cantrell et al.</i> 1990]	#1, 350 nm	Diel	1154	3500
		#1, 330 nm	Diel	1154	2500 ^d
GLY	see Section 5.1.2	#1, 450 nm	Alu	386	1500
		#1, 450 nm	Diel	1154	500 ^d
Benzene	[<i>Etz Korn et al.</i> 1999]	#1, 272 nm	Alu	386	500
Toluene	[<i>Etz Korn et al.</i> 1999]	#1, 272 nm	Alu	386	650
p-Xylene	[<i>Etz Korn et al.</i> 1999]	#1, 272 nm	Alu	386	450
TMB	[<i>Etz Korn et al.</i> 1999]	#1, 272 nm	Alu	386	1900
BALD	[<i>Etz Korn et al.</i> 1999]	#1, 284 nm	Alu	386	180
pTALD	[<i>Etz Korn et al.</i> 1999]	#1, 284 nm	Alu	386	350
DMBA	[<i>Ücker</i> 1999]	#1, 284 nm	Alu	386	900
PHEN	see Section 5.1.1	#1, 272 nm	Alu	386	50
pCRE	[<i>Etz Korn et al.</i> 1999]	#1, 272 nm	Alu	386	100
DMP	[<i>Etz Korn et al.</i> 1999]	#1, 272 nm	Alu	386	1200
TMP	[<i>Etz Korn et al.</i> 1999]	#1, 272 nm	Alu	386	1700

^a first number: # of grating (see Section 3.2.3), second number: central wavelength.

^b Alu: Aluminum coating; Ag: Silver coating; Diel: dielectric coating.

^c for typical experimental conditions, conversion factor: 1 ppt $\equiv 2.46 \cdot 10^7$ molec \cdot cm⁻³.

^d possible with optimized set-up.

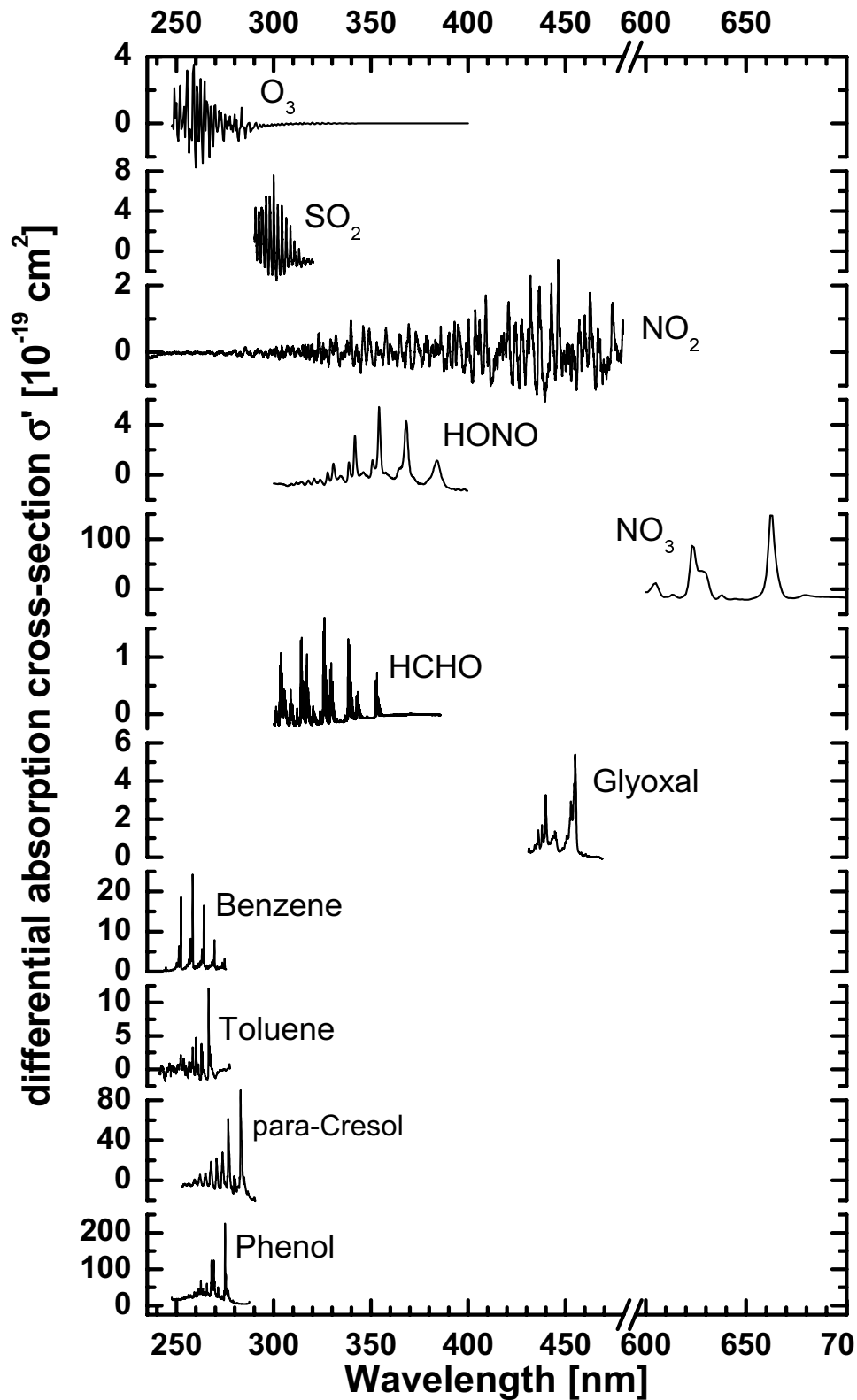


Figure 3.5: Differential absorption cross-sections $\sigma'(\lambda)$ of selected trace gases and typical detection limits for the DOAS measurement using the set-up at EUPHORE at the respectively indicated absorption pathlength L .

- NO_x -monitor: a gas phase chemoluminescence NO_x -analyser equipped with photolytic NO_2 -converter (ECO Physics CLD 770) was used for the detection of NO and NO_2 . It was typically operated in the maximum NO_x -range of 500 ppb. The integration-time of the three sequentially measured channels was 30 seconds, resulting in a time-resolution of the measurements of about 2 minutes. The calibration of the NO_2 -channel of the device was performed periodically.
- ozone-monitor: a photometric ozone-monitor (Monitor Labs ML9810) was used. It was operated in either the 500 ppb or 1 ppm range.
- particle-counter: a TSI particle counter (model 3022A) was used in selected experiments. This device only obtained information about the integral number-density of particles (diameters between 7 nm and $3\ \mu\text{m}$) and no information about the particle volume was accessed.
- hygrometer: the dewpoint temperature T_{DEW} and air-temperature inside the reactor was monitored by a Walz TS-2. With one exception (experiments using radical-source (2), see Section 3.4.4) the chamber air during the experiments was dry ($T_{DEW} < -40^\circ\text{C}$) reflecting that water was efficiently removed from the air-drying-system (see above).
- thermo-sensors: temperature was measured in addition from at least two Pt-100 temperature dependent resistors, one measuring the floor-temperature and the other the air-temperature inside the chamber. Inter-comparison of the PT-100 and Walz TS-2 measurements of the air-temperature yielded agreement within $\Delta T \leq 0.2^\circ\text{C}$ throughout the experiments.

The data from the J_{NO_2} filter radiometers, NO_x monitor, ozone-monitor, particle-counter, hygrometer and thermo-sensors were stored to the hard-disk of a PC acting as a data-acquisition-unit. In addition, data from the OH-LIF device (laser induced fluorescence) is shown (see Figure 4.7) that was obtained from joint experiments with the BUGH Wuppertal. The OH-LIF was operated by the BUGH Wuppertal and is described in more detail elsewhere [Becker *et al.* 1999]. As further employed equipment GC-ECD (electron capture detection) was used for measurements of PAN in selected experiments (not shown). For an overview of the available equipment at EUPHORE see Becker [1996].

Throughout this work the concentration-data derived from spectroscopic measurements is given in units of $\text{molec}\cdot\text{cm}^{-3}$. Only exceptionally these quantities have been converted into ppb (parts per billion, $0.001 \text{ ppm} = 1000 \text{ ppt} = 1 \text{ ppb} = 2.46 \cdot 10^{10} \text{ molec}\cdot\text{cm}^{-3}$ at $T = 298 \text{ K}$) for reasons of simplicity. The concentration-data from point-sampling devices (GC-FID, ozone-monitor, NO_x -monitor etc.) is given in units of ppb.

3.4 Experimental conditions

The experiments described in this work were set-up as follows. The closed chamber was flushed over night. After the flushing was turned off and a reference background spectrum was recorded with the DOAS and FTIR instrument in the clean chamber. After the data-acquisition-unit (see Section 3.3) had been started reactants were introduced. First, about $7.5 \cdot 10^{11} \text{ molec}\cdot\text{cm}^{-3}$ of SF_6 were added. The introduction of reactants is described in the respective Section. The radical production in the experiments was started as described in the respective part of Section 3.4.3. After each experiment, the closed chamber was flushed over the night.

3.4.1 Calibration experiments

For the experiments to measure absorption cross-section spectra (that serve as a calibration for the DOAS measurements), the chamber was first prepared as described above.

Phenol

For the determination of the PHEN absorption cross section, pre-weighed amounts of PHEN were dissolved in water and introduced into the reactor via the spraying unit. Spectra were recorded using a pathlength of 130 m at a spectral resolution of 0.2 nm (grating 1) at various PHEN concentrations between $2 \cdot 10^{11} \text{ molec}\cdot\text{cm}^{-3}$ and $8 \cdot 10^{11} \text{ molec}\cdot\text{cm}^{-3}$.

Glyoxal

For the determination of the UV-spectrum of GLY this compound was synthesized as follows. About equal amounts of glyoxal-trimer-dihydrate and phosphorus pentoxide were mixed in a glass reaction vessel and heated gently to about 180°C . The glyoxal monomer, formed as a product of dehydration in the gas-phase, was transferred

by a stream of nitrogen into an impinger cooled by a bath of liquified ethanol to a temperature of -80°C where it was trapped. When the reaction had ceased, the trap was disconnected and maintained cold while it was connected to the chamber. GLY was extracted by removing the cold trap from the ethanol bath and gently heating, allowing the GLY to sublimate in a stream of dried air connected to the chamber. Spectra were recorded at two absorption paths (386 m and 514 m) and spectrometer settings (grating 1: spectral resolution of 0.17 nm, central wavelength of the spectral range under observation: $\lambda_{centre} = 450$ nm; grating 3: spectral resolution of 0.84 nm, $\lambda_{centre} = 470$ nm) varying the observed column density of GLY and the resolution of the spectrometer.

3.4.2 Kinetic studies

For the experiments to determine the OH- and NO_3 rate-constants the chamber was first prepared as described above. Then, the target and reference compounds were introduced into the chamber injecting the liquid compounds via the sprayer unit. PHEN and isomers of CRE were dissolved in about 10 ml of water, while the 2,5-DMP was dissolved in about 1-2 ml of acetonitril and hence these compounds introduced into the chamber via the spraying unit. Typical concentrations of reactants ranged between $1.2 \cdot 10^{12}$ molec $\cdot\text{cm}^{-3}$ and $5 \cdot 10^{12}$ molec $\cdot\text{cm}^{-3}$ and were chosen to give a reasonable signal to noise ratio ($\text{S/N} \approx 50$) in the UV-absorption signal. For those experiments where the rate-constants of products of 1,3,5-TMB were determined relative to the rate-constant of 1,3,5-TMB the initial concentrations of reactants were chosen to influence the apparent decay by less than 3%. Prior to the experiment, the loss of reactants was monitored over periods between 30 minutes to 3 hours in the dark. For the OH-kinetic experiments HONO was used as a source of OH-radicals (see Section 3.4.4). For the NO_3 -kinetic experiments two different radical-sources were employed (see Section 3.4.5).

The photolysis of aromatic aldehydes

The experimental set-up is identical to that described above. As an OH-scavenger about $6 \cdot 10^{14}$ molec $\cdot\text{cm}^{-3}$ cyclohexane (CYHE) were added ($k_{\text{OH,CYHE}} = (7.20 \pm 0.53) \cdot 10^{-12}$ cm $^3 \cdot (\text{molec} \cdot \text{s})^{-1}$, [*Kramp and Paulson 1998*]). In addition to the aromatic aldehydes, about $2.8 \cdot 10^{14}$ molec $\cdot\text{cm}^{-3}$ of BEN were added as a tracer for OH-radicals (see Section 3.5.6).

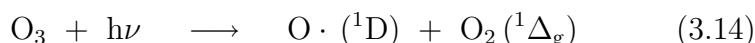
3.4.3 Product studies

For the experiments to determine the product yields the chamber was first prepared as described above. All investigated compounds were liquids and their amount was determined by volume from calibrated syringes before it was injected into the reactor via the spraying-unit. The initial gas-phase concentrations of each experiment is listed together with the respectively employed radical-source in Table 4.5 (BEN), Table 4.7 (pXYL) and Table 4.8 (product studies on GLY). The loss of compounds was monitored between 30 minutes to 3 hours in the dark.

3.4.4 Employed OH-radical-sources

To generate OH-radicals the following five sources were applied:

1. "Photosmog" system: In this system an aromatic reactant, NO and if applicable an OH-tracer were introduced into the chamber and the system was left approx. 30 minutes for stabilization in the dark. The radical formation in the experiments was started from opening the chamber housing. The origin of the initially formed OH-radicals is presently not completely clarified but most likely involves the photolysis of small amounts of HONO (see below).
2. Ozone-photolysis system: In this "NO_x-free" system, ozone (60 ppb to 300 ppb) and water vapor (approx. 50% relative humidity) were introduced into the chamber. The radical formation in the experiments was started by opening the chamber housing. Photolysis of ozone forms OH-radicals from the following reaction sequence:



where radical-type species are indicated by a dot. The primary photochemical process is most effective in the presence of light corresponding to $\lambda < 310$ nm. This OH-source was hence used primarily during the summer months, when the UV-flux is maximal. After exposing the chamber to sunlight, small amounts of NO_x were observed to build up in the reaction-system. Typical NO_x-concentrations were below 2 ppb.

3. HONO-system: About $5 \cdot 10^{11}$ molec·cm⁻³ to $2.5 \cdot 10^{12}$ molec·cm⁻³ of HONO were introduced together with small amounts of NO and NO₂ into the chamber.

The radical formation in the experiments was started by opening the chamber housing. Photolysis of HONO forms OH-radicals:



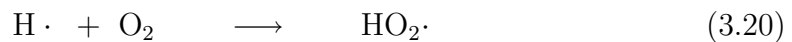
This process requires light corresponding to $\lambda < 390$ nm. Typically about 100 ppb of NO were added in addition to delay the formation of ozone in the system.

4. H₂O₂-system: About $5 \cdot 10^{11}$ molec·cm⁻³ of H₂O₂ were added by injecting an aqueous solution of 30 %. The radical formation in the experiments was started by opening the chamber housing. Photolysis of H₂O₂ forms OH-radicals:



The absorption cross-section of H₂O₂ rapidly drops above the cutoff wavelength at $\lambda \approx 290$ nm. As in the case of ozone, this OH-source was hence primarily used in the summer months, when the UV-flux is maximal. Again, small amounts of NO_x were observed to build up in the reaction-system, typically below 2 ppb.

5. HCHO-system: About $1.5 \cdot 10^{12}$ molec·cm⁻³ of HCHO and 20 ppb of NO were added. The radical formation in the experiments was started by opening the chamber housing. HCHO photolysis generated OH-radicals from the following reaction sequence:



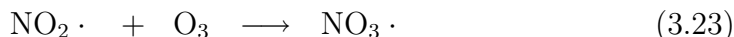
The primary photochemical process (reaction (3.18)) leads to the formation of OH-radicals, while reaction (3.19) forms non-radical products. Reaction (3.18) requires light corresponding to $\lambda < 330$ nm while reaction (3.19) is operative already at longer wavelengths [Atkinson *et al.* 1997]. Hence, the relative fraction of these photolysis channels will depend on the solar zenith angle (SZA) and the maximum OH-formation is expected around noon.

Selected rate-constants and photolysis-frequencies of relevance for these OH-sources are included in Table 3.2.

3.4.5 Employed NO₃-radical-sources

Two different sources to generate NO₃-radicals in the closed chamber were employed:

1. The NO₂/ozone-system: NO₃-radicals were generated from the reaction:



The rate-constant for this reaction at T = 298 K is $k_{3.23} = 3.2 \cdot 10^{-17} \text{ cm}^3 \cdot (\text{molec} \cdot \text{s})^{-1}$ [DeMore *et al.* 1997]. About 200 ppb of ozone were introduced into the reactor together with the reactants (described above). Ozone was generated by passing a stream of pure oxygen through an ozone generator. This device generates oxygen atoms from silent discharge that further re-combine with molecular oxygen to produce ozone. The radical formation in the experiments was started by adding about 200 ppb of NO₂ into the gas-stream connected to the chamber.

2. The N₂O₅-system: NO₃-radicals were generated from the thermal decomposition of N₂O₅.



The method is described in detail by *Wängberg et al.* [1997] and uses a separate reaction volume (pre-reactor) to form N₂O₅ from the titration reaction of NO₂ with ozone. The NO₃-radicals formed from the above Reaction 3.23 in the pre-reactor primarily react with NO₂ to form N₂O₅ which decomposes back to reactants. At typical reactor temperatures, the thermal lifetime of N₂O₅ is of the order of several ten seconds and almost instantaneously forms NO₃-radicals once the N₂O₅ is diluted in the reactor. The radical formation in the experiments was started from connecting the gas-stream of N₂O₅ to the reactor.

The main difference between the two employed NO₃-radical-sources is the NO₂-concentration during the initial phase of the experiment. With the first method the initial concentration of NO₂ is comparably high (200 ppb) and decreases with the reaction progresses. Using the second method almost no NO₂ is present in the initial phase of an experiment and the NO₂ concentration increases with reaction-time due to the continuously added N₂O₅.

3.5 Evaluation procedures

This Section first gives an overview about the rate-constants employed in the various evaluation procedures to derive the results of this study. The well established relative-rate method (employed to derive the OH- and NO₃ rate-constants) is briefly described and the evaluation methods employed to derive the monoexponential loss-rates, i.e. photolysis-frequencies, wall-deposition-rates and leakage. Finally, the various evaluation methods that were used to derive the product yields are presented.

3.5.1 The kinetic data used in the evaluation

In Table 3.2 the rate-constants of aromatic reactants, products and further inorganic species are listed as they were used in the evaluations for this work. The data correspond to the recommended values at T = 298 K (see also the notes in the Table). The temperature dependent recommendations quoted in the notes were used to calculate corresponding values at different temperatures. The accuracy of the rate-constants is discussed where applicable in the respective Sections. Table 3.2 also includes selected kinetic data that was determined within this work (see Section 4.2). Results have been quoted here if either no kinetic data was up-to-now available in the literature or the error limits of the presently recommended k-values were significantly reduced within this work (see Section 5.2). The photolysis-frequencies of glyoxal (J_{GLY}) and formaldehyde (J_{HCHO}) are given as estimates here. Photolysis-frequencies in general were scaled linearly, relative to the measured J_{NO₂}, before applied. The J-value for GLY was calculated from the expression listed in the notes of Table 3.2. The J-value for NO₃-photolysis was calculated as J_{NO₃} = 20.6 · J_{NO₂}. That for HCHO-photolysis was calculated using the parametrization from *Derwent et al.* [1998] and was scaled accordingly. The atmospheric lifetime $\tau_{daytime}$ was calculated from the listed kinetic parameters of Table 3.2 based on the assumptions described in the notes of the Table.

3.5.2 Calibration experiments

The absorption cross-section of PHEN was determined as follows. After each injection the wall-deposition of the compound was characterized and the optical density of PHEN at 275 nm was back-interpolated to derive the optical density at the injection time (see also Section 3.5.4 and Section 4.2.1). The difference in optical density before and after each addition was added and compared with the pre-weighed amounts

Table 3.2: Kinetic parameters and atmospheric lifetimes for selected compounds.

Compound	k_{OH}	k_{NO_3}	k_{O_3}	$J_{phot.}^a$	atmospheric lifetime
	[$10^{-12} \text{ cm}^3 \cdot (\text{molec} \cdot \text{s})^{-1}$]			[10^{-6} s^{-1}]	$\tau_{daytime}^b$
Benzene	1.23 ^c	$< 2.3 \cdot 10^{-5}$			1 d 21 h
Toluene	6.0 ^d	$1.8 \cdot 10^{-5}$			9 h 15 min
p-Xylene	14.3	$1.4 \cdot 10^{-4}$			3 h 53 min
1,3,5-TMB	57.5	$8 \cdot 10^{-4}$			58 min
BALD	12.9	$2.6 \cdot 10^{-3}$		8 ^x	3 h 50 min
pTALD	21.2 ^x			$< 6^x$	2 h 37 min
3,5-DMBA	34.2 ^x			$< 6^x$	1 h 37 min
PHEN	26.3 ^e	3.8			1 h 58 min
pCRE	47	11.2 ^x			1 h 4 min
2,5-DMP	81.7 ^x	24.4 ^x			37 min
2,4,6-TMP	131 ^x				25 min
GLY	11.5	$\approx 2 \cdot 10^{-3}^g$		79 ^h	2 h 2 min
HCHO	9.2 ^{f,k}	$2 \cdot 10^{-3}$		26 ⁱ	3 h 51 min
Ozone	0.068 ^k	$1 \cdot 10^{-5}^l$		26 ⁱ	≈ 4 d
NO ₂	8.9 ^k	1.27 ^k	$3.2 \cdot 10^{-5}^k$	7500 ⁱ	2 min 12 sec
HONO	4.5 ^k		$< 5 \cdot 10^{-7}^k$	1770 ⁱ	9 min 18 sec
NO	7.5 ^k	26 ^k	0.018 ^k		≈ 1 min
H ₂ O ₂	1.7 ^k			6.3 ⁱ	18 h 46 min

The rate-constants correspond to recommended values at $T = 298\text{K}$ [Atkinson 1994].

^a photolysis-frequencies, scaled relative to $J_{NO_2} = 7.5 \cdot 10^{-3} \text{ s}^{-1}$ (see also other notes).

^b based on: $[OH] = 5 \cdot 10^6$; $[NO_3] = 2.5 \cdot 10^6$; $[O_3] = 9.8 \cdot 10^{11}$, units: $\text{molec} \cdot \text{cm}^{-3}$.

^c $k = 2.47 \cdot 10^{-12} \cdot \exp(-207/T) \text{ cm}^3 \cdot (\text{molec} \cdot \text{s})^{-1}$ [Atkinson 1994]

^d $k = 1.81 \cdot 10^{-12} \cdot \exp(+355/T) \text{ cm}^3 \cdot (\text{molec} \cdot \text{s})^{-1}$ [Atkinson 1994]

^e $k = 6.75 \cdot 10^{-12} \cdot \exp(+405/T) \text{ cm}^3 \cdot (\text{molec} \cdot \text{s})^{-1}$ [Atkinson 1994]

^f $k = 8.59 \cdot 10^{-12} \cdot \exp(+20 \text{ K}/T) \text{ cm}^3 \cdot (\text{molec} \cdot \text{s})^{-1}$ [Atkinson et al. 1997]

^g estimated value, based on: $k_{NO_3}(\text{HCHO})$.

^h based on [Klotz et al. 2001]: $J_{GLY} \approx 0.0105 \cdot J_{NO_2}$; here: $J_{NO_2} = 7.5 \cdot 10^{-3} \text{ s}^{-1}$.

ⁱ based on [Derwent et al. 1998]; here: $\text{SZA} = 16$ degrees, $J_{NO_2} = 7.5 \cdot 10^{-3} \text{ s}^{-1}$.

^k reference: [DeMore et al. 1997]

^l reference: [Hjorth et al. 1992]

^x determined as part of this work. See Section 4.2.

of PHEN following in the further the procedure described in [Etzkorn *et al.* 1999].

The absolute value of the absorption cross-section of GLY was determined from cross-calibration with the FTIR. The IR absorption cross-section of [Moortgat 2000] were used for calibration.

3.5.3 The relative-rate method

In the kinetic experiments to obtain the OH- and NO₃-reaction rate-constants the relative-rate method was employed which determines the ratio of the rate-constant of a target compound (k_{target}) relative to the known value of a reference compound ($k_{reference}$) [Atkinson 1986]. The principle of this method is described by:

$$\ln \left(\frac{[\text{TAR}]_{t=0}}{[\text{TAR}]_t} \right) = \frac{k_{\text{TAR}}}{k_{\text{REF}}} \cdot \ln \left(\frac{[\text{REF}]_{t=0}}{[\text{REF}]_t} \right) \quad (3.25)$$

where $[\text{TAR}]_{t=0}$ and $[\text{REF}]_{t=0}$ denote the concentration of the target and reference compound at the start of the experiment, $[\text{TAR}]_t$ and $[\text{REF}]_t$ their concentration at the time t . A graphical representation of $\ln([\text{TAR}]_{t=0}/[\text{TAR}]_t)$ as a function of $\ln([\text{REF}]_{t=0}/[\text{REF}]_t)$ hence should yield a straight line, with the slope corresponding to the ratio between the rate-constant of the target compound k_{TAR} and the rate-constant of the reference compound k_{REF} . In praxis most compounds are not only lost by the reaction under investigation but show further loss through e.g. deposition to the chamber walls, leakage or photolysis. Thus Equation 3.25 needs to be extended:

$$\ln \left(\frac{[\text{TAR}]_{t=0}}{[\text{TAR}]_t} \right) - R_{\text{TAR}} \cdot t = \frac{k_{\text{TAR}}}{k_{\text{REF}}} \cdot \left\{ \ln \left(\frac{[\text{REF}]_{t=0}}{[\text{REF}]_t} \right) - R_{\text{REF}} \cdot t \right\} \quad (3.26)$$

where t denotes the reaction-time and R_{TAR} and R_{REF} represent the sum of all monoexponential loss-processes for the two compounds. The different R -values were determined in separate experiments.

3.5.4 Monoexponential loss-processes

Three loss-processes were approximated monoexponentially in this work: (1) The leakage of the reactor L , (2) the wall-deposition-rate W (see Section 4.2.1) and (3) the photolysis-frequency J (see Section 4.2.4). Any monoexponential loss-process can be characterized by a single parameter, the time constant L , W or J , which all

are expressed in units of s^{-1} . Any loss-rate R , that may be due to one or several of the above processes was determined from:

$$R = \ln \left(\frac{[\text{Comp}]_{t_1}}{[\text{Comp}]_{t_2}} \right) \cdot t^{-1} \quad (3.27)$$

where $[\text{Comp}]_{t_1}$ and $[\text{Comp}]_{t_2}$ correspond to the concentrations of the tracer at the begin and end of the period for which the respective loss-process is studied. If $\ln([\text{Comp}]_{t_2}/[\text{Comp}]_{t_1})$ is plotted as a function of time, a straight line is expected for truly monoexponential loss-processes and R corresponds to the slope of the plotted data. To determine the system-leakage L $[\text{Comp}]$ in Equation 3.27 corresponded to the concentration of SF_6 . For wall-deposition and photolysis $[\text{Comp}]$ corresponded to the concentration of the respective chemical compound under investigation.

The monoexponential loss-processes (1) to (3) are additive. In most cases two or even all three processes were operative. Individual loss-rates were determined by subtracting the respective further processes. The W used to correct for wall-deposition in most experiments were comparable to the mean-values listed in Table 4.1 of Section 4.2.1. Photolysis-frequencies were derived as described in Section 3.5.1.

Further, any compound (e.g. PHEN) that is lost through bimolecular reaction with a reaction partner (e.g. OH-radical) can be attributed a monoexponential loss-rate R_{OH} if the rate-constant, i.e. $k_{OH,PHEN}$ and the concentration of $[\text{OH}]$ are known:

$$R_{OH} = k_{OH,PHEN} \cdot [\text{OH}] \quad (3.28)$$

This is a helpful concept to compare the relative importance of loss via bimolecular reactions and monoexponential loss-processes. The reciprocal value of R , L , W or J is generally identical to the lifetime of the compound for the respective loss-process (in units of seconds).

3.5.5 Employed methods to derive product yields

The following five evaluation procedures (a, b₁, b₂, b₃, c) were employed to determine the product yields $\Phi_{Product}$:

a) The steady-state assumption

The product yield $\Phi_{Product}$ was determined from the measured concentrations of the product and educt when steady-state was reached in the course of an experiment according to:

$$\Phi_{\text{Product}} = \frac{(k_{\text{OH,Product}} \cdot [\text{OH}] + J_{\text{Product}}) \cdot f_c}{k_{\text{OH,Educt}} \cdot [\text{OH}] \cdot [\text{Educt}]} \quad (3.29)$$

where $k_{\text{OH,Educt}}$, $k_{\text{OH,Product}}$ represent the OH-rate-constant of the reactant and product, J_{Product} denotes the photolysis-frequency of the product, values in squared brackets are concentrations of the respective compounds. The concentration of OH was determined from equation 3.36 in Section 3.5.6. The correction factor $f_c = (1+W/(k_{\text{OH,Product}} \cdot [\text{OH}]))$ accounts for product loss to the wall (see Section 3.5.4 and Section 4.2.1).

In the case, the product does not photolyse, Equation 3.29 can be simplified:

$$\Phi_{\text{Product}} = \frac{k_{\text{OH,Product}} \cdot [\text{Product}] \cdot f_c}{k_{\text{OH,Educt}} \cdot [\text{Educt}]} \quad (3.30)$$

In this case the yield becomes essentially independent of the OH-concentration (only f_c depends on [OH]).

b) Direct kinetic analysis of product yields

Three different approaches were applied: approach b₁) derived the product yield within the first few minutes of an experiment with the advantage that loss-processes of the product as well as effects of temperature changes were small in this phase. Approach b₂) determined the product yield over a time span that was considerable longer and corrections for product loss through OH-reaction, wall-deposition were applied as well as temperature changes considered. Approach b₃) determines the ratio of the yield of a target product (Φ_{target}) relative to the known yield of a reference product ($\Phi_{\text{reference}}$).

b₁) Determination of Φ_{Product} from the product production-rate

The product yield Φ_{Product} from the measured production-rate of the product:

$$\Phi_{\text{Product}} = \frac{P_{\text{Product}}}{k_{\text{OH,Educt}} \cdot [\text{OH}] \cdot [\text{Educt}]} \quad (3.31)$$

where P_{Product} denotes the average production-rate of the product over the first few minutes of reaction-time (as measured by DOAS). The average OH-concentration [OH] for this time-interval was determined from equation 3.36 in Section 3.5.6. The average educt concentration [educt] was calculated from the initial educt concentration subtracting the half amount of reacted educt as calculated from the average OH-concentration.

b₂) Determination of $\Phi_{Product}$ from the educt-product time-series

The measured product concentrations determined experimentally were corrected for losses through reaction with OH-radicals, photolysis and wall-deposition. The total amount of product lost from the start time t_0 of an experiment until the time t (coincides with the central recording time of a DOAS spectrum) was then calculated from:

$$[\text{Product}]_{\text{loss}} = \int_{t=0}^t (k_{\text{OH,Product}} \cdot [\text{OH}]_t + J_{\text{Product,t}} + W) \cdot [\text{Product}]_t \cdot dt \quad (3.32)$$

where the OH-concentration $[\text{OH}]_t$ was calculated from equation 3.36. $J_{\text{Product,t}}$ was calculated as described in Section 3.5.1 and was set zero for products that do not photolyse. The wall-deposition-rate W was determined in separate experiments as described in Section 3.5.4 and Section 4.2.1. For the temperature dependent studies, the k -values were determined from the mean temperature of the experiment (see Table 3.2).

A correction factor F was calculated:

$$F = 1 + \frac{[\text{Product}]_{\text{loss}}}{[\text{Product}]_t} \quad (3.33)$$

and applied:

$$[\text{Product}]_{\text{corr}} = [\text{Product}]_t \cdot F \quad (3.34)$$

to determine the concentration of formed product, corrected for secondary loss-processes $[\text{Product}]_{\text{corr}}$. The product yield was hence calculated from the slope of the corrected product concentration plotted as a function of the amount of reacted educt. Data points for which $F > 2$ were discarded in the evaluation throughout this work.

b₃) Relative yield method

The relative yield method is inspired from the well established relative rate method described above.

The measured product concentrations determined experimentally were corrected for losses through reaction with OH-radicals, photolysis and wall-deposition as described above. The ratio of the yield of a target product (Φ_{target}) relative to the known yield of a reference product ($\Phi_{\text{reference}}$) was determined from:

$$\frac{\Phi_{\text{TAR}}}{\Phi_{\text{REF}}} = \frac{P_{\text{TAR}}}{P_{\text{REF}}} = \frac{[\text{TAR}]_{\text{corr}}}{[\text{REF}]_{\text{corr}}} \quad (3.35)$$

From a plot of the corrected concentration of the target product as a function of the corrected concentration of the reference product a straight line is expected if both products are formed as primary products. Any secondary formation of the product leads to deviations from the linear relation. The yield ratio was determined from the slope of the data. The relative yield method was employed in this work to determine the PGLY yield relative to a ring-retaining primary product that was formed from the same educt (see Section 4.6). Nevertheless, this is not necessarily a limitation and the two products may in principle also form from different educts.

c) Numerical simulation of educt-product time-profiles

Product yields were determined by a method similar to that used for toluene experiments reported by *Klotz et al.* [1998]. Briefly, numerical simulations were carried out in which the OH-concentrations were fitted to the observed degradation rate of educt or an respectively added OH-tracer substance. The yields were fitted so that the observed concentration-time-profile of the product was reproduced. The fits were performed with the ChemSimul software package which was developed at the Danish Research Center at Risø. Additional loss-processes that were taken into account were reaction of product with OH-radicals and monoexponential loss-processes.

3.5.6 Employed methods to trace the OH-concentration

Two different methods were employed to trace the OH-radical concentration.

Following the degradation of an OH-tracer substance

The relative loss of an OH-tracer substance (Trac) was used to calculate the concentration of OH-radicals from:

$$[\text{OH}]_{(t_n-t_{n-1})} = \frac{\ln([\text{Trac}]_{t_{n-1}}/[\text{Trac}]_{t_n}) + (L + W) \cdot (t_n - t_{n-1})}{k_{\text{OH,Trac}} \cdot (t_n - t_{n-1})} \quad (3.36)$$

where (t_n-t_{n-1}) denotes a time interval between two consecutive DOAS spectra recorded at times t_n and t_{n-1} . The compounds "Trac" used were: di-n-butylether,

1,3,5-TMB and pCRE. In experiments with no OH-tracer was added, "Trac" corresponded to the educt. L denotes the system leakage and W the wall-deposition-rate which corresponded to the mean W in most cases (see Section 4.2.1).

Alternatively, the OH-concentration was also derived from the numerical simulation of the concentration-time-profiles of the reactant decay as described above.

Following the formation of a product

Benzene was added to trace extremely low levels of OH. Thereby it was exploited that benzene effectively forms phenol upon OH-attack (see Section 4.3). The phenol formation was measured in the system and used to calculate the OH-radical concentration from:

$$[\text{OH}] = \frac{\delta[\text{PHEN}]/\delta t + (L + W)}{k_{\text{OH,BEN}} \cdot \Phi_{\text{PHEN}} \cdot [\text{BEN}] - k_{\text{OH,PHEN}} \cdot [\text{PHEN}]} \quad (3.37)$$

where $\delta[\text{PHEN}]/\delta t$ denotes the temporal variation of the phenol concentration (as measured by DOAS), $k_{\text{OH,BEN}}$ and $k_{\text{OH,PHEN}}$ denote the OH-reaction rate-constants of benzene and phenol (listed in Table 3.2), Φ_{PHEN} is the phenol yield (see Section 4.3), values in squared brackets correspond to concentrations in $\text{molec}\cdot\text{cm}^{-3}$. L and W correspond to the PHEN loss-rate through leakage and wall-deposition as defined above. It was assumed that only BEN formed PHEN in the system. If there were other pathways forming PHEN, Equation 3.37 would give an upper-limit for the OH-concentration. Under the conditions specified in Section 3.4.2 for the experiment on the photolysis of aromatic aldehydes it was possible to trace the OH-concentration down to levels of about $1 \cdot 10^4 \text{ molec}\cdot\text{cm}^{-3}$.

To the best of our knowledge it is the first time that the OH-concentration was traced following the formation of a product (here PHEN) and not, like it is generally done, the decay of an OH-tracer substance.

3.5.7 Employed methods to trace the NO₃-concentration

Two different methods were employed to trace the NO₃-radical concentration.

The steady-state approach

The NO₃-concentration was calculated from Equation 3.38 assuming its concentration to be in steady-state between sources and known sinks. In the example of the pXYL system this approach leads to the following expression:

$$[\text{NO}_3]_t = \frac{k_{\text{NO}_2,\text{O}_3} \cdot [\text{NO}_2]_t \cdot [\text{O}_3]_t}{J_{\text{NO}_3,t} + k_{\text{NO}_3,\text{NO}} \cdot [\text{NO}]_t + k_{\text{NO}_3,\text{DMP}} \cdot [\text{DMP}]_t} \quad (3.38)$$

where k-values represent the respective reaction rate-constant, values in squared brackets correspond to concentrations of the respective species at time t and J_{NO_3} is the photolysis frequency of NO₃ at time t (see Section 3.5.1). This method will only yield an upper-limit estimate of the NO₃-concentration.

Following the degradation of a NO₃-tracer substance

The concentration-time-profile of 2,5-DMP was used to trace the average NO₃-concentration. The following equation was used:

$$[\text{NO}_3] = \frac{-\delta[\text{DMP}]/\delta t + [\text{OH}] \cdot (k_{\text{OH},\text{pXYL}} \cdot \Phi_{\text{DMP}} \cdot [\text{pXYL}] - k_{\text{OH},\text{DMP}} \cdot [\text{DMP}]) - (W + L)}{k_{\text{NO}_3,\text{DMP}} \cdot [\text{DMP}]} \quad (3.39)$$

where $\delta[\text{DMP}]/\delta t$ denotes the temporal variation of the 2,5-DMP concentration (as measured by DOAS), [OH] the OH-concentration (see above), k-values denote rate-constants (pXYL: p-xylene), Φ_{DMP} is the yield of 2,5-DMP from pXYL (see Section 4.4.1), values in squared brackets correspond to concentrations of the respective species, W and L denote the wall-deposition-rate and leakage of the 2,5-DMP. This method was employed in combination with a chemical model that described the OH-chemistry and monoexponential loss-rates (see Figure 4.11 and Section 3.5.5).

Chapter 4

Results

4.1 Calibration

The calibration of the DOAS measurements requires the knowledge of the absorption cross-section of the measured species (see Section 3.2.1). In the further the results obtained for the absorption cross-sections of phenol and glyoxal are presented.

4.1.1 Phenol absorption cross-section

The σ of phenol in the UV spectral range was re-determined in the course of this study at a spectral resolution of 0.2 nm (FWHM, determined at 253.65 nm). The error of the cross section of phenol hereby was dominated by uncertainties of the exact volume of the reactor, which is known with an accuracy of approximately 3%. The value of σ from the absorption band at 275 nm was $\sigma_{275\text{ nm}} = (1.97 \pm 0.08) \cdot 10^{-17}$ cm² (see Table 5.1). Application of a 1000-times triangular high-pass filter, reduced the differential absorption cross-section at 275 nm to 0.83 times of its un-filtered value ($\sigma'_{275\text{ nm}} = 1.64 \cdot 10^{-17}$ cm²).

4.1.2 Glyoxal absorption cross-section

The σ of glyoxal in the UV-vis spectral range between 431 nm and 461.6 nm is shown in Figure 4.1 for a spectral resolution of 0.17 nm (FWHM, determined at 435.84 nm). Calibration was performed from the simultaneously recorded FTIR spectra using the cross-sections from [Moortgat 2000]. The value of σ' from the absorption band at 455 nm was determined $\sigma_{455\text{ nm}} = (5.5 \pm 1.1) \cdot 10^{-19}$ cm² (see also Table 5.2). The absorption cross-sections was observed to decrease (about 6 %) if at

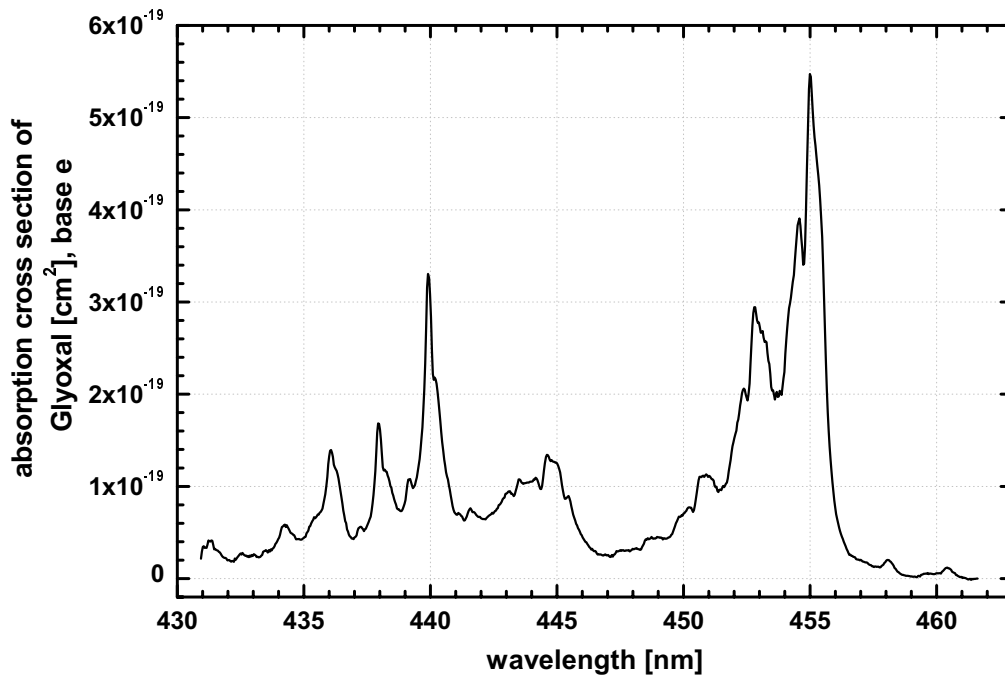


Figure 4.1: Absorption cross-section spectrum of glyoxal recorded at a spectral resolution of 0.17 nm (FWHM at 435.84 nm).

a given spectral resolution the observed column density of glyoxal was increased. The cross-section spectrum shown in Figure 4.1 was recorded observing a glyoxal-column-density $C \cdot L \approx 4.5 \cdot 10^{17}$ molec \cdot cm² and corresponded to the maximum observed absorption cross-section.

4.2 Kinetic studies

The determination of the OH- and NO₃-rate-constant requires the knowledge of the deposition-rate of polar compounds in order to accurately correct for the influence of the chamber walls. It is further of fundamental interest to what extent the chamber walls represent a sink for polar products that form from a chemical reaction.

4.2.1 The influence of the chamber-walls

In Table 4.1 the experimentally determined W-values are listed. For each compound the observed maximum and minimum W is given together with a mean W determined for all values. W varied by more than two orders of magnitude for the investigated compounds and was found maximal for the 2,4,6-TMP. Systematic variations with the degree of alkyl-substitution were visible for the mean W-values in Table 4.1 for the different classes of aromatic compounds, i.e. the alkylbenzenes, the aldehydes and the phenols. The minimum W was observed for glyoxal. Two compounds, i.e. pTALD and phenol were investigated in more detail and the results for the pTALD are shown in Figure 4.2. As can be seen the variability of W is considerable. At a given time (e.g. 2 hours) the individual W-values scatter by up to a factor of 3. This factor was assumed as the maximum uncertainty of the W-value in different experiments. The scatter among the W-values indicate the influence of other parameters (e.g. temperature, the chemical composition of the walls surface) that were not further considered here (see Section 5.2.2). Nevertheless, the decrease of W with time is clearly visible. This effect was observed in all experiments and can be explained from the progressive saturation of the chamber walls with pTALD. The maximum W decreased to about one fourth of its initial value after about 3 hours. Moreover, the decrease was observed most prominent in the initial phase of an experiment. Similar results were observed for the phenol. This variation was used to estimate the desorption-rate for pTALD in the dark using the following approach:

$$W(t) = -R_{\text{adsorption}} + R_{\text{desorption}} \cdot \frac{[\text{pTALD}]_{\text{deposit}}(t)}{[\text{pTALD}]_{\text{gas-phase}}(t)} \quad (4.1)$$

where $W(t)$ corresponds to the wall-loss-value observed after the time t relative to the injection into the reactor, $R_{\text{adsorption}}$ is the adsorption-rate (which here was identified with the initial wall-loss-rate), $R_{\text{desorption}}$ corresponds to the desorption-rate, $[\text{pTALD}]_{\text{gas-phase}}(t)$ corresponds to the concentration of pTALD in the gas-phase at time t and $[\text{pTALD}]_{\text{deposit}}(t)$ is the calculated amount of pTALD deposited on the chamber walls at time t . Using the numbers from Figure 4.2 for $t=2$

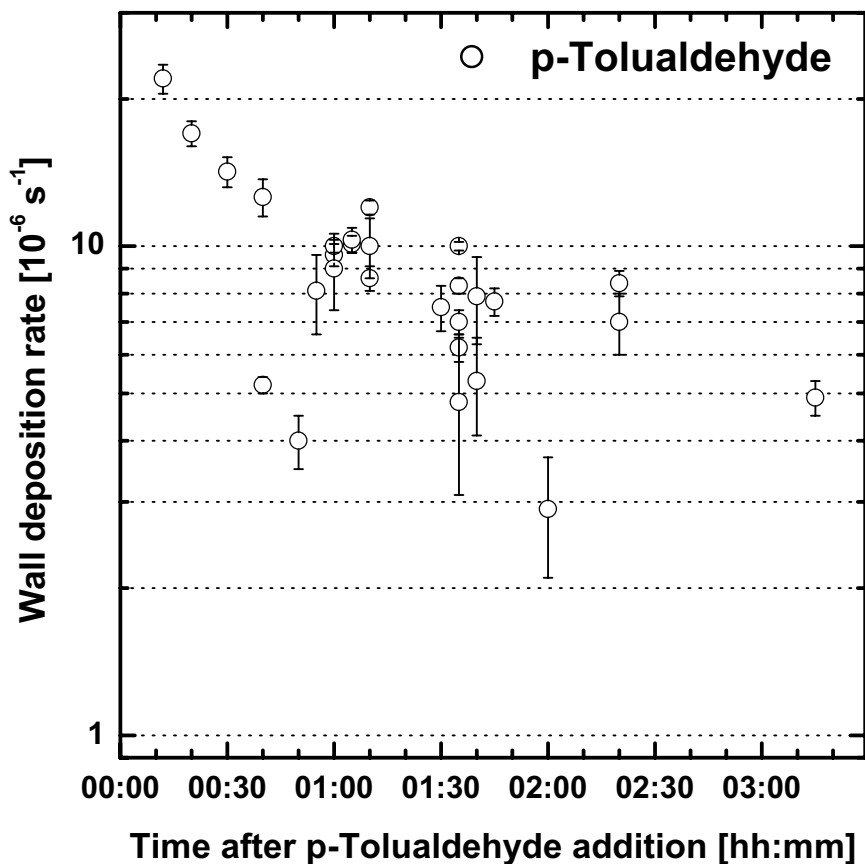


Figure 4.2: The deposition-rate of pTALD to the chamber walls as a function of the time after the injection of pTALD into the chamber. The data was corrected for leakage.

hours ($W(t) = 8 \cdot 10^{-6} \text{ s}^{-1}$, $R_{adsorption} = 2.2 \cdot 10^{-6} \text{ s}^{-1}$, $[pTALD]_{gas-phase}(t) = 50 \text{ ppb}$, $[pTALD]_{deposition}(t) = 4 \text{ ppb}$) a value of the deposition-rate of $R_{desorption} \approx 2 \cdot 10^{-4} \text{ s}^{-1}$ was derived. This value corresponds to a lifetime of pTALD on the dark walls with respect to desorption back into the gas-phase of 1 hour 30 minutes.

The value of $R_{adsorption}$ nevertheless may still have been underestimated here. From Figure 4.2 it is in fact expected higher and correspondingly the deposition-rate W may be higher. The ratio of the maximum (observable) W and mean W was found 3.4 for pTALD and phenol (see Table 4.1). The similarity of this value for both compounds reflects the fact that the mean W for both, and i.e. also all the other compounds, was determined - on average - after the same time. This factor in a first approximation is representative for all compounds and was applied to estimate the initial wall-deposition-rate also for the other products (mean W multiplied by 3.4)

Table 4.1: Wall deposition-rates W of reactants and products.

Compound	Wall deposition-rates [10^{-6} s^{-1}]				walls as a sink	
	W_{max}^a	W_{min}^b	W_{mean}^c	$W_{initial}^d$	$\tau_{initial}^e$	[%] ^f
Benzene	< 0.3	< 0.3	< 0.3			
Toluene	1.4	0.3	1.0 ± 0.7			
p-Xylene	2.3	0.5	1.5 ± 0.7			
1,3,5-TMB	5.6	2.1	3.1 ± 2.6			
BALD	4.3	1.4	2.6 ± 1.4	9	1 d 7 h	14
pTALD	22	2.9	6.9 ± 2.2	24	11 h 30 min	23
3,5-DMBA	17.2	9.7	13.1 ± 3.4	45	6 h 10 min	27
Phenol	26	4.4	7.2 ± 3.8	26	10 h 40 min	20
p-Cresol	20	10.8	15.3 ± 4.6	52	5 h 20 min	22
2,5-DMP	21.4	16.6	19.0 ± 3.4	65	4 h 15 min	16
2,4,6-TMP	55	19.2	28.4 ± 11.6	97	2 h 50 min	15
Glyoxal	0.6	0.2	0.4 ± 0.2	1.4	8 d 6 h	< 2

^a loss-rate R corrected for leakage L ; observed maximum value.

^b observed minimum value.

^c average value from various experiments.

^d initial wall-loss-rate, estimated value (see text).

^e lifetime with respect to initial wall-loss, calculated as $W_{initial}^{-1}$.

^f W_{max} divided by R_{OH} ($[OH]=5 \cdot 10^6 \text{ molec} \cdot \text{cm}^{-3}$, see Equation 3.28).

and is listed in Table 4.1. In a further approximation, the loss to the chamber walls was assumed independent of whether the compound was manually injected into the reactor or formed as a product from a chemical transformation. The importance of the walls as a sink in the product studies was estimated from dividing the initial W by the product loss-rate through e.g. OH-reaction ($k_{OH} \cdot [OH]$, k_{OH} from Table 3.2). It turned out that between 15 % and 25 % of the product loss occurred on the chamber walls. With the exception of glyoxal, this number was found to be about equal for all the investigated products.

4.2.2 Reaction rate-constants towards the OH-radical

The relative-rate technique, see Section 3.5.3 was used to determine the OH-reaction rate-constants of the compounds listed in Table 4.2. The investigated target compounds were pTALD, 3,5-DMBA as well as 2,4,6-TMP. For these compounds no values of k_{OH} so-far were available in the literature. In addition, it was decided to determine the rate-constants of BALD, phenol and 2,5-DMP, since for these compounds literature values are available and hence allowed to confirm the employed evaluation method. The most intensively studied compound was pTALD for which k_{OH} was determined in a total of 14 experiments relative to four different reference compounds, i.e. toluene, m-xylene, 1,3,5-TMB and phenol. Table 4.2 gives an overview about the investigated pairs of target and reference compounds. Several experiments (two to five) were carried out relative to each of these reference compounds. The results are also included in Table 4.2. The listed rate-constant ratios correspond to the average ratios with the error indicating the 2-sigma variability among the different experiments. The individual experiments agreed within their uncertainties. Figure 4.3 shows the experimental data of an experiment where the rate-constants of pTALD and 3,5-DMBA were determined relative to the reference compound m-xylene. The data has been corrected for compound loss through leakage, wall-deposition and for BALD also photolysis (see Section 3.5.4). For reasons of simplicity, the experimental error bars were only shown for a single data point (for each compound). The excellent correlation observed for both pairs of compounds was representative also for the other experiments. The slopes of the plotted data correspond to the rate-constant ratios as described by Equation 3.5.3. These were found reproducible as is reflected in the small variations of the mean rate-constant ratios listed in Table 4.2 (mostly 3 % to 7 %, exceptionally > 10 %).

The rate-constants used to place k_{OH} of the target compounds on an absolute basis are included in Table 4.2 (bottom line) and were obtained combining the recommended values [Atkinson 1994] with recent kinetic data [Kramp and Paulson 1998], [Semadeni et al. 1995] and the results of this work. For 1,3,5-TMB the k_{OH} value from Kramp and Paulson [1998] was used which agrees well with the presently recommended value [Atkinson 1994] but is reduced in error (9 %). For toluene and m-xylene the recommended values from Atkinson [1994] were preferred. Though the k-values of Kramp and Paulson [1998] agree within the uncertainties, their use would have resulted into systematic discrepancies for the rate-constants of pTALD, 3,5-DMBA and 2,4,6-TMP. However, comparing the minimum value that falls within the experimental error of Kramp and Paulson [1998] to the recommended value

Table 4.2: The OH-rate-constants determined in this work.

Target compound	Reference compounds ($k_{target}/k_{reference}$) ^a				k_{OH} ^b [10 ⁻¹² cm ³ ·(molec·s) ⁻¹]
	Toluene	m-Xylene	1,3,5-TMB	Phenol	
BALD			0.24 ± 0.05	0.5 ± 0.1	12.5 ± 2.5
pTALD	3.57 ± 0.12	0.85 ± 0.07	0.36 ± 0.01	0.85 ± 0.02	21.2 ± 2.5
3,5-DMBA		1.39 ± 0.10	0.70 ± 0.04	1.22 ± 0.16	34.2 ± 6.8
Phenol		1.18 ± 0.04	0.45 ± 0.03		26.4 ± 3.8
2,5-DMP			1.42 ± 0.04		81.7 ± 8.5
2,4,6-TMP		5.47 ± 0.18	2.54 ± 0.07		131 ± 15
k_{OH} reference compounds ^c	6.0 ± 1.0 ^d	23.6 ± 4.0 ^d	57.3 ± 5.3 ^e	26.3 ± 1.6 ^f	

^a mean values of various experiments.

^b mean values of all the individual experiments (not listed, the overall error is listed).

^c the data was placed on an absolute basis using these values. units: 10⁻¹² cm³·(molec·s)⁻¹.

^d value: [Atkinson 1994]; error reduced using data from [Krampp and Paulson 1998] (see text).

^e reference: [Krampp and Paulson 1998].

^f value: [Atkinson 1994]; error reduced using data from [Semadeni et al. 1995] (see text).

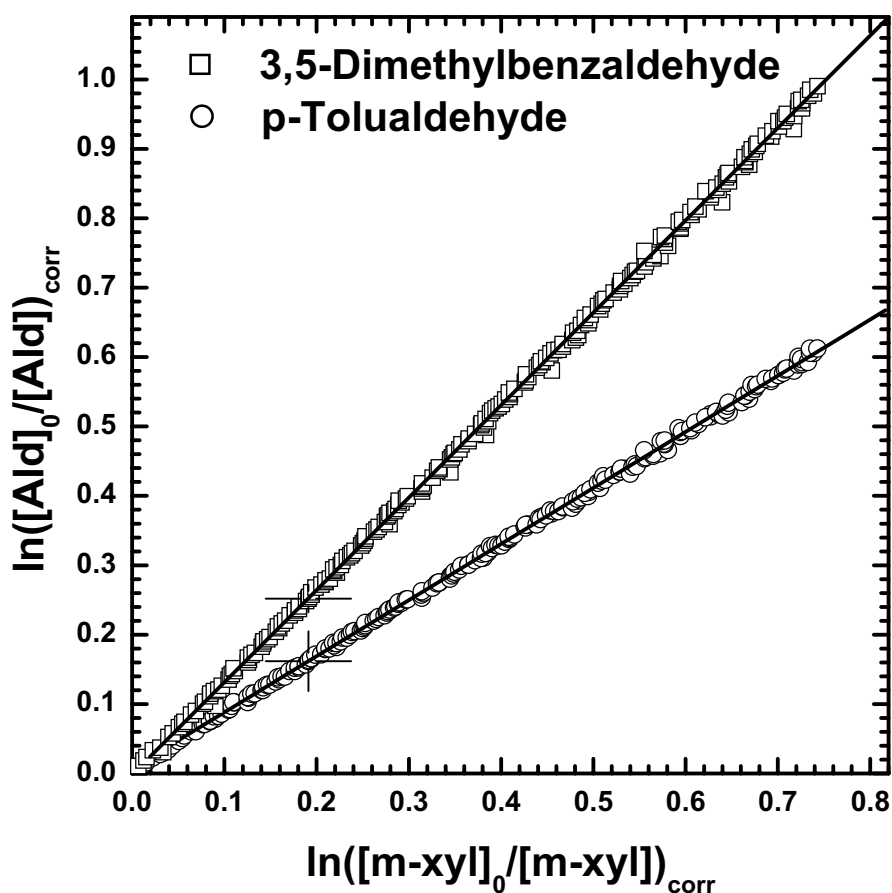


Figure 4.3: Plot of Equation 3.26 for an experiment where m-xylene was used as a reference compound to determine the rate-constants of OH-radicals with pTALD and 3,5-DMBA.

[Atkinson 1994] this data was used to reduce the error of the toluene and m-xylene rate-constants (both $\approx 17\%$). Similarly the experimental error of the phenol value [Atkinson 1994] was reduced to 6% using the data by Semadeni et al. [1995]. Excellent agreement was observed for the target compounds if placed on an absolute basis using this data set of reference rate-constants.

Table 4.3: The NO_3 -rate-constant determined in this work.

Target compound	$k_{\text{target}}/k_{\text{PHEN}}^a$	$k_{\text{NO}_3}^b$ [$10^{-12} \text{ cm}^3 \cdot (\text{molec} \cdot \text{s})^{-1}$]
pCRE	2.97 ± 0.17	11.2 ± 1.3
2,5-DMP	6.45 ± 0.64	24.4 ± 3.4
PHEN		3.78 ± 0.39^c

^a mean values of various experiments.

^b placed on an absolute basis using $k_{\text{NO}_3, \text{PHEN}}^c$; error: 2- σ overall error.

^c value: [Atkinson 1994]; reduced error (see text).

4.2.3 Reaction rate-constants towards the NO_3 -radical

The relative-rate technique, see Section 3.5.3 was used to determine the k_{NO_3} values of p-cresol and 2,5-DMP relative to the reference compound phenol. The target compound of principal interest was 2,5-DMP where no value of k_{NO_3} was so-far available in the literature. It was decided to further determine the rate-constant of p-cresol, since for this compound several literature values are available and hence allowed to confirm the employed evaluation method. The results are listed in Table 4.3. The listed rate-constant-ratios correspond to the average ratios with the error indicating the 2-sigma variability among the different experiments. Figure 4.4 shows experimental data for the loss of p-cresol and 2,5-DMP as compared to that of phenol. The data has been corrected for compound loss through leakage and wall-deposition (see Section 3.5.4). For reasons of simplicity, the experimental error bars were only shown for a single data point (for each compound). The excellent correlation observed for both pairs of compounds was representative for the other experiments.

Though the differences among individual experiments were slightly larger than in the case of the OH-kinetic experiments the rate-constant ratios were still in satisfactory agreement and varied by less than 10%.

The rate-constant of phenol used to place k_{NO_3} on an absolute basis is included in Table 4.3 (bottom line). It corresponded to the recommended value [Atkinson 1994]. Nevertheless, the error was reduced using the data from [Atkinson *et al.* 1992] and this work. From the well agreement of the p-cresol rate-constant with literature values (see Section 5.2.1, Table 5.3) and the comparably small error among the available literature values for p-cresol [Carter *et al.* 1981; Atkinson *et al.* 1984;

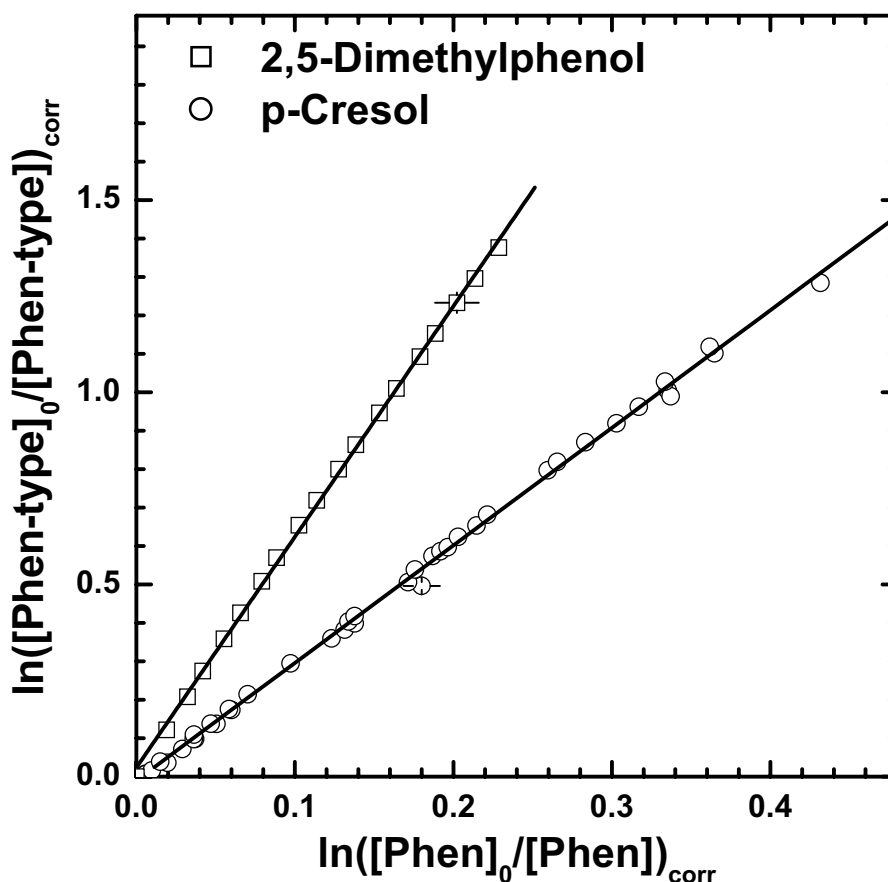


Figure 4.4: Plot of Equation 3.26 for two experiments. In both experiments phenol was used as an reference compound to determine the NO_3 -rate-constants of p-cresol and 2,5-DMP.

[Atkinson *et al.* 1992] (see section 5.2.1, Table 5.3) the value of the phenol rate-constant was assumed to be more accurate than the 35% uncertainty specified by Atkinson [1994]. The uncertainty was hence calculated from comparing the maximum value that falls within the error limits of Atkinson *et al.* [1992] with the recommended value [Atkinson 1994]. The error of the reference rate-constant of phenol was hence estimated 10% (see Table 4.3).

The rate-constant ratio of p-cresol and phenol was found independent from the NO_2 concentration. Among the two employed sources for the NO_3 -radical (see Section 3.4.5) the initial NO_2 concentration varied by about an order of magnitude. Despite this variability, only insignificant scatter was observed in the ratio of the rate-constants of phenol and p-cresol (< 6%).

Table 4.4: The photolysis-frequencies determined in this work.

Compound	$J_{phot.}^a$ [10^{-6} s^{-1}]
BALD	8 ± 6
oTALD	200 ± 10
mTALD	11 ± 8
pTALD	< 6
3,5-DMBA	< 6

^a experimental conditions: $J_{NO_2} \approx 7.5 \cdot 10^{-3} \text{ s}^{-1}$; SZA = 50° .

4.2.4 Photolysis of aromatic aldehydes

The photolysis of BALD, o-, m-, pTALD and 3,5-DMBA was studied in one experiment with the aim to characterize the importance of the photolytic sink of these compounds in the OH-kinetic experiments. The measured photolysis-frequencies are listed in Table 4.4. The given data was corrected for loss of the compounds through leakage, deposition to the chamber walls and OH-reaction (see Section 3.5.4). The OH-concentration was determined $[OH] \leq 5 \cdot 10^4 \text{ molec}\cdot\text{cm}^{-3}$ (see Section 3.5.6) and corrections due to OH-loss in general were small. For the fastest aldehyde, i.e. 3,5-DMBA (see Table 4.2) the above OH-concentration corresponds to an OH-loss-rate $R_{OH} \leq 1.7 \cdot 10^{-6} \text{ s}^{-1}$. R_{OH} was lower for the other compounds indicating that the OH-radicals had been effectively suppressed. For pTALD and 3,5-DMBA no photolytic-loss was observed and the photolysis-frequencies listed in Table 4.4 are upper-limit values that were estimated from the experimental error of the measurements. For BALD, o- and mTALD however, significant photolytic-loss was observed. The highest value was observed for the oTALD which showed a distinctly different behaviour than the other aromatic aldehydes. This is illustrated in Figure 4.5, where the total-loss of o- and pTALD is shown (no corrections applied). Both compounds were found to be lost at a comparable rate in the initial phase when the chamber was closed (overall loss-rate $R \approx 1.9 \cdot 10^{-5} \text{ s}^{-1}$ for both compounds) that can be explained from leakage (here: $L = 1.1 \cdot 10^{-5} \text{ s}^{-1}$) and the mean deposition-rates of pTALD listed in Table 4.1. The chamber was opened at 12:03 GMT (Greenwich Mean Time \approx local time). In the presence of sunlight the oTALD was rapidly lost while pTALD continued to be lost at essentially the same rate as in the absence of sunlight. The mean NO_2 -photolysis-frequency (J_{NO_2}) was determined

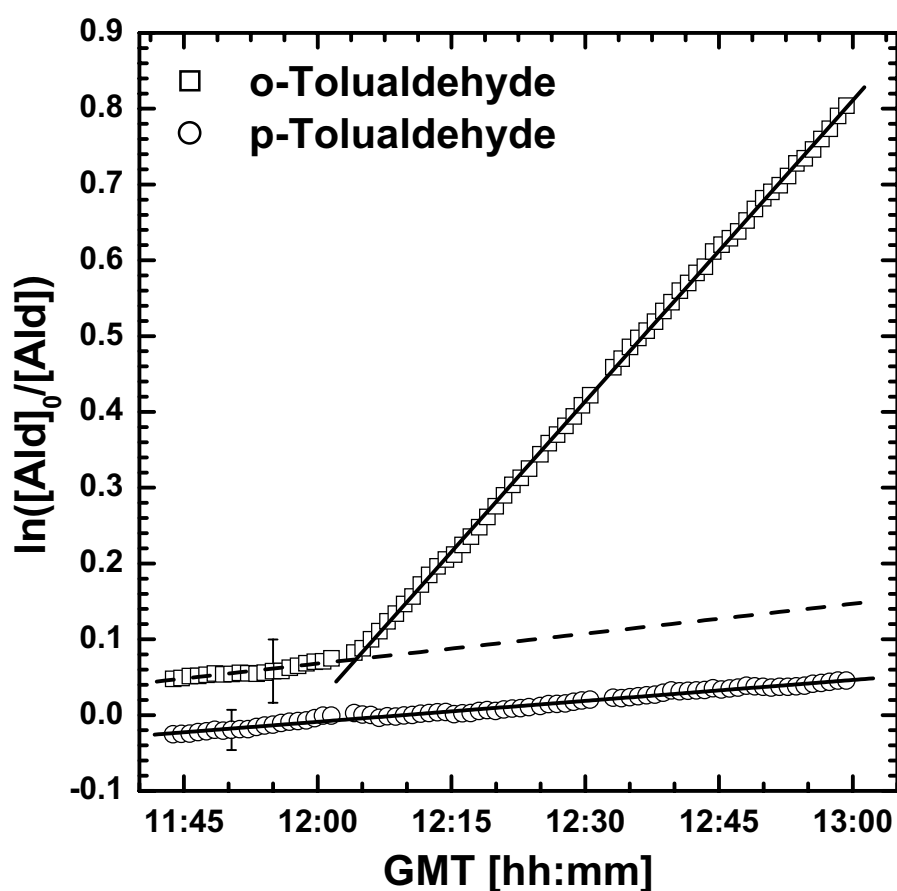


Figure 4.5: Plot of the total-loss of o- and pTALD in the presence of cyclohexane as a function of time. From 12:00 to 12:05 GMT the chamber housing was opened. Solid lines indicate linear regressions to the data. The dashed line indicates the loss of oTALD in the dark chamber, where both compounds were lost at comparable rate.

$J_{NO_2} \approx 7.5 \cdot 10^{-3} \text{ s}^{-1}$. The mean solar zenith angle (SZA) during the measurements was $\text{SZA} = 50^\circ$ which is a typical value around noon during winter (February).

4.3 The phenol yield from benzene

A total of 26 experiments on the photooxidation of benzene were conducted. In these experiments the initial benzene concentration was varied by two-to-three orders of magnitude, while the initial NO_x -concentrations were varied by three-to-four orders of magnitude (see Table 4.5) by principally varying the initially added NO . In addition, the parameters OH-source, temperature and oxygen concentration were varied to obtain information on the phenol formation mechanism in the OH-initiated oxidation of benzene. The results on benzene are exemplary for the other investigated aromatic compounds. The numbers of reactions and intermediate compounds in this paragraph refer to the numbers given in Figure 2.1.

The phenol yields determined for the individual experiments are listed in Table 4.5. Also included are the results from seven experiments which were conducted and evaluated by Dr. Björn Klotz at the indoor simulation-chamber at NIES, Tsukuba/Japan (indicated NBE1-NB21 in the lower part of Table 4.5). In order to assess the influence of the employed evaluation procedure together with each yield two errors are specified (both referring to the 2-sigma confidence interval). The first error denotes the error that refers to the evaluation procedure excluding the systematic errors due to calibration and errors in the kinetic parameters, while the second denotes the overall error of the absolute phenol yield.

In the following, the data of two example-experiments is presented. In Figure 4.6 the experimental data obtained during the first five minutes of experiment BE26 is shown that was used to determine the phenol yield (see Table 4.5). The OH-profile determined from Equation 3.36 (not shown) was used here to calculate the amount of reacted benzene and to correct the measured phenol concentration for loss through reaction with OH ($F < 1.08$). An average OH-concentration of $1.3 \cdot 10^7 \text{ molec}\cdot\text{cm}^{-3}$ was traced from the decay of 1,3,5-TMB for this experiment. In Figure 4.6 phenol was identified to form as a primary product. The yield determined from the slope of the linear regression (included in Figure 4.6) corresponded to a phenol yield of $(50.3 \pm 2.1)\%$. The error indicates the 2-sigma error from the evaluation (see Section 4.3.6).

Figure 4.7 shows the results of the numerical simulation of experiment BE15, an experiment without added OH tracer. In this experiment, some formaldehyde was added to the reaction mixture in order to enhance the reactivity of the system. The high radical concentrations in this experiment lead to a high turnover of benzene, and despite the fact that a large proportion of the phenol reacted with OH-radicals

Table 4.5: Experimental conditions and results for the experiments on benzene.

Name	Benzene [10^{12} cm $^{-3}$]	NO $_x$ [ppb]	Phenol Yield, Φ_{phenol} [%]	Error of evaluation only [%]	Overall Error [%]	Experi- mental type $^{\alpha}$	Evaluation method $^{\beta}$
BEN1	58.3	95	47.7	5.4	6.8	(1)	(c)
BEN2	28.9	105	49.4	7.8	9.8	(1)	(c)
BEN3	29.3	150	44.1	9.0	11.3	(1)	(c)
BEN4	29.2	105	48.3	5.7	7.1	(1)	(c)
BEN5 ¹	57.3	195	47.3	3.1	5.1	(1)	(c)
BEN6 ¹	28.0	245	51.4	2.5	4.2	(1)	(c)
BEN7	28.3	210	46.9	4.6	5.8	(1)	(c)
BEN8 ¹	28.5	51	49.2	2.4	4.0	(1)	(c)
BEN9 ¹	11.8	100	54.6	3.3	5.5	(1)	(c)
BEN10	24.1	53	55.3	6.2	7.7	(1)	(c)
BEN11	1.5	50	56.1	6.0	7.4	(1)	(a)
BEN12	9.9	(2)*	55.8	2.3	5.6	(2)	(a)
BEN13	1.6	(6)*	58.4	6.1	7.4	(2)	(a)
BEN14	1.4	(2)*	66.6	6.3	8.4	(4)	(a)
BEN15 $^{\gamma}$	23.6	21	54.5	5.8	7.2	(5)	(c)
BEN16	84.2	200	47.8	3.8	4.7	(1)	(c)
BEN17	113.0	260	43.5	3.4	4.2	(1)	(c)
BEN16II $^{\gamma}$	22.1	13	56.6	7.5	9.1	(5)	(c)
BEN17II	13.5	135	54.5	3.2	4.5	(3)	(a)
BEN18	26.8	120	50.5	8.0	9.0	(3)	(b ₁)
BEN19	1.1	86	57.8	7.0	8.5	(3)	(a)
BEN24 ²	105.9	176	50.4	5.6	7.9	(3)	(b ₁)
BEN26 ²	48.9	113	50.3	2.1	5.8	(3)	(b ₁)
BEN28 ³	441.8	790	42.1	2.1	5.2	(3)	(b ₁)
BEN28II ³	411.5	1705	26.6	3.0	4.4	(3)	(b ₁)
BEN31 ^{3,δ}	378.2	240	53.5	4	7	(3)	(b ₁)
NBE1 ¹	122.3	1072	33.5	5.4	5.9	(1)	(b ₂)
NBE2 ¹	122.5	1084	34.6	2.9	3.9	(1)	(b ₂)
NBE3 ¹	49.7	1940	25.0	4.9	5.0	(1)	(b ₂)
NBE4 ¹	123.2	2009	25.8	2.1	2.8	(1)	(b ₂)
NB19 ¹	185.7	213	42.7	4.3	5.1	(1)	(b ₂)
NB20 ¹	183.3	106	44.8	5.1	5.6	(1)	(b ₂)
NB21 ¹	185.8	314	43.1	6.4	7.1	(1)	(b ₂)

* NO $_x$ -free at start of experiment.

¹ di-n-butylether added as tracer for OH-radicals.

² 1,3,5-TMB added as tracer for OH-radicals.

³ p-cresol added as tracer for OH-radicals.

$^{\alpha}$ the number refers to the OH-source used, see Section 3.4.4.

$^{\beta}$ see Section 3.5.5.

$^{\gamma}$ Experiments performed in collaboration with Forschungszentrum Juelich.

$^{\delta}$ the mixing ratio of oxygen in this experiment was raised to 40%.

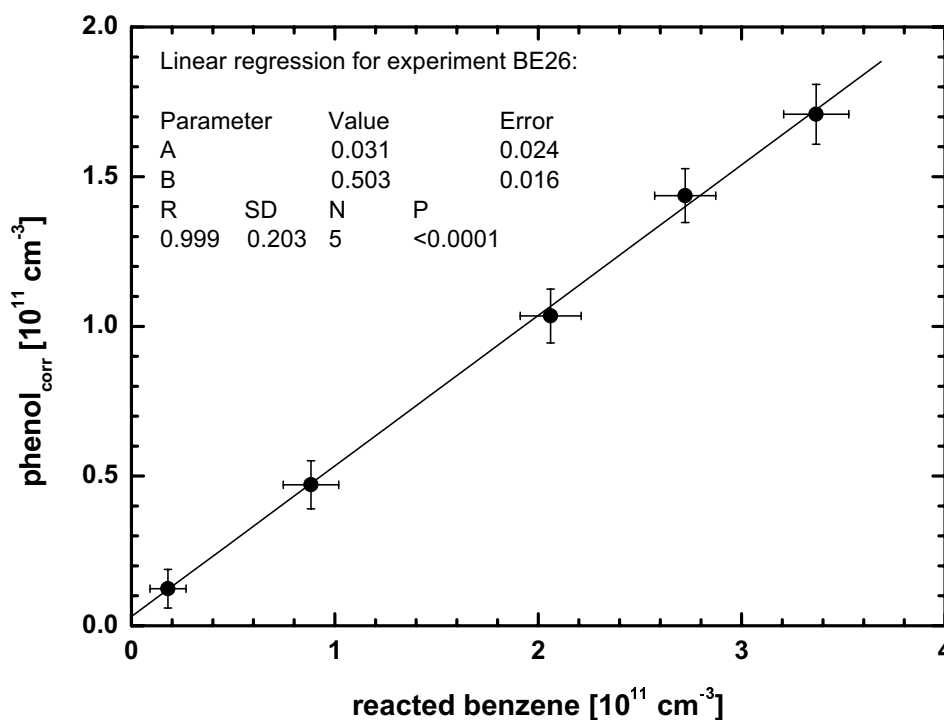


Figure 4.6: Plot of the phenol concentration, corrected for OH-reaction as a function of the amount of reacted benzene as determined during the initial phase (roughly 5 minutes) of experiment BE26.

(see the dotted line in Figure 4.7), the calculated concentration-time-profile of phenol closely matched the measured one. The thin line included in Figure 4.7 shows an experimentally determined concentration-time profile of OH-radicals. This profile was measured with an LIF (laser induced fluorescence) system, which had been installed in the chamber just prior to this experiment [Becker *et al.* 1999]. The device was undergoing first tests during this experiment, and though the calculated OH-concentration-time-profile showed an almost 20% higher maximum concentration than the measurement, the agreement was generally satisfactory. The performance of the methods employed to calculate the OH-radical concentrations from the hydrocarbon decays was hence confirmed by these direct OH- measurements, though only in a single experiment. Despite the large correction factors of phenol (up to $F = 2$) the phenol yield agreed well with the average yield from this work. The correction of phenol-loss through OH-reactions are therefore believed to be accurate.

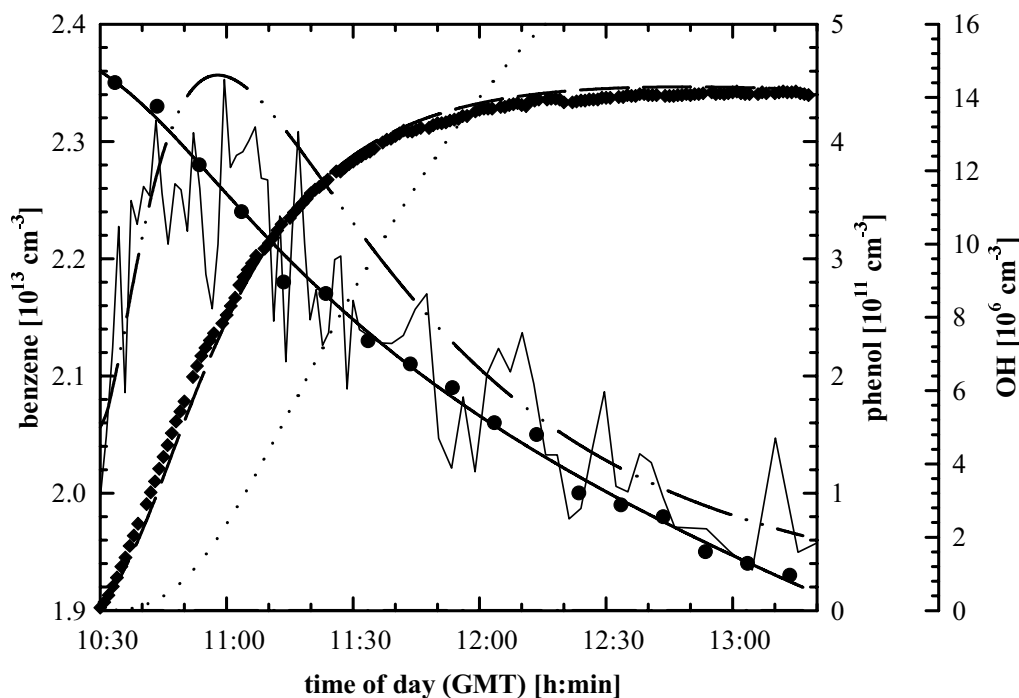


Figure 4.7: Result of the numerical simulation of experiment BE15. The following data is shown: (dots) benzene; (solid line) calculated benzene decay, left axis; (thin jagged line) OH-concentration as measured by the OH-LIF instrument; (dashed-dot-dotted line) calculated OH-concentration; (dotted line) loss of phenol, both right scale, divided by 10^6 ; (diamonds) phenol; (dashed line) calculated phenol.

4.3.1 Dependence on the NO_x -concentration

In Figure 2.1 the initial reaction steps of the oxidation of benzene are shown. Given these loss-processes from the equilibrium of intermediates **2/3** the phenol yield Φ_{phenol} is described by Equation 4.2:

$$\Phi_{phenol} = \frac{k_{phenol}}{k_{phenol} + k_8 + k_9 / K_{eq} + k_{10} \cdot [\text{NO}_2] / (K_{eq} \cdot [\text{O}_2]) + k_{12} \cdot [\text{NO}]} \quad (4.2)$$

Hereby, the following simplifications were made:

- the effective sum of the pathways that form phenol was defined as $k_{phenol} = k_3 / K_{eq} + k_4$.
- the dissociation reaction (-1) of **2** was not considered since it accounts for less than one percent of the total loss-rate from the equilibrium **2/3** under atmospheric conditions [Knispel et al. 1990; Bohn and Zetzsch 1999].

- the rate-constant for channel (5) was set to zero based on the results of *Bohn and Zetzsch* [1999] who estimated an upper-limit of 5 % for this pathway.
- the rate-constant for channel (6) was assumed to be zero.
- channel (11) was assumed to be essentially negligible for NO concentrations up to > 10 ppm [*Zetzsch* 1997] and hence was not considered here.

The following rate coefficients were used that are valid for a temperature of $T = 298 \text{ K}$ and atmospheric oxygen concentrations: $K_{eq} = (2.7 \pm 0.4) \cdot 10^{-19} \text{ cm}^3$ [*Bohn and Zetzsch* 1999], $k_{tot} = (k_3 + k_9) / K_{eq} + k_4 + k_8 = (760 \pm 80) \text{ s}^{-1}$ [*Bohn and Zetzsch* 1999], $k_{10} = (2.75 \pm 0.2) \cdot 10^{-11} \text{ cm}^3 \cdot \text{s}^{-1}$ [*Knispel et al.* 1990], $k_{12} = (1.1 \pm 0.4) \cdot 10^{-11} \text{ cm}^3 \cdot \text{s}^{-1}$ [*Bohn and Zetzsch* 1999]. The phenol yield was used to calculate k_{phenol} .

In Figure 4.8 the experimental data of the phenol yield as determined in the individual experiments of this study is shown. The errors of the phenol yield correspond to the specific error sources of the evaluation method only. The error bars with respect to NO_x -values in the Figure 4.8 correspond to the variability of the respective NO_x species over the time span of evaluation. In the upper part indicated (a) the phenol yield as a function of the NO mixing ratio and (b) the NO_2 mixing ratio is given. The solid line indicates the theoretical phenol yield as calculated from Equation 4.2 assuming only influence from the NO_x species plotted on the x-axis of Figure 4.8a and 4.8b, respectively. The dotted lines indicate respective uncertainties in the rate-constants k_{10} and k_{12} . As can be seen this approach allowed to reproduce the experimental data for the low NO_x -concentrations (several 10 ppb). The differences of the experimental and theoretical data nevertheless become significant with increasing concentrations of NO_x (> 100 ppb) where the influence of reactions (10) and (12) becomes competitive. It is also apparent that NO_2 influences the phenol yield already at a lower concentration as compared to NO reflecting the fact that k_{10} is about 2.5 times higher than k_{12} .

In Figure 4.8c and 4.8d, the influence of NO_2 and NO have been corrected, respectively. The NO and NO_2 values used in the corrections were taken from the experimental data averaged for the time period when the phenol yield was determined. Correction factors were calculated as the ratio of Equation 4.2 assuming $k_{10} = 0$ divided by Equation 4.2 assuming $k_{10} \neq 0$ to correct for the NO_2 influence in Figure 4.8c. These factors for most experiments were smaller than 1.035 with a

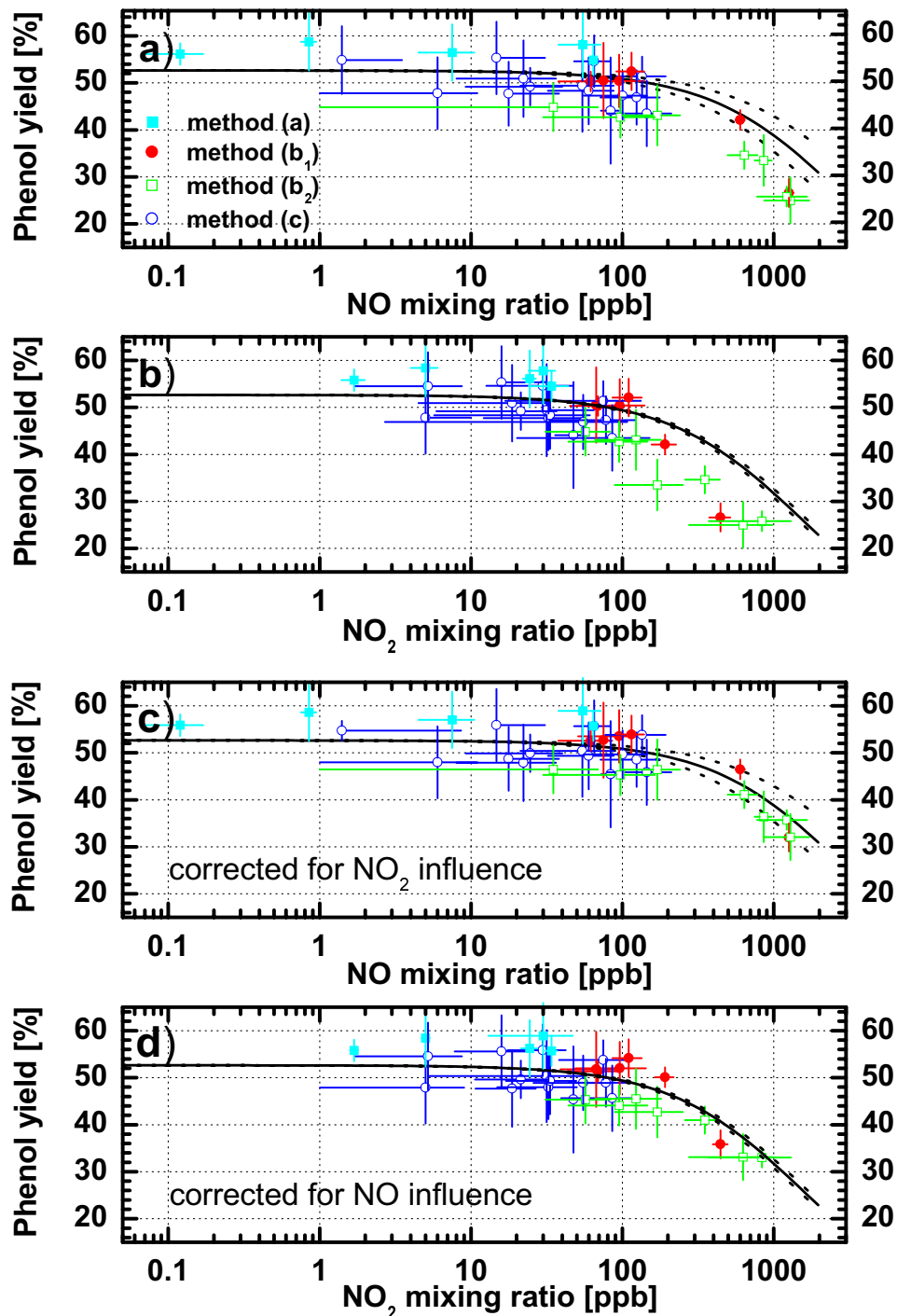


Figure 4.8: The phenol yield as a function of the mixing ratio of (a) NO and (b) NO₂ was well as (c) NO, corrected for NO₂-influence and (d) NO₂, corrected for NO influence. Different symbols represent the different evaluation methods (a) to (c) (see text). Further: (solid line) phenol yield calculated from Equation 4.2; (dashed line) uncertainties in the calculated yields due to the error of k_{10} and k_{12} in Equation 4.2.

maximum of 1.34. Accordingly, in Figure 4.8d the corrections for NO were calculated assuming $k_{12} = 0$ and $k_{12} \neq 0$. Here, the factors ranged between 1.0 and 1.22. The represented phenol yields in Figure 4.8c and 4.8d correspond to the phenol yields in Figure 4.8a and 4.8b multiplied with the respective factors.

When Figure 4.8c and 4.8d are compared to Figure 4.8a and 4.8b it is evident that the corrections significantly improve the agreement with the calculated yields from Equation 4.2. As can be seen, Equation 4.2 equally well describes the dependence of the phenol yield with respect to NO and NO₂ for the high NO_x-range (> 100 ppb). Within the uncertainties excluding systematic errors all data points are in good agreement with the calculated phenol yields indicating that the mechanism described by Equation 4.2 is suitable to represent the observed dependence of the phenol yield on the NO_x-concentration.

4.3.2 The average phenol yield

The parameter k_{phenol} in Equation 4.2 was determined as follows. All the experiments with added OH-tracer (see Table 4.5) were considered. In addition, BE15 and BE16II were considered due to the enhanced benzene turn-over and the correspondingly reduced error of these experiments. Further the experiments evaluated from method (a) (see Section 3.5.5) were considered since these phenol yields were essentially uninfluenced from uncertainties in the OH concentration. Experiment BE14 was not considered due to the systematically higher phenol yield that was observed using radical-source (4) (see also Section 5.4.3). The yields of the individual experiments were corrected for NO_x influence using the correction factors described above. Experiments with overall correction factors > 1.4 were neglected to avoid the overall error to be dominated from the uncertainties in k_{10} and k_{12} and to avoid that the high NO_x-concentration influenced the decay of the OH-tracer.

Independent of the evaluation procedure (see also Section 4.3.6) the yields were found to coincide within the specific evaluation error. The average phenol yield of this work was found to be $(53.0 \pm 6.6)\%$. The error hereby represents the overall 2-sigma confidence interval.

Based on the value for the total loss from the equilibrium **2/3**, i.e. $k_{tot} = (760 \pm 80) \text{ s}^{-1}$ [Bohn and Zetzsch 1999] the average phenol yield corresponds to a value of $k_{phenol} = (403 \pm 66) \text{ s}^{-1}$ in Equation 4.2. Consequently, the value of the effective sum of loss-rates through channels (8) and (9), i.e. $k_{otherproducts} = (k_{tot} - k_{phenol}) = (k_9/K_{eq} + k_8)$ is estimated $k_{otherproducts} = (357 \pm 59) \text{ s}^{-1}$.

4.3.3 Dependence on the oxygen concentration

The mixing ratio of oxygen was raised in a single experiment to about 40 % (BE31, Table 4.5). No effect of the phenol yield was observed; the yield of (53.5 ± 4) % agreed well with the average yield determined in air.

This result further confirmed Equation 4.2 under low NO_x conditions where the reactions (10) and (12) (Figure 2.1) were found to be unimportant and the intermediates **2/3** exclusively reacted with oxygen.

4.3.4 Dependence on the temperature

The phenol yields used to determine the average phenol yield are plotted as a function of temperature in Figure 4.9a. The solid line denotes the error weighted linear regression to the data points. For relative comparison, the plotted error bars correspond to the 2-sigma confidence interval neglecting systematic error sources. The annual cycle of the ambient temperature of EUPHORE is reflected in the temperature scale that covers about 20 K. An upper-limit of about 307 K (34°C) corresponds to a hot day during summer while the lower-limit of about 287 K (14°C) reflects typical achievable temperatures in EUPHORE during winter. The slope of $\Phi_{phenol}(T)$ is determined $(0.026 \pm 0.1) \% \cdot \text{K}^{-1}$ (Figure 4.9a). Though positive it is essentially zero within the experimental error.

Attempts were made to use the enthalpy data from *Lay et al.* [1996] to estimate whether channel (3) or channel (4) lead to the formation of phenol. The enthalpy and entropy data of *Lay et al.* [1996] is in reasonable agreement with the measured K_{eq} value of *Bohn and Zetzsch* [1999]. From this data, K_{eq} is expected to change by a factor of five over a 20 K temperature range around room temperature. Further, *Lay et al.* [1996] gave detailed enthalpy data for the rate-constants k_3 , k_4 , k_8 and k_9 that essentially determine the phenol yield here. Even though, the calculated absolute values for these rate-constants may be wrong [*Bohn and Zetzsch* 1999] the enthalpy data is promising to describe the variations of the rate-constants with temperature adequately. The values of k_3 , k_4 , k_8 and k_9 from *Lay et al.* [1996] were scaled linearly (by ≈ 24 for k_3 and k_4 ; by ≈ 7 for k_8 and k_9) to match the absolute value of k_{phenol} and $k_{otherproducts}$ using K_{eq} from *Bohn and Zetzsch* [1999] at $T = 296$ K. Equation 4.2 was then used to calculate the temperature dependent phenol yield. In Figure 4.9b the relative change of the phenol yield is shown for two scenarios. First, k_3 was set to zero (dotted line) and second, k_4 was set to zero (dashed line). In addition, the relative change of the phenol yield from the

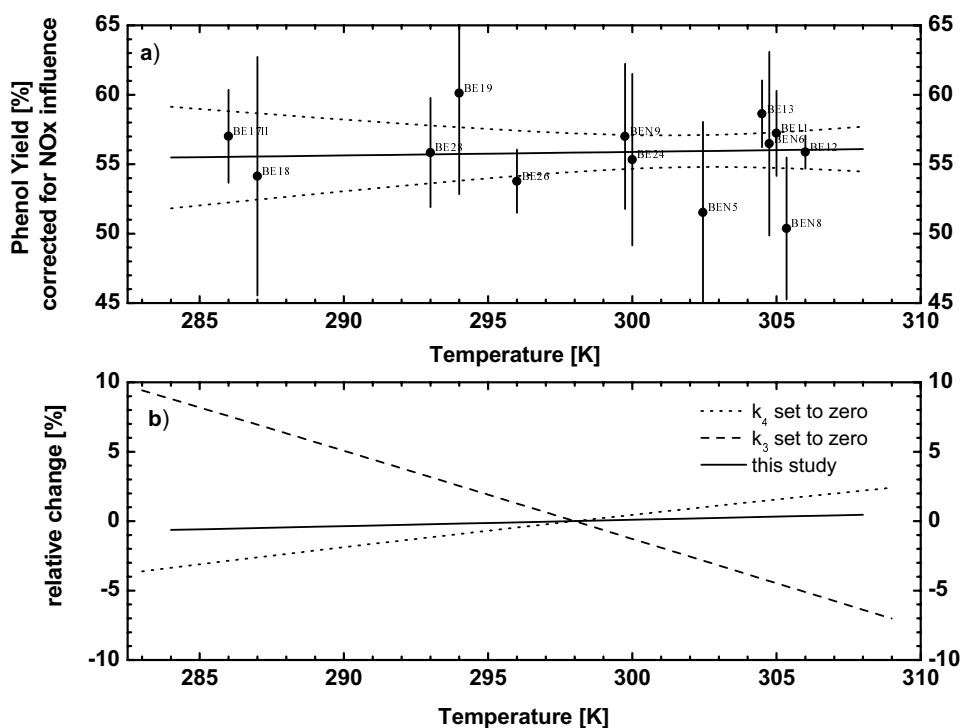


Figure 4.9: The phenol yield as a function of temperature for experiments with OH-tracer. In the upper part the data points are labeled with the name of the respective experiment. In the lower part, the relative change of the phenol yield is estimated from the enthalpy data by Lay et al. (1996) and are compared to the observed variation (see text).

regression to the experimental data is included (solid line). The three lines have been normalized to $T = 298$ K in this representation.

As can be seen in Figure 4.9b, the two phenol forming channels (3) and (4) exhibit a distinctly different temperature dependence. In the case of only channel (3) forming phenol the yield is expected to increase with temperature though only slightly with a assumed linear relative change of $+0.23\% \cdot \text{K}^{-1}$. On the contrary, if only channel (4) forms the phenol a pronounced decrease of the phenol yield is expected at a rate of $-0.63\% \cdot \text{K}^{-1}$. This characteristic behaviour allowed to distinguish both channels already within the small temperature interval covered by the data points. From the slope of the linear regression to the data points a relative change of $0.05 \pm 0.2\% \cdot \text{K}^{-1}$ is obtained which is consistent with channel (3) contributing about $(80 \pm 25)\%$ of the phenol and channel (4) contributing about $(20 \pm 25)\%$. Despite the large errors this result points to the major fraction, if not all the phenol is formed through channel (3) meanwhile it is not conclusive with only channel (4) forming the phenol.

4.3.5 The formation mechanism of phenol

Attempts were made to distinguish the relative contributions of pathways (3) to (5) in Figure 2.1 that result in the direct formation of phenol (primary phenol) from pathway (6) which forms phenol via the stable, i.e. a "long-lived" intermediate compound benzeneoxide-oxepin [Klotz *et al.* 1997] (secondary phenol).

The photolysis of benzeneoxide-oxepin, reaction (7) in Figure 2.1 forms phenol at a yield of $(43.2 \pm 4.5)\%$ [Klotz *et al.* 1997]. Additionally, the reaction with OH-radicals is fast at a rate-constant of $k_{OH}(\text{benzeneoxide-oxepin}) = 1 \cdot 10^{-10} \text{ cm}^3 \cdot (\text{molec} \cdot \text{s})^{-1}$ [Klotz *et al.* 1997]. Assuming an OH-radical concentration of $3 \cdot 10^6 \text{ cm}^{-3}$ and an NO_2 -photolysis-frequency of $J_{\text{NO}_2} = 8.5 \cdot 10^{-3} \text{ s}^{-1}$ (typical for the experiments conducted here) loss of the benzeneoxide/oxepin due to photolysis and OH-reaction is about equal. Assuming a unity yield for the formation of benzeneoxide/oxepin the sequence (6/7) in Figure 2.1 could form no more than 40-50% of the observed phenol.

The overall loss-rate of benzeneoxide/oxepin in this example was about $6.8 \cdot 10^{-4} \text{ s}^{-1}$ which corresponds to a lifetime of roughly 25 minutes. Hence, any formation of secondary phenol via pathway (6/7) should become operative with considerable delay and should influence the formation kinetics of phenol during the first few minutes of reaction-time to a very minor extend. Nevertheless, the primary phenol yield determined for experiment BE26 in Figure 4.6, see Table 4.5, compared well to the yield as it was calculated from Equation 4.2 of $(52.1 \pm 0.4)\%$ for the corresponding NO and NO_2 concentrations of BE26. Since Equation 4.2 fitted equally well the phenol yields determined after several hours of reaction-time (e.g. experiment BE12, Figure 4.8) there was no indication that pathway (6/7) contributed to the observed phenol.

Further, the numerical simulations conducted in this study adequately reproduced the concentration-time-profile of phenol by a mechanism involving channel (3) only, as is evident from Figure 4.7. This study therefore provided no evidence for channel (6/7) to be operative in the OH initiated oxidation of benzene. The combined experimental errors from the relative comparison of two phenol yields, i.e. at the very start (BE26) and after several hours of reaction-time (BE12) was 3.1%. Under the conditions of experiments BE12 and BE26 about 26% and 34% of benzeneoxide/oxepin were expected to photolyse, respectively. Hence, an upper-limit for the formation of benzeneoxide/oxepin of about 24% was estimated on the basis of the uncertainty of the phenol yields.

4.3.6 Error considerations

In Table 4.6 the error sources of Φ_{phenol} are listed. They were grouped in systematic and specific error sources. In the column denoted "method" the evaluation method is indicated where the respective error applied (see Section 3.5.5).

Systematic error sources of Φ_{phenol} were the uncertainties in the absorption cross-sections σ and the OH-reaction rate-constants of phenol, benzene and the OH-tracer substances. The σ of benzene and phenol are known with an error of 3.9 % and 2.6 % [Etzkorn *et al.* 1999]. Also, the benzene and phenol concentrations measured just after addition into the chamber were consistent with the concentrations calculated from the added amounts and the volume of the chamber and hence further support the agreement between literature values [Troost 1997; Etzkorn *et al.* 1999]. See Section 5.1.1 for a detailed discussion for the phenol. The values of the OH-reaction rate-constants are comparably well known with a remaining uncertainty of about 4 % for the OH-reaction of benzene and < 6 % for that of phenol [Semadeni *et al.* 1995; Atkinson 1994] (and references therein). The OH-reaction rate-constants for the tracer substances are known with an accuracy of about 3 %, 9 % and 11 % for the di-nbutyl ether [Wallington *et al.* 1988; Wallington *et al.* 1989; Nelson *et al.* 1990; Semadeni and Kerr 1993; Mellouki *et al.* 1995; Kramp and Paulson 1998], 1,3,5-TMB [Kramp and Paulson 1998; Atkinson 1994] (see also Section 4.2.2) and p-cresol [Semadeni *et al.* 1995; Atkinson 1994], respectively. The overall systematic uncertainty of Φ_{phenol} for the different evaluation procedures is listed in Table 4.6 and ranged between 7.5 % and 12 %. Additional error sources were specific for the employed methods of evaluation of Φ_{phenol} and included the evaluation error of the spectra (depending on the signal to noise ratio, typically few percent) [Stutz and Platt 1996].

For method a the correction factor f_c employed in Equation 3.29 ranged between 1.025 ± 0.014 to 1.08 ± 0.04 reflecting the minor but non negligible influence of the walls for phenol. The uncertainty of f_c adds a minor amount of < 4 % to the overall uncertainty of the phenol yield. Further, for the runs where ozone-photolysis was used to generate OH-radicals, traces of NO_2 were detected to build up that may form NO_3 -radicals from reaction with ozone. Under the experimental conditions (ozone: 80 ppb, NO_2 : 2 ppb) the NO_3 -concentration may have reached levels of about 0.1 ppt corresponding to a phenol loss-rate of about $9 \cdot 10^{-6} \text{ s}^{-1}$. This loss-process may have become comparable to the rate for phenol deposition to the chamber walls and was included into the errors given in Table 4.5 (about 3 %).

Table 4.6: Error sources for the experiments on benzene.

Error source	Error [%]	Method ^ψ	Reference / Remarks
Systematic error sources			
Absorption cross-section of benzene	3.9	a, b ₁ , b ₂ , c	see text
Absorption cross-section of phenol	2.6	a, b ₁ , b ₂ , c	see text
$k_{OH,benzene}$	4	a, b ₁ , b ₂ , c	see text
$k_{OH,phenol}$	6	a, b ₂ ^α , c ^α	see text
$k_{OH,di-n-butylether}$	3	b ₂ , c	see text
$k_{OH,1,3,5-TMB}$	9	b ₁ , b ₂	see text
$k_{OH,p-cresol}$	11	b ₁	see text
Overall systematic error	8.6	a	
Overall systematic error	10.9 - 12.6	b ₁	
Overall systematic error	7.5 - 11.3	b ₂	
Overall systematic error	7.5	c	
Specific error sources			
Evaluation of the DOAS spectra	1 - 10	a, b ₁ , b ₂ , c	see text
Evaluation of the FTIR spectra	2.5 - 25	a, b ₁ , b ₂ , c	see text
Conversion of benzene	1.5	b ₁	see Section 3.5.5
OH-concentration without OH-tracer	3.2 ^γ - 16 ^δ	c	see Section 3.5.6
Correction of OH-tracer leakage			
di-n-butylether	0.2 ^γ - 0.7 ^δ	b ₂ , c	see Section 3.5.6
1,3,5-TMB	< 0.1 ^γ - 0.3 ^δ	b ₁	see Section 3.5.6
p-cresol	0.1 ^γ - 0.4 ^δ	b ₁	see Section 3.5.6
Correction of OH-tracer deposition to the wall			
1,3,5-TMB	0.1 ^γ	b ₁	see Section 3.5.6
p-cresol	1.5 ^γ	b ₁	see Section 3.5.6
Temperature dependence $k_{OH,benzene}$	1.6	b ₂ , c ^ε	see Table 3.2
Deposition of phenol to the chamber walls			
Correction factor ^β f _c	2.5	a	see Section 3.5.5
Correction for wall losses ^α	2.5	b ₂	
Unaccounted wall loss ^{α,δ}	5	c	see Section 5.2.2
phenol loss through reaction with NO ₃ -radicals	3	a	only (2) ^π , see text
Temperature dependence of $k_{OH,phenol}$	2.7	b ₂ , c ^ε	see Table 3.2
Temperature dependence of $k_{OH,tracer}$			
di-n-butylether	< 2	b ₂ , c ^ε	see text
1,3,5-TMB	< 2	b ₁ ^φ	see text
p-cresol	< 2	b ₁ ^φ	see text
Overall specific error	4.1 - 14.7	a	
Overall specific error	2.5 - 3.1	b ₁	
Overall specific error	4.5	b ₂	
Overall specific error	5.8 - 16.6	c	

^α correction of phenol loss through OH-reaction. Here: F = 1.5.

^β f_c applied in Equation 3.29. Here: f_c = 1.05.

^γ OH-source (3)^π and (5)^π: [OH] = 1.3 · 10⁷ cm⁻³, L = (5.5 ± 0.6) · 10⁻⁶ s⁻¹.

^δ OH-source (1)^π: [OH] = 3 · 10⁶ cm⁻³, L = (5.5 ± 0.6) · 10⁻⁶ s⁻¹.

^ε typical temperature change. Here: T = 298 K, ΔT = 6 K.

^φ typical temperature change. Here: T = 298 K, ΔT = 2 K.

^π the number refers to the OH-source used, see Section 3.4.4.

^ψ see Section 3.5.5.

For methods b and c, the major uncertainties arised from the uncertainty of the traced OH-concentration. As can be seen in Table 4.5, the error of the experiments without OH-tracer was considerably higher due to an error of the leakage-correction (up to 17%). For the experiments with OH-tracer substance this error was reduced to $< 2\%$. All tracer compounds exclusively reacted with OH-radicals. The wall loss could be adequately corrected if necessary. The main error sources in method b₂ and c were the correction of phenol deposition to the walls (about 3%) and the effect of temperature on the OH-reaction rate-constants of benzene and phenol. Though the latter was taken into account based on the average temperature of the respective experiment, temperature changes of about 6 K resulted in a minor though non-negligible error of about 3%, respectively [Semadeni *et al.* 1995; Bohn and Zetzsch 1999]. The overall error due to the specific uncertainties of the employed evaluation methods are listed in Table 4.6. The overall uncertainty of the phenol yields for experiments with OH-tracer, identified as the sum of the average specific error (7.5%) and the average systematic error (10%), was about 12.5%.

In Figure 4.10 the phenol yields are plotted as a function of the evaluation method. All yields but not those obtained at high NO_x concentration (overall NO_x correction $F > 1.4$) were plotted. Note that the yields were plotted on an expanded y-axis. The error of the plotted data corresponds to the 2-sigma uncertainty of the evaluation method only (that is described in more detail in Section 4.3.6) neglecting systematic error-sources. In general, the individual experiments agreed even within the thus reduced experimental error. However, the peak-to-peak scatter was considerable (26%). The horizontal bars in Figure 4.10 indicate average phenol yields that were calculated for the experiments covered by the bars. For method (c) the data was split in two groups. Group 1 consists of six experiments of which four were carried out with an added OH-tracer substance. In two experiments a different OH-source (see Table 4.5) was used to enhance the benzene turn-over. Group 2 of the method-(c)-experiments used the decay of benzene to trace the OH-concentration. Though the experiments of both groups agreed within the uncertainties of the individual experiments, the scatter among the Group-2-experiments was considerably higher. This is in part due to the higher uncertainties in the OH-concentration with these experiments. Moreover, the average yield of these experiments tended to be systematically lower. These Group-2-experiments were hence not considered in the evaluation of the average phenol yield. Further, the yields obtained at NIES tended to be systematically lower than those measured at EUPHORE. The reason for this

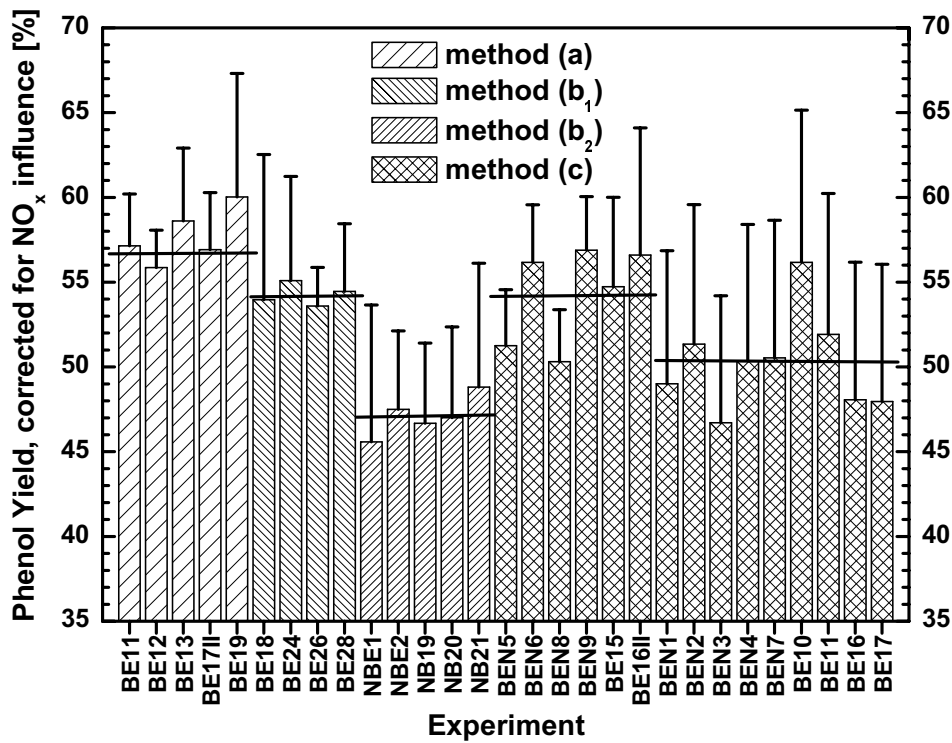


Figure 4.10: The phenol yields are plotted as a function of the evaluation method. The error corresponds to 2-sigma uncertainty of the specific errors of each method only (see text) and neglects systematic error sources. Despite the considerable variation among individual experiments the yields agree within their error limits. The horizontal bars indicate average phenol yields calculated for the respectively covered yields (see text).

discrepancy is not clear at present. The NIES experiments were considered in the average phenol yield of this work.

Selected data from this Section has been presented on a Workshop [Volkamer et al. 2000] and a publication is currently in preparation [Volkamer et al. 2001].

4.4 The ring-retaining yields from p-xylene

The yields of pTALD and 2,5-DMP were evaluated from 11 experiments on the photooxidation of p-xylene. The obtained yields of both compounds as well as the initial conditions of the individual experiments are summarized in Table 4.7 together with the employed OH-source and the evaluation procedure that was used to derive the results. The 2,5-DMP yields are given in two columns. The raw-yields of the first column were normalized to a temperature of $T = 298\text{ K}$ and the corrected yields of 2,5-DMP are given in a second column. The data from experiment PXY7 (see Table 4.7) confirm the systematic deviations in the product yields already observed for benzene (see also Table 4.5) for experiments using radical-source (4). This data was not considered in the further discussion of this Section and is discussed separately in Section 5.4.3. In the following, the results of an example-experiment PX10 are presented. In the upper part of Figure 4.11 (designated a)), the results of the numerical simulations are shown, the bottom part b shows the measured NO_x -species, NO_3 and ozone (see the caption for further explanations).

The high turn-over of p-xylene is typical for this system. It is well reproduced by the model and allowed to trace the number of OH-radicals directly from the decay of p-xylene. The calculated concentration-time-profile of pTALD closely matches the measured one. This is also the case for the concentration-time-profile of 2,5-DMP, though it is reproduced satisfactorily only in the initial phase of the experiment. The yield of the phenol was determined from this part of the experiment. Significant amounts of 2,5-DMP are lost through reaction with OH-radicals already in the early part of the experiment. The deviations of the 2,5-DMP concentration-time-profile after about 45 minutes of reaction-time however could not be explained in terms of OH-chemistry. It was rather found to coincide with the number of NO_3 -radicals, as calculated from Equation 3.38 increased. The NO_3 -reaction of phenol-type compounds is known to be fast (several $10^{-12}\text{ cm}^3\cdot(\text{molec}\cdot\text{s})^{-1}$, see Section 4.2.3) while it is three orders of magnitude slower for the aldehyde-type compounds (see Table 3.2). Hence, only the phenolic compound is sensitive to the considerable concentration of NO_3 (several ppt at maximum, see also Section 4.8). The formation of NO_3 -radicals is known to be a significant sink for phenols under simulated atmospheric conditions [Carter *et al.* 1981; Klotz *et al.* 1998]. It forms also an significant sink for phenols in the daytime atmosphere [Volkamer *et al.* 1998; Ackermann *et al.* 2000] as is discussed in Section 7. As further aspects of this experiment, the particle formation is discussed in the Section 4.8.

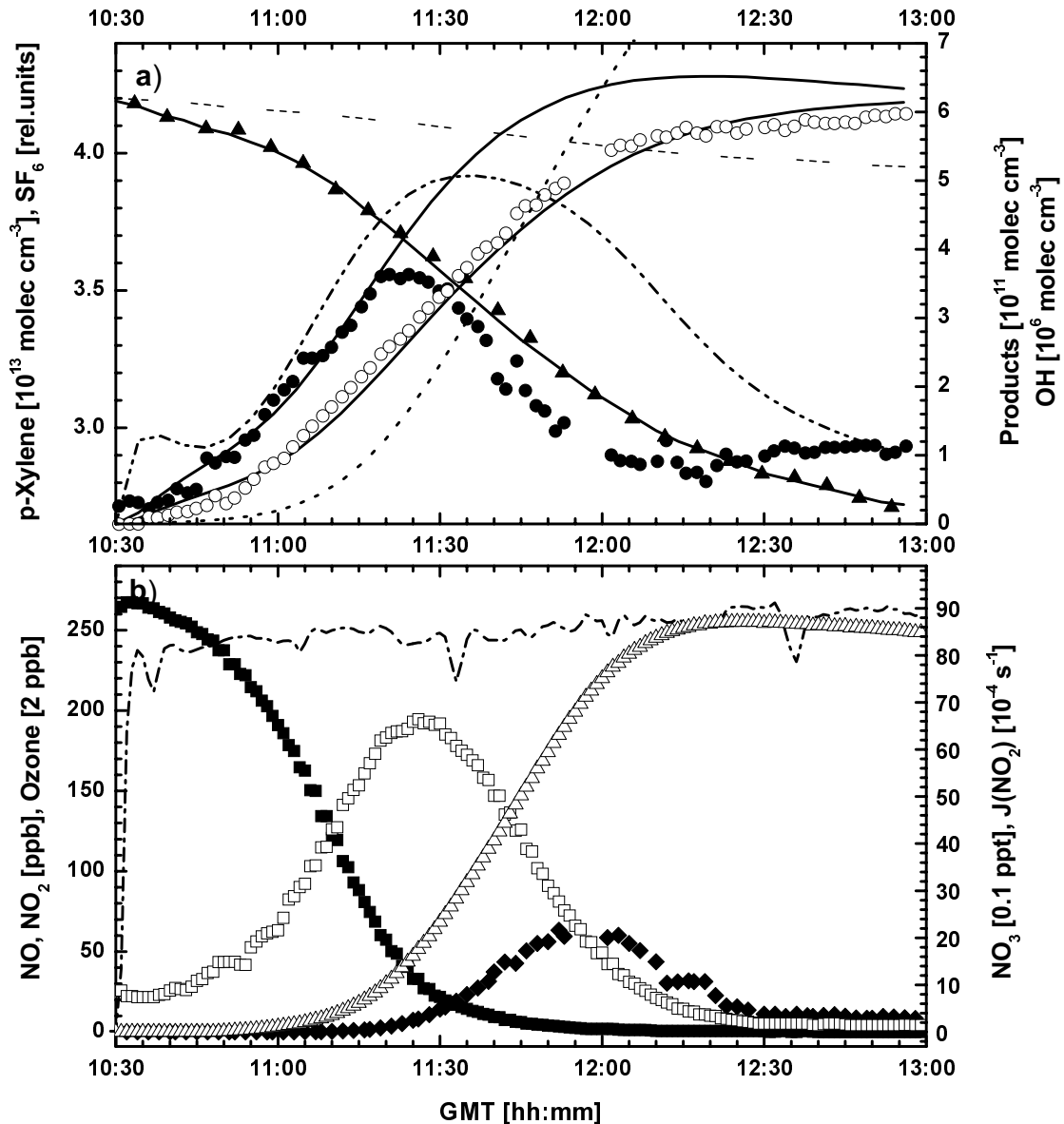


Figure 4.11: Concentration-time-profiles from experiment PX10. Upper part (a): Simulated data, describing the OH-chemistry neglecting NO_3 -radical initiated processes are indicated by solid lines. The calculated OH-concentration-time-profile is given by the dash-dot-dotted line; the 2,5-DMP-loss due to OH-reaction by the dotted line (both right scale "Products", OH-divided by 10^6). Experimental data: (solid triangle) p-xylene; (dashed line) relative SF_6 -decay, both left axis; (solid dot) 2,5-DMP; (open dot) pTALD, both right axis. Lower part: (solid square) NO; (open square) NO_2 ; (open triangle) ozone, scaled by a factor of two; all left axis; (diamonds) NO_3 ; (dotted line) J_{NO_2} ; both right axis.

Table 4.7: Experimental conditions and results for the experiments on p-xylene.

Name	p-Xylene [10^{12} cm $^{-3}$]	NO $_x$ [ppb]	pTALD		2,5-DMP		Experi- mental type $^{\beta}$	Evalu- ation method $^{\gamma}$
			Yield Φ_{PTALD} [%]		Yield Φ_{DMP} [%]	Yield $\Phi_{DMP,corr}$ $^{\alpha}$ [%]		
PXY1	28.0	46	6.6 ± 1.1	12.9	12.1 ± 1.4	(1)	(c)	
PXY3	83.1	143	9.4 ± 1.4	14.0	13.2 ± 1.7	(1)	(c)	
PXY4	55.3	1.5*	7.7 ± 2.1	10.5	9.9 ± 2.1	(2)	(c)	
PXY7	38.4	0.3*	$1.6 - 7.3^{\delta}$	17.5	17.2 ± 2.8	(4)	(c)	
PX10	41.2	285	8.0 ± 1.0	13.7	13.1 ± 1.4	(1)	(c)	
PX11	40.8	19	8.6 ± 2.0	10.8	10.2 ± 1.5	(1)	(c)	
PX12	41.3	800	10.1 ± 1.4	12.9	12.9 ± 1.5	(1)	(c)	
PX14	40.8	450	9.2 ± 1.3	10.9	11.2 ± 1.1	(1)	(c)	
PX15	19.8	65	8.4 ± 1.0	12.2	12.8 ± 1.4	(1)	(c)	
PX16	83.1	68	7.3 ± 1.0	9.1	9.3 ± 2.0	(1)	(c)	
PX24	18.5	68	6.9 ± 1.8	10.0	11.7 ± 2.5	(3)	(b $_2$)	

* NO $_x$ -free at start of experiment.

$^{\alpha}$ values in this column have been normalized to T = 298 K (see text).

$^{\beta}$ the number refers to the OH-source used, see Section 3.4.4.

$^{\gamma}$ see Section 3.5.5.

$^{\delta}$ the yield is not constant; numbers indicate the range of the yield (see text).

4.4.1 Dependence on the NO $_x$ concentration

In Figure 4.12 the experimental data of the yields of pTALD and 2,5-DMP as determined in the individual experiments of this study are shown. The Figure shows the yields of both compounds as a function of the NO- and NO $_2$ -concentration. The yields of both compounds were observed constant over the employed range of NO $_x$ concentrations, indicating that the influence of NO $_x$ reactions is reduced for the p-xylene as compared to benzene (see Section 4.3.1). The yields of pTALD and 2,5-DMP, calculated as average values of the data listed in Table 4.7 (neglecting PXY7, see above) were determined (8.2 ± 2.3)% and (11.6 ± 2.8)%, respectively. Thereby, the normalized yields were used in case of the 2,5-DMP. Using these values did not affect the observed mean value of Φ_{DMP} but reduced the scatter among the individual experiments. The data from this Section has been published [Volkamer *et al.* 1998].

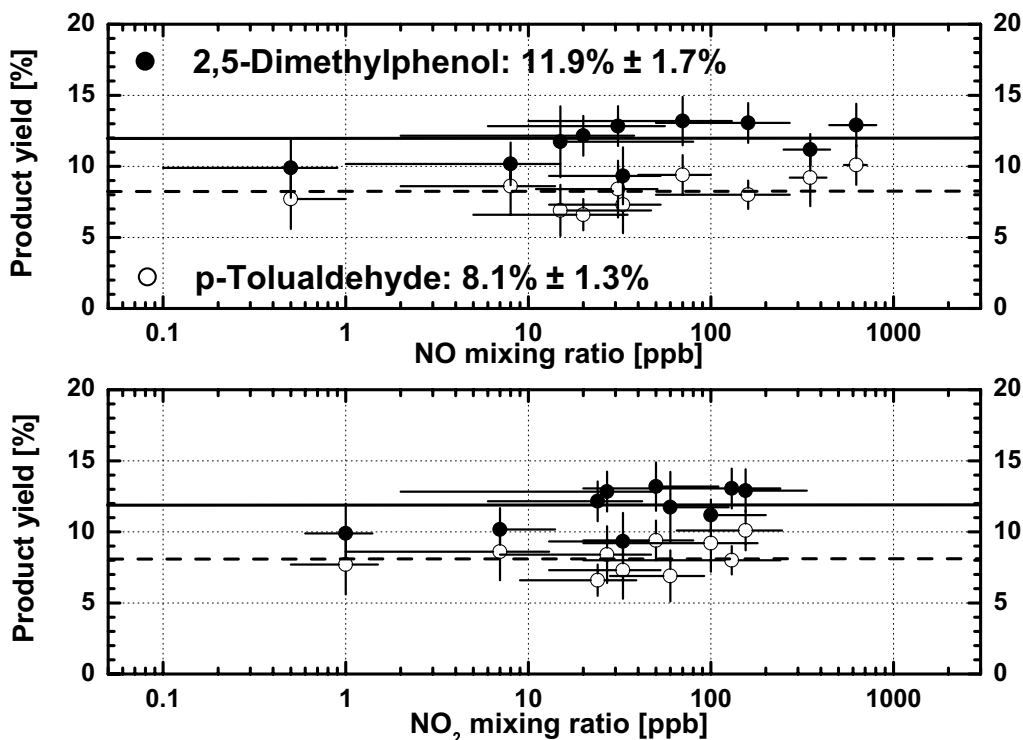


Figure 4.12: The yields of the ring-retaining products from p-xylene are plotted as a function of the NO- (upper part) and NO₂-concentration (lower part). The dashed line corresponds to the average pTALD yield of all experiments. The 2,5-DMP yields were normalized to T = 298 K (see text) and the solid line corresponds to the average normalized yield. The NO_x-concentrations correspond to the mean concentrations over the time-interval when the yield was determined and error bars correspond to the variability over this time-interval.

4.4.2 Dependence on the temperature

The raw-yields of pTALD and 2,5-DMP are shown as a function of temperature in Figure 4.13. The plotted lines in the upper diagram denote the error weighted linear regressions to the pTALD (dotted line) and 2,5-DMP (solid line) data. The covered temperature range of $\Delta T \approx 18$ K corresponded to the seasonal cycle of the ambient temperature, as discussed in Section 4.3.4. The Φ_{pTALD} was found independent of the temperature (slope: $(0.006 \pm 0.1) \% \cdot K^{-1}$, upper part of Figure 4.13). However, the Φ_{DMP} was found to increase towards higher temperatures at a rate of $(0.14 \pm 0.10) \% \cdot K^{-1}$. This temperature dependence of $\Phi_{DMP}(T)$ was used to normalize Φ_{DMP} to a temperature of T = 298 K. The applied corrections were as high as 6 %.

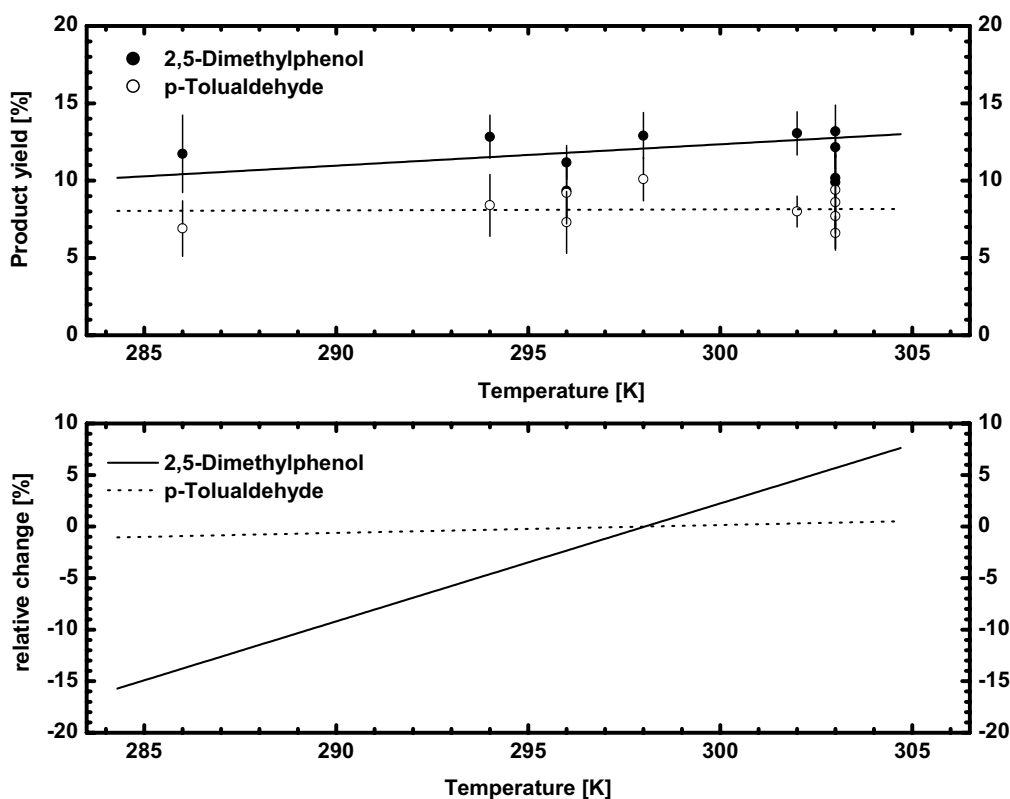


Figure 4.13: The ring-retaining product yields from p-xylene are plotted as a function of the temperature. The lines in the upper part indicate a regression to the pTALD yields (dashed line) and the 2,5-DMP yields (solid line). For the lower part, the yields were normalized to the value at $T = 298$ K and the relative variation of the yields is plotted as a function of the temperature.

The fact that pTALD and 2,5-DMP showed a different temperature dependence rule out any systematic error sources that influenced both yields in a similar way (e.g. temperature dependence of the k -value of OH-reaction of p-xylene, wall-deposition etc.). One possible source of error may be the unknown temperature dependence of the rate-constants used in the applied OH-correction of both compounds. It will be small for the pTALD. However, it is assumed significant for the 2,5-DMP which, in analogy to phenol and the cresol-isomers [Oliaru *et al.* 2000], most likely reacts predominantly through OH-addition to the aromatic ring. It was decided to adopt the temperature dependence of the k -value of phenol for the 2,5-DMP (see Section 3.5.5). Though the temperature dependence might be different for the 2,5-DMP it is not expected to influence significantly the results on the Φ_{DMP} since the yields were determined mainly during the initial phase of an experiment (see Figure 4.11) where

the corrections due to OH-loss were small ($F < 1.2$). Hence, the error in the assumed temperature dependence of the OH-reaction rate-constant of 2,5-DMP affects Φ_{DMP} only marginally.

The observed difference in the temperature dependence of Φ_{pTALD} and Φ_{DMP} may rather be explained from the different formation pathways of pTALD and 2,5-DMP. With respect to the formation pathway of the 2,5-DMP the enthalpy data is limited for the p-xylene system. However, the increase of the 2,5-DMP with temperature points towards a 2,5-DMP formation proceeding directly from the reaction of p-xylene-OH-adduct with O_2 , in analogy to the phenol formation from benzene discussed in Section 4.3.4 (see channel (3) in Figure 2.1).

4.5 The ring-retaining yields from 1,3,5-TMB

In a previous work, *Ücker* [1999] estimated the yields of 3,5-DMBA and 2,4,6-TMP, the ring-retaining products of 1,3,5-TMB. At that time no kinetic data was available to correct for the product loss through OH-reaction and estimated values were used in that work. However, the errors then were dominated from the uncertainty of the estimates. The rate-constants are now available (see Section 5.2.2). They were used to re-determine the yields based on the data from *Ücker* [1999]. In addition, an improved evaluation method (see Section 3.5.5) and the results on wall-deposition (see Section 4.2.1) were employed. The correction factor for the DMBA was $F < 1.34$; in case of the TMP all data points with $F > 2$ were neglected. The amount of product formed is plotted in Figure 4.14 as a function of the reacted amount of TMB. The error bars, which were indicated for one data point, correspond to the overall 2-sigma confidence interval. Both products were identified as primary products. The yields of DMBA and TMP were determined $(2.7 \pm 0.4) \%$ and $(6.7 \pm 1.0) \%$, respectively. The employed corrections lead to essentially no change of the yield of DMBA as determined by *Ücker* [1999] though with a considerably reduced error. For the TMP, the re-determined yield is about 25% higher than the value by *Ücker* [1999] but still falls within the specified error margins of that work. Again, the error of the re-determined value is considerably reduced.

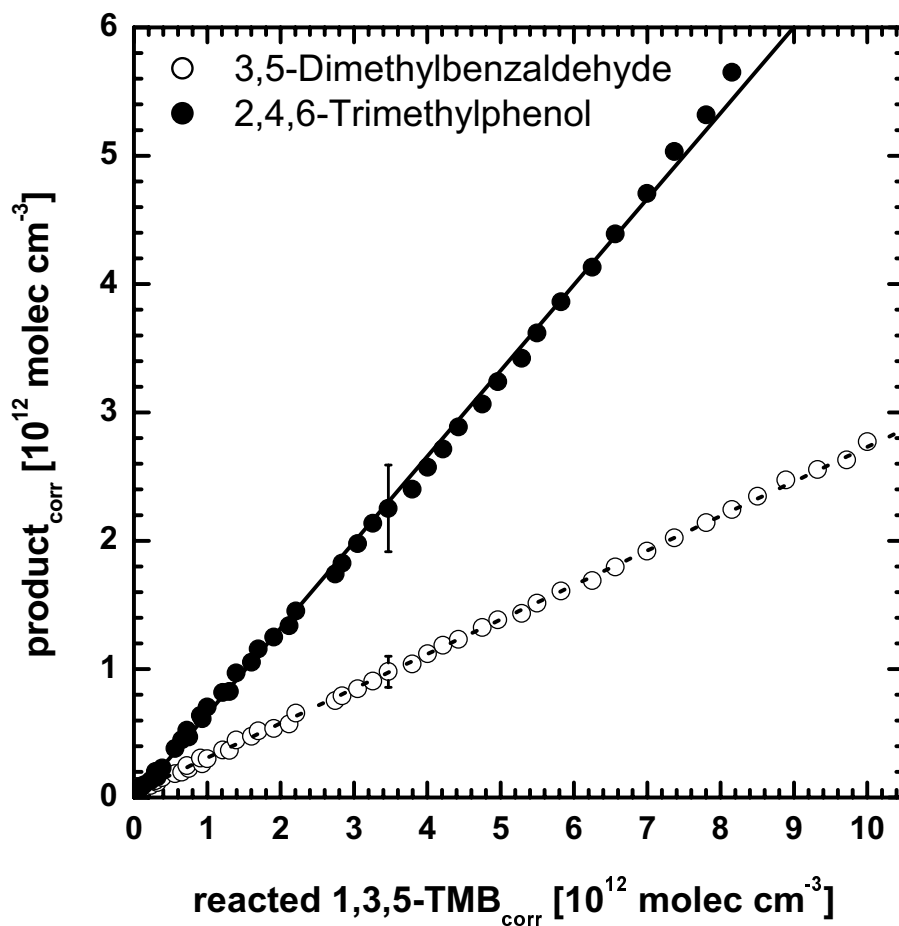


Figure 4.14: Plot of the concentration of ring-retaining product concentrations, corrected for OH-reaction (see text) as a function of the amount of reacted amount of 1,3,5-TMB.

4.6 The glyoxal yields from BTX

In this Section the separation of the fraction of glyoxal formed as a primary product (primary glyoxal yield, see Section 4.6.1) from the overall yield of glyoxal is demonstrated for BTX. The glyoxal yields determined in a series of experiments on the oxidation of benzene, toluene and p-xylene are listed in Table 4.8. The errors correspond to the 2-sigma confidence interval without consideration of the uncertainty of the differential absorption cross-section of glyoxal ($\approx 20\%$, see Section 4.1.2, see Table 5.8 for absolute uncertainties). Experiments where both yields are specified used DOAS for the separation of the primary and secondary glyoxal yields. In the other experiments the glyoxal concentration was obtained from FTIR. Also included in Table 4.8 are the initial conditions, the experimental type (see Section 3.4.4) and the employed evaluation method. The data from experiment PXY7 (see Table 4.8) confirm the systematic deviations in the product yields obtained for the benzene system in experiments using radical-source (4) (see Table 4.5 and 4.7). This data was not considered in the further discussion of this Section and is discussed separately in Section 5.5.4.

In the following, the data of experiment PX24 on p-xylene is presented (see Figure 4.15). OH-radicals in this experiment were generated from the photolysis of nitrous acid (HONO). The values of J_{NO_2} (dotted line) show a steep rise upon opening of the chamber housing; later variations are due to passing clouds. The OH-concentration, as calculated from the decay of p-xylene, was maximum ($[OH] \approx 8 \cdot 10^6$ molec cm^{-3} , see Equation 3.36) directly after the opening of the chamber housing. The decay in p-xylene then is most pronounced as can be seen from comparing the p-xylene decay (solid line, fit through data points) to the dilution (dashed line). The concentrations of glyoxal and the ring-retaining products were observed to build up quickly and in fact all these compounds were detected in the very first DOAS spectra after the opening of the chamber housing. The concentration-time-profiles of pTALD and 2,5-DMP were observed to be similar to those shown in Figure 4.11 and discussed in Section 4.4. Note, that these concentrations have been scaled by a factor of ten as compared to those of glyoxal and formaldehyde. The concentration of glyoxal steadily increased up to a distinct maximum concentration of about $1.5 \cdot 10^{12}$ molec cm^{-3} ($\approx 62\text{ppb}$) at 11:50 GMT. By that time almost clear sky conditions prevailed. The OH-concentration had decreased to about $[OH] \approx 2.3 \cdot 10^6$ molec cm^{-3} . Afterwards, the glyoxal concentration dropped until the end of the experiment with photolytic loss of glyoxal gaining importance

Table 4.8: Experimental conditions and results for the product studies on glyoxal.

Compound	Name	Aromatic [10 ¹² cm ⁻³]	NO _x [ppb]	Glyoxal		Experi- -mental type ^α	Evaluation method ^β
				Primary Yield Φ _{PGLY} [%]	Overall Yield Φ _{GLY} [%]		
Benzene	BE18	25.2	118	36.3 ± 3.9	35.5 ± 6.6	(3)	(b ₁ , b ₂ , b ₃)
Toluene	TOL2	21.2	120	40.0 ± 4.2	37.9 ± 6.5	(3)	(b ₁ , b ₂ , b ₃)
	TOL4	103	107	29.3 ± 3.0	30.3 ± 6.9	(3)	(b ₂ , b ₃)
p-Xylene	PXY1	28.0	46		36.4 ± 4.4	(1)	(c)
	PXY3	83.1	143		37.1 ± 4.5	(1)	(c)
	PXY4	55.3	1.5*		41.9 ± 10.1	(2)	(c)
	PXY7	38.4	0.3*		9.2 ± 1.4	(4)	(c)
	PX10	41.2	285		34.3 ± 4.2	(1)	(c)
	PX11	40.8	19		37.4 ± 4.6	(1)	(c)
	PX12	41.3	800		37.1 ± 4.5	(1)	(c)
	PX14	40.8	450		31.5 ± 5.2	(1)	(c)
	PX15	19.8	65		36.7 ± 4.5	(1)	(c)
	PX16	83.1	68		28.0 ± 3.5	(1)	(c)
	PX24	18.5	68	42.3 ± 5.3	38.4 ± 7.0	(3)	(b ₁ , b ₂ , b ₃)

* NO_x-free at start of experiment.

^α the number refers to the OH-source used, see Section 3.4.4.

^β see Section 3.5.5.

with decreasing reactivity in the reaction-system. The concentration of NO₃-radicals was estimated from Equation 3.38 and reached levels of about 2.5 ppt. Under these conditions, the fast reaction of phenol-type compounds with NO₃-radicals becomes an important sink, as discussed in Section 4.4. However, for glyoxal and the aldehydes loss due to reaction with NO₃-radicals is found negligible due to the slow reaction of these species with NO₃. For benzene however, NO₃ levels were effectively suppressed from added NO. The reactions of NO₃-radicals were neglected in the further evaluation.

The concentration-time-profiles of the ring-retaining products and glyoxal were evaluated to determine the glyoxal yields at different times during each experiment, as indicated by the arrows in Figure 4.15. The left arrow indicates the primary glyoxal yield that was obtained from the relative yield method (see next Section), the

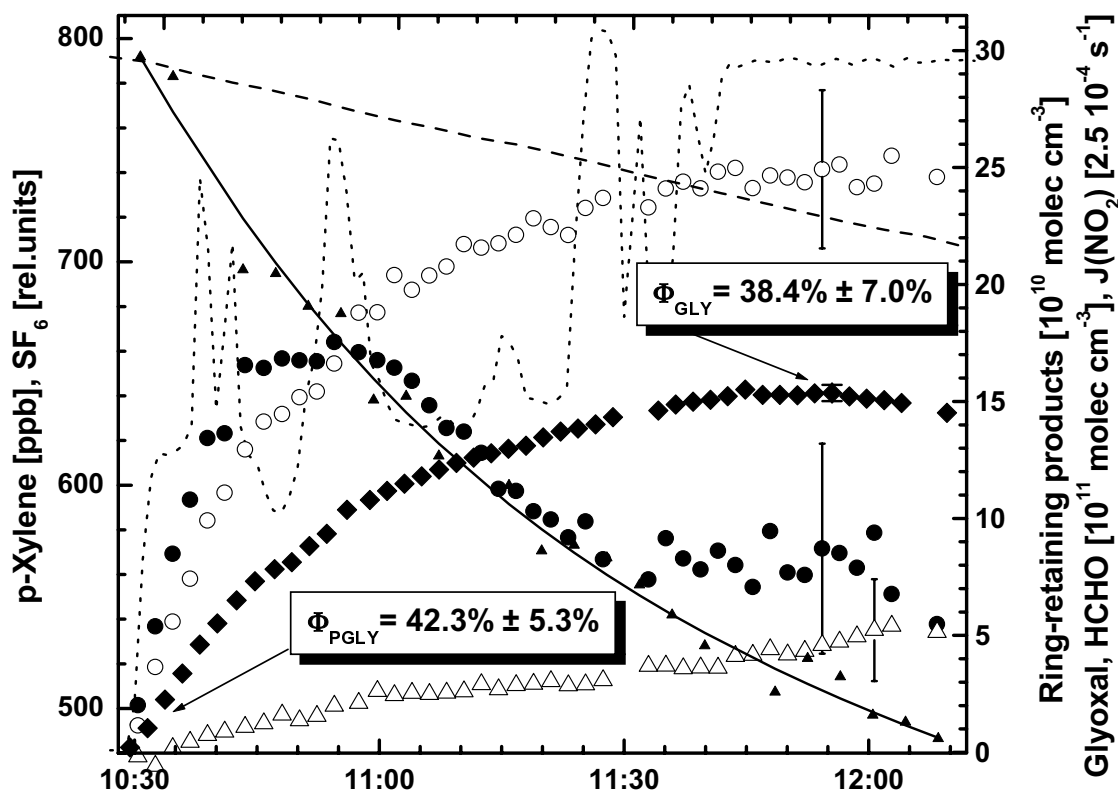


Figure 4.15: Concentration-time-profiles from experiment PX24. The following data is shown: (solid triangle) p-xylene; (solid line) fit to the p-xylene data; (dashed line) SF_6 , all left axis; (solid dot) 2,5-DMP; (open dot) pTALD; (diamond) glyoxal; (open triangle) HCHO; (dotted line) J_{NO_2} ; all right axis. Also included are Φ_{PGLY} the primary glyoxal yield and Φ_{GLY} the overall glyoxal yield.

right arrow indicates the overall yield of glyoxal after about 1 hour and 30 minutes of reaction-time (see Section 4.6.2).

4.6.1 The primary glyoxal yields

The primary glyoxal yield from benzene, toluene and p-xylene was determined relative to the yield of a ring-retaining product using the relative yield method described in Section 3.5.5 (indicated b_3).

Ring-retaining product yields as reference yields

The reported yields of aldehyde-type compounds from toluene, i.e. BALD [Smith *et al.* 1998; Klotz *et al.* 1998] and p-xylene, i.e. pTALD (see Table 5.5

for literature values) are found to be constant over a wide range of experimental conditions (see e.g. Figure 4.12 of this work). There exists little uncertainty in the yields of aldehyde-type compounds. The aldehyde yields of toluene and p-xylene are therefore well suited reference yields to quantify the yield of the direct formation of glyoxal.

The use of phenol-type compounds suffers several disadvantages. First, they are considerably (about a factor of four times) more reactive towards the OH-radical than the respective aldehyde-type product (see Table 3.2). Second, they are highly reactive to the NO₃-radical. Consequently, where possible the less reactive aldehyde-type compounds were chosen as reference compounds to determine the yield of glyoxal from toluene and p-xylene. For benzene, however, the only ring-retaining reference yield is that of phenol. This is not necessarily a limitation for this system. First, the DOAS technique is very sensitive to phenol (about a factor of 10-times more sensitive than for most other phenol-type compounds). Second, benzene is by far the slowest reacting aromatic compound. It is therefore well possible to suppress the formation of NO₃-radicals effectively over an extended time-span. For benzene, the phenol yield was used as reference yield to quantify the yield of the direct formation of glyoxal.

The reference yields employed in this work were the phenol yield (see Section 4.3.2) for benzene, the mean BALD yield of $\Phi_{BALD} = (5.9 \pm 0.6) \%$ for toluene [Smith *et al.* 1998; Klotz *et al.* 1998] and the mean literature value of the pTALD yields listed in Table 5.5 for p-xylene.

The relative-yield plot

At the time-resolution of the DOAS system, the initial three-to-seven data points after opening the chamber housing were essentially not influenced by OH losses ($F < 1.1$, Equation 3.33). In order to be able to include more data points in the analysis it was decided to account for secondary loss of products. Under the conditions described above, the photolytic-loss of glyoxal is about comparable to that through reaction with OH-radicals and both processes needed to be corrected. The ring-retaining products were essentially lost through OH-reaction. Photolysis of the aromatic aldehydes as well as deposition of the products, i.e. phenolic compounds to the chamber walls were minor loss-processes here and were therefore neglected in the further evaluation.

In Figure 4.16 the glyoxal concentration is plotted against the respective ring-

retaining products from benzene (Figure 4.16a, $F_{phenol} < 1.7$, $F_{GLY} < 1.4$), toluene (Figure 4.16b, $F_{BALD} < 1.17$, $F_{GLY} < 1.13$) and p-xylene (Figure 4.16c, $F_{p-TALD} < 1.13$, $F_{GLY} < 1.1$). The glyoxal concentration is observed to increase linearly with respect to the formation of the respective primary ring-retaining products. From Figure 4.16a-c the ratios of the glyoxal production-rate relative to that of the respective ring-retaining product were determined from a least square fit to the data. The primary glyoxal yield (Φ_{PGLY} in Table 4.8), i.e. within the first five-to-ten minutes, was hence calculated by multiplying this ratio with the respective reference yield (described above). The resulting yield for p-xylene is indicated in Figure 4.15 by the left arrow.

Identification of glyoxal as a primary product from BTX

The linear relations of glyoxal and the respective ring-retaining product in Figure 4.16a-c indicate that glyoxal was formed without observable delay as compared to the reference compounds. The aldehyde-type reference compounds are formed from the OH-radical abstraction reaction with alkyl-substituted aromatic compounds. The reaction sequence of this abstraction reaction is well understood and in the presence of NO (only a few ppb) it is expected to form aldehyde-type compounds at close-to-unity yield. From the reaction sequence shown in Figure 2.2, the NO-to-NO₂ conversion reaction is expected to be the rate-limiting step for the formation of the aldehydes. In the presence of 2 ppb of NO the delay from this reaction will be as small as a few seconds. Initial concentrations of NO in this study were in the range of several tens of ppbs and the aldehyde-type compounds were formed within less than a second after the initial OH-radical attack on the side-chain. Hence, the aldehydes were observed as primary products. The pathway of phenol-formation has been identified as part of this work (see Section 4.3.5) to proceed directly from the reaction of the aromatic-OH adduct with oxygen. The delay resulting from this reaction for phenol formation under atmospheric conditions was of the order of milliseconds. Accordingly phenol was also observed as a primary product (see also Section 4.3. Consequently also glyoxal is formed as a primary product.

4.6.2 The overall glyoxal yields

The sum of the primary and secondary glyoxal formed through a sequence of stable intermediate compounds was determined for benzene, toluene and p-xylene following method a. After about 90 minutes of reaction-time the concentration-time-profile

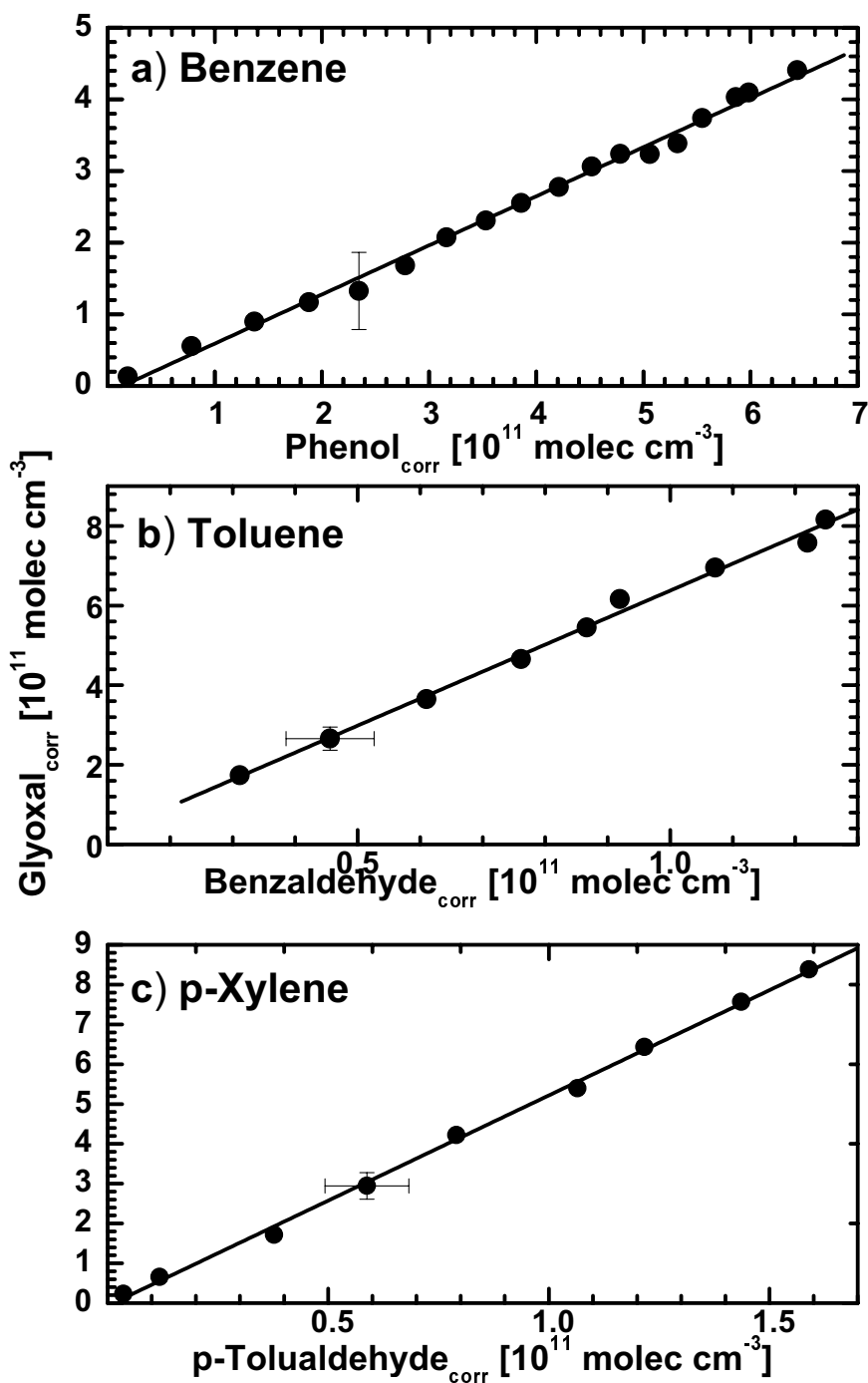


Figure 4.16: Plot of the concentration of glyoxal, corrected for reaction with OH-radicals and photolysis (see text) as a function of the concentration of a ring-retaining product, corrected for loss through OH-reaction, from (a) benzene, (b) toluene and (c) p-xylene. The primary glyoxal yield was determined from the slope of the data (see Section 3.5.5).

of glyoxal showed a well characterized maximum concentration indicating that a steady-state concentration of glyoxal had been reached. The overall yield was calculated from Equation 3.29 and is given in Table 4.8 as Φ_{GLY} . For p-xylene it is also indicated by the right arrow in Figure 4.15.

4.6.3 The negligible formation of secondary glyoxal

The overall yield of glyoxal determined after approximately 90 minutes of reaction-time was found to be essentially identical to the primary glyoxal yield for all the three investigated systems. Hence, no significant indication for any secondary formation of glyoxal through the further reaction of stable intermediate compounds was observed.

This result is further confirmed by the data shown in Figure 4.17a-c where the amounts of glyoxal ($F < 1.6$) and a respective ring retaining product ($F < 1.55$) are plotted against the reacted amount of benzene (Figure 4.17a), toluene (Figure 4.17b) and p-xylene (Figure 4.17c), as determined from the GC-FID data (corrected for dilution). The highly time-resolved DOAS data was correlated to match the sampling time of the GC. The given data cover about 90 minutes of reaction-time. A fixed relation (i.e. straight line) was observed for the amount of ring-retaining product and glyoxal formed from a given amount of aromatic hydrocarbon. The yields were calculated following method b_2 (see Section 3.5.5) and were found to be in good agreement with those determined from method a and b_3 . The linear increase observed for glyoxal further reflects the insignificant secondary contributions to the overall yield of glyoxal from BTX.

It is concluded that the glyoxal formed from BTX can be explained essentially in terms of primary glyoxal (**10a** in Figure 5.3). Any secondary sources of glyoxal are found to be of minor importance under the experimental conditions of this work. The uncertainty in the absorption cross-section of glyoxal cancels out if two yields are compared relatively. Hence, the conclusion on the negligible importance of secondary glyoxal formation under the conditions of this work is unaffected from this uncertainty.

4.6.4 Identification of the bicycloalkyl-radical intermediate

From the good time-resolved detection of glyoxal, it was possible to assess the role of stable intermediate species in the ring-cleavage pathways of BTX. Any hypothetical stable intermediate compound involved in glyoxal formation was either lost

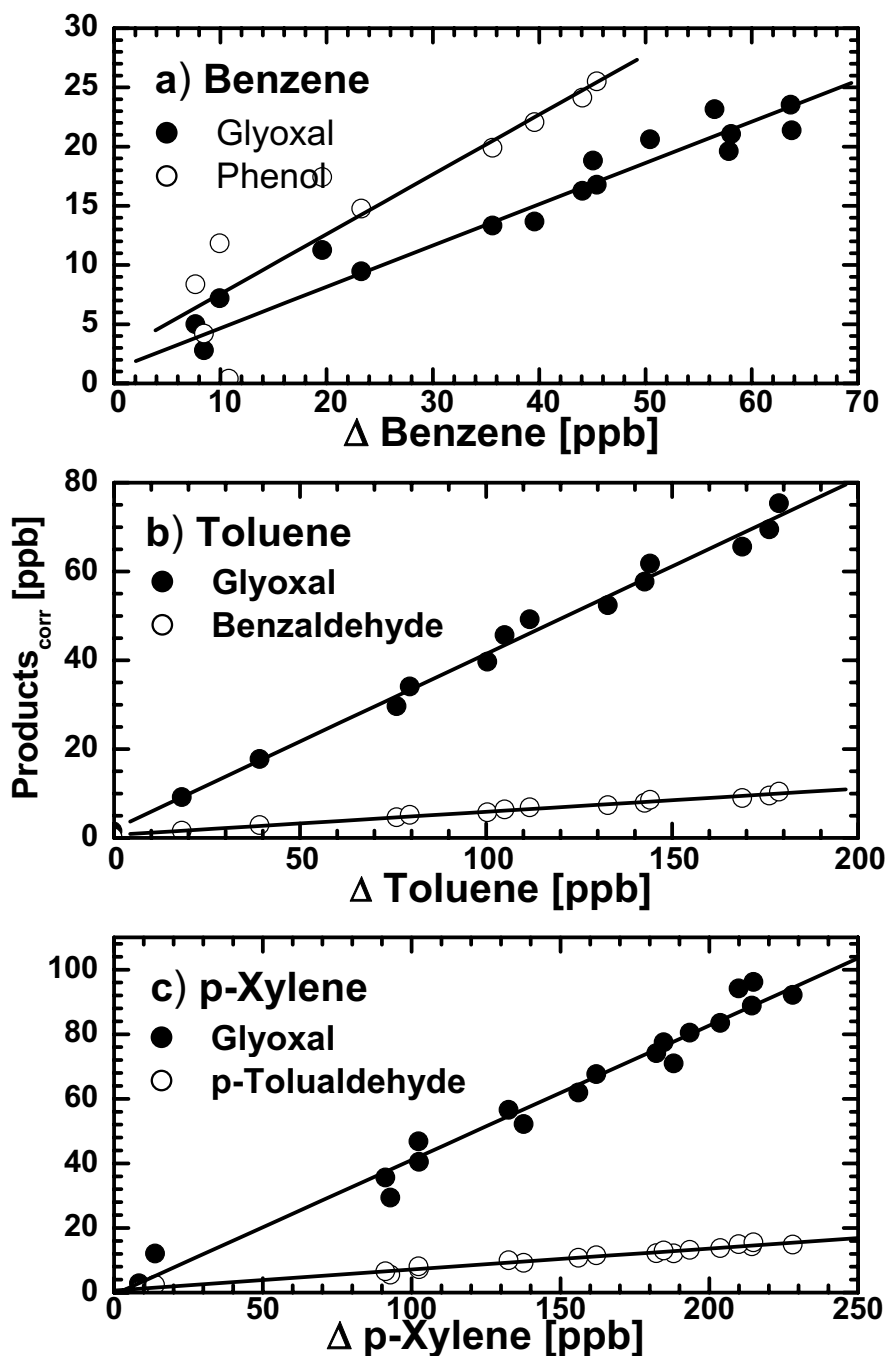


Figure 4.17: Plot of the concentration of glyoxal, corrected for reaction with OH-radicals and photolysis and a ring-retaining product, corrected for OH-reaction (see text), as a function of the amount of reacted (a) benzene, (b) toluene and (c) p-xylene. The aromatic decay was determined by GC-FID and all units were accordingly converted into ppb.

via photolysis or OH-reaction. During the initial phase of the experiments further processes could be ruled out. Likely glyoxal precursors are listed in Table 5.7 (see Section 5.5.2). The fastest photolysis-frequency from these compounds is $1.6 \cdot 10^{-3} \text{ s}^{-1}$. Moreover, a fast (nearly collision-rate limited) OH-reaction rate-constant of $k_{OH} = 1 \cdot 10^{-10} \text{ cm}^3 \cdot (\text{molec} \cdot \text{s})^{-1}$ may be assumed to estimate an upper-limit of the loss-rate through OH-reaction of $1.0 \cdot 10^{-3} \text{ s}^{-1}$ (based on an upper-limit OH-radical concentration of $[\text{OH}] = 10^7 \text{ molec} \cdot \text{cm}^{-3}$). Hence, assuming both loss-processes, a lower-limit for the overall lifetime is obtained to be 385s, i.e. 6-to-7 minutes. Any hypothetical in-this-way-delayed glyoxal formation would be observable at the time-resolution of our measurements. No delay was observed for the formation of glyoxal from benzene, toluene and p-xylene as compared to the directly formed ring-retaining products (see Figure 4.16a-c), respectively. Consequently, no reaction pathway including the stable intermediates listed in Table 5.7 (see Section 5.5.2) is fast enough to contribute to the observed primary yield of glyoxal.

The rapid glyoxal formation is consistent with a reaction sequence involving the bicycloalkyl-radical (intermediate **3**, Figure 2.2)) since glyoxal is formed from this pathway rapidly in a sequence of radical reactions without the involvement of stable intermediate compounds. The rate-limiting step for glyoxal formation from this sequence is supposed to be the conversion of the bicyclic-peroxy-radical to the bicyclic-alkoxy-radical through reaction with NO [Atkinson *et al.* 1980; Yu *et al.* 1997]. This reaction is not expected to delay the formation of glyoxal significantly (< 2 secs). Assuming this reaction to be the only fate of the bicyclic-peroxy-radical [Atkinson *et al.* 1980; Yu *et al.* 1997] will result in the formation of α -dicarbonyls, i.e. glyoxal as primary products, and the primary yield of glyoxal can be identified as a quantitative indicator for the formation yield of the bicycloalkyl-radical intermediate **3** formed from the reaction of the aro-OH **2** with oxygen for benzene and is a lower-limit for the alkyl-substituted aromatics.

4.6.5 Dependence on the NO_x concentration

In Figure 4.18 the experimental data of the yields of glyoxal determined in the individual experiments on p-xylene are shown. The error bars here correspond to the 2-sigma overall error but neglects the calibration error of glyoxal. The Figure shows the overall glyoxal yield of p-xylene (which under the experimental conditions of this work was accounted for essentially from the primary glyoxal yield, see above) as a function of the NO- and NO_2 -concentration in the upper and lower part, respectively.

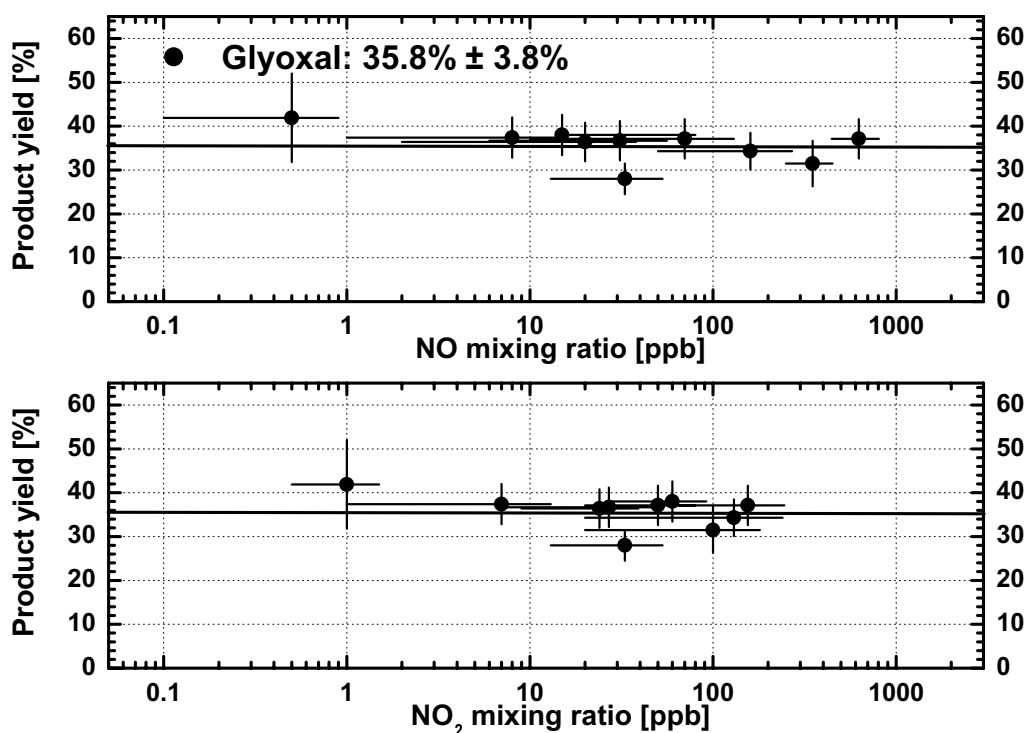


Figure 4.18: The overall glyoxal yield from p-xylene is plotted as a function of the NO- (upper part) and NO₂-concentration (lower part) of the individual experiments. The NO_x-concentrations were determined as mean concentrations over the time-interval when the yield was determined. Their error bars correspond to the variability over this time-interval. The solid line indicates the average glyoxal yield of all experiments.

With increasing concentrations of NO and NO₂ the glyoxal yield was observed to be constant over the employed range of NO_x-concentrations, as it was observed also for the ring-retaining products. The glyoxal yield from p-xylene, calculated as average values of the data listed in Table 4.8, corresponded to $(35.8 \pm 3.8)\%$. If further the 20% uncertainty of the glyoxal calibration is considered the absolute glyoxal yield is determined $(35.8 \pm 8.1)\%$.

The glyoxal yield from toluene, calculated as average values of the data listed in Table 4.8, was determined $(34.4 \pm 11.5)\%$. The error hereby includes the 20% uncertainty of the glyoxal calibration. A publication of selected data from Section 4.6 is currently in preparation and will soon be available in the literature [Volkamer *et al.* 2001]. Further, the data from Section 4.6.5 has been presented at a Workshop [Volkamer *et al.* 2000].

4.7 The overall formaldehyde yields from toluene

The relative yield method was employed to compare the formation of formaldehyde to that of glyoxal. In Figure 4.19 the concentrations of formaldehyde (open dots, $F \leq 1.24$) and glyoxal (solid dots, $F \leq 1.7$), corrected for OH-loss and photolysis (see Equation 3.32 and Section 3.5.1), are plotted as a function of the BALD concentration ($F \leq 1.22$), corrected for OH-reaction for experiment TOL4. The photolysis of BALD was not corrected in this representation. However, given the small correction factor of BALD, this is expected to be of minor importance (error $< 3\%$). The plotted data was obtained during the first about 2 hours and 20 minutes of reaction-time.

The glyoxal concentration increased in a fix relation to the BALD-concentration, as it was also observed in Figure 4.16b. This confirms the formation of glyoxal as a primary product (see Section 4.6.1). The regression to the data (solid line, hardly visible behind the solid dots) yielded $[\text{GLY}]_{\text{corr}} = 4.95 \cdot [\text{BALD}]_{\text{corr}} - 1.08 \cdot 10^{11}$ molec $\cdot \text{cm}^{-3}$. The offset is not significantly different from zero. If the slope is multiplied by the BALD yield the primary glyoxal yield listed in Table 4.8 was obtained. The formaldehyde concentration showed a distinctly different behaviour. Formaldehyde in this experiment was first detected after about 20 minutes of reaction-time. This is in part due to the less sensitive detection of formaldehyde as compared to glyoxal. A dotted line was drawn from the origin of the plot to the first formaldehyde detection. Once formaldehyde was detected its concentration increased in a fix relation to that of BALD for about 40 minutes until about one hour of reaction-time. In the further a change in the ratio of the formaldehyde and BALD concentration was observed ($[\text{BALD}]_{\text{corr}} \approx 4.0 \cdot 10^{11}$ molec $\cdot \text{cm}^{-3}$). After about 1 hour 40 minutes, the formaldehyde concentration again was observed to increase in a fix relation to that of BALD until the end of the observation period. From the regression to the formaldehyde data during the first time-span (dashed line), the following expression could be obtained: $[\text{HCHO}]_{\text{corr}} = 6.31 \cdot [\text{BALD}]_{\text{corr}} - 8.48 \cdot 10^{11}$ molec $\cdot \text{cm}^{-3}$. The offset here is non-zero within the combined error of the BALD and formaldehyde measurements, indicating that formaldehyde is indeed formed as a secondary product from toluene. The slope during this time-interval corresponded to a formaldehyde yield of $\Phi_{\text{HCHO}} = (37.2 \pm 7.9)\%$. Further evidence for the formation of formaldehyde as a secondary product was found from the comparison of the dotted line and the dashed line in Figure 4.19. The slope of the dotted line would correspond to a hypo-

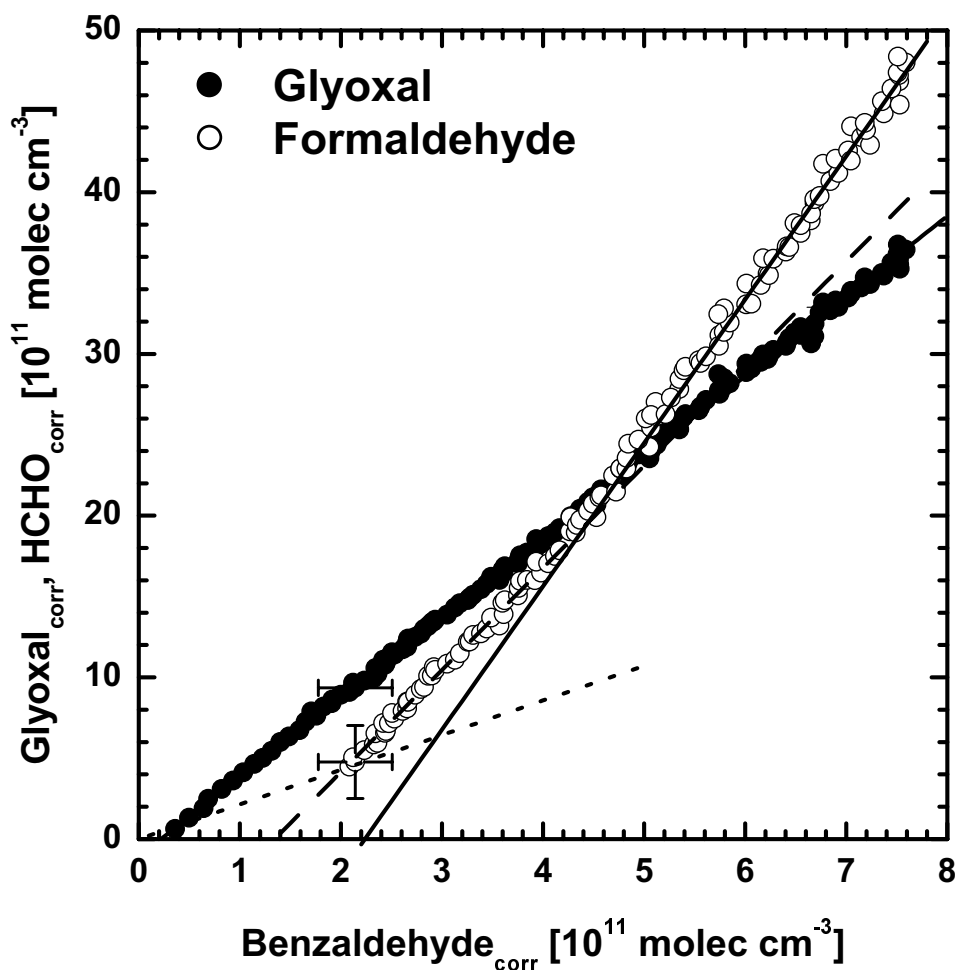
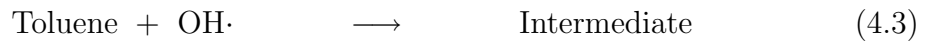


Figure 4.19: Relative-yield plot of the concentration of glyoxal and formaldehyde in the toluene-OH system, corrected for reaction with OH-radicals and photolysis as a function of the concentration of BALD, corrected for loss through OH-reaction, for experiment TOL4. The different lines were adjusted to the formaldehyde concentration-time profile at different times of the experiment (see text).

thetical primary formaldehyde yield of 12.6 %. However, this number considerably overestimated the true yield as is evident in Figure 4.19 from the non-steady change in the slopes of the dotted line and the dashed line. The data is in fact compatible with a zero primary formaldehyde yield in agreement with the present understanding of toluene oxidation. It is concluded that the predominant fraction (possibly all of the formaldehyde) was formed as a secondary product from toluene. The dashed line was extrapolated to $[\text{HCHO}]_{\text{corr}} = 0$. The corresponding BALD concentration of $1.34 \cdot 10^{11} \text{ molec} \cdot \text{cm}^{-3}$ was formed after about 10 minutes of reaction-time. The delay in the formation of formaldehyde can be explained from the following simplified reaction sequence:



where the intermediate compound "Intermediate" is a stable, i.e. long-lived, non-radical-type primary product from toluene. Under the conditions of the experiment (high NO concentration, absence of ozone) the "Intermediate" may have reacted with OH-radicals or have been photolysed. From this sequence, the delay in formaldehyde formation will be of the order of the lifetime of the short-lived "Intermediate" formaldehyde precursor substance. Given a lifetime of ten minutes, the Intermediate compound will reach its steady-state concentration after less than half an hour. Formaldehyde formation will then be operative from the above sequence at a maximum production-rate, in agreement with the observed linear relation to BALD.

After the change in the yield ratio $\Phi_{\text{HCHO}}/\Phi_{\text{BALD}}$ (observed at about one hour of reaction-time) a linear regression to the data (solid line) yielded $[\text{GLY}]_{\text{corr}} = 8.86 \cdot [\text{BALD}]_{\text{corr}} - 19.82 \cdot 10^{11} \text{ molec} \cdot \text{cm}^{-3}$. The slope during this time-interval corresponds to a formaldehyde yield of $\Phi_{\text{HCHO}} = (52.3 \pm 11.1) \%$.

4.8 Secondary Organic Aerosol formation

In the experiments on the photo-oxidation of p-xylene (and other experiments on TOL, oXYL, mXYL, 1,2,4-TMB and 1,3,5-TMB) particle numbers were counted. Though the employed measurement device did not allow to give quantitative information on the particle mass, it allowed to determine whether or not a formation of Secondary Organic Aerosol (SOA) occurred. Moreover, it allowed to determine the time when SOA formation started with quite good precision. In Figure 4.20 the results related to SOA formation obtained from experiment PX10 are presented (see also Figure 4.11 in Section 4.4 for further data from this experiment). SOA formation was observed shortly after 11:30 GMT when the number-density of particles increased to $1.75 \cdot 10^5$ particles \cdot cm $^{-3}$ within about 15 minutes of reaction-time. After this steep increase, the number-density slowly decreased probably accompanied with particle growth from the association of fine particles. This decrease contained no information about the actual particle mass (see Section 3.3) which despite the decreasing particle number may have further increased.

In the following Section special interest was paid to the role NO $_3$ -radicals may play in the formation of SOA. If not noted elsewhere, the presently recommended temperature dependent rate-constant data by *DeMore et al.* [1997] was used at a temperature of $T = 305$ K, representative for experiment PX10.

4.8.1 The NO $_3$ -radical balance

The principal source of NO $_3$ -radicals in experiment PX10 was the reaction of NO $_2$ with O $_3$ (see Section 3.4.5). Both compounds, NO $_2$ and O $_3$ were measured during the experiment and their data is shown in Figure 4.11b (see Section 4.4). The accumulated production of NO $_3$ -radicals from this data was calculated. Over the entire experiment PX10, Reaction 3.23 formed about (88.7 ± 13.4) ppb of NO $_3$ -radicals that reacted in the system. The error hereby represents the combined error of the temperature dependent rate-constant data and an assumed 5% uncertainty of the ozone and NO $_2$ measurements.

The obvious sinks to the NO $_3$ -radical were the reaction with NO, photolysis and the fast reaction of NO $_3$ -radicals with 2,5-DMPs. The relative importance of these sinks varied throughout the experiment as can be seen in the upper part of Figure 4.20 (indicated a). By the time the maximal NO $_2$ concentration had been reached (11:25 GMT), their relative importance was about 100 : 44 : 1. Half an hour later, when the maximum NO $_3$ -concentration had been reached the importance of the DMP-reaction

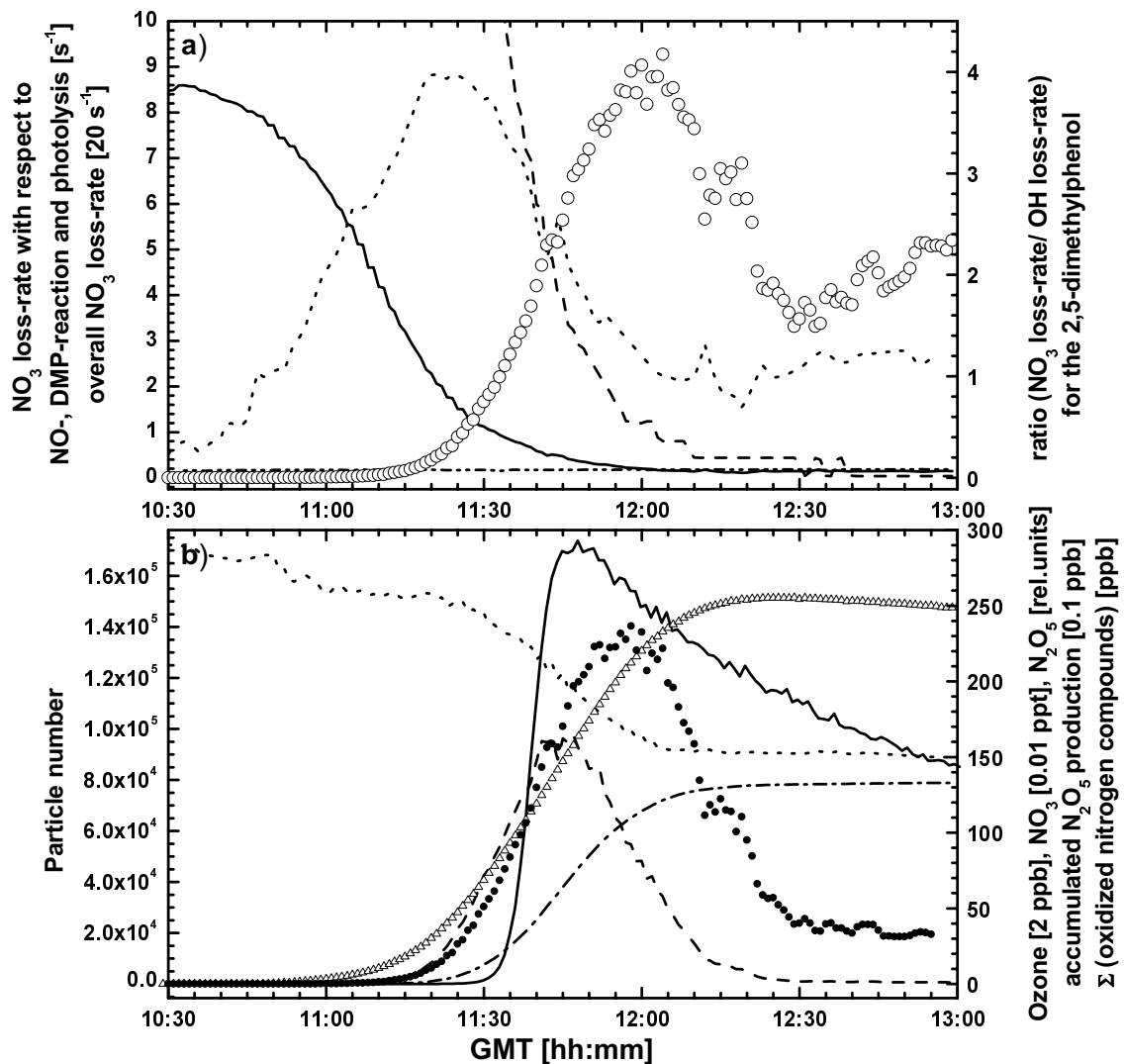
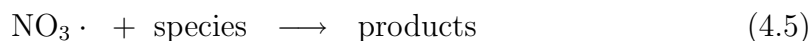


Figure 4.20: Data related to SOA formation from experiment PX10. Upper part: Calculated loss-rates for the NO_3 -radical. (solid line) overall loss-rate, divided by 20; (dashed line) NO -loss-rate; (dotted line) 2,5-DMP-loss-rate; (dashed-dot-dotted line) photolytic-loss-rate, all left axis; (open dots) calculated ratio of the 2,5-DMP loss-rates towards NO_3 - and OH-reaction, right axis; Lower part: (solid line) particle numbers, left axis; (solid dots) calculated NO_3 -radical mixing ratio (see text); (open triangles) ozone mixing ratio; (dashed line) calculated relative N_2O_5 profile (see text); (dashed-dotted line) accumulated N_2O_5 formation; (dotted line) sum of ONC (see text), all right axis.

dominated (relative importance 6:18:1). Towards the end of the experiment the relative importance of the three sinks was 0.2:14:1 (12:45 GMT). Photolysis of NO_3 -radicals became a non-negligible sink only in the later phase of the experiment. As can be seen in Figure 4.11a about $(5.7 \pm 0.7) \cdot 10^{11}$ molec $\cdot\text{cm}^{-3}$ of 2,5-DMP were lost via the reaction with NO_3 -radicals. This sink hence contributed about 23 ppb of NO_3 -radical loss. Over the course of the experiment, the time-integrated amount of NO_3 -radicals that was lost through NO-reaction and photolysis was estimated from the loss-rates shown in Figure 4.20a. It accounted for an about similar amount of ≈ 18 ppb. Hence from this estimate an integral amount of NO_3 -radicals of about 47 ppb was identified to react with further species over the entire experiment:



The concentration-time-profile of NO_3 -radicals was calculated in a first estimate from Equation 3.38. NO_3 -peak levels reached mixing ratios of up to ≈ 5 ppt. However, this is only an upper limit value for the actual NO_3 -concentration, since Equation 3.38 neglects further NO_3 -sink-reactions.

In a second approach, the NO_3 -concentration was traced from Equation 3.39 using the temporal variation of 2,5-DMP to determine the number density of NO_3 -radicals (see Section 3.5.7). Over the time-interval from 11:30 to 11:50 GMT, when maximal NO_3 was expected, this approach yielded an average NO_3 -concentration of $[\text{NO}_3] = (1.8 \pm 0.3)$ ppt. If the NO_3 -concentration as calculated from the first approach (see above) was averaged for the same time-interval, a mean value of $[\text{NO}_3] = (4 \pm 0.8)$ ppt was obtained. This difference of about a factor of (2.2 ± 0.6) indicates, that the lifetime of the NO_3 -radical was indeed determined from the reaction with other species to a similar extend than it was limited from the NO- and 2,5-DMP-sinks. The concentration-time-profile of NO_3 -radicals shown in Figure 4.20b (and Figure 4.11b) was derived from dividing the NO_3 -concentrations (as calculated from Equation 3.38) by the difference-factor of 2.2 and in this form reproduces the traced NO_3 -concentrations. The thus determined NO_3 -concentrations were used to determine the relative importance of NO_3 -radicals as compared to OH-radicals for the loss-processes of 2,5-DMP. Therefore, the OH- and NO_3 -loss-rate of 2,5-DMP were calculated over the course of the experiment. In Figure 4.20a the ratio of the loss-rates towards NO_3 - and OH-reaction of the 2,5-DMP were plotted as a function of time (right scale). This data demonstrates, that the influence of NO_3 -radicals is found to dominate the OH-reaction in the later phase of the experiment. The NO_3 -loss of 2,5-DMP peaks shortly after the maximum concentration of

NO₃-radicals had been reached. At that time about 80 % of the 2,5-DMP was lost via NO₃-reactions.

In the further the actual production-rate of products from these unknown reactions 4.5 was calculated as the sum of the reaction-rates of NO and 2,5-DMP towards NO₃-radicals ($k_{NO_3,NO} \cdot [NO] + k_{NO_3,DMP} \cdot [DMP]$) multiplied by the difference-factor observed for the NO₃-radical concentration (i.e. 2.2). It turned out that the overall production of products from reactions 4.5 were operative at an average production-rate of $P(\text{products}) \approx 6 \cdot 10^8 \text{ molec} \cdot (\text{cm}^3 \cdot \text{s})^{-1}$. Over the time span of 20 minutes this corresponded to a time-integrated production of about 28.8 ppb of unknown products from Reaction 4.5. This amount was scaled over the entire experiment (comparing the amount of 2,5-DMP lost at 11:40 GMT and 12:30 GMT) and corresponded to ≈ 50 ppb of unknown products. It is hence in good agreement with the estimated 47 ppb (see above).

One possible sink of NO₃-radicals could be the reaction of NO₂ to form N₂O₅. This compound is thermally in-stable and under the experiment conditions rapidly decomposed back into reactants (thermal lifetime $(R_{N_2O_5,th})^{-1} \approx 1 \text{ s}$ at $T = 305 \text{ K}$). Hence, the reaction with NO₂ is not expected to influence the NO₃-radical balance (and was therefore not considered in Equation 3.38). However, if N₂O₅ was lost via alternative pathways, the reaction with NO₂ would become a net-sink for NO₃-radicals. The calculated concentration-time-profile of N₂O₅ is shown in Figure 4.20b (dashed line). It was derived from the steady-state assumption of sources and sinks of N₂O₅ (see Equation 3.38 for a similar approach for the NO₃-radical). Assuming thermal decomposition of N₂O₅ as only loss-process, the peak N₂O₅-concentration corresponded to a value of $[N_2O_5]_{max} \approx 8 \text{ ppt}$. However, due to the uncertainties related to the sinks of this compound (see Section 5.7) it was preferred to include only the relative profile in Figure 4.20b (scaled to fit the diagram). The hydrolysis of N₂O₅ is a known removal process of N₂O₅ in the atmosphere [Wayne *et al.* 1991; Geyer 2000]. At EUPHORE hydrolysis primarily takes place on the chamber walls (dry air was used in the experiments, see Section 3.3). The N₂O₅-lifetime with respect to hydrolysis was determined $(R_{N_2O_5,hy})^{-1} \approx 6 \text{ hours}$ 30 minutes [Wängberg *et al.* 1996] and hence hydrolysis is too slow to be of importance. However, the maximal - though hypothetical - NO₂-influence was estimated assuming all N₂O₅ to be instantaneously lost. The accumulated N₂O₅ production from NO₃-reactions with NO₂ was calculated and the result is shown in Figure 4.20b (dashed dotted line). It was scaled by a factor of 10 for better representation. Over

the course of the experiment, this amount was as high as (13.3 ± 6.8) ppb. If instantaneous N_2O_5 -loss is assumed, the NO_3 -reaction with NO_2 accounts for roughly 15 % of all NO_3 -reactions. Though the NO_2 influence may be significant it can not explain the missing NO_3 -sink.

Overall, the NO_3 -radicals reacted besides with NO and 2,5-DMP with further species. These further NO_3 -reactions were operative at high rate in the later course of the experiment, i.e. by the time when also SOA formation was observed. The reaction with NO_2 can not explain the missing NO_3 -sink though it in principle may contribute about 30 % of the unaccounted NO_3 -sink-reactions.

No SOA formation from the NO_3 -reaction of 2,5-DMP

No SOA formation was observed, when approx. 120 ppb 2,5-DMP were consumed by the reaction with NO_3 -radicals in the dark (see discussion in Section 5.7).

4.8.2 The NO_x -balance

Attempts were made to estimate the NO_x -balance from the oxidized nitrogen compounds (ONC) shown in Figure 4.20b (dotted line). The considered ONC-compounds were NO , NO_2 , NO_3 , HNO_3 and PAN-type compounds (sum of peroxy nitrates as measured by FTIR). The HNO_3 as measured by the FTIR was corrected for deposition to the chamber walls ($F < 1.27$). Of the overall formed (57 ± 8) ppb of HNO_3 , about (20 ± 3) ppb were formed from the reaction of OH with NO_2 (as calculated from the OH profile in Figure 4.11a and the measured NO_2 concentrations in Figure 4.11b, error: $\Delta[\text{NO}_2] = 5\%$, $\Delta[\text{OH}] = 10\%$, rate-constant error: 8% [DeMore *et al.* 1997]). Additional HNO_3 is expected to form from the NO_3 -reaction of 2,5-DMP. This reaction contributed an about equal amount of HNO_3 ((23 ± 3) ppb). Interestingly, these two reactions account for about 75 % of the formed HNO_3 . The missing amount of HNO_3 ((14 ± 4) ppb) was well below the unaccounted amount of NO_3 -radicals ((47 ± 8) ppb) and hence could be understood from further NO_3 -reactions. However, the majority of the unaccounted NO_3 -radicals was lost through pathways that do not form HNO_3 , e.g. via addition-reaction to the double-bond of unsaturated oxidation products from p-xylene.

If the sum of ONC at the end of the experiment (150 ppb) was compared to the initial amount, corrected for leakage (273 ppb), it turned out that only 55 % of the initially added NO_x was detected then in form of the measured ONC. Despite this poor NO_x -balance, the sum of ONC showed a characteristic time-profile that was

in the following separated into three time-intervals. The first interval was defined from the start of the experiment (10:30 GMT) until the time when the maximum NO_2 concentration had been reached (11:25 GMT). The second interval ranged from 11:25 GMT until the time, when the number of NO_3 -radicals began to drop (12:05 GMT). During this second time-interval the highest activity of NO_3 -radical reactions occurred. In addition, during this time-interval most of the NO_2 was converted into non-observed species (NOS) and the production of NO_3 -radicals finally ceased. In this second period the sum of ONC was observed to show maximal variability. The third interval ranged until the end of the experiment and was characterized by an essentially constant sum of ONC and a significant decrease of the reactivity in the system.

It should be noted however, that the sum of ONC represented in Figure 4.20b accounted for a selection of all ONC formed in the reaction of p-xylene and hence represents a lower-limit for the total amount of gas-phase ONC.

4.8.3 The temporal coincidence of NO_3 and SOA formation

The formation of SOA in the reaction-system was observed to be delayed until NO was widely converted into NO_2 . The formation of SOA was found to coincide with the time the concentration of NO_3 -radicals progressively increased in the reaction-system (see Figure 4.20b). Since, in the presence of NO_2 the formation of N_2O_5 depends solely on the presence of NO_3 -radicals the moment of SOA formation also correlates well with the moment of N_2O_5 formation.

Chapter 5

Discussion

5.1 Calibration

5.1.1 Comparison of the $\sigma(\text{phenol})$ with literature values

The re-determined absorption cross-section of phenol (see Section 4.1.1) was inter-compared with the spectra of *Etzkorn et al.* [1999] and the result is given in Table 5.1. The listed values were scaled relative to the their work due to the smaller error of σ' . The calibration of both spectra is in excellent agreement. However, the re-determined phenol spectrum was used in the evaluation of the experiments of this study in order to accurately account for the wavelength calibration, that is somewhat uncertain in the work of *Etzkorn et al.* [1999]. Further included in Table 5.1 are available literature data together with the spectral ranges observed in the respective study. The inter-comparison value for *Trost* [1997] was adopted from *Etzkorn et al.* [1999]. The two values compare well. The observed good agreement is especially interesting, since *Trost* [1997] used an essentially different calibration based on the vapor pressure of phenol, in contrast to the method employed in this study and by *Etzkorn et al.* [1999].

Inter-comparison of the phenol measurements performed by the DOAS and FTIR systems is shown in Figure 5.1. Different symbols represent the different experiments BEN1 to BE10. Only data that overlap at least 50% of the measurement time are shown. The linear regression to the data yield: $[\text{PHEN}]_{FTIR} = (1.0004 \pm 0.0026) \cdot [\text{PHEN}]_{DOAS} - (5.6 \pm 1.0) \cdot 10^9$. It is evident that the agreement between the DOAS and FTIR techniques is excellent. In Figure 4, error bars have been included for some data points, and it becomes clear that the offset of $-5.6 \cdot 10^9 \text{ cm}^{-3}$ is lower than the

Table 5.1: Comparison of the phenol absorption cross-section to literature values.

Reference	spectral range ^a	diff. cross-section σ' ^b	rel. cal. ^{c,d}
[<i>Bjergbakke et al.</i> 1996] ^e	UV: 275 nm	$6.6 \cdot 10^{-18} \text{ cm}^2$	0.40 ± 0.08
[<i>Trost</i> 1997]	UV: 245-283 nm	$1.88 \cdot 10^{-17} \text{ cm}^2$	1.13 ± 0.14
[<i>Etzkorn et al.</i> 1999]	UV: 248-287 nm	$1.66 \cdot 10^{-17} \text{ cm}^2$	1
	IR: 400-4000 cm^{-1}		1
[<i>Berndt et al.</i> 1999]	IR: 1000-4000 cm^{-1}		1.20 ± 0.12
[<i>Berndt</i> 2000]	IR: 1000-4000 cm^{-1}		1.10 ± 0.12
this work	UV: 255-282 nm	$1.64 \cdot 10^{-17} \text{ cm}^2$	0.99 ± 0.04

^a respective spectral ranges under observation; UV: ultraviolet; IR: infrared.

^b UV: σ' of the 275 nm absorption band at a resolution of 0.2 nm (FWHM).

^c relative calibration, normalized to the values from *Etzkorn et al.* [1999].

^d IR: integrated σ -values of four bands were compared, see [*Etzkorn et al.* 1999].

^e the specified absolute $\sigma = 7.9 \cdot 10^{-18} \text{ cm}^2$ was multiplied by 0.83 (see Section 4.1.1).

uncertainties of the individual measurements ($\approx 7 \cdot 10^{10} \text{ cm}^{-3}$ for the FTIR). The errors also show that the phenol concentrations determined by DOAS are significantly more accurate than those determined by FTIR. Therefore, in the experiments where both systems were available, the DOAS data have been employed in the evaluations. This good correlation of the both techniques demonstrates the quality of the phenol measurements in this work and reflects the fact that calibration of the UV- and IR-data is based on simultaneously determined UV- and IR- absorption cross-sections [*Etzkorn et al.* 1999].

Comparing the data from this work to the independent calibration of *Berndt et al.* [1999] gives agreement within $\pm 20\%$. The re-determined cross-section [*Berndt* 2000] leads further to a minor correction of their σ and agreement with the value of this work is within $\pm 10\%$. Larger deviations are observed for the UV-absorption cross-section as specified in the work of *Bjergbakke et al.* [1996]. The authors measured the whole spectrum of phenol at $T = 300 \text{ K}$ and specify a value of the absorption cross-section at the 275 nm band, which is about a factor of 2.5 smaller than that of the other studies. This discrepancy can however be explained by the experimental conditions employed in the work of *Bjergbakke et al.* [1996]. Based on the differential cross-section of this work, the differential optical density calculated for the conditions specified by *Bjergbakke et al.* [1996] should have been about 2.2 (base e). If such optical densities of narrow absorption features i.e. as

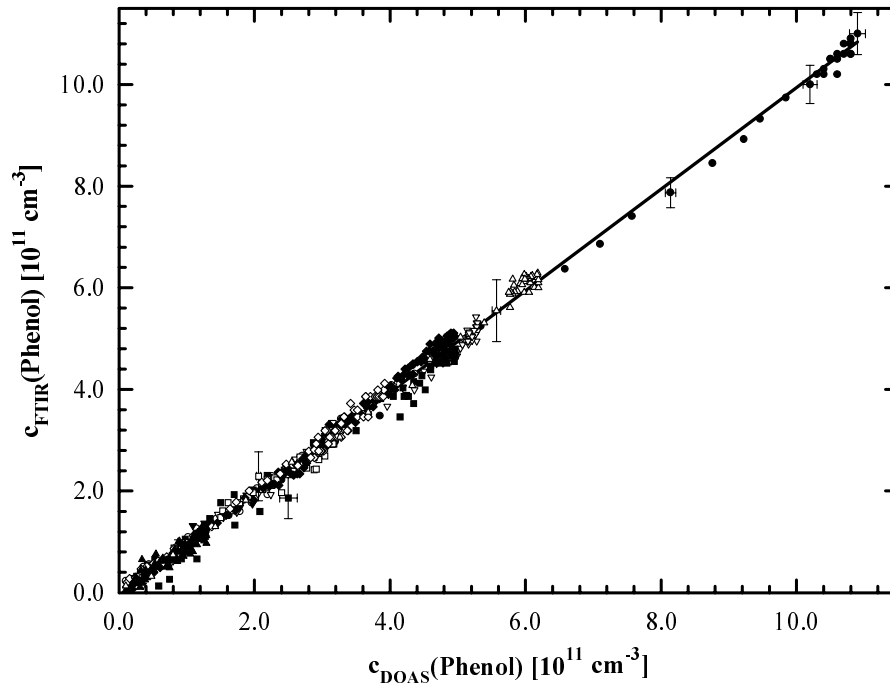


Figure 5.1: Plot of the phenol concentrations measured by DOAS and FTIR during experiments BEN1-BE10. Different symbols indicate the different experiments (see text).

that of phenol are observed at a resolution that is lower than the natural line-width of the observed absorption-band, deviations from Lambert-Beers law are likely to influence the apparent unresolved absorption signal. In fact, this was tested for benzene, comparable to phenol in this aspect, and the apparent differential absorption signal decreased by about 10% at an apparent (low resolution) optical density of roughly 0.5 (base e). Such "saturation"-effects are documented in the literature [Volkamer *et al.* 1998; Mellqvist and Rosén 1996] and lead to an underestimation of the apparent absorption cross-section. Given the fact that this effect is non-linear the observed factor of 2.5 difference between the two values can be rationalized.

The larger absorption cross-section used in [Berndt *et al.* 1999] leads to an underestimation of the specified phenol yield of 23%. On the basis of the calibration of this work their published value would correspond to 28%. Similarly, the specified phenol yield of 25% by Bjergbakke *et al.* [1996] is obtained 10% if it is based on the calibration of this work. The re-evaluated phenol yields are given in Table 5.4 and are discussed in Section 5.3.1.

Table 5.2: Comparison of the glyoxal absorption cross section to literature values.

Reference	spectral resolution ^a	λ_{peak} [nm]	σ' ^b [cm ²]	rel. cal. ^c
[<i>Bierbach</i> 1994]	IR: 1 cm ⁻¹			0.83
[<i>Moortgat</i> 2000]	IR: 1 cm ⁻¹			1
[<i>Klotz</i> 2001]	IR: 1 cm ⁻¹			0.9
[<i>Plum et al.</i> 1983]	UV-vis: n.n.*	456.69	4.08 10 ⁻¹⁹	1.04
[<i>Horowitz and Moortgat</i> 1999]	UV-vis: n.n.*	454.68	5.22 10 ⁻¹⁹	1.08
this work ^d	UV-vis: 0.17 nm	454.99	5.47 10 ⁻¹⁹	1

* no number.

^a UV-vis: ultraviolet-visible; IR: infrared; FWHM: Full Width at Half Maximum.

^b differential absorption cross-section σ' at λ_{peak} in the UV-vis spectral range.

^c relative calibration, normalized to the values from [*Moortgat* 2000], see text.

^d placed on an absolute basis from the IR-value of [*Moortgat* 2000].

5.1.2 Comparison of the σ (glyoxal) with literature values

The absorption cross-section of glyoxal is inter-compared with literature values in Table 5.2. From the simultaneously recorded FTIR and DOAS spectra of this work it was possible to inter-compare literature values measured in both spectral ranges.

The peak to peak scatter among the available values listed in Table 5.2 is found to be $\approx 25\%$. Thereby, the IR-calibration of *Moortgat* [2000] is bracketed from the other values and indeed represents a good approximation. The maximum deviation of the calibration used in this work is 17% towards the value of *Bierbach* [1994]. Hence, the glyoxal calibration of this work is believed to be correct within 20%.

However, additional uncertainties arise for the values recorded in the UV-visible spectral range (UV-vis) where the spectral resolution varies with the spectral range under observation. For the instruments [*Plum et al.* 1983; *Horowitz and Moortgat* 1999] it is characterized by two quantities: (1) The FWHM-value (value in nanometers of the full width of an atomic emission line at half maximum if observed in the spectral interval of interest) and (2) wavelength of the measured emission line. The direct comparison of the peak absorption cross-section at about 455 nm suffers uncertainties in the exact characterization of the resolution among the literature values. However, the integrated absorption between 459.25 nm and 447.1 nm was compared and normalized relative to this work (see Table 5.2, indicated "relative calibration"), which in principle should be less sensitive to the uncer-

tain spectral resolution. If the peak absorption is weighted by the thus obtained relative calibration factors, the lowest peak absorption cross-section is observed for the spectra recorded at a comparably low spectral resolution *Plum et al.* [1983] while the values by *Horowitz and Moortgat* [1999] and this work are about equal and higher than the value by *Plum et al.* [1983]. Furthermore, in the recording of the spectra by *Horowitz and Moortgat* [1999] a dependence of the apparent absorption signal on the column-density of glyoxal was observed [*Moortgat and Horowitz* 2000], which as discussed above is an indication for non-resolved fine-structure in the apparent absorption signal of glyoxal observed under moderate resolution (see Section 5.1.1). Even though the UV-absorption cross-section of glyoxal is not well known at present, the uncertainties influence the σ' only to a minor extent [*Etzkorn et al.* 1999; *Stutz et al.* 1999]. The main uncertainties are due to the saturation effects of individual lines measured at rather low spectral resolution which result in distortions in the apparent absorption cross-section spectra. These line-shape changes in this work were eliminated by recording a reference spectrum of glyoxal using the same apparatus as for the measurements.

A general solution to these problems can be derived from the high-resolved cross-section spectrum of glyoxal. First measurements using the Fourier Transform Spectrometer at the Institut für Umweltp Physik, University of Bremen have been carried out and a further collaboration is planned.

5.2 Kinetic studies

5.2.1 Comparison with literature values

The OH-rate-constants

The study of the OH-reaction rate-constants of selected ring-retaining products of the OH-initiated oxidation of p-xylene and 1,3,5-TMB was necessary for this work since i.e. for the alkyl-substituted aldehydes and 2,4,6-TMP no values were available in the literature. The knowledge of k_{OH} nevertheless is a prerequisite to accurately account for OH-loss in the products studies and hence is indispensable to determine accurate product yields (see Section 3.5.5). Literature values were available for BALD, phenol and 2,5-DMP and hence allowed to confirm the employed evaluation method.

For BALD the available values of k_{OH} in the literature in general show little scatter ($< 15\%$ peak to peak difference). The value determined in this work is found to be in excellent agreement with the reported values. The photolysis-correction applied for BALD thereby resulted in a downward correction of the mean k-value for this compound of 8%. Though this was a minor correction the observed value was higher than the highest reported value if no correction had been applied. Taking BALD as an indicator for the other aromatic aldehydes this result indicates the importance of photolysis-correction in the OH-kinetic studies on aromatic aldehydes for rate-constants that are determined in the presence of sun-light.

For phenol the available literature values of k_{OH} were found to be in even better agreement (scatter $< 7.7\%$). The value determined in this work was again found to be in excellent agreement with all available data. The overall error of the value (14.6%) hereby was dominated from the error of the reference compounds. Excluding this systematic error source the evaluation error was $< 7\%$.

For 2,5-DMP the value determined in this study was found to be in good agreement with the only available literature value [Atkinson and Aschmann 1990]. The overall error for this rate-constant (10.4%) was again dominated from the error of the reference compound. In fact, the rate-constant determined in this work is considerably reduced in error (a factor of 2.7) as compared to the previously available rate-constant [Atkinson and Aschmann 1990].

In addition, literature values exist on isomers of the DMBA and the TMP [Tse et al. 1997], though only on different isomers than those that were investigated in this work. For the DMBA the reported values vary by a factor of two and

Table 5.3: Comparison of the kinetic parameters with literature values.

Compound	k_{OH} [$10^{-12} \text{ cm}^3 \cdot (\text{molec} \cdot \text{s})^{-1}$]	k_{NO_3}	$J_{phot.}$ [10^{-6} s^{-1}]	Reference ^a
BALD	13 ± 0.9			[<i>Niki et al.</i> 1978]
	11 ± 2			[<i>Kerr and Sheppard</i> 1981]
	12.3 ± 2.5			[<i>Semadeni et al.</i> 1995]
	12.9 ± 3.2^b			[<i>Atkinson</i> 1994]
	12.5 ± 2.5		8 ± 6^d	this work
oTALD	n.n. ^c		200 ± 10^d	this work
mTALD	n.n. ^c		11 ± 8^d	this work
pTALD	21.2 ± 2.5^d		$< 6^d$	this work
3,5-DMBA	34.2 ± 6.8^d		$< 6^d$	this work
PHEN	28 ± 6			[<i>Rinke and Zetzsch</i> 1984]
	26 ± 2			[<i>Witte</i> 1987]
	26 ± 3			[<i>Semadeni et al.</i> 1995]
	26.3^b			[<i>Atkinson</i> 1994]
	26.4 ± 3.8			this work
pCRE		13.0 ± 2.0		[<i>Carter et al.</i> 1981]
		12.7 ± 3.6		[<i>Atkinson et al.</i> 1984]
		10.7 ± 1.0		[<i>Atkinson et al.</i> 1992]
		10.7 ± 5.35^b		[<i>Atkinson</i> 1994]
		11.2 ± 1.3		this work
2,5-DMP	80 ± 23			[<i>Atkinson and Aschmann</i> 1990]
	81.7 ± 8.5	24.4 ± 3.4^d		this work
2,4,6-TMP	131 ± 15^d			this work

^a for data from this work see Section 4.2.2.

^b present recommendation.

^c no number, see also the text.

^d to the best of our knowledge, no data is available for comparison at the time of this writing.

range from $(2.14 \pm 0.34) \cdot 10^{-11} \text{ cm}^3 \cdot (\text{molec} \cdot \text{s})^{-1}$ (2,5-DMBA) to $(4.37 \pm 0.68) \cdot 10^{-11} \text{ cm}^3 \cdot (\text{molec} \cdot \text{s})^{-1}$ (3,4-DMBA). The value of $(3.42 \pm 0.68) \cdot 10^{-11} \text{ cm}^3 \cdot (\text{molec} \cdot \text{s})^{-1}$ determined in this work for the 3,5-isomer is found to be bracketed by these values. For the TMP the available values for a comparison with this work are $(11.8 \pm 1.8) \cdot 10^{-11} \text{ cm}^3 \cdot (\text{molec} \cdot \text{s})^{-1}$ (2,3,6-TMP) and $(12.5 \pm 1.8) \cdot 10^{-11} \text{ cm}^3 \cdot (\text{molec} \cdot \text{s})^{-1}$ (2,3,5-TMP) and hence are comparable in the range of their experimental errors. The value of $(13.1 \pm 1.5) \cdot 10^{-11} \text{ cm}^3 \cdot (\text{molec} \cdot \text{s})^{-1}$ determined in this work for the 2,4,6-TMP is found to be in good agreement to these values.

The small scatter observed among the OH-rate-constants from different experiments reflects the successful correction of wall-influence in the sun-lit chamber.

The NO_3 -rate-constants

The study of the rate-constant of 2,5-DMP was a prerequisite to obtain valuable information on the concentration of the NO_3 -radical in the oxidation of p-xylene (see Sections 4.8). No information was available in the literature for this compound. In addition, k_{NO_3} of p-cresol was re-determined to confirm the employed evaluation method.

For p-cresol the available k_{NO_3} -literature-values vary by about 20 % (peak to peak difference). Nevertheless, the reported literature values are all conclusive within their specified experimental errors that range down to a minimum error of 9 % [Atkinson *et al.* 1992]. As discussed in Section 4.2.3 the comparably small error of p-cresol determined in this work could be transferred into an reduced error of k_{NO_3} -value of phenol (10 %). On the basis of this reduced uncertainty in the phenol value the agreement between the p-cresol value determined here and the value from Atkinson *et al.* [1992] is still excellent. The rate-constant ratio of p-cresol and phenol was found independent from the NO_2 -concentration. This result confirms the independence of the rate-constant from the NO_2 concentration in the low NO_2 range (≈ 15 ppb to 200 ppb) as it was already reported for the high NO_2 -concentration range (several ppm) by [Atkinson *et al.* 1992].

The rate-constant of 2,5-DMP was determined with an overall uncertainty of about 14 %. Thereby the error is dominated from the uncertainty of the k-value of the reference compound.

The small observed scatter among the NO_3 -rate-constants from different experiments reflect the successful correction of wall-influence in the dark chamber.

The photolysis of aromatic aldehydes

The photolysis-frequencies listed in Table 5.3 are representative for February. Though almost clear sky conditions prevailed during the experiment the UV-flux here was reduced by about a factor of 2 as compared to similar conditions during summer. Despite this uncertainty the results indicate that the photolysis-quantum-yields will be considerably lower than unity, in agreement with the qualitative preliminary data presented by *Thiault et al.* [2000]. Hence, the OH-reaction will be the predominant fate for compounds like BALD, pTALD as well as 3,5-DMBA. Taking BALD for example, more than 90 % were lost via OH-reaction rather than photolysis under the employed experimental conditions. From the observed variability of the measured photolysis-frequencies (see Table 5.3) the photolysis-quantum-yields however are expected to vary considerably among the different isomers. No information is presently available with respect to the wavelength dependency of these quantities. If, like for other aldehydes photolysis primarily takes place at wavelengths around 300 nm an additional uncertainty in the J-values of a factor of 2 to 3 is expected. Due to the uncertainties related to the photolytic correction it was decided to correct only the k_{OH} -value of BALD (see Section 4.2.2) for photolytic-loss, where the photolysis is slow and experiments under comparable experimental conditions were available. For the o- and mTALD the uncertainty in their photolysis-frequency becomes a dominate error source and their OH-kinetic data is still under evaluation. Further investigation on the aldehyde photolysis is therefore necessary.

5.2.2 Influence of the walls in the dark and sun-lit reactor

The motivation for the puzzling and time-consuming task to characterize the deposition of polar compounds to FEP was two-fold. First, the deposition-rate was indispensable preliminary information for the kinetic experiments on polar compounds. It was found to vary by a factor of three from one experiment to another and by a factor of four within a single experiment (see Section 4.2.1). If not corrected adequately this would have introduced a systematic error in the determined rate-constants as high as 25 % (see Table 4.1).

Second, the wall-influence is of fundamental interest for smog-chamber studies. It is an ongoing debate [*Jeffries et al.* 1999] to what extent the chamber walls influence the radical production in smog-chamber studies and represent a sink for products that form from a chemical reaction. It is presently known that for compounds such as HNO_3 [*Finlayson-Pitts and Pitts, Jr.* 2000] this sink is non-negligible. At EU-

PHORE the loss-rate of HNO_3 in the dark chamber was determined to vary between $5.7 \cdot 10^{-5} \text{ s}^{-1} \leq W_{\text{HNO}_3} \leq 1.5 \cdot 10^{-4} \text{ s}^{-1}$ and deviations from the first order decay have been observed [Wirtz and Martín-Reviejo 1997]. The estimates given in Table 4.1 for the initial wall-deposition-rate of the aromatic hydrocarbons investigated in this study suggest that the importance of the walls as a sink may be as high as 25 % of the loss through OH-reaction. Interestingly, this number was found to be rather constant (variation between 15 % and 25 %) and on average was estimated 20 % for the investigated compounds of this study.

The wall-deposition-rates listed in Table 4.1 are representative for the dark chamber. During the setup-phase of an experiment the chamber housing was closed and considerable amounts of compound deposited on the walls. For example, in the experiment on aldehyde-photolysis, described in Section 4.2.4, about 6.5 % of the initially added pTALD (here 4 ppb out of 60 ppb) had deposited on the walls over the period of two hours prior to the opening of the chamber housing. This amount corresponded to $\approx 9.85 \cdot 10^{10} \text{ molec}\cdot\text{cm}^{-3}$ or $1.85 \cdot 10^{19} \text{ molec}$ which had been lost to the walls.

Upon opening of the chamber housing the temperature inside the reactor typically increased a few degrees ($\Delta T < 15 \text{ K}$) and most likely shifted the equilibrium between adsorption (of gas-phase molecules to the sheet) and desorption (of adsorbed molecules back into the gas-phase) towards desorption. In addition, light-absorption of compounds adsorbed on the FEP-sheet may have facilitated desorption of molecules contained within the organic film on the FEP-sheet. If the 4 ppb of pTALD deposited on the walls were instantaneously desorbed from the walls upon opening of the chamber housing (assuming $R_{\text{deposition}}$ to increase by a factor of 100) this would have been observed in a change of the observable R (see Section 3.5.4). However, a change in R was not significant in the open chamber in Figure 4.2 and $R_{\text{deposition}}$ changed by a factor of ≤ 4 .

Further support comes from experiment PX10 (see Figure 4.11 and 4.20, HNO_3 not shown) where HNO_3 formation was measured by FTIR in the oxidation of p-xylene. After about 12:15 GMT, the HNO_3 production of the system had ceased and the concentration as measured by FTIR decreased (not shown) due to the loss of HNO_3 to the walls of the sun-lit chamber. This decrease could be adequately compensated assuming a wall-deposition-rate of HNO_3 of $W_{\text{HNO}_3} = 11 \cdot 10^{-5} \text{ s}^{-1}$. This value is close to the upper-limit W reported by Wirtz and Martín-Reviejo [1997] in the closed chamber. The wall-depositon rate of HNO_3 in the sun-lit chamber during this experiment hence agreed well with the wall-deposition in the dark.

It is concluded that the loss-rate of products to the chamber walls in the sun-lit chamber was rather similar to that of the dark chamber. It ranged between 5% and 25% of product loss-rate through OH-reaction for all the aromatic compounds investigated in this study. These numbers may represent a lower-limit for the wall influence (see Section 4.2.1).

5.3 The phenol yield from benzene

5.3.1 Comparison with literature values

The phenol yield obtained in this work is compared to literature values in Table 5.4. It is evident that the value given here is more than twice as high as the previously reported values. There are two studies that used a spectroscopic technique for the detection of phenol [Bjergbakke *et al.* 1996; Berndt *et al.* 1999]. An advantage with the spectroscopic techniques is, that calibration solely depends on physical properties that are independent of the measurement instrument, i.e. the absorption cross-section spectrum $\sigma(\lambda)$ of phenol. Both studies have been scaled to match the calibration of this work in the column indicated "re-evaluated" in Table 5.4 (as described above). As can be seen, the apparently conclusive literature values show considerable scatter if placed on a common basis of calibration.

Under NO_x -free conditions the phenol yield by Bjergbakke *et al.* [1996] was calculated based on residual absorptions observed at a wavelength of 275 nm in a pulse radiolysis study. The OH-concentration observed around 309 nm was used to calculate the benzene decay at a temperature of $T = 340$ K. A considerably lower phenol yield at this temperature would be in contradiction with the enthalpy data from Lay *et al.* [1996] and would further contradict the observed temperature dependence of this work. The difference in the yields is too high in order to be explained on the basis of a temperature change of 40 K. The reason for the differences in the phenol yield may be found in the high radical concentrations that Bjergbakke *et al.* [1996] reported for their system. Given the considerably lower re-evaluated phenol yield of 10 %, residual reactions that were not completely suppressed may have contributed significant amounts to the observed phenol. In the presence of oxygen, the high concentrations of H atoms produced in the pulse radiolysis would form HO_2 radicals which react with the aromatic-OH adduct thus introducing an additional loss process from the equilibrium **2/3** which could explain the lower phenol yield. In addition, an uncertainty about the experimental conditions arises from the proposed formation mechanism of phenol, that Bjergbakke *et al.* [1996] attribute to channel (5) in Figure 2.1. This conclusion is in conflict with a recent study [Bohn and Zetzsch 1999] in which an upper limit of 5 % is determined for this reaction.

The phenol formation yield given by Berndt *et al.* [1999] was determined in a flow system using FTIR spectrometry for the detection of both benzene and phenol. OH-radicals were generated by microwave discharge of H_2 in the presence of O_2 . The resulting HO_2 -radicals gave OH by self-reaction. According to the authors, no cor-

Table 5.4: Comparison of the phenol yield with literature values.

Reference	NO [ppm]	NO ₂ [ppm]	phenol yield [%]	
			literature	re-evaluated ^a
[<i>Bjergbakke et al.</i> 1996]	NO _x -free		25 ± 5	10 ± 5
[<i>Berndt et al.</i> 1999]	NO _x -free		23 ± 7	28 ± 7
this work	NO _x -free ^b		66.6 ± 8.4	66.6 ± 8.4
[<i>Atkinson et al.</i> 1989]	0.6-10	0.6-10	23.6 ± 4.4	n.n.*
this work	< 0.01 - 1.2	< 0.01 - 0.5	53.0 ± 6.6	53.0 ± 6.6

* no number.

^a see Section 5.1.1

^b conditions: initially NO_x-free, several ppm of H₂O₂ present, see Section 5.4.3.

rection of measured product concentrations for secondary reactions were necessary. However, this appears to be in contrast to the observation of CO and formic acid as products of the benzene + OH reaction, which, according to all currently proposed benzene degradation schemes, should be secondary products. Also, the two strongest absorptions observed in the residual FTIR spectra of *Berndt et al.* [1999] (Fig. 3 in that paper) are very similar to those of E,E-2,4-hexadienedial published by Klotz et al. The most likely pathway for the formation of this compound under NO_x-free conditions is reaction of the hydroxycyclohexadienyl peroxy radical (**3** in Figure 2.1) with another organic peroxy radical RO₂ to give a hydroxycyclohexadienyl oxy radical, an RO radical and O₂. The hydroxycyclohexadienyl oxy radical can then ring-open and react with O₂ to give HO₂ and Z,Z-2,4-hexadienedial, which can isomerise to the more stable E,E-2,4-hexadienedial. If this were the case in the study of *Berndt et al.* [1999] it would indicate the presence of extremely high radical concentrations in their reaction system. This reaction sequence would represent an additional loss channel of hydroxycyclohexadienyl peroxy radicals **3** not present under atmospheric conditions, which could explain the lower phenol yields. Alternatively, an intramolecular H transfer from the OH group to the peroxy group of **3**, followed by elimination of OH may also account for the formation of E,E-2,4-hexadienedial, but this channel thought to be energetically unfavourable [*Lay et al.* 1996]. Additionally, this pathway would also be operative under the conditions of the present study, however, no E,E-2,4-hexadienedial was observed in our experiments and an upper limit for the formation of hexadienedials from benzene was determined to be 8% (see Section 5.5.2).

In this study, different phenol yields were observed in the presence and absence of NO_x . A definitive reason for this discrepancy and the differences observed among the literature values listed in Table 5.4 under NO_x -free conditions still needs to be elucidated. One possible explanation for the differences in the phenol yield may be found in the different experimental conditions as is discussed in Section 5.4.3).

The study of Atkinson et al. (1989) was conducted in a 6.4 m^2 reaction chamber, OH-radicals were generated by blacklight irradiation of $\text{CH}_3\text{ONO}/\text{NO}/\text{air}$ mixtures with the initial NO_x -concentration being varied between about 1 ppm and 20 ppm. Benzene was determined by GC-FID, phenol by collecting samples on Tenax adsorbent followed by GC-FID analysis. Corrections were applied for secondary reactions of phenol with OH-radicals. The lower phenol yield is in agreement with the results of this work which were obtained at high NO_x (≈ 1 ppm). A direct comparison with Equation 4.2 suffers from the marginal overlap of the employed NO_x -concentrations. Nevertheless, there is one experiment, i.e. ITC#1295 [Atkinson et al. 1989] that was carried out at an initial NO_x -concentration of 1.25 ppm comparable to the upper-limit of NO_x -concentrations employed in this study. From the given experimental data a phenol yield for the initial phase of this experiment of 34.8 % can be calculated. The mean mixing ratios of NO and NO_2 over the corresponding time span are 0.61 ppm and 0.64 ppm respectively that transfer into a phenol yield as calculated from Equation 4.2 of 33.8 %. The agreement is surprisingly good and confirms Equation 4.2 to be valid up to a NO_x -concentration of 1 ppm without any major formation of phenol from the competing NO_x reactions.

5.3.2 The high NO_x -concentration range

As shown in the previous Section the phenol yield decreases with increasing concentrations of NO_x . This dependence is reasonably well reproduced from Equation 4.2 over the range of NO_x -concentrations employed in this work. However a discrepancy arises if the results from Atkinson et al. [1989] are compared with the predictions made from Equation 4.2 for NO_x -concentrations of several ppm. For the upper-limit NO_x -range of the conditions employed by [Atkinson et al. 1989] the phenol yield is expected to decrease down to about 5 %. This behavior contrasts with the mean phenol yield of 23.6 % [Atkinson et al. 1989]. Though from the scatter in their plotted data (Figure 5 of [Atkinson et al. 1989]) the yield rather ranges between 19.4 % and 34.8 % it does not decrease significantly below 20 %. This observation points

towards a phenol forming chemistry under high NO_x concentrations (several ppm) which is different to the one described by Equation 4.2 for NO_x -concentrations below about 1 ppm. *Atkinson et al.* [1989] propose the formation of phenol to proceed from the reaction of the aromatic-OH adduct with NO_2 which for the upper-limit NO_x concentrations of their work accounts for the predominant fraction of the total loss from equilibrium 2/3 in Figure 2.1.

Assuming the yield of phenol from channel (10), in the further denoted $\Phi_{\text{phenol},10}$ to be non-zero Equation 4.2 can be extended to 5.1:

$$\Phi_{\text{phenol}} = \frac{k_{\text{phenol}} + \Phi_{\text{phenol},10} \cdot k_{10} \cdot [\text{NO}_2] / (K_{\text{eq}} \cdot [\text{O}_2])}{k_{\text{phenol}} + k_8 + k_9 / K_{\text{eq}} + k_{10} \cdot [\text{NO}_2] / (K_{\text{eq}} \cdot [\text{O}_2]) + k_{12} \cdot [\text{NO}]} \quad (5.1)$$

From the raw data given by *Atkinson et al.* [1989] a phenol yield from channel (10) of about $\Phi_{\text{phenol},10} = 18\%$ was deduced. Given this value, the deviation of Equation 5.1 from Equation 4.2 for the NO_x -values of ITC#1295 (see above) is below 15%. The estimate from Equation 4.2 hence is still reasonable. The good agreement with *Atkinson et al.* [1989] remains astonishing given the fact that indications of NO_3 -radical formation were observed in their reaction-system (ITC#1295 [*Atkinson et al.* 1989]), though only at longer irradiation times. The estimated phenol yield from ITC#1295 is based on the initial phase of the experiment and seems not yet to be affected by NO_3 -radicals, though this can not be ruled out from the given data. The additional phenol loss through reaction with NO_3 -radicals could nevertheless by chance correspond to the amount that Equation 4.2 possibly underestimates the phenol yield. Finally, it is remarked that the uncertainties in k_{10} ($\approx 10\%$) and k_{12} ($\approx 35\%$) become important error sources for the calculated phenol yields at 1 ppm of NO_x .

The conclusion on the different phenol forming chemistry under high NO_x -concentrations thereby remains unchanged. At present, the exact value of $\Phi_{\text{phenol},10}$ is not known. Equation 4.2 gives a reasonably good estimate for the phenol yield up to NO_x -concentrations of about 1 ppm. From Equation 4.2 it is evident, that for several 10 ppb of NO_x (here: $[\text{NO}] = 10$ ppb; $[\text{NO}_2] = 10$ ppb) the phenol yield undergoes a relative change of less than 1%. The phenol yield will hence be essentially uninfluenced for most NO_x concentrations as they are observed in the atmosphere.

5.3.3 The formation mechanism of phenol

The results of Section 4.3 indicate that the observed decrease of the phenol yield at high NO_x -levels can be quantitatively understood from Equation 4.2 in terms of

the channels (9) to (12) that begin to compete with the channels (3) to (6). This indicates that the channels (9) to (12) form phenol much less efficient than channels (3) to (6) under the experimental conditions employed in this work.

With regard to channel (6) no definite statement on the occurrence of benzene oxide/oxepin in the OH initiated oxidation of benzene can be made from the present data. However, it can be said that the majority of the phenol formed must come from either channel (3) or (4), and that the observed temporal variability of phenol can be adequately described by these channels, without invoking pathway (6/7).

Within this study it is not possible to explicitly differentiate whether the phenol is formed from channel (3) or channel (4) since both pathways lead to the same products. Nevertheless, it is in principle possible to differentiate both processes from temperature dependent studies of the phenol yield. Our attempts to determine the temperature dependency of the phenol yield result in essentially no correlation of the phenol yield with temperature. Although the temperature range covered in this study is limited this result shows that the major fraction, if not all of the phenol is formed through channel (3) (see Section 4.3.4). In particular it also shows that channel (4) can only make a minor contribution ($20 \pm 25\%$). The determination of the temperature dependence of the phenol yield over a wider temperature range seems to be promising to pin down the relative importance of channel (3) and (4).

5.3.4 Additional support

The high phenol yield from benzene in this work is further supported from the results obtained for glyoxal (see Section 4.6). As can be seen in Figure 4.16 the ratio of the glyoxal yield to that of a respective ring-retaining product from benzene, toluene and p-xylene (BTX) is in fix relation for all the three systems. For the toluene and p-xylene system the data was found to be compatible with the well known yields of BALD and the pTALD, respectively. Nevertheless, the observed ratio in the benzene system can not be explained on the basis of the low phenol yields and was found consistent only with the high phenol yield discussed in this Section.

Further evidence for the high phenol yield comes from recent field studies [Ackermann *et al.* 2000] which indicate that the phenol/benzene ratios observed by DOAS in urban areas are significantly higher than it can be explained by known sources of phenol and the previously accepted phenol yields in the OH initiated oxidation of benzene.

Finally, a high phenol yield of around 50% is also consistent with the results of a recent study by *Bohn and Zetzsch* [1999] who indirectly determined the formation of HO₂-radicals through channels (3) or (4) in Figure 2.1. Despite the large error, *Bohn and Zetzsch* [1999] concluded that the observed yield of "prompt" HO₂ is higher than the 25% inferred from previous phenol yields. This observation is in-line with the high phenol yields of this work.

5.3.5 The influence of O₂-concentration and temperature

As described in Section 4.3.3 the elevated concentration of oxygen employed in experiment BE31 was found to have no influence on the phenol yield under the comparably low NO_x-concentrations employed in this work, in agreement with Equation 4.2. Though the phenol yield from this experiment tends to be slightly higher than the values observed in air at comparable NO_x-concentrations (see Table 4.5) it compares well with the average phenol yield determined in this work from the NO_x corrected values. This tends to further confirm Equation 4.2 though the data is not significant to demonstrate the oxygen concentration dependence of Φ_{phenol} that is predicted from Equation 4.2 under different experimental conditions, when the influence of reaction (10) is significant. Finally, elevated O₂ has no effect on the influence of NO. The parameter "oxygen concentration" hence can be used in future studies to vary the relative importance of influencing NO and NO₂ reactions.

A further parameter of interest in laboratory studies is temperature. As discussed in Section 4.3.4 an increase in temperature by 20 K is expected to lower the value of K_{eq} by a factor of five [*Lay et al.* 1996; *Bohn and Zetzsch* 1999]. From Equation 4.2 this is expected to increase the relative importance of channels (3), (9) and (10) as compared to channels (4), (8) and (12). In Section 4.3.4 the variation of temperature was used to distinguish between the two phenol forming channels (3) and (4) (see also Section 5.3.3). Similarly, temperature dependent product studies may give further insight in the future.

Temperature and oxygen concentration are promising parameters to be varied in the future work on degradation pathways of aromatic hydrocarbons. The theory of the phenol yield formulated by Equation 4.2 accounts for both parameters under atmospheric conditions.

5.4 The ring-retaining yields from alkylbenzenes

5.4.1 Comparison with literature values

p-Xylene

The results for the yields of pTALD and 2,5-DMP (see Section 4.4) are compared to available literature values in Table 5.5.

For the yield of pTALD there is in general good agreement among the numerous available literature values. The average value calculated from all available values is found almost identical to the value of this work. There is excellent agreement among the studies by *Bandow and Washida* [1985, *Atkinson et al.* [1991, *Barnes et al.* [1991] (the specified error of Φ_{pTALD} from these studies ranges between 12.5% and 23%) and this work. The agreement is also reasonable with the most recent value determined by *Smith et al.* [1999]. The experimental conditions with respect to NO and NO₂ concentrations have been included in Table 5.5 where specified. The yield of pTALD is found insensitive to the NO and NO₂ concentration for NO_x-concentrations between < 1 ppb (this work) up to levels of 20 ppm [*Atkinson et al.* 1991]. Overall, there exists little uncertainty on the yield of pTALD from p-xylene.

For a comparison of the yield of 2,5-DMP there are five values available in the literature. The mean value of these is found to almost coincide with the value of this work (see Table 5.5). However, the peak to peak variability among the literature values is as high as a factor of two. With the exception of the data from *Etzkorn* [1998], all values are representative for a temperature of T = 298 K. The value of *Etzkorn* [1998] was listed in Table 5.5 as the average value of two experiments (6.11.96: $\Phi_{DMP} = (9.4 \pm 2.4)\%$, mean temperature T = (292 ± 5) K; 21.11.96: $\Phi_{DMP} = (5.3 \pm 1.3)\%$, mean temperature T = (295 ± 5) K). Both values were determined at a lower temperature as the reference temperature of T = 298 K. If the temperature dependence of Φ_{DMP} (see Section 4.4.2) is used to calculate the yield for the temperature of the first experiment ($\Phi_{DMP,292K} = (10.8 \pm 2.7)\%$, error: including the uncertainty of the temperature dependence) this value agrees well. The temperature of 292 K is also representative for the initial phase of the second experiment of *Etzkorn* [1998]. However, the differences with this experiment can not be explained in terms of a temperature dependence of Φ_{DMP} and the value tends to be low. Nevertheless, the average value of both experiments agrees within the error limits with the value calculated at 292 K. The lower values may be taken

Table 5.5: Comparison for p-xylene and 1,3,5-TMB with literature values.

Compound	NO [ppm]	NO ₂ [ppm]	$\Phi_{Aldehyde}$ [%]	$\Phi_{Phenols}$ [%]	Reference
p-Xylene	NO _x -free ^a		7.0 ± 7.0		[Perry et al. 1977]
	NO _x -free ^a		4.0 ± n.n. *		[Nicovich et al. 1981]
	200 - 4000		15.0 ± 2.0		[Kenley et al. 1981]
	≤ 1.5	≥ 0.5	8.0 ± 1.0		[Bandow and Washida 1985]
	ppm-range ^b		10.0 ± n.n. *		[Becker and Klein 1987]
	0.85 - 10	0 - 10	7.0 ± 1.0	18.8 ± 3.8	[Atkinson et al. 1991]
	NO _x -free		6.4 ± 1.5	8.0 ± n.n. *	[Barnes et al. 1991]
	< 0.04	< 0.04	4.9 ± 3.8 ^c	7.3 ± 4.3 ^c	[Etzkorn 1998]
	0.25 - 1.08	0.34 - 0.7 ^d	10.3 ± 1.6	13.0 ± 1.8	[Smith et al. 1999]
			8.1 ± 3.3 ^e	11.8 ± 5.3 ^e	average value
< 0.01 - 0.82	< 0.01 - 0.25	8.2 ± 2.3	11.6 ± 2.8	this work	
	NO _x -free ^f	4.5 ± 4.0 ^g	17.2 ± 2.8	this work	
1,3,5-TMB	200 - 4000		2.1 ± 0.6		[Kenley et al. 1981]
	0.7	0.3	3.0 ± 1.0	4.0 ± 1.0	[Smith et al. 1999]
	< 3	0.4 - 1.2	2.7 ± 0.4	6.7 ± 1.0	this work ^h

* no number.

^a derived from temperature dependence studies.

^b conditions not further specified.

^c average yield of two experiments (see text).

^d estimated value for experiment pX61004.

^e calculated from the listed literature values, error: 1-sigma variability among these values.

^f conditions: initially NO_x-free, several ppm of H₂O₂ present, see Section 5.4.3.

^g average yield, error: reflects the observed variability (see Section 4.4).

^h the data from [Ücker 1999] were re-evaluated here (see Section 4.5).

as an indication for a confirmation of the temperature dependence of Φ_{DMP} observed in this work. Nevertheless, given the uncertainties related to the second value [Etz Korn 1998] the values were not considered in the calculation of the temperature dependence (see Figure 4.13).

For the other literature values good agreement is observed at moderate NO_x -concentrations [Smith *et al.* 1999]. The value by Barnes *et al.* [1991] determined in the absence of NO_x , though slightly lower, is still in reasonable agreement with the value of this work, determined in the presence of moderate concentrations of NO_x though it differs significantly from the value determined in the presence of H_2O_2 (see Section 5.4.3).

However, the value of $\Phi_{DMP} = (18.8 \pm 3.8) \%$ determined by Atkinson *et al.* [1991] is considerably higher. The study by Atkinson *et al.* [1991] differs from the other studies with respect to the employed NO_x -concentrations that are up to one order of magnitude higher than the upper-limit NO_x -concentration of the other studies. A direct comparison with the values of this work suffers from the marginal overlap of the employed NO_x -concentrations. Nevertheless, there are two experiments, i.e. ITC#1562 and ITC#1562 [Atkinson *et al.* 1991] that was carried out at an initial NO_x -concentration of 1.46 ppm and 0.96 ppm, respectively and hence these experiments are comparable to the upper-limit of NO_x -concentrations employed in this study. From the given experimental data the yields of 2,5-DMP can be calculated for the initial phase of the experiments to be 10.6% and 10.2%, respectively. The mean NO_x mixing ratios over the corresponding time span were $[\text{NO}] = 0.79$ ppm and $[\text{NO}_2] = 0.67$ ppm as well as $[\text{NO}] = 0.66$ ppm and $[\text{NO}_2] = 0.30$ ppm, respectively. Both values are in excellent agreement with those values obtained under comparable NO_x -concentrations in this and other studies. The differences with the higher mean value specified by [Atkinson *et al.* 1991] is hence attributed to the higher mean NO_x -concentrations as is discussed in more detail below.

1,3,5-trimethylbenzene

There are only few studies available to compare the yields of 3,5-DMBA and 2,4,6-TMP (that were re-evaluated here from the data by Ücker [1999], see Section 4.5) with literature values. As can be seen in Table 5.5, the agreement is excellent for the DMBA. Even within the reduced experimental error of the re-evaluation (15%) the values can be regarded as identical. The good agreement is observed despite the quite different concentrations of NO and NO_2 that were employed in the different studies

(see Table 5.5). In the experiments of *Ücker* [1999] high initial concentrations of NO (3 ppm) were employed in order to suppress the formation of ozone (and hence NO₃) over an extended time span. As a consequence of the rapid conversion of NO into NO₂, typical for the 1,3,5-TMB, high concentrations of NO₂ accumulated during an experiment (mean [NO₂] = (806 ± 414) ppb). The insensitivity of the DMBA yield on the NO_x-concentration hence confirms the above discussion on p-xylene also for the TMB system.

The only TMP-yield which is presently available [*Smith et al.* 1999] is smaller than the re-evaluated value from this work. Within the specified 2-sigma confidence error-limits (see Table 5.5) the difference of the two values is significant. This result confirms the increase of the phenol-type yield with increasing NO_x-concentration observed for p-xylene (see above discussion) also for the TMB.

5.4.2 Comparison to the results from benzene

The high NO_x concentration range

The NO_x dependent considerations of the phenol yield from benzene lead to the extension of Equation 4.2 (applicable under atmospherically relevant NO_x concentrations) to Equation 5.1 (see Section 4.3.1 and Section 5.3.2).

Similarly to the benzene system, the yields of phenol-type products from p-xylene and TMB were observed to depend on the NO_x-concentration when the yields from this work are compared to literature values (see above). This is most obvious for the p-xylene, where more data is available in the literature (see Table 5.5). The mean value of $\Phi_{DMP} = 18.8 \pm 3.8\%$ [*Atkinson et al.* 1991] is significantly higher than the other values. However, from the scatter in their plotted data (Figure 2 of *Atkinson et al.* [1991]) the yield rather ranges between 10.6% and 23.5% and shows a clear tendency to increase towards higher NO_x-values. Qualitative evidence for tentatively higher phenol-type yields from p-xylene at elevated NO_x-concentrations were further reported by *Wiesen* [1995]. In the context of the results from benzene this behavior seems to be in contradiction with Equation 5.1 from which the influence of NO is expected to reduce the phenol-type yield also for the p-xylene. Nevertheless, the fact that Φ_{DMP} from p-xylene increases by about a factor of 2 with the levels of NO₂ increase points to a more effective formation of phenol-type products from reaction (10) in Figure 2.1 for p-xylene as compared to benzene. The apparently reduced influence of NO for p-xylene is not in contradiction with Equation 5.1 but may rather reflect different experimental conditions and a higher

$\Phi_{DMP,10}$ in the case of p-xylene. From the raw-data given by *Atkinson et al.* [1991] the phenol yield from reaction (10) is estimated $\Phi_{DMP,10} = 40\%$ for p-xylene.

For toluene, the yield of o-cresol was found to increase with increasing concentrations of NO_x [*Atkinson and Aschmann* 1994]. Under NO_x -free conditions the o-cresol yield by *Atkinson and Aschmann* [1994] is essentially identical with the value from [*Klotz et al.* 1998; *Smith et al.* 1998]. At NO_x -concentrations of ≈ 3 ppm and ≈ 14 ppm, the yield of o-cresol increased to about $(14.5 \pm 0.7)\%$ and $(16.0 \pm 0.8)\%$, respectively [*Atkinson and Aschmann* 1994]. Similar conclusions were drawn by *Bierbach* [1994] who observed comparable, though slightly lower, o-cresol yields Φ_{oCRE} than *Atkinson and Aschmann* [1994] ($\Phi_{oCRE} = (14.3 \pm 2.5)\%$ at $[\text{NO}_x] = 20$ ppm, $\Phi_{oCRE} = (18.8 \pm 1.5)\%$ at $[\text{NO}_x] = 40$ ppm, $\Phi_{oCRE} = (23.3 \pm 2.5)\%$ at $[\text{NO}_x] = 75$ ppm). Similarly to p-xylene, this data points towards an effective o-cresol formation from the reaction of the toluene-OH adduct with NO_2 . Thereby, the values of *Bierbach* [1994] most likely represent lower-limit values since a significant influence of wall-reactions was observed. The further discussion is primarily based on the values of *Atkinson and Aschmann* [1994] where the explicit concentrations of NO and NO_2 were specified. In a first approximation the results on o-cresol were scaled by a factor of 1.5 to calculate the overall sum of cresol-isomers. This generalization of the o-cresol data seems to be a feasible approach, although it may slightly overestimate the cresol-yield since the NO_2 -reaction forms m-cresol less effective than the other isomers [yield-ratios of o-, m- and p-cresol (isomer/sum-of-isomers) determined by *Klotz et al.* [1998] under conditions with negligible NO_x -influence (o:m:p = $(67 \pm 12):(15 \pm 4):(18 \pm 4)$) were compared to the respective ratios determined by *Gery et al.* [1985] under conditions of influencing NO_x -reactions (o:m:p = $(81 \pm 9):(2.5 \pm 2.1):(17 \pm 7)$)]. Since the major product is o-cresol the error in this interpolation is estimated $< 15\%$. The overall sum of cresol yields [*Atkinson and Aschmann* 1994] is hence supposed to vary between 21.8% and 24% over the specified NO_x -range. Given this variability, the cresol yield from reaction (10) is estimated $\Phi_{CRE,10} = 40\%$ also for toluene.

In Table 5.6 the values of the kinetic parameters that enter in Equation 5.1 are listed for benzene, toluene and p-xylene. The benzene data [*Bohn and Zetzsch* 1999] was already specified in Section 4.3.1 and was included in Table 5.6 for a better comparison with the values of toluene and p-xylene. Toluene is the only alkyl-substituted aromatic compound for which the elementary kinetic data (K_{eq} , k_{tot} and

Table 5.6: Experimental data and estimated values of kinetic parameters in Equation 5.1.

Compound	K_{eq} [10^{-19} cm ³]	k_{hot} [10^2 s ⁻¹]	k_{10} [10^{-11} cm ³ ·(molec·s) ⁻¹]	k_{12}	k_{phenol} [10^2 s ⁻¹]	$\Phi_{phenol,10}$ [%]	Reference
Benzene	2.7 ± 0.4	7.6 ± 0.8	2.75 ± 0.2	1.1 ± 0.4			[Bohn and Zetzsch 1999] [Zetzsch et al. 1990]
Toluene	3.25 ± 0.33	18.5 ± 1.5	3.6 ± 0.3	$1.1^{+0.9}_{-0.6}$	4.03 ± 0.66^a	18 ± 6^b	this work [Bohn 2001] [Krispel et al. 1990]
p-Xylene	3.7 ± 0.8^e	26.9 ± 8.6^f	3.2 ± 0.3	$1.1^{+0.9}_g$	3.31 ± 0.54^c	$40^{+25}_{-15}^d$	this work ^{c,d} this work ^{e,f,g} [Koch et al. 1993] this work ^{h,i}

^a calculated value. basis: [Bohn and Zetzsch 1999], this work (see also Section 4.3.1).

^b estimated value. basis: Raw-data specified in [Atkinson et al. 1989], this work (see also Section 5.3.2).

^c calculated value. basis: [Bohn 2001] and [Klotz et al. 1998] (see text).

^d estimated value. basis: Raw-data specified in [Atkinson and Aschmann 1994; Klotz et al. 1998].

^e estimated value. basis: Reaction coordinate diagram from [Andino et al. 1996], (see text).

^f estimated value. basis: Rate-constant data from [Koch et al. 1993], (see text).

^g the value by [Bohn 2001] from toluene was adopted.

^h calculated value. basis: see ^f, this work, error: Due to $\Delta\Phi_{DMP}$ only (see Section 4.4.1).

ⁱ estimated value. basis: Data from this and other work listed in Table 5.5 (see text).

k_{12}) as yet is available [Bohn 2001]. The ring-retaining yields of toluene have been subject to a previous study [Etzkorn 1998; Klotz 1998] and literature data on the cresol-yields (here considered as the sum of all isomers) was used [Klotz *et al.* 1998; Smith *et al.* 1998] to estimate a value for k_{phenol} , consistent with the results from Bohn [2001]. For the p-xylene system no experimental data so-far is available for the parameters K_{eq} , k_{tot} and k_{12} . The values listed in Table 5.6 for the p-xylene were estimated from analogy considerations to benzene and toluene using the data from Andino *et al.* [1996] and Koch *et al.* [1993]. Slightly higher values for K_{eq} are expected for p-xylene as compared to toluene if the relative energy data from both compounds (reaction-coordinate diagrams by [Andino *et al.* 1996]) are compared. Similarly, the value of k_{tot} is expected higher for p-xylene from a relative comparison of the rate-constants for the reaction of the aromatic-OH adduct with oxygen [Koch *et al.* 1993]. The value of k_{12} was adopted from toluene.

The data from this work are also included in Table 5.5 and the yields of phenol-type compounds from benzene (phenol), toluene (cresol-isomers) and p-xylene (2,5-DMP) were calculated from Equation 5.1. The resulting phenol-type yields are plotted in Figure 5.2 as a function of the NO_x -concentration. In the upper part of the Figure two lines were drawn for each educt (one solid and one dotted line). Solid lines indicate phenol-type yields that were calculated assuming equal amounts of NO and NO_2 ($[\text{NO}_x] = 2 \cdot [\text{NO}] = 2 \cdot [\text{NO}_2]$). Dotted lines indicate yields that were calculated assuming that all NO_x corresponds to NO and the effect of NO_2 hence is negligible ($[\text{NO}_x] = [\text{NO}]$, $[\text{NO}_2] = 0$ ppb). In the lower part of the Figure the solid lines correspond to the lines in the upper part, re-drawn here to facilitate comparison with the dashed lines. Dashed lines indicate the yields as calculated assuming that all NO_x corresponds to NO_2 and the effect of NO hence is negligible ($[\text{NO}_x] = [\text{NO}_2]$, $[\text{NO}] = 0$ ppb).

The range of scatter observed for the phenol-type yields from benzene [Atkinson *et al.* 1989] (see Section 5.3.2), toluene [Atkinson and Aschmann 1994] and p-xylene [Atkinson *et al.* 1991] (see above) is thereby well reproduced from the solid lines for the NO_x -ranges employed in these studies (typically between 1 ppm and 20 ppm). Further, the cresol-yields of Bierbach [1994] are reasonably fit for the value at $[\text{NO}_x] = 20$ ppm (see above). At higher NO_x -concentrations (between 40 ppm and 75 ppm) the calculated cresol-yields are lower than their measured data. This discrepancy can in principle be explained from the uncertainties in the rate-constant data for the NO_x -reactions (k_{10} and k_{12} in Table 5.6) and is reflected in the error of the value of $\Phi_{phenol,10}$ listed in Table 5.6.

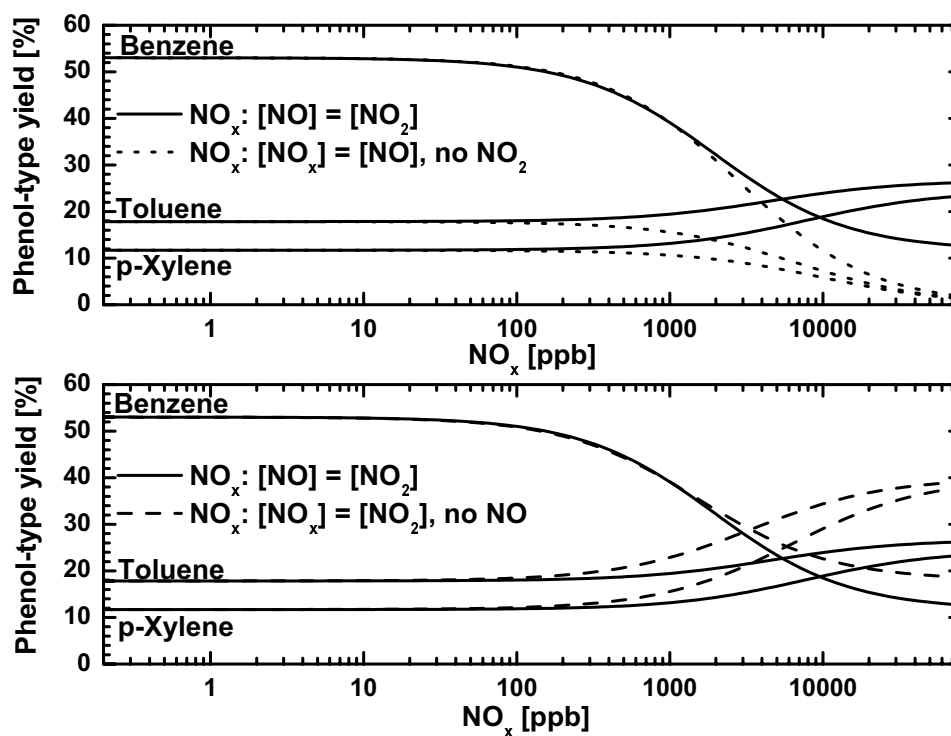


Figure 5.2: The NO_x -dependence of the phenol-type yields from benzene, toluene and p-xylene as calculated from Equation 5.1 using the kinetic data from Table 5.6. The NO_x in this plot corresponds to three different scenarios: (solid line) $[\text{NO}] = [\text{NO}_2]$; (dotted line) $[\text{NO}_x] = [\text{NO}]$; (dashed line) $[\text{NO}_x] = [\text{NO}_2]$ (see text).

The constant yields obtained for the atmospherically relevant low NO_x -range were discussed for benzene already in Section 5.3.2. They are confirmed constant also for the toluene and p-xylene though over a slightly extended NO_x -range. The comparison of the two lines drawn for each aromatic educt in the upper part indicate, that the influence of NO leads to a reduction of the phenol-type yields for all three compounds. As it is seen in the lower part of Figure 5.2, the influence of NO_2 is observed to increase the phenol-type yields from toluene and p-xylene. This contrasts with the behavior of benzene and is in agreement with the experimental results. The results point to significantly higher values of $\Phi_{\text{phenol},10}$ for the alkyl-substituted aromatic compounds as compared to benzene.

The formation mechanism of 2,5-dimethylphenol

The significant temperature dependence of the yields of 2,5-DMP (see Section 4.3.4) tends to confirm the results from benzene, that phenol formation proceeds directly

from the reaction of the aromatic-OH adduct with oxygen (pathway (3) in Figure 2.1). However, no enthalpy data is as-yet available for the p-xylene system and this conclusion at present is based on the enthalpy data of benzene [Lay *et al.* 1996] (see Section 4.3.4).

5.4.3 Differences under NO_x-free conditions

In those experiments where several ppm of H₂O₂ were added as a source of OH-radicals (radical-source (4), see Section 3.4.4) systematically higher yields of phenol-type compounds were observed from benzene (see Table 5.4) and p-xylene (see Table 5.5). These higher phenol-type yields are consistent with the results observed previously [Seuwen and Warneck 1996; Bierbach 1994; Becker *et al.* 1997] in the toluene/H₂O₂ system, where more than two times higher cresol yields have been observed. Bierbach [1994] observed the yields of cresol-isomers to increase with higher amounts of H₂O₂ were present in the reaction-system and concluded that the cresol-yields back-interpolated to atmospheric conditions should not be significant. Similar results were observed by Wiesen [1995] for the 2,5-DMP yield from p-xylene (see also [Becker *et al.* 1997]). However, this is in contrast to the results of various other studies on the phenol-type-yields from toluene [Atkinson and Aschmann 1994; Klotz *et al.* 1998; Smith *et al.* 1998] and p-xylene (see Table 5.5) where comparable yields were obtained in the presence and absence of NO_x and the yields are found to be non-negligible. Although the higher phenol-type yields from benzene and p-xylene observed in the presence of H₂O₂ in this work tend to confirm the results described above it should be noted, that for benzene (see Table 5.4) and p-xylene (Table 5.5, [Wiesen 1995] and references therein) considerable scatter is visible among the phenol-yields determined in the absence of NO_x.

One possible explanation for the differences in the yields may be linked to the presence of H₂O₂. This radical-source may influence the formation of phenol-type products via reactions involving H₂O₂ or HO₂-radicals (which are expected to form in considerable amounts). Reaction rate-constants for the reaction of the benzene-OH adduct with H₂O₂ ($k_{H_2O_2} \leq 1 \cdot 10^{-14} \text{ cm}^3 \cdot (\text{molec} \cdot \text{s})^{-1}$ [Bohn and Zetzsch 1999]) and HO₂ ($k_{HO_2} = (7 \pm 4) \cdot 10^{-11} \text{ cm}^3 \cdot (\text{molec} \cdot \text{s})^{-1}$ [Bohn *et al.* 1999]) however indicate that both reactions are too slow in order to contribute significant amounts of phenol under the experimental conditions of this work. For example, for a 10 % change in the phenol-yield from benzene more than 220 ppm of H₂O₂ or 30 ppb of HO₂-radicals were needed. However, the concentrations of both species were lower

by more than a factor of ten under the experimental conditions employed in this work. Consequently, the formation of additional phenol from the aromatic-OH adduct via these reactions can be ruled out. However, these pathways become important under different experimental conditions [Bierbach 1994; Wiesen 1995; Seuwen and Warneck 1996]. It is concluded, that the presence of H_2O_2 is not directly responsible for the observed higher phenol yield under NO_x -free conditions.

An explanation for the higher phenol yields in the absence of NO_x can be found on the basis of a single assumption: the reversibility of the non-phenol-forming-loss-processes from equilibrium **2/3**, i.e. reactions (8) and/or (9) in Figure 2.1. Both pathways may form the bicycloalkyl radical which at present is considered to decompose at an almost negligible rate [Lay *et al.* 1996]. Further reversible addition of oxygen is thought to give the bicycloperoxy radical. However, unless converted into the respective oxy radical (through reaction with another peroxy radical or NO), decomposition via the bicycloalkyl radical may in principle yield back the species **2/3** (in Figure 2.1). With the above assumption the phenol yield becomes dependent on the peroxy radical concentration under conditions when the overall lifetime of the bicycloperoxy radical (and other peroxy radicals) is considerably larger than the lifetime of the bicycloalkyl radical with respect to decomposition. In the absence of NO_x and in the presence of low radical concentrations the phenol yield should increase. Indeed, the variable pTALD yield observed for experiment PXY7 indicates that peroxy + peroxy-radical reactions were actually in competition with peroxy-radical + NO reactions. On the basis of the above assumption the higher yield of phenol-type compounds observed in this experiment as in experiment BE14 can be understood in terms of additional phenol which was formed via the known pathways (see Section 4.3.4 for benzene; Section 4.4.2 for p-xylene). On the other hand, lower phenol yields [Bjergbakke *et al.* 1996; Berndt *et al.* 1999] may be explained from high radical concentrations (see discussion of this data in Section 5.3.1).

At present, difficulties in the exact quantification of the low NO_x -concentration in the presence of considerable amounts of H_2O_2 (variable with time) limit the further discussion of these results. The phenol formation in the absence of NO_x is subject to ongoing investigations.

5.5 The glyoxal yields from BTX

In this Section, the separation of the primary and the overall glyoxal yield described in Section 4.6 is discussed in the context of available literature data. In Section 5.5.1 the various pathways - proposed or identified - in the literature to form glyoxal are discussed (see also Section 4.6.4 on the identification of the bicycloalkyl-radical pathway). In Section 5.5.2 the negligible secondary glyoxal formation (see Section 4.6.2) is quantitatively understood. Finally, in Section 5.5.3 the glyoxal yields from this work are compared to the available literature data.

5.5.1 Precursors for the formation of glyoxal

In Figure 5.3 several possible pathways resulting in the formation of glyoxal are shown for the toluene system. In principle all five intermediates **3-8** formed from the reaction of the toluene-OH adduct with oxygen may result in glyoxal, either as a primary product **10a** or a higher-generation product **10b**. The experimentally identified products are shown in round-edged boxes, and the products that were demonstrated to yield glyoxal in the laboratory are shown on a shaded background. The thick arrows indicate the ring-cleavage pathway in agreement with the results of this study. Similar schemes can be adapted for the other aromatic compounds. Phenols **4** are highly reactive towards the OH- and NO₃-radical. Despite the importance of NO₃-radical reactions for these compounds (see Sections 4.4, 4.8 and 7) the principal fate of phenol will be reaction with the OH-radical. The major primary products from this reaction are dihydroxybenzenes, nitrophenols and benzochinones [Oliaru *et al.* 2000]. Only a minor fraction (less than 10%) may undergo ring-cleavage and thereby lead to the formation of glyoxal as a secondary product **10b**.

The formation of a peroxy-radical **3** was postulated in the late seventies [Darnall *et al.* 1979], but it took until recent years for tentative experimental evidence of its formation to be reported for the benzene system [Bjergbakke *et al.* 1996]. More recently, the existence of a peroxy-radical **3** has been proven experimentally, though indirectly, for benzene [Bohn and Zetzsch 1999] and toluene [Bohn 2001] by cw UV-laser long-path absorption spectroscopy. The further fate of the peroxy-radical **3** may be intramolecular rearrangement [Bartolotti and Edney 1995] or reaction with NO. The reaction with NO may result in the formation of muconaldehydes (di-unsaturated 1,6-dicarbonyls; **11a,11b** as primary products

[Hoshino *et al.* 1978; Dumdei and O'Brien 1984; Yu *et al.* 1997]. The formation of glyoxal **10b** from muconaldehydes may proceed via OH-reaction of the hexadienedials formed from benzene or the methyl-substituted derivatives of type **11a** formed from toluene and p-xylene. Moreover, the methyl-substituted derivatives of type **11b** may react with OH and form an unsaturated 1,4-dicarbonyl that under further OH attack may form glyoxal. This indirect glyoxal formation was demonstrated from the 2-methylhexa-2,4-dienedial **11b** to proceed through the further OH reaction of butenedial **12** [Klotz *et al.* 1995]. For both, the muconaldehydes [Klotz *et al.* 1999] and the unsaturated 1,4-dicarbonyl-type products [Sørensen and Barnes 1997; Graedler and Barnes 1997], photolysis competes with OH-reaction and only the OH-reaction of the latter yields glyoxal.

The bicycloalkyl-radical **7** may form from the peroxy-radical **2** through intramolecular 1,3-oxygen-bridge formation and has in fact been identified as one of the three likely intermediates to form on the basis of density-function-based-calculations on the reaction of the toluene-OH adduct with oxygen [Bartolotti and Edney 1995]. The bicycloalkyl-type radicals **3** can add additional O₂ and then react with NO to form the respective alkoxy-radical. Alternative pathways are in principal possible [Atkinson *et al.* 1980] though considered non-operative [Andino *et al.* 1996; Atkinson *et al.* 1980] (see Section 5.6). The alkoxy-radical can further decompose in a sequence of two unimolecular decomposition steps into two radicals that subsequently yield an α -dicarbonyl (glyoxal **10a** from benzene; glyoxal **10a** and methylglyoxal (not shown) for alkylsubstituted aromatics) and an unsaturated 1,4-dicarbonyl compound **12,13**, respectively, as primary products. The following 1,4-dicarbonyls of type **12,13** have been experimentally identified: butenedial **12** [Besemer 1982; Shepson *et al.* 1984; Dumdei and O'Brien 1984; Dumdei *et al.* 1988; Bierbach 1994; Yu *et al.* 1997; Smith *et al.* 1998] and 4-oxopentenal **13** [Shepson *et al.* 1984; Dumdei and O'Brien 1984; Dumdei *et al.* 1988; Bierbach 1994; Yu *et al.* 1997; Smith *et al.* 1998] from toluene, as well as 2-methylbutenedial (not shown) [Becker *et al.* 1997; Smith *et al.* 1999] and 3-hexene-2,5-dione (not shown) [Becker and Klein 1987; Wiesen 1995; Smith *et al.* 1999; Bandow and Washida 1985; Becker *et al.* 1997] from p-xylene. For the unsaturated 1,4-dicarbonyl coproducts of glyoxal **10a**, photolysis competes with OH-reaction. With the exception of 3-hexene-2,5-dione the OH-reaction of the unsaturated 1,4-dicarbonyls may contribute to the secondary formation of glyoxal **10b**.

The epoxide-alkoxy-radical **8**, the most stable of the three intermediate species proposed by *Bartolotti and Edney* [1995], may either form directly when oxygen is added to the ring or through intramolecular oxygen transfer from the peroxy-radical **3** [*Bartolotti and Edney* 1995]. As primary products, stable ring-retaining or stable long-chain (C₆ to C₈) ring-cleavage epoxide-type compounds **14** were proposed [*Yu and Jeffries* 1997]. Experimentally, these compounds were tentatively identified in product studies on different alkylbenzenes including toluene [*Yu and Jeffries* 1997] and p-xylene [*Kwok et al.* 1997; *Yu and Jeffries* 1997] with the molecular weights of the expected primary epoxide-type products **14,15** matching the observed mass peaks from PFBHA-derivative GC/MS [*Yu and Jeffries* 1997] and API-MS [*Kwok et al.* 1997] analysis. However, positive quantitative confirmation of the formation of these compounds still requires standards. A secondary formation of glyoxal **10b** may result from the OH-reaction or ozonolysis of type **14** epoxides [*Yu and Jeffries* 1997]. Furthermore, these compounds may undergo photolysis and yield type **15** epoxide-type products [*Yu and Jeffries* 1997]. Presumably, products of type **15** may further react with OH and also contribute to the secondary formation of glyoxal. From the aldehyde-type structure of these compounds it is likely that, as in the case of the dicarbonyls, photolytic-loss competes with OH-reaction. However, little is known about the formation yield and principal fate of these epoxide-type compounds **14,15** in the atmosphere.

A second epoxide-type intermediate, benzeneoxide/oxepin, and its methylated derivatives, termed areneoxides **5/6**, was postulated by *Klotz et al.* [1997]. The main difference between this pathway and the epoxide-alkoxy-radical **8** pathway [*Bartolotti and Edney* 1995] is that a stable epoxide-type species **5** and additional "prompt HO₂" are formed as primary products of the reaction of the aromatic-OH adduct with oxygen. Apart from the tentative assignment of 1,6-dimethylbenzeneoxide/oxepin (not shown) in the oxidation of o-xylene [*Shepson et al.* 1984], the areneoxides **5/6** so far have not been observed experimentally [*Bjergbakke et al.* 1996]. Even though the OH-reaction of benzeneoxide/oxepin [*Klotz et al.* 1997] may result in the formation of the epoxide-alkoxy-radical **8**, the only products identified from this reaction are muconaldehydes **11a,11b** [*Klotz et al.* 1997]. The further fate of the muconaldehydes **5/6** and the pathways presumably leading to secondary glyoxal **10b** are discussed above.

The primary glyoxal **10a** yield was separated from further glyoxal **10b** formation via stable intermediate compounds in this work (see Section 4.6.1). The primary glyoxal **10a** yield is high in any investigated system (see Table 4.8), indicating that fast ring-cleavage, involving the bicycloalkyl-radical intermediate **7**, is a major operative ring-cleavage pathway for aromatic hydrocarbons, i.e. BTX.

5.5.2 Photolytic processes

As indicated in Figure 5.3 the principal fate of precursors for secondary glyoxal **10b** is either OH-reaction or photolysis. Table 5.7 gives an overview of the available kinetic data for the OH-reaction and photolysis of likely glyoxal precursors and glyoxal. The photolysis-frequencies given were scaled relative to J_{NO_2} to reflect the experimental conditions during the experiments, as described in the notes of Table 5.7.

For butenedial **12** and the 4-oxo-pentenal **13**, the measured values for the photolysis-frequency [Sørensen and Barnes 1997] correspond to the cis-isomers. In the following discussion no difference for the trans-isomer is assumed. Photolysis and OH-reaction will be the prominent loss-processes for the two compounds. Under the employed experimental conditions photolysis was found to be extremely fast (photolytic lifetimes are only of the order of ten minutes) for both compounds, dominating the OH-reaction by a factor of five. Only a small fraction of about 15% may undergo OH-reaction and thereby yield some secondary glyoxal **10b**. Assuming unity yield for the glyoxal formation from this reaction, secondary glyoxal **10b** would still be in the range of the experimental error. Since the formation of maleic-anhydrid is an alternative pathway of this reaction [Bierbach *et al.* 1994] the secondary glyoxal **10b** yield should be even lower.

The atmospheric chemistry of the 2-methyl-butenedial is unknown at present. Nevertheless, it is likely from the structural similarity of this compound with butenedial that photolysis will be the dominant fate in the presence of sunlight. Though the OH-reaction may be faster than that of butenedial **12**, the secondary yield of glyoxal from 2-methyl-butenedial is expected to be well below unity and thus should not significantly contribute to secondary glyoxal formation.

For 3-hexene-2,5-dione, the listed photolysis-frequency [Graedler and Barnes 1997] corresponds to an equilibrium mixture of E/Z-isomers with a measured E/Z-ratio of 1/2. This ratio was used to estimate an effective OH-reaction rate-constant, given in Table 5.7. In addition, reaction with ozone may be of importance for the

Table 5.7: Kinetic parameters of selected glyoxal precursors.

Compound	Photolysis-	OH-Rate	Photolytic lifetime	OH- lifetime ²	Overall lifetime	Relative OH-loss [%]
	frequency ¹ J [10 ⁻⁵ s ⁻¹]	Constant k _{OH} [10 ¹¹ cm ³ .(molec.s) ⁻¹]				
Butenedial	134 ^a	5.2 ^h	12.4	64	10.3	16
4-Oxo-2-pentenal	162 ^b	5.6 ^h	10.3	59.5	8.8	15
2-Methyl-butenedial ³	134	5.2	12.4	64	10.3	16
3-Hexene-2,5-dione	4.3 ^c	5.9 ^h	390	61	51.5	86
EZ-2,4-Hexadienedial	111 ^d	7.4 ^d	15	45.1	11.3	25
EE-2,4-Hexadienedial	9.2 ^e	7.6 ^d	180	43.9	35.3	81
EE-2-Methyl-2,4-hexadienedial	9.2 ^f	11.8 ^f	180	28.3	21.5	87
Glyoxal	7.9 ^g	1.15 ⁱ	210	290	122	42

¹ scaled to $J_{NO_2} = 7.5 \cdot 10^{-3} \text{ s}^{-1}$, representative for the experiments.

² basis: $[OH] = 5 \cdot 10^6 \text{ molec cm}^{-3}$, representative for the experiments.

³ no kinetic data is available. The given data corresponds to that of butenedial (see text).

^a based on [Sørensen and Barnes 1997]: $J(\text{cis-butenedial})/J_{NO_2}=0.18$.

^b based on [Sørensen and Barnes 1997]: $J(\text{cis-4-oxo-2-pentenal})/J_{NO_2}=0.22$.

^c based on [Graedler and Barnes 1997]: $J(\text{E/Z-3hexene2,5dione})/J_{NO_2}=5.7 \cdot 10^{-3}$.

^d [Klotz et al. 1999]; photolysis: $J(\text{EZ-2,4-hexadienedial})/J_{NO_2}=0.148$.

^e effective loss-rate based on [Klotz et al. 1999]: $J(\text{EE-2,4-hexadienedial})/J_{NO_2}=0.0122$.

^f $J(\text{EE-2,4-hexadienedial})$ adapted; OH-rate-constant from [Klotz et al. 1995].

^g based on [Klotz et al. 2001]: $J(\text{GLY})/J_{NO_2}=0.0105$.

^h [Bierbach et al. 1994], effective rate-constant of 3-hexene-2,5-dione was calculated assuming

a ratio of Z/E-isomers of 2/1 [Graedler and Barnes 1997].

ⁱ [Plum et al. 1983].

3-hexene-2,5-dione [Liu *et al.* 1999]. On the basis of the ozonolysis rate-constant $k_{O_3} = 3.6 \cdot 10^{-18} \text{ cm}^3(\text{molec}\cdot\text{s})^{-1}$ and about 300 ppb of ozone, this pathway may contribute about 10 % to the total loss of 3-hexene-2,5-dione, making reaction with OH its dominant fate. From the OH- and O_3 -reactions, however, methylglyoxal is expected to be formed primarily [Bierbach *et al.* 1994] and glyoxal **10b** is expected to be a minor product. In summary, secondary glyoxal formation from 3-hexene-2,5-dione should be insignificant.

The EZ-2,4-hexadienedial in the presence of sunlight is found to rapidly isomerize into the EE-isomer (similar to **11**) [Klotz *et al.* 1999]. From the described photolytic behavior of the EE-2,4-hexadienedial [Klotz *et al.* 1999] loss through OH-reaction will be the dominant removal process for this isomer. Hence, high yields of hexadienedials were expected to result in significant amounts of secondary glyoxal **10b** in the benzene system. The negligible secondary formation of glyoxal observed from benzene is thus an indicator that hexadienedials were not formed in significant amounts under the experimental conditions employed in this work. From the experimental error of the measurements (6.6 % for the overall glyoxal yield from benzene) an upper-limit of the formation yield of hexadienedial-type compounds can be estimated to be < 8 %. Similarly, the EE-2-methyl-2,4-hexadienedial (**11b** in Figure 5.3) expected to form from toluene will primarily react with the OH-radical yielding butenedial **12** as primary product. Hence, the secondary formation of glyoxal **10b** from this compound should not be observable due to the rapid photolysis of butenedial **12** under the employed experimental conditions.

Overall, the negligible contribution of secondary glyoxal **10b** observed from BTX (see Section 4.6.2) can be understood from the rapid photolysis of the unsaturated 1,4-dicarbonyls. This result contrasts with the predictions made by state-of-the-art chemical models that up to 40 % of the glyoxal should be formed as secondary glyoxal. Possibly, photolysis is underestimated by these models.

Secondary glyoxal **10b** formation may, nevertheless, become important if under different experimental conditions OH-reactions dominate over the photolytic-loss of glyoxal precursors.

5.5.3 Comparison with literature values

In Table 5.8 the glyoxal yields of this study are compared to the available literature values. The values of this work are given as average values of the data from Table 4.8. The error includes the uncertainty of the σ of glyoxal. The values are in

general found to be comparable to the reported upper-limit values or even above. A direct comparison to the listed values suffers the differences in the experimental conditions, that have been characterized in Table 5.8 in terms of the employed NO- and NO₂ concentrations. An additional uncertainty in the direct comparison of the data obtained from this work with literature values arises from the fact, that most studies did not correct for secondary loss of glyoxal via OH-reaction and photolysis. Excellent agreement is found for the p-xylene system, with the value of a recent study [Smith *et al.* 1999] being virtually identical to the value from this work. The NO_x-concentrations employed by Smith *et al.* [1999] actually overlap with the NO_x-concentration employed in this work. In addition, excellent agreement is observed with the value of $\Phi_{GLY} = 36\%$ determined by Becker and Klein [1987] in the absence of light. In the same study a significantly lower glyoxal yield of $\Phi_{GLY} = 10\%$ was observed in the presence of light. The reason for this discrepancy is not immediately obvious and may be found in different experimental conditions. Unfortunately a further comparison with the data of this work is not possible due to the limited information about their experimental conditions. In an attempt to re-investigate the glyoxal yield Wiesen [1995] determined a yield of $(9.7 \pm 1.8)\%$ C (per cent carbon) and concluded that a direct comparison with the value from Becker and Klein [1987] was not possible due to differences in the experimental conditions. Agreement was reported with the value by [Tuazon *et al.* 1984]. However, if their value is multiplied by 4 in order to obtain molar yields, the value agrees well with the value of this work.

As is apparent from Table 5.8 studies that employed elevated concentrations of NO_x (several ppm) determined tendentially lower glyoxal yields [Tuazon *et al.* 1984; Bandow and Washida 1985; Tuazon *et al.* 1986]. As discussed in Section 5.4.2, the p-xylene system is the less sensitive among the BTX species towards the NO_x-influence in the formation of ring-retaining, i.e. phenol-type compounds. The well agreement of the glyoxal yields from p-xylene between this work and Smith *et al.* [1999] (mean NO_x concentrations are about five times higher than in this work) tends to confirm this result also for a ring-cleavage product. The constant glyoxal yield over the range of NO_x-concentrations employed in this work indicates that the ring-cleavage pathways from p-xylene are essentially uninfluenced from the NO_x-concentration up to roughly 1 - 1.5 ppm of NO_x.

In fact, for toluene the differences in the glyoxal yields from this work and Smith *et al.* [1998] (mean NO_x-concentrations are about three time higher than in

Table 5.8: Comparison of the glyoxal yield with literature values.

Compound	NO [ppm]	NO ₂ [ppm]	glyoxal yield Φ_{GLY} [%]	Reference
Benzene	< 5	$\leq 1-8^a$	20.7 ± 1.9	[Tuazon <i>et al.</i> 1986]
	< 0.01 - 0.1	< 0.01 - 0.12	35.9 ± 9.6	this work
Toluene	1.9 - 4.7	< 4.2 ^b	$8.0 \pm \text{n.n.}^*$	[Shepson <i>et al.</i> 1984]
	< 5	$\leq 1-8^a$	11.1 ± 1.3	[Tuazon <i>et al.</i> 1984]
		$\approx 4.5 - 20^c$	$9.8 \pm \text{n.n.}^*$	[Gery <i>et al.</i> 1985]
	< 0.17 - 1.5	0.5 - 1.8 ^d	15.0 ± 4.0	[Bandow <i>et al.</i> 1985]
	< 5	$\leq 1-8^a$	10.5 ± 1.9	[Tuazon <i>et al.</i> 1986]
	< 0.9	0.05 - 0.85 ^a	$20.3 \pm \text{n.n.}^*$	[Dumdei <i>et al.</i> 1988]
	< 0.075 - 0.42	0.046 - 0.6	23.8 ± 2.5	[Smith <i>et al.</i> 1998]
	< 0.01 - 0.1	< 0.01 - 0.09	34.4 ± 11.5	this work
p-Xylene	< 5	$\leq 1-8^a$	12.0 ± 2.0	[Tuazon <i>et al.</i> 1984]
	≤ 1.5	≥ 0.5	24.0 ± 2.0	[Bandow and Washida 1985]
	< 5	$\leq 1-8^a$	22.5 ± 3.9	[Tuazon <i>et al.</i> 1986]
		ppm-range ^e	$36.0 \pm \text{n.n.}^g$	[Becker and Klein 1987]
		ppm-range ^e	$10.0 \pm \text{n.n.}^h$	[Becker and Klein 1987]
		NO _x -free	14.0 ± 6.0	[Barnes <i>et al.</i> 1991]
	0.25 - 1.08	0.34 - 0.7 ^f	39.4 ± 11.0	[Smith <i>et al.</i> 1999]
	< 0.01 - 0.82	< 0.01 - 0.25	35.8 ± 8.1	this work
	NO _x -free ⁱ	9.2 ± 1.4	this work	

* no number.

^a author estimate: NO₂ concentration range.

^b author estimate of the final NO₂ concentration.

^c range of the initial NO_x-concentration.

^d author estimate of the final NO₂ concentration (run# 3).

^e the concentrations were not further specified.

^f final NO₂ concentration for experiment pX61004 (Smith *et al.*, 1999).

^g OH-radicals generated from PNA in the dark.

^h determined in a p-xylene/NO_x-system in the presence of light.

ⁱ conditions: initially NO_x-free, several ppm of H₂O₂ present, see Section 5.5.4.

this work) are observed larger. Further, the glyoxal yields from studies that employed NO_x -concentrations in the several-ppm-range tends to be lower for toluene ($8\% \leq \Phi_{GLY} \leq 15\%$) as compared to the p-xylene system ($12\% \leq \Phi_{GLY} \leq 24\%$). *Bandow et al.* [1985] systematically varied the initial NO-to- NO_2 ratio in their experiments. Though they finally averaged their data and do not discuss explicitly the dependence on the NO_x -concentration, their Φ_{GLY} -values vary by a factor of almost two. A systematic dependence on the employed experimental conditions on first sight is not obvious (see Table 2 of their work). However, the highest glyoxal yield was observed in the experiment with lowest NO_x ($\Phi_{GLY} = 20\%$, $[\text{NO}_x] = 0.67$ ppm). This value is in reasonable agreement with that from *Smith et al.* [1998] which was determined under comparable, though slightly lower, NO_x -concentrations. Further, from the two experiments that *Bandow et al.* [1985] carried out at a NO_x -concentration of 2 ppm, the experiment with initial NO being in excess over NO_2 (ratio of $[\text{NO}]/[\text{NO}_2] = 3$) resulted in a yield of $\Phi_{GLY} = 15\%$ while the experiment carried out with NO_2 in excess over NO (initial $[\text{NO}]/[\text{NO}_2] = 0.33$) resulted in $\Phi_{GLY} = 11\%$. In fact, this lower-most glyoxal yield is in good agreement with the average yield obtained from the other studies that employed NO_x -concentrations of several ppm. These lower glyoxal yields hence seem to reflect the influence of reactions involving NO_x rather than to be due to experimental scatter. The dependence on the ratio of $[\text{NO}]/[\text{NO}_2]$ may be taken as an indication that once NO_x -reactions become important, the NO_2 -influence is more pronounced than that of NO with respect to a reduction of the glyoxal yield. From a comparison of the values of [*Bandow et al.* 1985; *Smith et al.* 1998] and this work it appears, that NO_x -reactions reduce the glyoxal yield already at NO_x -levels between 500 ppb to 1 ppm for toluene.

In the case of benzene only one study is available for comparison. In the study by *Tuazon et al.* [1986] considerably higher NO_x -concentrations were employed. However, it is the only study that explicitly corrected for secondary loss of glyoxal via OH-reaction and photolysis. The differences to the results of this work are significant. Interestingly, the observed difference in the glyoxal yields for benzene is smaller than that observed for the toluene system and is rather comparable to that observed for p-xylene (see above). The similarity of the NO_x -influence for benzene and p-xylene seems to be in contradiction with benzene being the most sensitive system towards these NO_x -reactions. However, in the presence of high NO_x -concentrations [*Tuazon et al.* 1986] the peroxy-radical (intermediate 3 in Figure 2.1) will react with NO and most likely form hexadienedials. The glyoxal for-

mation from the further OH-reaction of these compounds is expected to occur in high yields (see Section 5.5.2). Hence it is likely, that glyoxal in their study will form from essentially different pathways as in this work. However, the lower glyoxal yields observed by *Tuazon et al.* [1986] tend to confirm the discussion on toluene, that the influencing NO₂-reaction does not result into the formation of glyoxal in high yields.

Table 5.8 gives convincing evidence that lower glyoxal yields were observed for BTX at elevated NO_x-concentration (several ppm). With respect to the ring-retaining product yields from BTX and TMB (see Section 5.4.2) the influence of NO_x-reactions was only identified for the phenol-type compounds but not for the aldehyde-type compounds. Since phenols and glyoxal both are formed from the OH-addition reaction to the aromatic ring, the influence of NO_x reactions on the glyoxal forming pathways is in principle in-line with the results obtained for the phenols. However, the analogy to the ring-retaining products seems not to be straightforward. Moreover, the direct comparison of the glyoxal yields suffers various uncertainties such as (1) unaccounted secondary loss-reactions of glyoxal, (2) possible differences in the glyoxal forming chemistry as well as (3) possible differences in the calibrations. A systematic study of the NO_x-influence of Φ_{GLY} is therefore desirable.

5.5.4 Differences under NO_x-free conditions

In experiment PXY7, where several ppm of H₂O₂ were added as a source of OH-radicals (radical-source (4), see Section 3.4.4) an about a factor of four times lower glyoxal yield was observed from p-xylene (see Table 5.8). The lower glyoxal yield is in reasonable agreement with the value by *Barnes et al.* [1991] which was determined in the absence of NO_x. However, it should be noted that the consistency among the lower glyoxal yields from both studies contrasts with the discrepancies observed for the 2,5-DMP yields (see Section 5.4.3). Nevertheless, it appears that under conditions of low NO_x, where peroxy + peroxy-radical reactions are in competition with peroxy-radical + NO reactions lower glyoxal yields are observed. The confirmation of this result in the absence of H₂O₂ is subject to ongoing investigations.

5.6 The formaldehyde formation from toluene

Formaldehyde was identified in Section 4.7 to form as a secondary product from the OH-radical initiated oxidation of toluene. The distinctly different behavior of the formation of formaldehyde and glyoxal further confirms that the separation of primary products from secondary products that are formed from secondary reactions of rapidly reacting stable intermediate compounds indeed has been demonstrated in this work (see Section 4.6 and Section 5.5.1).

5.6.1 Evidence for short lived stable intermediates

An efficient formaldehyde production was identified in Section 4.7 to become operative already shortly after the start of the experiment shown in Figure 4.19. The fact, that formaldehyde is formed rather quickly as a secondary product from toluene indicates that the formaldehyde-precursors must be rather short-lived stable intermediate compounds. The overall lifetime of the intermediate with respect to OH-reaction and photolysis was identified to be of the order of 10 minutes (see Section 4.7).

Potential intermediates with comparable lifetime are the likely co-products of the α -dicarbonyls, listed in Table 5.7. For toluene, the two γ -dicarbonyl-type co-products are butenedial (intermediate **12** in Figure 5.3) and 4-oxo-pental (intermediate **13** in Figure 5.3). Both compounds have been identified in various product studies on the OH-radical initiated oxidation of toluene (see Section 5.5.1). However, so-far only two studies are available where the yields of butenedial **12** ($\Phi_{BUDIAL} = 0.5\text{-}1\%$ [Shepson *et al.* 1984; Dumdei and O'Brien 1984]) and 4-oxo-pental **13** ($\Phi_{OPEAL} \approx 3.1\text{-}8.1\%$ [Dumdei *et al.* 1988; Smith *et al.* 1998]) have been quantified, respectively. These yields are significantly lower (about a factor of ten to forty) than the simultaneously determined yields of the α -dicarbonyls. From the discussion in Section 5.5.2 this may in part be due to the fact that the dominant photolytic sink of the γ -dicarbonyls (see Section 5.5.2) was not corrected in either of these studies. Under experimental conditions representative for experiment TOL4, both compounds are expected to live about ten minutes, see Table 5.7. The temporal coincidence with the delay in formaldehyde formation in the reaction-system is striking.

Experimental evidence for the formation of formaldehyde as a major product from 4-oxo-pental **13** has been derived from Bierbach *et al.* [1994] in the irradiation of 4-oxo-pental **13** with light from VIS lamps ($\lambda_{max} = 360\text{ nm}$) in the laboratory. In the same study, no formation of formaldehyde was reported from butenedial **12**. In a

further study, using natural sun-light as light source, *Liu et al.* [1999] found considerable amounts of formaldehyde to form from 4-oxo-pentenal **13**. Considerably lower formaldehyde amounts were observed to form from butenedial **12** (see Figures 3 and 4 of their work) and possibly may be attributed to secondary reactions of glyoxal **10b** in their study. From the γ -dicarbonyls listed in Table 5.7 only the 4-oxo-pentenal **13** hence is expected to yield formaldehyde on a sufficiently fast time-scale. The 4-oxo-pentenal may form formaldehyde via the formation of methyl-radicals ($\text{CH}_3\cdot$) upon photolysis and OH-reaction. The formation of formaldehyde from methyl-radicals in air is expected to proceed at unity yield [*Bandow et al.* 1985] (on a time-scale of milliseconds under the employed experimental conditions of this work). The expected co-product of the methyl-radicals may result into the formation of maleic anhydrid [*Bierbach et al.* 1994; *Forstner et al.* 1997].

The formaldehyde formation on a short time-scale in principle is a useful tracer substance to determine the role short-lived non-radical intermediate compounds such as e.g. 4-oxo-pentenal **13**. The following argument is based on the hypothesis that 4-oxo-pentenal **13** is the single formaldehyde precursor of the Reaction-sequence 4.3 in the toluene system. Equation 5.2 describes the link of the yield of 4-oxopentenal **13** (Φ_{OPEAL}) to the observed formaldehyde concentration from toluene:

$$\Phi_{\text{OPEAL}} = \frac{[\text{HCHO}]_{\text{corr}} \cdot \Phi_{\text{BALD}}}{[\text{BALD}]_{\text{corr}}} \cdot \frac{J_{\text{OPEAL}} + k_{\text{OH,OPEAL}} \cdot [\text{OH}]}{\Phi_{\text{HCHO,J}} \cdot J_{\text{OPEAL}} + \Phi_{\text{HCHO,OH}} \cdot k_{\text{OH,OPEAL}} \cdot [\text{OH}]} \quad (5.2)$$

where the first ratio denotes the formaldehyde yield as calculated from the relative yield plot (see above), J_{OPEAL} and $k_{\text{OH,OPEAL}}$ denote the photolysis-frequency and OH-reaction rate-constant of 4-oxo-pentenal **13**, $[\text{OH}]$ the OH-concentration, $\Phi_{\text{HCHO,J}}$ and $\Phi_{\text{HCHO,OH}}$ denote the formaldehyde yields from the photolysis and OH-reaction of 4-oxo-pentenal **13**. If $\Phi_{\text{HCHO,J}} = \Phi_{\text{HCHO,OH}} = 1$ is assumed the observed formaldehyde yield from toluene (see Section 4.7) corresponds to a 4-oxo-pentenal-yield of ($\Phi_{\text{OPEAL}} = (37.2 \pm 7.9)\%$), as calculated from Equation 5.2. The measured glyoxal **10a** yield in this experiment was $\Phi_{\text{GLY}} = (29.8 \pm 9.1)\%$. Despite, the apparently larger calculated yield of 4-oxo-pentenal **13**, both values agree within their error limits. The high formaldehyde yield hence can be accounted for taking 4-oxo-pentenal **13** as only formaldehyde precursor.

On the other hand, any additional formaldehyde-precursor would lower the calculated 4-oxo-pentenal **13** yield. The α -dicarbonyl co-product butenedial **12** was not observed to form formaldehyde upon photolysis or OH-reaction [*Bierbach et al.* 1994].

Further, the glyoxal to methylglyoxal yield-ratios from toluene typically range between 1 and 1.4 [Dumdei *et al.* 1988; Smith *et al.* 1998; Becker *et al.* 1997]. On the basis of the glyoxal yields from this work the α -dicarbonyls and their respective co-products hence account for roughly 65% of the primary products from toluene. If further the sum of ring-retaining products is considered, about 90% of the primary products formed from toluene are accounted for. Further primary products may be hexadienedial-type compounds **11a,11b**. However, the low upper-limit-value determined for the formation of hexadienedials from benzene (see Section 5.5.2) may be taken as an indication that also the methylated derivatives, if formed from toluene, are most likely minor pathways. Moreover, these compounds, though highly reactive, do not react fast enough (see Table 5.7) to explain the observed fast formaldehyde formation from toluene. Hence hexadienedials can be ruled out to contribute substantial amounts of formaldehyde here. Finally, the epoxide-type compounds **14,15** may contribute some formaldehyde. However, based on the above estimate these compounds most likely constitute minor pathways in the oxidation of toluene ($\leq 10\%$). Little is known about the atmospheric chemistry of the epoxides, i.e. whether they react fast enough in order to contribute significantly to the observed fast formaldehyde formation. Hence, 4-oxo-pentenal **13** seems to be the only presently identified formaldehyde precursor in the oxidation of toluene which, as was demonstrated, would in principle further allow to understand the observed rapid formation of formaldehyde. However, additional formaldehyde was observed in the later phase of the toluene-oxidation (see Section 4.7), indicating that further intermediate species form formaldehyde with some delay.

Despite the uncertainties related to the atmospheric chemistry of the γ -dicarbonyls and epoxide-compounds, the effective and fast formaldehyde formation from toluene in principle could be understood from the formation of 4-oxo-pentenal as coproduct of glyoxal. However, the fate of the bicycloalkyl-radical is presently not well understood and may result into the formation of further glyoxal co-products. The observation of 5-methyl-3(2H)-2-furanone as a primary product [Smith *et al.* 1998] seems to support this hypothesis. Given that formation of this compound from the bicycloalkyl-radical requires intramolecular rearrangement it is likely that further C_4 - or C_5 -type hydrocarbons may form, which according to their molecular structure were not immediately obvious to form as coproducts of glyoxal (e.g. further long-chain α -dicarbonyls, furan-type compounds, furandiones etc.).

The formaldehyde data suggests two criteria for the intermediate compounds that actually form from the toluene + OH reaction: (1) short-lived (lifetime of the order of 10 minutes) and (2) efficient formation of methyl-radicals upon further degradation. In order to elucidate the fate of the bicycloalkyl-radical the simultaneous and direct determination of the yields of α - and γ -dicarbonyls under consideration of their highly effective photolytic sink (ideally in the dark) is desirable.

5.7 Secondary Organic Aerosol formation

The results of the qualitative aerosol measurements in the photo-oxidation experiments of different aromatics (see Section 4.8 for results on pXYL) indicate that the formation of Secondary Organic Aerosol (SOA) started at a time when NO was largely converted into NO₂, and NO-levels were too low to suppress the formation of ozone effectively. Ozone is generally assumed to play an important role in SOA formation [Odum *et al.* 1997] and the role of NO₃ radicals has so far been fairly neglected. However, as was seen in Figure 4.20b NO₃-radicals form simultaneously with ozone.

The results obtained from the NO₃-radical balance in the example-experiment PX10 (see Section 4.8.1) indicate that considerable levels of NO₃-radicals are present at the time SOA formation is observed. The overall time-integrated amount of NO₃-radicals that are formed and react is as high as 88 ppb. The known NO₃-radical sinks due to reaction with NO and photolysis (together ≈ 20 %) and reaction with 2,5-DMP (≈ 26 %) thereby only account for less than half of the NO₃-reactions. Although the influence of sunlight on SOA formation from the reaction of NO₃-radicals with 2,5-DMP was not yet investigated, the absence of any particle formation in the dark (under the conditions specified in Section 4.8) indicates that this reaction is unlikely to be directly responsible for the observed SOA formation from p-xylene. The major fraction of 53 % (47 ppb) of the overall formed NO₃-radicals was lost through presently un-identified sink-reactions. Because, the reaction with NO₂, if important at all, is a minor pathway for the NO₃-radicals (< 14 %, see Section 4.8) it is likely that the predominant fraction of 39 % to 53 % (≈ 34 ppb to 47 ppb) of all formed NO₃-radicals are lost via the reaction with presently unknown hydrocarbons, most likely in majority unsaturated oxidation products from p-xylene.

In order to distinguish between the role of ozone and NO₃-radicals in the conversion of NO_x into NOS (not-observed species containing oxidized nitrogen, gas-phase or heterogeneous phase), in Figure 4.20b (see Section 4.8) the calculated concentration-time-profile of the NO₃-radicals was drawn as an indicator for the simultaneous presence of ozone and NO₂. Also included was the N₂O₅-profile as an indicator for the simultaneous presence of NO₂- and NO₃-radicals. The latter profile is observed to exactly match the prominent decrease in ONC (ONC: Sum of NO, NO₂, NO₃, HNO₃ and PAN-type compounds, see Section 4.8.2). The maximum N₂O₅ concentration thereby is observed at the time of maximum variability in ONC (11:45 GMT). This

is taken as an indication that NO_3 -radicals rather than ozone are involved into the conversion of ONC into NOS. This conclusion is further supported from the fact, that about 70 % of the overall variability of ONC took place within the about 40 minutes of reaction-time when maximum concentrations of NO_3 -radicals were observed. The amount of NO_x (mostly NO_2) that was converted into NOS during this time-span corresponds to 100 ppb. If the loss of ONC that was already observed during the first period (in part due to the formation of nitrophenols and organic nitrates; nitroalkylbenzene-formation will be negligible under the experimental conditions of this work, see Section 5.4.2) is interpolated, this amount corresponds to a net-loss of 80 ppb of ONC due to reactions only occurring during period 2.

Possible NO_3 -radical reactions that result into the formation of NOS are: (1) reaction with phenol-type products to form nitro-phenols [Atkinson 1994] (2) reaction with NO_2 to form N_2O_5 and heterogeneous N_2O_5 -removal on organic aerosol surfaces (proposed in this work). As a further reaction (3) the NO_3 -reaction with presently unknown unsaturated products from p-xylene (identified in Section 4.8) under conditions of high NO_2 may lead to the formation of small amounts of dinitrates [Finlayson-Pitts and Pitts, Jr. 2000]. With respect to the OH- and NO_3 -reaction of 2,5-DMP at present the nitro-phenol yields are unknown. However, in Figure 4.20a the degradation pathways of 2,5-DMP were demonstrated to undergo a change from conditions where all 2,5-DMP reacts with OH-radicals to conditions where NO_3 -reactions form the predominant loss-process for 2,5-DMP. It is noteworthy that the time-integrated amounts of 2,5-DMP that were lost via reaction with OH-radicals ($\approx 66\%$) and NO_3 -radicals ($\approx 33\%$) in principle reflect the approximate relative importance of OH- and NO_3 -loss-reactions for this compound in the daytime atmosphere (OH-loss: NO_3 -loss $\approx 80:20$ [Volkamer et al. 1998]), although the changing experimental conditions are not representative for the atmosphere. In fact, during the later phase of the experiment, NO_3 -reactions substitute OH-radicals with respect to the atmospherically relevant branching-ratio of 2,5-DMP loss-processes. Similarly, the degradation pathways of the presently unknown species that were identified to react with NO_3 -radicals are likely to be influenced from the changing experimental conditions over the course of such a photooxidation-experiment. It is interesting to note, that the moment of SOA formation thereby coincides with the time when NO_3 -reactions begin to dominate the sink-reactions of 2,5-DMP.

Given the fact, that the NO_3 -reaction of phenol and the cresol-isomers show considerably higher nitrophenol yields [Atkinson 1994] than the OH-reaction [Atkinson 1994; Oliaru et al. 2000] the NO_3 -reaction may contribute considerable amounts of NOS

(between 5 ppb and 17 ppb, depending on the nitro-phenol yield). The observation of nitrophenols in the particle phase [Forstner *et al.* 1997] confirms that NO_x -losses and SOA are actually inter-linked. If further the heterogeneous reaction of N_2O_5 on organic aerosol surfaces effectively removes N_2O_5 from the gas-phase (two ONC -molecules were lost per N_2O_5 molecule) this reaction in principle could contribute up to 30% (26 ppb) of the NOS formed from NO_3 -reactions during period 2. Neglecting any contribution from process (3) the NO_3 -reactions of type (1) and (2) in sum could in principle explain about half of the NOS formed from NO_3 -radical initiated reactions during period 2. The relation of the observed NO_x -losses to SOA is further supported from the high amounts of different NOS that were observed in the particle phase [Grosjean 1984; Forstner *et al.* 1997; Lee *et al.* 2001].

The initial steps that lead to the formation of SOA are unclear at present. Given the considerable amounts of unaccounted NO_3 -reactions (47 ppb) in the example-experiment NO_3 -reactions may in principle be involved in the initial processes that lead to the formation of SOA from aromatic hydrocarbons (either directly or via further reactions of NO_3 -reaction products). For example, in the NO_3 -radical initiated oxidation of biogenic hydrocarbons, SOA formation has been observed already at a much lower product concentration, i.e. few ppb for β -pinene [Hjorth *et al.* 1999]. However, it is evident that the source-strength for the formation of NO_3 -radicals in smog-chamber experiments that are typically carried out in the presence of several hundred ppbs of NO_x and ozone [Odum *et al.* 1997; Forstner *et al.* 1997] is increased by rather two-to-three orders of magnitude as compared to the conditions that prevail in urban air. It is concluded that the chemistry of NO_3 -radicals needs to be considered if smog-chamber data on SOA formation obtained under elevated concentrations of NO_x is extrapolated to atmospheric conditions. Given the fact that the reaction of NO_3 -radicals with phenols is operative in significant amounts also during daytime [Volkamer *et al.* 1998; Kurtenbach *et al.* 2001], the involvement of NO_3 -radical reactions in SOA formation in the atmosphere can not be ruled out.

Chapter 6

Summary and conclusions

The overall objective of this work was to obtain a better understanding of the OH-radical initiated oxidation mechanism of benzene, toluene, p-xylene (in sum referred to as BTX) and 1,3,5-trimethylbenzene (TMB). The results of this work can be divided in three major parts: (1) the investigation of the ring-retaining pathways from benzene, p-xylene and TMB (investigated products: aldehyde- and phenol-type compounds), (2) the ring-cleavage pathways from BTX (investigated products: glyoxal as well as formaldehyde from toluene) and (3) the formation of secondary organic aerosol (SOA).

Within the first part of this work, the formation of ring-retaining products from the OH-reaction of benzene (phenol: PHEN), p-xylene (p-tolualdehyde: pTALD; 2,5-dimethylphenol: DMP) and TMB (3,5-dimethylbenzaldehyde: DMBA; 2,4,6-trimethylphenol: TMP) was investigated. In a first step missing rate-constant data (k -values) for the OH-reaction of pTALD, DMBA and TMP were determined. In addition, the k_{OH} of benzaldehyde (BALD), PHEN and DMP were re-determined in order to validate the method. Deposition of such polar compounds to the FEP-foil (chamber walls) was found responsible for significant scatter among rate-constants determined from individual experiments (up to 25 %). The wall-loss of all the investigated compounds was characterized and taken into account resulting in a significantly reduced scatter for individual experiments (generally between 4 % to 7 %). The rate-constants of the latter set of compounds were found to be in excellent agreement with the presently recommended literature values. In the case of DMP the experimental error of k_{OH} could be considerably reduced as compared to the literature value. Further, the NO_3 -rate-constant k_{NO_3} of DMP was determined for the first time and that of p-cresol (pCRE) was re-determined in order to validate

the method. It was found to be in excellent agreement with recommended literature values. In addition, first estimates of the photolysis-frequencies of BALD, m-tolualdehyde (mTALD) and o-tolualdehyde (oTALD) were determined and upper-limit values for pTALD and DMBA could be obtained.

The kinetic data was employed to determine the product yield of the ring-retaining products from benzene ($\Phi_{PHEN} = (53.0 \pm 6.6) \%$) and p-xylene ($\Phi_{pTALD} = (8.2 \pm 2.3) \%$, $\Phi_{DMP} = (11.6 \pm 2.8) \%$). The data presented by *Ücker* [1999] was re-evaluated to obtain the ring-retaining yields from TMB ($\Phi_{DMBA} = (2.7 \pm 0.4) \%$, $\Phi_{TMP} = (6.7 \pm 1.0) \%$). In combination with the recent results from the toluene and the TMB system [*Smith et al.* 1998; *Klotz et al.* 1998; *Smith et al.* 1999] a dependence of the ring-retaining product yields (Φ_{RR} : sum of aldehyde- and phenol-yields) on the alkyl-substitution of the parent aromatic became visible: the yield was highest for benzene $\Phi_{RR} = 53 \%$ (only phenol is formed) and was found lower for toluene $\Phi_{RR} \approx 24 \%$ and p-xylene $\Phi_{RR} \approx 20 \%$ to be lowest for TMB $\Phi_{RR} \approx 7 \%$. Both, the phenol-type yields and Φ_{RR} decreased when the number of alkyl-groups substituted on the aromatic ring increased. This systematic dependence reflects the influence of the alkyl-groups on the aromatic ring as it is already visible in the overall OH-rate-constants (see Table 3.2). The more reactive among the investigated aromatic compounds were identified to more efficiently break the ring.

In the following, the reaction mechanism of the ring-retaining products was investigated. Within the time-resolution of our measurements all the investigated ring-retaining products were identified as primary products. The formation mechanism of phenol (intermediate **4** in Figure 2.1) was identified to proceed directly from the reaction of the aromatic-OH adduct (aro-OH) with oxygen (see pathway (3) in Figure 2.1). This pathway accounts for $(80 \pm 25) \%$ of the overall phenol formation from benzene. Additional phenol from the decomposition of the peroxy-radical (aro-OH-O₂) remains possible though it will be only a minor pathway. There was no evidence for the involvement of benzeneoxide/oxepin in the phenol-formation from benzene. The conclusion on the direct phenol-forming channel (3) is further supported by the results obtained for the 2,5-DMP formation from p-xylene.

The Φ_{PHEN} from benzene was determined to be more than twice as high as available literature values. While the yield was found to decrease at high NO_x-concentrations,

the high phenol yield from benzene was found to be representative for most conditions of the urban atmosphere. The decreasing phenol yields at higher NO_x -concentrations, as they are typical for most smog chamber studies, indicate a change in the oxidation mechanism of benzene. Based on the experimental data from this and other studies [Knispel *et al.* 1990; Bohn and Zetzsch 1999] the observed NO_x -dependence of the phenol yield was adequately reproduced from elementary kinetic parameters up to about 2 ppm of NO_x . The phenol yield from Atkinson *et al.* [1989], which is about a factor of two lower, was understood from Equation 4.2. The difference was identified to be due to the reactions of aro-OH with NO_2 and aro-OH- O_2 with NO that are essentially unimportant in this study as in the atmosphere. The results from the p-xylene system gave evidence that the NO_x -influence was reduced for this compound as compared to benzene. However, the comparison of the results of this study with available literature values, including toluene and TMB (see Table 5.5 and Table 5.6) confirmed the influence of reactions involving NO_x for all the investigated aromatic compounds (BTX and TMB). For the high- NO_x -range, available literature values on the phenol yields from BTX were used to estimate the phenol yields from the reaction of aro-OH with NO_2 ($\Phi_{phenol,10}$). Considerably higher values of $\Phi_{phenol,10}$ were derived for the alkyl-substituted aromatic compounds as compared to benzene. It is concluded that under conditions of high NO_x (several ppm) quite different chemical mechanisms are operative.

In the second part of this work, the yields of glyoxal (GLY, intermediate **10a** in Figure 5.3) were determined from benzene ($\Phi_{GLY} = (35.9 \pm 9.6)\%$), toluene ($\Phi_{GLY} = (34.4 \pm 11.5)\%$) and p-xylene ($\Phi_{GLY} = (35.8 \pm 8.1)\%$). Moreover, glyoxal was identified a primary product from the oxidation of BTX indicating that ring-cleavage pathways involving the bicycloalkyl-radical (intermediate **7** in Figure 2.2) are major operative pathways in the OH-initiated oxidation of aromatic compounds.

Further, formaldehyde (HCHO) was identified to form rapidly as a high-yield secondary-product from toluene ($\Phi_{HCHO} = 37.2\%$). The yield of formaldehyde is compatible with 4-oxo-pentenal (intermediate **13** in Figure 5.3), the respective unsaturated 1,4-dicarbonyl-type co-product of glyoxal, being a high yield primary product from toluene. These results give evidence that α -dicarbonyls (i.e. glyoxal and methylglyoxal: MGLY) and unsaturated 1,4-dicarbonyls are formed from the further reaction of the bicycloalkyl-radical. Based on typical ratios of Φ_{GLY}/Φ_{MGLY} (≈ 1.2) the branching ratio for the bicycloalkyl-radical pathway was estimated 65 %

from toluene. Including further the ring-retaining pathways (see above) about 90 % of the primary reaction pathways from toluene were accounted for.

Systematic differences in the glyoxal yields were observed for BTX when the yields from this work were compared to literature values. In analogy to the results obtained for the phenol-type products (see above) these differences could be attributed to influencing NO_x -reactions which lower the yields of glyoxal from BTX. The glyoxal yields determined in this study were found to be constant over the range of NO_x -concentrations employed for p-xylene (≤ 1.1 ppm) and are representative for the atmosphere for BTX.

The glyoxal formation from BTX under the experimental conditions of this study was essentially understood in terms of glyoxal which is formed as a primary product (primary glyoxal). The negligible contribution of pathways forming glyoxal through the OH-reaction of stable intermediate compounds (secondary glyoxal) was found to be consistent with the dominant photolysis of potential precursors for secondary glyoxal, i.e. the unsaturated 1,4-dicarbonyl-type products. It further indicates that - under the experimental conditions employed in this work - hexadienedial-type compounds (HDD) are minor products from benzene ($\Phi_{HDD} < 8\%$). The secondary formation of glyoxal may nevertheless become important under different experimental conditions. Despite the fact that the atmospheric chemistry of 1,4-dicarbonyls is widely unknown at present, the fast and effective formation of formaldehyde observed from toluene is in line with the results presented by *Bierbach et al.* [1994] according to which the degradation of 4-oxo-pentenal forms radical-type products. The importance of these radical forming pathways is very likely to have important consequences for the photooxidant formation from aromatic compounds.

In the third part of this work, substantial evidence was found that NO_3 -radicals play an important role in the oxidation of aromatic compounds under simulated atmospheric conditions. It was demonstrated that under conditions of elevated NO_x -concentrations (several 100 ppb), as they are typically applied in smog-chamber studies [*Odum et al.* 1997; *Forstner et al.* 1997], NO_3 -chemistry is closely correlated with the observed NO_x -losses in p-xylene/ NO_x /Air irradiations. However, it is evident that the NO_3 -source-strength in photosmog experiments in the presence of several hundred ppbs of NO_x and ozone [*Grosjean* 1984; *Odum et al.* 1997; *Forstner et al.* 1997] exceeds the NO_3 -source-strength of the daytime atmosphere

by two-to-three orders of magnitude. In addition, the relative importance of NO_3 -radical reactions is variable in a way as it is not representative for the atmosphere. NO_3 -radicals were demonstrated to be involved in the conversion of NO_x into oxidized nitrogen compounds (ONC). The observation of ONC in the particle phase [Grosjean 1984; Forstner *et al.* 1997] further indicates that an overall loss of NO_x into the particles occurs. No definite statement on the involvement of NO_3 -radicals in the processes that initiate secondary organic aerosol (SOA) formation can yet be given. However, the fact that the moment of SOA formation is delayed and coincides with the moment when NO_3 -reactions become competitive with OH-reactions as a sink for 2,5-DMP may be taken as an indication for such an involvement. It was concluded that if the role of NO_3 -radicals in SOA formation is not understood, the extrapolation of the results obtained from smog-chamber data to atmospheric conditions remains speculative.

It was demonstrated that the formation of phenol-type compounds from BTX under conditions of high NO_x (ppm-range) proceeds through quite different mechanisms as under typical NO_x -concentrations that prevail in the atmosphere. Similarly, the glyoxal yields and possibly also SOA formation are influenced under conditions of high NO_x (and ozone) as they are typical for most smog-chamber studies. The following question arises: how representative are the degradation schemes of aromatic compounds developed to fit the smog-chamber data obtained at high NO_x -concentrations in order to describe the atmospheric chemistry of these compounds in the urban atmosphere?

Outlook

During the last few years, the understanding of aromatic oxidation has improved principally from the joint approach of experimental and theoretical studies on aromatic compounds. The future experimental work should be aimed at elucidating the phenol forming chemical mechanisms under elevated concentrations of NO_x as well as under NO_x -free conditions. Similarly, a NO_x dependent study of the glyoxal yields is required. The atmospheric degradation of aromatic aldehydes requires further investigation. In addition, temperature and oxygen concentration dependent studies over a wider range of experimental conditions would be desirable. Moreover, the experimental error of the glyoxal yields determined in this study is dominated by the uncertainty of the UV-absorption cross-section of glyoxal. An improved determination of the absolute cross-section is needed. Finally, the role of NO_3 -radicals in the observed NO_x -losses and SOA formation in the degradation of aromatic compounds needs further investigation.

From the data presented in this work, the atmospheric chemistry of unsaturated 1,4-dicarbonyls and possibly also the epoxide-type compounds is likely to have a significant impact on the radical regeneration from the oxidation of aromatic compounds. The chemistry of these compounds is incompletely understood at present and requires further investigation.

Chapter 7

Atmospheric Implications

The results on the oxidation mechanism of the OH-reaction of BTX and TMB, as summarized in the previous chapter, have direct implications on the formation and degradation of airborne toxics (i.e. phenol- and dicarbonyl-type compounds) as well as the expected photooxidant formation from aromatics.

With respect to the formation of toxic phenol-type compounds, the yields determined within this study are representative for the atmosphere. For example, the phenol yield from benzene obtained for NO_x -concentrations of several 10 ppb is essentially constant. Hence, the value of $\Phi_{PHEN} = (53.0 \pm 6.6) \%$ should be representative for the boundary layer, including most conditions of the urban atmosphere. Under conditions with exceptionally high NO_x -concentrations, i.e. near the exhaust tubes of cars or near traffic tunnels, Φ_{PHEN} may be lower. Benzene was demonstrated to be the most sensitive aromatic compound among the BTX species. The phenol-type yields from toluene and p-xylene will be essentially uninfluenced from NO_x -reactions in the urban atmosphere.

The observed direct formation mechanism of phenol-type compounds implies that BTX species will photochemically form phenolic compounds already in the urban atmosphere. This is especially important for the alkyl-substituted aromatic compounds which, despite the lower phenol-yields, are considerably more reactive than benzene. Their atmospheric lifetime is comparably short (TMB: 1 hour; xylenes: 4 hours, see Table 3.2) and hence these compounds will already form considerable amounts of phenol close to their source of emission i.e. < 50 km distance from the source. Despite the relatively low reactivity of benzene as compared to the alkyl-substituted aromatics, the high Φ_{PHEN} indicates that considerable amounts of phenol will also be formed from benzene, though on a differ-

ent timescale (atmospheric lifetime of benzene: ≈ 2 d to several weeks). Assuming a typical relative concentration among the BTX aromatics in urban air (benzene:toluene:xylenes = 0.4:1:0.6, see e.g. [Ackermann 2000]; all xylenes assumed to form phenol-type compounds with Φ_{DMP} from p-xylene), the phenol production-rate ($k_{OH} \cdot \Phi_{(phenol-type)} \cdot [Aromatic] \cdot [OH]$) will be highest from xylenes (see also [Volkamer et al. 1998]). In industrial air masses, where TMB concentrations may be considerably higher, phenol-production from TMB may even exceed that of the xylenes.

The further fate of the phenol-type compounds will be the reaction with OH- and NO₃-radicals. Based on typical daytime concentrations of OH-radicals (0.2 ppt) and NO₃-radicals (0.1 ppt) about 10% to 20% of the total radical induced daytime phenol loss is due to NO₃-reactions [Volkamer et al. 1998; Kurtenbach et al. 2001]. Recent experimental evidence for a missing phenol-sink in urban air was derived from field measurements by Ackermann [2000] who concluded that the daytime concentration of NO₃-radicals in the urban environment may actually be higher than in the above estimate (≈ 0.5 ppt). Under these conditions, the daytime NO₃-reaction becomes a competitive daytime phenol-sink, and in fact dominates over the OH-loss for the cresol-isomers and 2,5-DMP. The atmospheric implications of the NO₃-reaction of phenols are twofold. First, the reaction forms HNO₃ and hence contributes to the acidification of the atmosphere. Second, the NO₃-reaction leads to the formation of nitro-phenol-type compounds in much higher yields as the reaction with OH-radicals [Atkinson 1994; Oliaru et al. 2000]. The formation of phenol-type compounds in the urban environment (see above) is hence of relevance for the formation of nitro-phenol-type compounds, which are phytotoxic and have been observed in the gas- and particulate-phase, as well as in fogwater, rainwater, snow and in clouds [Kelly et al. 1994; Forstner et al. 1997; Barletta et al. 2000] (and references therein).

Of further relevance for the formation of airborne hazards in the urban environment is the identification of a fast ring-cleavage mechanism as a major pathway from BTX. The products formed from ring-cleavage are typically attributed the mutagenic effects of aromatic hydrocarbon photooxidation products [Shepson et al. 1985; Dumdei et al. 1988; Eder et al. 1994]. Since further the more reactive among the investigated aromatic compounds tend to form higher yields of ring-cleavage products, considerable amounts of ring-cleavage products will already be formed close to their source of emission.

The impact on photooxidant formation in the troposphere requires a detailed analysis based on chemical modeling [Atkinson *et al.* 1980; Jenkin *et al.* 2000]. However, the recent model results on the TMB [Jenkin *et al.* 2000] were used here in order to illustrate the relevance of the results of this study for photooxidant formation in the atmosphere. Jenkin *et al.* [2000] determined the photochemical ozone creation potentials (POCP; a concept used to rank the VOCs relative to ethene by their ability to form ozone; $\text{POCP}_{\text{ethene}} = 100$) of the five pathways starting from comparable intermediates as **3-8** in Figure 2.2. The bicycloalkyl-radical pathway was ascribed by far the highest POCP value ($\text{POCP} = 111$).

The identification of this pathway as a major pathway for the oxidation of BTX, can explain significant amounts of photooxidants as they have been predicted to form from aromatic hydrocarbons [Derwent *et al.* 1996]. Moreover, the POCP values were found to be sensitively coupled to the kinetic parameters used for the photolysis-reactions of e.g. α -dicarbonyls [Jenkin *et al.* 2000]. Apart the identification of high yields of α -dicarbonyls the importance of further photolysis reactions (of unsaturated 1,4-dicarbonyls) becomes obvious in this study. The presently used photolysis-frequencies of compounds like butenedial and 4-oxopentenal are underestimated by more than two orders of magnitude and need to be updated. Since the photolytic pathways are likely to represent significant radical-sources (see Chapter 6) this update most likely will lead to a substantial increase of the as-yet high POCP-values assigned to the bicycloalkyl-radical pathway in the future.

On the other hand, the ring-retaining pathways were ascribed low POCP values ($\text{POCP}_{\text{TMP}} = 15$). In consequence, the higher alkyl-substituted aromatic compounds will form photooxidants much more efficient than benzene (per reacted amount of aromatic compound). This is particularly true because the alkylbenzenes are chemically transformed widely in air masses where sufficient NO_x is available to promote the photochemical formation of ozone. This may not necessarily be the case for benzene which given its much longer residence time in the atmosphere is sufficiently long-lived as to be transported into remote regions where not enough NO_x may still be available to promote the formation of ozone (i.e. NO_x -limited air-masses).

A fundamental aspect of the results' relevance in the atmosphere is linked to the fact that chemical mechanisms in the past have been developed from high- NO_x smog

chamber data. It was demonstrated in Chapter 5 that the distribution among the oxidation products changes as levels of NO_x increase. At high NO_x -concentrations (several ppm) the product spectrum is essentially changed and no longer relevant for the atmosphere. In especially the alkylbenzenes tend to form higher yields of phenol-type and further ring-retaining products (e.g. nitrophenols and possibly also nitroalkylbenzenes [Atkinson and Aschmann 1994]). These ring-retaining products are much longer lived and less effective to regenerate radicals than the dicarbonyl-type products of ring-cleavage (atmospheric lifetimes are increased by up to two orders of magnitude). Further, under conditions when reactions involving NO_x are in competition with oxygen in the early stages of oxidation, the yields of primary ring-cleavage products (i.e. primary glyoxal) were demonstrated to decrease, thus reducing an efficient radical source (from the consecutive degradation of ring-cleavage products) and thus lowering the formation of photooxidants. Consequently, smog-chamber experiments which in the past were conducted at high- NO_x concentrations are very likely to have resulted into a reduced photooxidant formation - which transferred into the predictions made from chemical mechanisms developed from such data. Unless the elementary reactions steps are known and are treated explicitly by the model code, the in principle possible extrapolation to atmospheric conditions remains questionable. Deviations in the oxidation routes at an early stage together with limitations in our understanding of aromatic oxidation and the need for "adjusted oxidation schemes" due to limited resources in computational-power are very likely to have resulted in a systematic underestimation of the photooxidant formation from e.g. the alkylbenzenes in the past.

The contribution of aromatic hydrocarbons to the overall photooxidant formation from non-methane hydrocarbons emitted into the urban atmosphere is presently estimated $\approx 40\%$ [Derwent *et al.* 1996]. From the results of this work this portion seems to be a lower limit estimate of the role that aromatic compounds play in the formation of photooxidants today.

Glossary

Φ	molar branching-ratio (yield); units: % (mol./mol.)
Aromatic	molecule containing the base-structure of benzene (BEN)
BALD	benzaldehyde (C ₇ H ₆ O); CHO-substituted benzene
BEN	benzene (C ₆ H ₆); hexagonal planar-ring-molecule, simplest aromatic
BTX	generally referred to as the sum of BEN, TOL and XYL in this work also referred to as the sum of BEN, TOL and pXYL
BUDIAL	butenedial (C ₄ H ₄ O ₂); unsaturated 1,4-dicarbonyl, different stereo-isomers
BUGH	Bergische Universität und Gesamthochschule, Wuppertal/Germany
CEAM	Centro de Estudios Ambientales del Mediterraneo, Paterna/Spain
CRE	cresol (C ₇ H ₈ O); oCRE: ortho-cresol (2-methyl-phenol), mCRE: meta-cresol (3-methyl-phenol), pCRE: para-cresol (4-methyl-phenol)
DMBA	dimethylbenzaldehyde (C ₉ H ₁₀ O); different isomers
DMP	dimethylphenol (C ₈ H ₁₀ O); different isomers
DOAS	Differential Optical Absorption Spectroscopy
EUPHORE	European Photo Reactor located at CEAM-Institute
FEP	fluorine-ethene-propene
FTIR	Fourier Transform InfraRed Spectroscopy
FWHM	Full Width at Half Maximum
GLY	glyoxal (C ₂ H ₂ O ₂); 1,2-dicarbonyl-type compound
GMT	Greenwich Mean Time
HCHO	formaldehyde (CH ₂ O)
HDD	hexadienedial (C ₆ H ₆ O ₂); unsaturated 1,6-dicarbonyl, different stereo-isomers
IUP	Institut für Umweltphysik, University of Heidelberg/Germany
MGLY	methylglyoxal (C ₃ H ₄ O ₂); 1,2-dicarbonyl-type compound
NIES	National Institute for Environmental Studies, Tsukuba/Japan
NMHC	Non Methane HydroCarbons
NOS	reactive N-compounds that were not considered in this study (NO _y - ONC)
NO _x	sum of NO and NO ₂
NO _y	sum of NO _x , PAN, HNO ₃ , NO ₃ ⁻ (Particles), 2 N ₂ O ₅ , reactive N-compounds
ONC	Oxidized Nitrogen Compounds, defined as the sum of the considered reactive N-compounds: NO, NO ₂ , NO ₃ , HNO ₃ , 2 N ₂ O ₅ , PAN-type comp.
OPEAL	4-oxo-pentenal (C ₅ H ₆ O ₂); unsaturated 1,4-dicarbonyl, different stereo-isomers
PAN	Peroxy-Acetyl-Nitrate (C ₂ H ₃ NO ₅); structure: CH ₃ C(O)OONO ₂
PAN-type	PAN and other molecules with structural similarity: RC(O)OONO ₂
PGLY	glyoxal which is formed as a primary product
PHEN	phenol (C ₆ H ₆ O); OH-substituted benzene
SOA	Secondary Organic Aerosol
SZA	Solar Zenith Angle
TALD	tolualdehyde (C ₈ H ₈ O, methyl-BALD): oTALD, mTALD, pTALD (see CRE)
TMB	trimethylbenzene (C ₉ H ₁₂); different isomers
TMP	trimethylphenol (C ₉ H ₁₂ O); different isomers
TOL	toluene (C ₇ H ₈); CH ₃ -substituted benzene
VOC	Volatile Organic Compounds
XYL	xylene (C ₈ H ₁₀ , dimethylbenzene): oXYL, mXYL, pXYL (see CRE)

References

- Ackermann, R. (2000). *Auswirkungen von Kraftfahrzeugemissionen in der urbanen Atmosphäre*. Dissertation, Institute for environmental physics, University of Heidelberg. 1, 3.2, 3.2.3, 7
- Ackermann, R., K. H. Becker, A. Geyer, J. A. G. Gomes, R. Kurtenbach, C. Lörzer, and U. Platt (2000). Chemical Behaviour of Aromatic Hydrocarbons in the Troposphere. In K. H. Becker (Ed.), *Chemical Behaviour of Aromatic Hydrocarbons in the Troposphere*, pp. 125–130. Fachbereich 9, BUGH Wuppertal: http://www.physchem.uni-wuppertal.de/PC-WWW_Site/workshops.html. 4.4, 5.3.4
- Albritton, D. L., A. L. Schmeltekopf, and R. N. Zare (1976). An Introduction to the Least-Squares Fitting of Spectroscopic Data. In R. K. Narahari and M. W. Weldon (Eds.), *Molecular Spectroscopy: Modern Research*. Orlando, Florida, USA: Academic Press. 3.2.2
- Alicke, B. (2000). *The Role of Nitrous Acid in the Boundary layer*. Dissertation, Institute for environmental physics, University of Heidelberg. 3.2.3
- Alicke, B., K. Hebestreit, J. Stutz, and U. Platt (1999). Iodine Oxide in the Marine Boundary Layer. *Nature*, Vol. 397, 572–573. 3.2
- Altshuller, A. O. P., I. R. Cohen, S. F. Sleva, and S. L. Kopczynski (1962). Air Pollution: Photooxidation of Aromatic Hydrocarbons. *Science*, Vol. 138, 442–443. 1
- Andino, J. M., J. N. Smith, R. C. Glagan, I. W. A. Goddard, and J. H. Seinfeld (1996). Mechanism of Atmospheric Photooxidation of Aromatics: A Theoretical Study. *J. Phys. Chem.*, Vol. 100, 10967–10980. 5.6, 5.4.2, 5.5.1
- Atkinson, R. (1986). Kinetics and Mechanisms of the Gas-Phase Reactions of the Hydroxyl Radical with Organic Compounds under Atmospheric Conditions. *Chem. Rev.*, Vol. 86, 69–201. 3.5.3
- Atkinson, R. (1994). Gas-Phase Tropospheric Chemistry of Organic Compounds. *J. Phys. Chem. Ref. Data*, Vol. Monograph No. 2, 1–216. 1, 2.2, 3.2, 4.2.2, 4.2, 4.3, 4.2.3, 4.3.6, 5.3, 5.7, 7
- Atkinson, R. (2000). Atmospheric Chemistry of VOCs and NO_x. *Atmos. Environ.*, Vol. 34, 2063–2101. 2.2
- Atkinson, R. and S. M. Aschmann (1990). Kinetics of the Gas-Phase Reactions of OH Radicals with Cresols and Dimethylphenols at 296 ± 2 K. *Int. J. Chem. Kinet.*, Vol. 22, 59–67. 5.2.1, 5.3
- Atkinson, R. and S. M. Aschmann (1994). Products of the Gas-Phase Reactions of Aromatic Hydrocarbons: Effect of NO₂ Concentration. *Int. J. Chem. Kinet.*, Vol.

- 26, 929–944. 5.4.2, 5.6, 5.4.2, 5.4.3, 7
- Atkinson, R., S. M. Aschmann, and J. Arey (1991). Formation of Ring-Retaining Products from the OH Radical-Initiated Reactions of o-, m- and p-Xylene. *Int. J. Chem. Kinet.*, Vol. 23, 77–97. 5.4.1, 5.5, 5.4.2, 5.4.2
- Atkinson, R., S. M. Aschmann, and J. Arey (1992). Reaction of OH and NO₃ Radicals with Phenol, Cresols, and 2-Nitrophenol at 296 ± 2 K. *Environ. Sci. Technol.*, Vol. 26, 1397–1403. 4.2.3, 5.3, 5.2.1
- Atkinson, R., S. M. Aschmann, J. Arey, and W. P. L. Carter (1989). Formation of Ring-Retaining Products from the OH Radical-Initiated Reactions of Benzene and Toluene. *Int. J. Chem. Kinet.*, Vol. 21, 801–827. 5.4, 5.3.1, 5.3.2, 5.3.2, 5.6, 5.4.2
- Atkinson, R., D. L. Baulch, R. A. Cox, R. F. Hampson, Jr., J. A. Kerr, M. J. Rossi, and J. Troe (1997). Evaluated Kinetic and Photochemical Data for Atmospheric Chemistry: Supplement VI. IUPAC Subcommittee on Gas Kinetic Data Evaluation for Atmospheric Chemistry. *J. Phys. Chem. Ref. Data*, Vol. 26, 521–1011. 5, 3.2
- Atkinson, R., W. P. L. Carter, K. R. Darnall, M. Winer, and J. N. Pitts, Jr. (1980). A Smog Chamber and Modelling Study of the Gas Phase NO_x-Air Photooxidation of Toluene and the Cresols. *Int. J. Chem. Kinet.*, Vol. 12, 779–836. 2.3, 4.6.4, 5.5.1, 7
- Atkinson, R., W. P. L. Carter, C. N. Plumb, A. M. Winer, and J. N. Pitts, Jr. (1984). Kinetics of the Gas-Phase Reactions of NO₃ Radicals with a Series of Aromatics at 296 ± 2 K. *Int. J. Chem. Kinet.*, Vol. 16, 887–898. 4.2.3, 5.3
- Bandow, H. and N. Washida (1985). Ring-Cleavage Reactions of Aromatic Hydrocarbons Studied by FT-IR Spectroscopy. II. Photooxidation of o-, m- and p-Xylenes in the NO_x-Air System. *Bull. Chem. Soc. Jpn.*, Vol. 58, 2541–2548. 1, 5.5, 5.5.1, 5.5.3, 5.8
- Bandow, H., N. Washida, and H. Akimoto (1985). Ring-Cleavage Reactions of Aromatic Hydrocarbons Studied by FT-IR Spectroscopy. I. Photooxidation of Toluene and Benzene in the NO_x-Air System. *Bull. Chem. Soc. Jpn.*, Vol. 58, 2531–2540. 2.2, 5.8, 5.5.3, 5.6.1
- Barletta, B., E. Bolzacchini, S. Meinardi, M. Orlandi, and B. Rindone (2000). The NO₃ Radical-Mediated Liquid Phase Nitration of Phenols with Nitrogen Dioxide. In K. H. Becker (Ed.), *Chemical Behaviour of Aromatic Hydrocarbons in the Troposphere*, pp. 45–50. Fachbereich 9, BUGH Wuppertal: http://www.physchem.uni-wuppertal.de/PC-WWW_Site/workshops.html. 7
- Barnes, I., K. H. Becker, A. Bierbach, and E. Wiesen (1991). Mechanisms of the OH Radical Initiated Oxidation of Aromatics in the Absence of NO_x. In R. A. Cox (Ed.), *Proc. of the Joint LACTOZ-HALIPP Workshop on the "Laboratory Studies on Atmospheric Chemistry" held 23-25 Sept. 1991 in York, England*, pp. 183–189. Brussels, Belgium: Commission of the European Communities. 5.5, 5.8
- Bartolotti, L. J. and E. O. Edney (1995). Density Functional Theory derived Intermediated from the OH initiated Atmospheric Oxidation of Toluene. *Chem. Phys. Lett.*, Vol. 245, 119–122. 2.2, 5.5.1
- Bass, A. M. and R. J. Paur (1985). The Ultraviolet Cross Section of Ozone, I. The Measurements. In Z. C. and A. Ghazy (Eds.), *Proc. of the Quadrennial Ozone*

- Symposium*, Chalkidiki, Greece, pp. 606–616. 3.1
- Becker, K. H. (1996). The European Photoreactor (EUPHORE). In K. H. Becker (Ed.), *Final Report, Contract No. EV5V-CT92-0059*. Brussels: European Commission. 3.1
- Becker, K. H., I. Barnes, A. Bierbach, K. J. Brockmann, F. Kirchner, B. Klotz, H. G. Libuda, A. Mayer-Figge, S. Mönninghoff, L. Ruppert, W. Thomas, E. Wiesen, K. Wirtz, and F. Zabel (1997). OH Initiated Oxidation of VOC under Variable NO_x Conditions. In G. LeBras (Ed.), *Transport and Chemical Transformation of Pollutants in the Troposphere, Volume 3 "Chemical Processes in Atmospheric Oxidation"*, pp. 79–90. Heidelberg, Germany: Springer-Verlag. 5.4.3, 5.5.1, 5.6.1
- Becker, K. H., A. Hofzumahaus, M. Pilling, U. Platt, I. Tanarro, and K. Wirtz (1999). In Situ EUPHORE Radical Measurement (EUPHORAM). In K. H. Becker (Ed.), *Final Report, Contract No. ENV4-CT95-0011*. Brussels, Belgium: European Commission. 3.3, 4.3
- Becker, K. H. and T. Klein (1987). OH-Initiated Oxidation of p-Xylene under Atmospheric Conditions. In G. Angeletti and G. Restelli (Eds.), *Proc. of the 4th European Symposium on the "Physico-Chemical Behaviour of Atmospheric Pollutants" held 23-25 Sept. 1986 in Stresa, Italy*, pp. 320–326. Dordrecht, Holland: D. Reidel Publishing Company. 2.2, 5.5, 5.5.1, 5.8
- Berndt, T. (2000). *personal communication*,. 5.1, 5.1.1
- Berndt, T., O. Böge, and H. Herrmann (1999). On the formation of benzene oxide/oxepin in the gas-phase reaction of OH radicals with benzene. *Chem. Phys. Lett.*, Vol. 314, 435–442. 2.1, 5.1, 5.1.1, 5.3.1, 5.4, 5.4.3
- Besemer, A. C. (1982). Formation of Chemical Compounds from Irradiated Mixtures of Aromatic Hydrocarbons and Nitrogen Oxides. *Atmos. Environ.*, Vol. 16, 1599–1602. 5.5.1
- Bevington, P. R. (1969). *Data Reduction and Error Analysis for the Physical Sciences*. New York: McGraw-Hill. 3.2.2
- Bierbach, A. (1994). *Produktuntersuchungen und Kinetik der OH-initiierten Gasphasenoxidation aromatischer Kohlenwasserstoffe sowie ausgewählter carbonylischer Folgeprodukte*. Dissertation, Fachbereich 9, Naturwissenschaften II, BUGH Wuppertal. 5.2, 5.4.3, 5.5.1
- Bierbach, A., I. Barnes, K. H. Becker, and E. Wiesen (1994). Atmospheric Chemistry of Unsaturated Carbonyls: Butenedial, 4-Oxo-pentenal, 3-Hexene-2,5-dione, Maleic Anhydride, 3H-Furan-2-one and 5-Methyl-3H-furan-2-one. *Environ. Sci. Technol.*, Vol. 28, 715–729. 2.2, 5.5.2, 5.7, 5.6.1, 5.6.1
- Bjergbakke, E., A. Sillesen, and P. Pagsberg (1996). UV Spectrum and Kinetics of Hydroxycyclohexadienyl Radicals. *J. Phys. Chem.*, Vol. 100, 5729–5736. 2.1, 5.1, 5.3.1, 5.4, 5.4.3, 5.5.1
- Blake, D. R., T. W. Smith, T.-Y. Chen, W. J. Whipple, and F. S. Rowland (1994). Effects of Biomass Burning on Summertime Nonmethane Hydrocarbon Concentration in the Canadian Wetlands. *J. Geophys. Res.*, Vol. 99, 1699–1719. 1

- Bohn, B. (2001). Formation of Peroxi Radicals from OH-Toluene Adducts and O₂ - Atmospheric Lifetimes and Secondary Reaction with NO. *J. Phys. Chem. A*, Vol. 105, 6092. 5.6, 5.4.2, 5.5.1
- Bohn, B., M. Elend, and C. Zetzsch (1999). Abbaumechanismen von Aromaten nach Anlagerung von OH und ihr Einfluss auf die Kreisläufe von HO_x unter Bildung von Photooxidantien. In *TFS-final report, TFS-Teilprojekt LT3-D3*. <http://www.gsf.de/PTUKF/tfsmain.html>. 5.4.3
- Bohn, B. and C. Zetzsch (1999). Gas-Phase of the OH-Benzene Adduct with O₂ - Reversibility and Secondary Formation of HO₂. *Phys. Chem. Chem. Phys.*, Vol. 1, 5097–5107. 2.1, 4.3.1, 4.3.2, 4.3.4, 4.3.6, 5.3.1, 5.3.5, 5.4.2, 5.6, 5.4.3, 5.5.1, 6
- Bufalini, J. J. (1989). Identification of Hazardous Products formed During Photochemical Transformatons of Pollutants. In J. J. Bufalini (Ed.), *BATELLE Final Report, NSI P.O. No. 8806RG1852*. 1
- Cantrell, C. A., J. A. Davidson, A. H. McDaniel, R. E. Shetter, and J. G. Calvert (1990). Temperature-Dependent Formaldehyde Cross Sections in the Near-Ultraviolet Spectral Region. *J. Phys. Chem.*, Vol. 94, 3902–3908. 3.1
- Carter, W. P. L. (1995). Computer Modeling of Environmental Chamber Measurements of Maximum Incremental Reactivities of Volatile Organic Compounds. *Atmos. Environ.*, Vol. 29, 2513–2527. 2.3
- Carter, W. P. L., A. Winer, and J. N. Pitts, Jr. (1981). Major Atmospheric Sink for Phenol and the Cresols. Reaction with the Nitrate Radical. *Environ. Sci. Technol.*, Vol. 15, 829–834. 1, 4.2.3, 4.4, 5.3
- Darnall, K. R., R. Atkinson, and J. N. Pitts, Jr. (1979). Observation of Biacetyl from the Reaction of OH Radicals with o-Xylene. Evidence for Ring Cleavage. *J. Phys. Chem.*, Vol. 83, 1943–1946. 2.2, 5.5.1
- DeMore, W. B., S. P. Sander, C. J. Howard, A. R. Ravishankara, D. M. Golden, C. E. Kolb, R. F. Hampson, M. J. Kurylo, and M. J. Molina (1997). Chemical Kinetics and Photochemical Data for Use in Stratospheric Modeling No. 12. *Jet Propulsion Laboratory, Pasadena, Publication 97-4*. 1, 3.2, 4.8.2
- Derwent, D., M. Jenkin, and S. Saunders (1998). Master Chemical Mechanism, version 2.0. <http://www.chem.leeds.ac.uk/Atmospheric/MCM/mcmproj.html>. 3.2
- Derwent, R. G. and M. Jenkin (1991). Hydrocarbons and the Long-Range Transport of Ozone and PAN across Europe. *Atmos. Environ.*, Vol. 25A, 1661–1678. 2.3
- Derwent, R. G., M. E. Jenkin, and S. M. Saunders (1996). Photochemical Ozone Creation Potentials for a Large Number of Reactive Hydrocarbons under European Conditions. *Atmos. Environ.*, Vol. 30, 181–199. 1, 7
- Dobson, G. M. B. and D. N. Harrison (1926). Measurements of the amount of ozone in the Earth's Atmosphere and its Relation to other Geophysical Conditions. *Proc. R. Soc. London*, Vol. 110, 660–693.
- Doyle, G. J., A. C. Lloyd, K. R. Darnall, A. M. Winer, and J. N. Pitts, Jr. (1975). Gas Phase Kinetic Study of Relative Rates of Reaction of Selected Aromatic Compounds with Hydroxyl Radicals in an Environmental Chamber. *Environ. Sci. Technol.*, Vol. 9, 237–241. 1

- Dumdei, B. E., D. V. Kenny, P. B. Shepson, T. E. Kleindienst, C. M. Nero, L. T. Cupit, and L. D. Claxton (1988). MS/MS Analysis of the Products of Toluene Photooxidation and Measurements of Their Mutagenic Activity. *Environ. Sci. Technol.*, Vol. 22, 1493–1498. 5.5.1, 5.8, 5.6.1, 5.6.1, 7
- Dumdei, B. E. and R. J. O'Brien (1984). Toluene Degradation Products in Simulated Atmospheric Conditions. *Nature*, Vol. 311, 248–250. 5.5.1, 5.6.1
- Eder, E., C. Hoffman, C. Deininger, and S. Schenckenbach (1994). Risk Assessment for Mutagenic and Carcinogenic Activities of α,β -Unsaturated Carbonyl Compounds by a Screening Strategy based on Structure-Activity Relationships. *Toxic. in Vitro*, Vol. 8, 707–710. 7
- Etzkorn, T. (1998). *Untersuchungen atmosphärisch relevanter Reaktionssysteme mittels Differentieller Optischer Absorptionsspektroskopie*. Dissertation, Institute for environmental physics, University of Heidelberg. 3.2, 3.2.3, 3.2.3, 3.2.4, 5.5, 5.4.1, 5.4.2
- Etzkorn, T., B. Klotz, S. Sørensen, I. V. Patroescu, I. Barnes, K. H. Becker, and U. Platt (1999). Gas-Phase Absorption Cross Sections of 24 Monocyclic Aromatic Hydrocarbons in the UV and IR Spectral Ranges. *Atmos. Environ.*, Vol. 33, 525–540. 3.2, 3.1, 3.5.2, 4.3.6, 5.1, 5.1.1, 5.1.2
- Etzkorn, T., R. Volkamer, and U. Platt (1996). The DOAS Instrument. In K. H. Becker (Ed.), *The European Photoreactor (EUPHORE), Final Report, Contract EV5V-CT92-0059*, pp. 65–76. Brussels, Belgium: Commission of the European Communities. 3.2.3
- Eyde, L. A. and G. N. Richards (1991). Analysis from Wood Smoke: Components derived from Polysaccharides and Lignins. *Environ. Sci. Technol.*, Vol. 25, 1133–1137. 1
- Finlayson-Pitts, B. and J. N. Pitts, Jr. (2000). *Chemistry of the Upper and Lower Atmosphere* (First ed.). San Diego: Academic Press. 1, 2.2, 5.2.2, 5.7
- Fontaine, H. (2000). *Les Composés Organiques Volatils dans les gaz d'échappement des automobiles: Etablissement de profils d'émission représentatifs de différentes conditions de conduite*. Dissertation, Université de Technologie de Compiègne. 1
- Forstner, H. J. L., R. C. Flagan, and J. H. Seinfeld (1997). Secondary Organic Aerosol from the Photooxidation of Aromatic Hydrocarbons: Molecular Composition. *Environ. Sci. Technol.*, Vol. 31, 1345–1358. 5.6.1, 5.7, 6, 7
- Gery, M. W., D. L. Fox, H. E. Jeffries, L. Stockburger, and W. S. Weathers (1985). A Continuous Stirred Tank Reactor Investigation of the Gas-Phase Reaction of Hydroxyl Radicals and Toluene. *Int. J. Chem. Kinet.*, Vol. 17, 931–955. 5.8
- Geyer, A. (1997). *Konzentrationsbestimmung des Nitrat-Radikals und aromatischer Kohlenwasserstoffe in der Troposphäre mittels eines DOAS-Vielfachreflexionssystems in Heidelberg*. Diplomarbeit, Institute for environmental physics, University of Heidelberg. 3.2.4
- Geyer, A. (2000). *The Role of the Nitrate Radical in the Boundary Layer*. Dissertation, Institute for environmental physics, University of Heidelberg. 4.8.1
- Glasson, W. A. and C. S. Tuesday (1970). Hydrocarbon Reactivities in the Atmospheric Photooxidation of Nitric Oxide. *Environ. Sci. Technol.*, Vol. 4, 916–924. 1

- Gomer, T., T. Brauers, F. Heintz, J. Stutz, and U. Platt (1993). *MFC User Manual, Vers. 1.98*. Institute for environmental physics, University of Heidelberg. 3.2.2, 3.2.4
- Graedler, F. and I. Barnes (1997). Photolysis of 1,2-Dicarbonyls. In K. Becker (Ed.), *EU-PHORE annual report*, pp. 146–148. BUGH Wuppertal, Germany: Physical Chemistry Department, Fachbereich 9. 5.5.1, 5.5.2, 5.7
- Grosjean, D. (1984). Atmospheric Reactions of Ortho Cresol: Gas Phase and Aerosol Products. *Atmos. Environ.*, Vol. 18, 1641–1652. 5.7, 6
- Haagen-Smit, A. J. and M. M. Fox (1956). Ozone Formation in Photochemical Oxidation of Organic Substances. *Ind. Eng. Chem.*, Vol. 48, 1484–1487. 1
- Harder, J. W., J. W. Brault, P. V. Johnston, and G. H. Mount (1997). Temperature-Dependent NO₂ Cross Sections at High Spectral Resolution. *J. Geophys. Res.*, Vol. 102, 3861–3879. 3.1
- Hausmann, M. and U. Platt (1994). Spectroscopic Measurements of Bromine Oxide and Ozone in the high Arctic during Polar Sunrise Experiment 1992. *J. Geophys. Res.*, Vol. 99, 25399–25413. 3.2
- Heiden, A. C., K. Kobel, M. Komenda, R. Koppmann, M. Shao, and J. Wildt (1999). Toluene Emissions from Plants. *Geophys. Res. Lett.*, Vol. 26, 1283–1286. 1
- Hjorth, J., J. Notholt, and G. Restelli (1992). A spectroscopic study of the equilibrium NO₂ + NO₃ + M = N₂O₅ + M and the kinetics of the O₃/N₂O₅/NO₃/NO₂/air system. *Int. J. Chem. Kinet.*, Vol. 24, 51–65. 3.2
- Hjorth, J., K. Wirtz, G. Moortgat, E. Ljungström, K. H. Becker, and G. Hayman (1999). Degradation Mechanisms of Biogenic VOC (BIOVOC). In J. Hjorth (Ed.), *Final Report, Contract No. ENV4-CT95-0059*. Brussels: European Commission. 5.7
- Horowitz, A. and G. Moortgat (1999). *personal communication*,. 5.2, 5.1.2
- Hoshino, M., H. Akimoto, and M. Okuda (1978). Photochemical Oxidation of Benzene, Toluene and Ethylbenzene Initiated by OH Radicals in the Gas Phase. *Bull. Chem. Soc. Jpn.*, Vol. 51, 718–724. 5.5.1
- Hunt, J. M., R. J. Miller, and J. K. Whelan (1980). Formation of C₄-C₇ Hydrocarbons from Bacterial Degradation of Naturally Occurring Terpenoids. *Nature*, Vol. 288, 577–578. 1
- Isidorov, V. A., I. G. Zenkevich, and B. V. Ioffe (1990). Volatile Organic Compounds in Solfataric Gases. *J. Atmos. Chem.*, Vol. 10, 329–340. 1
- Jeffries, H., K. Sexton, and Z. Adelman (1999). Auxiliary Mechanisms (Wall Models) for UNC Outdoor Chamber. In W. P. L. Carter (Ed.), *Summary of Presentations at the US/German - Environmental Chamber Workshop, Riverside, CA, October 4-6*. <http://www.cert.ucr.edu/carter/epacham/meeting1.htm>. 5.2.2
- Jenkin, M., S. M. Saunders, and R. G. Derwent (2000). Photochemical Ozone Creation Potentials for Aromatic Hydrocarbons: Sensitivity to Variations in Kinetic and Mechanistic Parameters. In K. H. Becker (Ed.), *Chemical Behaviour of Aromatic Hydrocarbons in the Troposphere*, pp. 81–87. Fachbereich 9, BUGH Wuppertal: http://www.physchem.uni-wuppertal.de/PC-WWW_Site/workshops.html. 7

- Juettner, F. and J. J. Henatsch (1986). Anoxic Hypolimnion is a Significant Source of Biogenic Toluene. *Nature*, Vol. 323, No. 30, 797–798. 1
- Kelly, T. J., R. Mukund, C. W. Spicer, and A. J. Pollack (1994). Concentrations and Transformations of Hazardous Air Pollutants. *Environ. Sci. Technol.*, Vol. 28, 378A–387A. 1, 7
- Kenley, R. A., J. E. Davenport, and D. G. Hendry (1981). Gas-Phase Hydroxyl Radical Reactions. Products and Pathways for the Reaction of OH with Aromatic Hydrocarbons. *J. Phys. Chem.*, Vol. 85, 2740–2746. 5.5
- Kerr, J. A. and D. W. Sheppard (1981). Kinetics of the Reactions of Hydroxyl Radicals with Aldehydes Studied under Atmospheric Conditions. *Environ. Sci. Technol.*, Vol. 15, 960–963. 5.3
- Killus, J. P. and G. Z. Whitten (1982). A Mechanism Describing the Photochemical Oxidation of Toluene in Smog. *Atmos. Environ.*, Vol. 16, 1973–1988. 2.3
- Klotz, B. (1998). *Mechanistische Untersuchungen zur atmosphärischen Oxidation aromatischer Kohlenwasserstoffe*. Dissertation, Fachbereich 9, Naturwissenschaften II, BUGH Wuppertal. 5.4.2
- Klotz, B. (2001). *personal communication*,. 5.2
- Klotz, B., I. Barnes, and K. H. Becker (1999). Kinetic Study of the Gas-Phase Photolysis and OH Radical Reaction of E,Z- and E,E-2,4-Hexadienedial. *Int. J. Chem. Kinet.*, Vol. 31, 689–697. 5.5.1, 5.7, 5.5.2
- Klotz, B., I. Barnes, K. H. Becker, and T. B. Golding (1997). Atmospheric Chemistry of Benzeneoxid/oxepin. *J. Chem. Soc., Faraday Trans.*, Vol. 93, 1507–1515. 2.1, 2.2, 4.3.5, 5.5.1
- Klotz, B., A. Bierbach, I. Barnes, and K. H. Becker (1995). Kinetic and Mechanistic Study of the Atmospheric Chemistry of Muconaldehydes. *Environ. Sci. Technol.*, Vol. 29, 2322–2332. 5.5.1, 5.7
- Klotz, B., F. Graedler, S. Sørensen, I. Barnes, and K. H. Becker (2001). A Kinetic Study of the Atmospheric Photolysis of α -Dicarbonyls. *Int. J. Chem. Kinet.*, Vol. 33, 9–20. 3.2, 5.7
- Klotz, B., S. Sørensen, I. Barnes, K. H. Becker, T. Eitzkorn, R. Volkamer, U. Platt, K. Wirtz, and M. Martin-Reviejo (1998). Atmospheric Oxidation of Toluene in a Large-volume Outdoor Photoreactor: In Situ Determination of Ring-Retaining Products Yields. *J. Phys. Chem. A*, Vol. 50, No. 102, 10289–10299. 2.1, 4.4, 4.6.1, 5.4.2, 5.6, 5.4.2, 5.4.3, 6
- Knispel, R., R. Koch, M. Siese, and C. Zetzsch (1990). Adduct Formation of OH Radicals with Benzene, Toluene and Phenol and Consecutive Reactions of the Adducts with NO_x and O_2 . *Ber. Bunsenges. Phys. Chem.*, Vol. 94, 1375–1379. 2.1, 4.3.1, 5.6, 6
- Knobloch, T. and A. A. W. Engewald (1997). Volatile Organic Compounds in Urban Atmospheres: long-term Measurements of Ambient Air Concentrations in different loaded Regions of Leipzig. *Fresenius J. Anal. Chem.*, Vol. 359, 189–197. 1.1
- Koch, R. (1997). Comment on "UV Spectrum and Kinetics of Hydroxycyclohexadienyl Radicals". *J. Phys. Chem. B*, Vol. 101, 293. 2.1

- Koch, R., R. Knispel, and C. Zetzsch (1993). Absolute Rate Constants and Products of Secondary Steps in the Atmospheric Degradation of Aromatics. In G. Angeletti and G. Restelli (Eds.), *Proc. of the 6th European Symposium on the "Physico-Chemical Behaviour of Atmospheric Pollutants" held 18-22 Oct. 1993 in Varese, Italy; EC Air Pollution Research Report 50, EUR 15609/1 EN 1994, Vol. 1*, pp. 143–149. Brussels, Belgium: Commission of the European Communities. 5.6, 5.4.2
- Kramp, F. and S. E. Paulson (1998). On the Uncertainties in the Rate Coefficients for OH Reactions with Hydrazones, and the Rate Coefficients of the 1,3,5-Trimethylbenzene and m-Xylene REactions with OH Radicals in the Gas Phase. *Journal of Physical Chemistry A*, Vol. 102, 2685–2690. 3.4.2, 4.2.2, 4.2, 4.3.6
- Kurtenbach, R., R. Ackermann, K. H. Becker, A. Geyer, J. A. G. Gomes, J. C. Lörzer, U. Platt, and P. Wiesen (2001). Verification of the Contribution of Vehicular Traffic to the total NMVOC Emissions in Germany and the importance of the NO₃ chemistry in the city air. *accepted in J. Phys. Chem.,.* 1.1, 1, 5.7, 7
- Kwok, E. S. C., S. M. Aschmann, R. Atkinson, and J. Arey (1997). Products of the Gas-Phase Reactions of o-, m- and p-Xylene with the OH Radical in the Presence and Absence of NO_x. *J. Chem. Soc., Faraday Trans.,* Vol. 93, 2847–2854. 2.2, 5.5.1
- Lay, T. H., J. W. Bozzelli, and J. H. Seinfeld (1996). Atmospheric Photochemical Oxidation of Benzene: Benzene + OH and the Benzene-OH Adduct (Hydroxyl-2,4-cyclohexadienyl) + O₂. *J. Phys. Chem.,* Vol. 100, 6543–6554. 2.1, 5.3.1, 5.3.5, 5.4.2, 5.4.3
- Lee, S.-H., D. M. Murphy, D. S. Thomson, and A. M. Middlebrook (2001). Nitrate and organic acids in single aerosol particles during the 1999 Atlanta SuperSite Experiment. *submitted to J. Geophys. Res.,.* 5.7
- Leggett, S. (1996). Forecast Distributions of Species and Their Atmospheric Reactivities for the U.K. VOC Emission Inventory. *Atmos. Environ.,* Vol. 30, 215–226. 1
- Leone, J. A., R. C. Flagan, D. Grosjean, and J. H. Seinfeld (1985). An Outdoor Smog Chamber and Modeling Study of Toluene-NO_x Photooxidation. *Int. J. Chem. Kinet.,* Vol. 17, 177–216. 2.3
- Levenberg, K. (1944). A Method for the Solution of Certain Non-Linear problems in Least Squares. *Quart. Appl. Math.,* Vol. 2, 164–168. 3.2.2
- Levy II, H. (1971). Normal Atmosphere: Large Radical and Formaldehyde Concentrations Predicted. *Science*, Vol. 166, 224–225. 1
- Liu, X., H. E. Jeffries, and K. G. Sexton (1999). Atmospheric Photochemical Degradation of 1,4-Unsaturated Dicarboxyls. *Environ. Sci. Technol.,* Vol. 33, 4212–4220. 5.5.2
- Lonnemann, W. A., T. A. Bellar, and A. P. Altshuller (1968). Aromatic Hydrocarbons in the Atmosphere of the Los Angeles Basin. *Environ. Sci. Technol.,* Vol. 2, 1017–1020. 1
- Marquardt, D. W. (1963). An Algorithm for Least Squares Estimation of Non-Linear Parameters. *Soc. Indust. Appl. Math,* Vol. 11, 431–441. 3.2.2
- Martín-Reviejo, K. Wirtz, and K. H. Becker (1996). Studies of Photochemical Ozone Formation in Toluene/NO_x/Air Systems by Empirical and Numerical Simulations.

- In I. Allegrini and F. DeSantis (Eds.), *NATO ASI Series, Partnership Sub-Series, 2. Environment - Volume 8 "Urban Air Pollution: Monitoring and Control Strategies"*, pp. 57–67. Heidelberg, Germany: Springer-Verlag. 2.3
- Mellouki, A., S. Teton, and G. LeBras (1995). Kinetics of OH Radical reactions with a Series of Ethers. *Int. J. Chem. Kinet.*, Vol. 27, 791–805. 4.3.6
- Mellqvist, J. and A. Rosén (1996). DOAS for Flue Gas Monitoring - II. Deviations from the Beer-Lambert Law for the U.V./Visible Absorption Spectra of NO, NO₂, SO₂ and NH₃. *J. Quant. Spectrosc. Radiat. Transfer*, Vol. 56, No. 2, 209–224. 5.1.1
- Moortgat, G. (2000). Evaluation of RADICAL sources in Atmospheric Chemistry through Chamber and Laboratory Studies (RADICAL). In G. Moortgat (Ed.), *Final Report, Contract No. ENV4-CT97-0419*. Brussels, Belgium: European Commission. 3.5.2, 4.1.2, 5.2
- Moortgat, G. and A. Horowitz (2000). *personal communication*,. 5.1.2
- Nelson, L., O. Rattigan, R. Neavyn, H. Sidebottom, J. Treacy, and O. J. Nielsen (1990). Absolute and Relative Rate Constants for the reactions of Hydroxyl Radicals and Chlorine Atoms with a Series of Aliphatic Alcohols and Ethers at 298 K. *Int. J. Chem. Kinet.*, Vol. 22, 1111. 4.3.6
- Nicovich, J. M., R. L. Thompson, and A. R. Ravishankara (1981). Kinetics of the Reactions of the Hydroxyl Radical with Xylenes. *J. Phys. Chem.*, Vol. 85, 2913–2916. 5.5
- Niki, H., P. D. Maker, C. M. Savage, and L. P. Breitenbach (1978). Relative Rate Constants for the Reaction of Hydroxyl Radical with Aldehydes. *J. Phys. Chem.*, Vol. 82, 132–134. 5.3
- Nojima, K., K. Fukaya, S. Fukui, and S. Kanno (1974). The Formation of Glyoxals by the photochemical Reaction of Aromatic Hydrocarbons in the presence of Nitrogen Monoxide. *Chemosphere*, Vol. 5, 247–252. 1
- Noxon, J. F. (1975). Nitrogen Dioxide in the Stratosphere and Troposphere measured by Ground-based Absorption Spectroscopy. *Science*, Vol. 189, 547–549.
- Noxon, J. F., E. C. Whipple, and R. S. Hyde (1979). Stratospheric NO₂. 1. Observational Method and Behavior at Midlatitudes. *J. Geophys. Res.*, Vol. 84, 5047–5076. 3.2
- Nutmagul, W. and D. R. Cronn (1985). Determination of Selected Aromatic Hydrocarbons at Remote Continental and Oceanic Locations Using Photoionization/Flame-Ionisation Detection. *J. Atmos. Chem.*, Vol. 2, 415–433. 1
- Odum, J. R., T. P. W. Jungkamp, R. J. Griffin, R. C. Flagan, and J. H. Seinfeld (1997). The Atmospheric Aerosol-Forming Potential of Whole Gasoline Vapor. *Science*, Vol. 276, 96–99. 1, 2.3, 5.7, 6
- Oliaru, R., I. Barnes, K. H. Becker, B. Klotz, and R. Mocanu (2000). FT-IR Primary Product Distribution Study for the Reaction of OH Radical with Phenol, o-, m-, p-Cresol. In M. J. Rossi and E. M. Rossi (Eds.), *Proc. of the EC/EUROTRAC-2 Joint Workshop "EC Cluster 4: Chemical Processes and Mechanisms; EUROTRAC-2: Chemical Mechanism Development" held 11-13 Sept. 2000 in Lausanne, Switzerland*, pp. 60–63. EFPL: michel.rossi@epfl.ch. 4.4.2, 5.5.1, 5.7, 7

- Pagsberg, P. (1997). Reply to Comment on "UV Spectrum and Kinetics of Hydroxycyclohexadienyl Radicals". *J. Phys. Chem. B*, Vol. 101, 294. 2.1
- Patyk, A. and U. Höpfner (August 1995). Komponenten-Differenzierung der Kohlenwasserstoffemissionen von KFZ. *Forschungsbericht 105 06 069 des Umweltbundesamtes*,. 1.1, 1
- Perner, D., D. H. Ehhalt, H. W. Paetz, U. Platt, E. P. Roeth, and A. Volz (1976). OH Radicals in the lower Troposphere. *Geophys. Res. Lett.*, Vol. 3, 466–468. 3.2
- Perner, D. and U. Platt (1979). Detection of Nitrous Acid in the Atmosphere by Differential Optical Absorption. *Geophys. Res. Lett.*, Vol. 6, 917–920. 3.2
- Perry, R. A., R. Atkinson, and J. N. Pitts, Jr. (1977). Kinetics and Mechanism of the Gas Phase Reaction of OH Radicals with Aromatic Hydrocarbons Over the Temperature Range 296–473 K. *J. Phys. Chem.*, Vol. 81, 296–304. 1, 5.5
- Piccot, S. D., J. J. Watson, and J. W. Jones (1992). A Global Inventory of Volatile Organic Compound Emissions from Anthropogenic Sources. *J. Geophys. Res.*, Vol. 97, No. D9, 9897–9912. 1
- Platt, U. (1978). Dry Deposition of SO₂. *Atmos. Environ.*, Vol. 12, 363–367. 3.2
- Platt, U. (1994). Differential Optical Absorption Spectroscopy (DOAS). In M. W. Sigrist (Ed.), *Monitoring by Spectroscopic Techniques*. New York: John Wiley & Sons, Inc. 3.2, 3.2.1, 3.2.1
- Platt, U., G. LeBras, G. Poulet, J. P. Burrows, and G. Moortgat (1990). Peroxy Radical from Night-time Reaction of NO₃ with Organic Compounds. *Nature*, Vol. 348, 147–149.
- Platt, U. and D. Perner (1980). Direct Measurements of Atmospheric CH₂O, HNO₂, O₃, NO₂ and SO₂ by Differential Optical Absorption in the Near UV. *J. Geophys. Res.*, Vol. 85, 7453–7458. 3.2
- Platt, U. and D. Perner (1983). Measurements of Atmospheric Trace Gases by Long Path Differential UV/visible Absorption Spectroscopy. In D. K. Killinger and A. Mooradian (Eds.), *Optical and Laser Remote Sensing*, pp. 95–105. New York: Springer Verlag.
- Platt, U., D. Perner, G. W. Harris, A. M. Winer, and J. N. Pitts, Jr. (1980). Detection of NO₃ in the Polluted Troposphere by Differential Optical Absorption. *Geophys. Res. Lett.*, Vol. 7, 89–92. 3.2
- Platt, U., D. Perner, and H. W. Pätz (1979). Simultaneous Measurement of Atmospheric CH₂O, O₃ and NO₂ by Differential Optical Absorption. *J. Geophys. Res.*, Vol. 84, 6329–6335.
- Plum, C. N., E. Sanhueza, R. Atkinson, W. P. L. Carter, and J. N. Pitts, Jr. (1983). OH Radical Rate Constants and Photolysis Rates of α -Dicarbonyls. *Environ. Sci. Technol.*, Vol. 17, 479–484. 5.2, 5.1.2, 5.7
- Rinke, M. and C. Zetzsch (1984). Rate Constants for the Reactions of OH Radicals with Aromatics: Benzene, Phenol, Aniline, and 1,2,4-Trichlorobenzene. *Ber. Bunsenges. Phys. Chem.*, Vol. 88, 55. 5.3

- Ritz, D. (1992). *Specialite: Chimie de la Pollution Atmospherique et Physique de l'Environnement*. Dissertation, Institut für Umweltphysik, Universität Heidelberg. 3.2.3
- Sanders, R. W., S. Solomon, M. A. Carroll, and A. L. Schmeltekopf (1988). Ground based Measurements of O₃, NO₂, OClO and BrO during the Antarctic Ozone Depletion Event. In R. D. Bjokov and P. Fabian (Eds.), *Ozone in the Atmosphere, Quadrennial Ozone Symposium 1988*, pp. 65–70. Hampton, Va.: Deepak Publishing. 3.2
- Semadeni, M., D. W. S. and J. A. Kerr (1993). Further studies of the Temperature Dependence of the Rate Coefficients for the reactions of OH with a Series of Ethers under Simulated Atmospheric Conditions. *J. Atmos. Chem.*, Vol. 16, 79–93. 4.3.6
- Semadeni, M., D. W. Stocker, and J. A. Kerr (1995). The Temperature Dependence of the OH Radical Reactions with Some Aromatic Compounds under Simulated Tropospheric Conditions. *Int. J. Chem. Kinet.*, Vol. 27, 287–304. 4.2.2, 4.2, 4.3.6, 5.3
- Seuwen, R. and P. Warneck (1996). Oxidation of Toluene in NO_x Free Air: Product Distribution and Mechanism. *Int. J. Chem. Kinet.*, Vol. 28, 315–332. 5.4.3
- Shepson, P. B., E. O. Edney, and E. W. Corse (1984). Ring Fragmentation Reactions on the Photooxidations of Toluene and o-Xylene. *J. Phys. Chem.*, Vol. 88, 4122–4126. 5.5.1, 5.8, 5.6.1
- Shepson, P. B., T. E. Kleindienst, E. O. Edney, G. R. Namie, J. H. Pittman, L. T. Cupitt, and L. D. Claxton (1985). The Mutagenic Activity of Irradiated Toluene/NO_x/H₂O/Air Mixtures. *Environ. Sci. Technol.*, Vol. 19, 249–255. 7
- Sigsby, J., S. Tejada, and W. Ray (1987). Volatile Organic Compound Emission from 46 In-Use Passenger Cars. *Environ. Sci. Technol.*, Vol. 21, 466–475. 1
- Smith, D. F., T. Kleindienst, and C. McIver (1999). Primary Product Distribution from the Reaction of OH with m-, p-Xylene, 1,2,4- and 1,3,5-Trimethylbenzene. *J. Atm. Chem.*, Vol. 34, 339–364. 2.2, 5.5, 5.4.1, 5.4.1, 5.5.1, 5.5.3, 5.8, 6
- Smith, D. F., C. McIver, and T. Kleindienst (1998). Primary Product Distribution from the Reaction of Hydroxyl Radicals with Toluene at ppb NO_x Mixing Ratios. *J. Atm. Chem.*, Vol. 30, 209–228. 2.1, 4.6.1, 5.4.2, 5.4.2, 5.4.3, 5.5.1, 5.8, 5.5.3, 5.6.1, 5.6.1, 6
- Solomon, S., A. L. Schmeltekopf, and R. W. Sanders (1987). On the interpretation of Zenith Sky Absorption Measurements. *J. Geophys. Res.*, Vol. 92, 8311–8319. 3.2
- Sørensen, S. and I. Barnes (1997). Photolysis of unsaturated 1,4-Dicarbonyls. In K. Becker (Ed.), *EUPHORE annual report*, pp. 149–150. BUGH Wuppertal, Germany: Physical Chemistry Department, Fachbereich 9. 5.5.1, 5.5.2, 5.7
- Stern, J. E., R. C. Flagan, D. Grosjean, and J. H. Seinfeld (1987). Aerosol Formation and Growth in Atmospheric Aromatic Hydrocarbon Photooxidation. *Environ. Sci. Technol.*, Vol. 21, 1224–1231. 2.3
- Stutz, J., E. S. Kim, U. Platt, P. Bruno, C. Perrino, and A. Febo (1999). UV-visible Absorption Cross-Section of Nitrous Acid. *J. Geophys. Res.*, Vol. 105, No. D11, 14585–14592. 3.1, 5.1.2

- Stutz, J. and U. Platt (1996). Numerical Analysis and Estimation of the Statistical Error of Differential Optical Absorption Spectroscopy Measurements with Least-Squares methods. *Appl. Opt.*, Vol. 35, No. 30, 6041–6053. 3.2.1, 3.2.2, 4.3.6
- Stutz, J. and U. Platt (1997). Improving Long-Path Differential Optical Absorption Spectroscopy with a Quartz Fiber Mode Mixer. *Appl. Opt.*, Vol. 36, No. 6, 1105–1115. 3.2.3
- Thiault, G., A. Mellouki, and G. L. Bras (2000). UV Spectra of Benzaldehyde and p-Tolualdehyde and their gas phase reactions with OH and Cl radicals. In M. J. Rossi and E. M. Rossi (Eds.), *Proc. of the EC/EUROTRAC-2 Joint Workshop "EC Cluster 4: Chemical Processes and Mechanisms; EUROTRAC-2: Chemical Mechanism Development" held 11-13 Sept. 2000 in Lausanne, Switzerland*, pp. 89–92. EFPL: michel.rossi@epfl.ch.
- Trost, B. (1997). UV-Absorption Cross Sections of a Series of Monocyclic Aromatic Compounds. *Atmos. Environ.*, Vol. 31, No. 23, 3999–4008. 3.2, 4.3.6, 5.1
- Tse, C. W., R. C. Flagan, and J. H. Seinfeld (1997). Rate Constants for the Gas-Phase Reaction of the Hydroxyl Radical with a Series of Dimethylbenzaldehydes and Trimethylphenols at Atmospheric Pressure. *Int. J. Chem. Kinet.*, Vol. 29, 523–525. 5.2.1
- Tuazon, E. C., R. Atkinson, H. MacLeod, H. W. Biermann, A. M. Winer, W. P. L. Carter, and J. N. Pitts, Jr. (1984). Yields of Glyoxal and Methylglyoxal from the NO_x-Air Photooxidations of Toluene and m- and p-Xylene. *Environ. Sci. Technol.*, Vol. 18, 981–984. 5.5.3, 5.8
- Tuazon, E. C., H. MacLeod, R. Atkinson, and W. P. L. Carter (1986). α-Dicarbonyl Yields from the NO_x-Air Photooxidations of a Series of Aromatic Hydrocarbons in Air. *Environ. Sci. Technol.*, Vol. 20, 383–387. 2.2, 5.5.3, 5.8, 5.5.3
- Ücker, J. (1999). *Absolutbestimmung atmosphärischer Aromatenkonzentrationen mittels DOAS-Langpfad und erste EUPHORE-Messungen zur Photooxidation von 1,3,5-Trimethylbenzol*. Diplomarbeit, Institute for environmental physics, University of Heidelberg. 3.2.4, 3.1, 5.5
- Umweltbundesamt (1998). www.umweltbundesamt.de/uba-info-daten/verkehremissionsentwicklung.html,. 1
- Utz, C. (1997). *Bestimmung von Reaktionskonstanten der Nitrat-Radikal-Reaktion mit Alkenen und Aldehyden über NO₃-Messungen mittels Differentieller Optischer Absorptionsspektroskopie am Europäischen Photoreaktor EUPHORE*. Diplomarbeit, Institute for environmental physics, University of Heidelberg. 3.2.4
- Vandaele, A. C., T. C. Simon, J. M. Goilmont, C. M. Carleer, and R. Colin (1994). SO₂ Absorption Cross Section Measurement in the UV using Fourier Transform Spectrometer. *J. Geophys. Res.*, Vol. 99, 25599–25605. 3.1
- Volkamer, R. (1996). *Absorption von Sauerstoff im Herzberg I System und Anwendung auf Aromatenmessungen am European PHOto REactor (EUPHORE)*. Diploma thesis, Institut für Umweltp Physik, Universität Heidelberg. 3.2.3
- Volkamer, R., K. Becker, B. Klotz, U. Platt, J. Uecker, and K. Wirtz (2000). OH-Radical initiated Oxidation of Aromatics: A DOAS Study on the Formation Mechanism of

- Ring-Retaining Products and Glyoxal. In K. H. Becker (Ed.), *Chemical Behaviour of Aromatic Hydrocarbons in the Troposphere*, pp. 15–23. Fachbereich 9, BUGH Wuppertal: http://www.physchem.uni-wuppertal.de/PC-WWW_Site/workshops.html. 4.3.6
- Volkamer, R., T. Etzkorn, A. Geyer, and U. Platt (1998). Correction of the Oxygen Interference with UV Spectroscopic (DOAS) Measurements of Monocyclic Aromatic Hydrocarbons in the Atmosphere. *Atmos. Environ.*, Vol. 32, 3731–3747. 3.2, 5.1.1
- Volkamer, R., B. Klotz, I. Barnes, K. Wirtz, N. Washida, K. H. Becker, and U. Platt (2001). OH-Initiated Oxidation of Benzene: I. Phenol formation under Atmospheric Conditions. *submitted to PCCP*,. 4.3.6
- Volkamer, R., U. Platt, J. Ücker, and K. Wirtz (1998). OH-Initiated Oxidation of p-Xylene: A DOAS Study on the Formation Mechanism of Ring-Retaining products. In I. Barnes and K. Brockmann (Eds.), *EUPHORE annual report 1998-1999*, pp. 257–268. Fachbereich 9, BUGH Wuppertal: <http://www.physchem.uni-wuppertal.de>. 4.4, 4.4.1, 5.7, 7
- Volkamer, R., U. Platt, and K. Wirtz (2000). OH-Initiated Oxidation of Aromatic Compounds: Fast Ring-Cleavage - a major operative pathway for BTX. In M. J. Rossi and E. M. Rossi (Eds.), *Proc. of the EC/EUROTRAC-2 Joint Workshop "EC Cluster 4: Chemical Processes and Mechanisms; EUROTRAC-2: Chemical Mechanism Development" held 11-13 Sept. 2000 in Lausanne, Switzerland*, pp. 106–111. EFPL: michel.rossi@epfl.ch. 4.6.5
- Volkamer, R., U. Platt, and K. Wirtz (2001). Primary and Secondary Glyoxal Formation from Aromatics: Experimental Evidence for the Bicycloalkyl-Radical Pathway from Benzene, Toluene and p-Xylene. *J. Phys. Chem.*, Vol. 105, 7865–7874. 4.6.5
- Wallington, T. J., J. M. Andino, L. M. Skewes, W. O. Siegl, and S. M. Japar (1989). Kinetics of the reaction of OH Radicals with a Series of Ethers under Simulated Atmospheric Conditions at 295 K. *Int J. Chem. Kinet.*, Vol. 21, 993. 4.3.6
- Wallington, T. J., R. Liu, P. Dagaut, and M. J. Kurylo (1988). The Gas Phase reactions of Hydroxyl Radicals with a Series of Aliphatic Ethers over the Temperature Range 240–440 K. *Int J. Chem. Kinet.*, Vol. 20, 41. 4.3.6
- Wängberg, I., T. Etzkorn, I. Barnes, U. Platt, and K. H. Becker (1997). Absolute Determination of the Temperature Behaviour of the $\text{NO}_2 + \text{NO}_3 + (\text{M}) \leftrightarrow \text{N}_2\text{O}_5 + (\text{M})$ Equilibrium. *J. Phys. Chem.*, Vol. 101, 9694–9698.
- Wängberg, I., B. Nozière, L. Thüner, G. Leverdet, A. E. Boudali, G. LeBras, A. Melouki, S. Téton, J. Bea, K. Wirtz, T. Etzkorn, R. Volkamer, and U. Platt (1996). NO_3 Radical Experiments in the EUPHORE chamber. In K. H. Becker (Ed.), *EUPHORE final report*, pp. 137–145. Brussels: Contract No. EV5V-CT92-0059, Commission of the European Communities. 4.8.1
- Wayne, R. P., I. Barnes, P. Biggs, J. P. Burrows, C. E. Canosa-Mas, J. Hjorth, G. LeBras, G. K. Moortgat, D. Perner, G. Poulet, G. Restelli, and H. Sidebottom (1991). The Nitrate Radical: Physics, Chemistry and the Atmosphere. *Atmos. Environ.*, Vol. 25A, 1–203. 3.1, 4.8.1
- Weinstock, B. (1969). Carbon Monoxide: Residence Time in the Atmosphere. *Science*, Vol. 166, 224–225. 1

- White, J. U. (1942). Long Paths of Large Aperture. *J. Opt. Soc. Am.*, Vol. 32, 285–288. 3.2.3
- White, J. U. (1976). Very Long Optical Paths in Air. *J. Opt. Soc. Am.*, Vol. 66, 411–416. 3.2.3
- Wiesen, E. (1995). *OH-initiierte Oxidation von p-Xylol und Produktuntersuchungen an ausgewählten Carbonylverbindungen*. Dissertation, Fachbereich 9, Naturwissenschaften II, BUGH Wuppertal. 5.4.3, 5.5.1
- Wirtz, K. and M. Martín-Reviejo (1997). Characterisation of Physical and Chemical Properties of the Chamber. In K. H. Becker (Ed.), *EUPHORE annual report*, pp. 3–16. BUGH Wuppertal, Germany: Physical Chemistry Department, Fachbereich 9. 5.2.2
- Witte, F. J. (1987). *Untersuchung der Temperaturabhängigkeit der Reaktion von HO-Radikalen mit heterocyclischen aromatischen Verbindungen*. Dissertation, Ruhr University, Bochum. 5.3
- Yu, J. and H. E. Jeffries (1997). Atmospheric Photooxidation of Alkylbenzenes - II. Evidence of Formation of Epoxide Intermediates. *Atmos. Environ.*, Vol. 31, 2281–2287. 2.2, 5.5.1
- Yu, J., H. E. Jeffries, and K. G. Sexton (1997). Atmospheric Photooxidation of Alkylbenzenes - I. Carbonyl Product Analysis. *Atmos. Environ.*, Vol. 31, 2261–2280. 1, 2.2, 4.6.4, 5.5.1
- Zetzsch, C. (1997). Abbaumechanismen von Aromaten nach Anlagerung von OH und ihr Einfluss auf die Kreisläufe von HO_x unter Bildung von Photooxidantien. In *TFS-annual report, TFS-Teilprojekt LT3-D3*, pp. 68. <http://www.gsf.de/PTUKF/tfsmain.html>. 2.1, 4.3.1
- Zetzsch, C., R. Koch, M. Siese, F. Witte, and P. Devolder (1990). In G. Restelli and G. Angeletti (Eds.), *Proc. of the 5th European Symposium on the "Physico-Chemical Behaviour of Atmospheric Pollutants"*, pp. 320. Dordrecht, Holland: Kluwer. 5.6

Appendix A

Annex

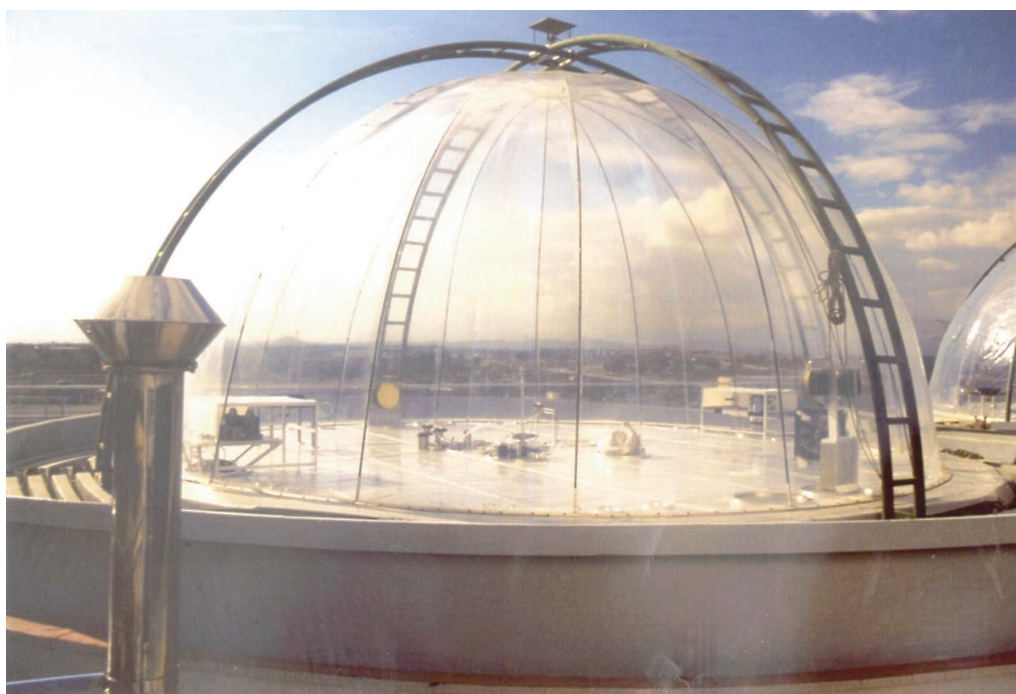


Figure A.1: Foto of the EUPHORE chamber A. The DOAS-system is mounted in the shadow of the teflon shades. For cleaning of the chamber air, purified air is lead into the chamber in the central part of the chamber and exhaled via the chimney (shown on the left side).

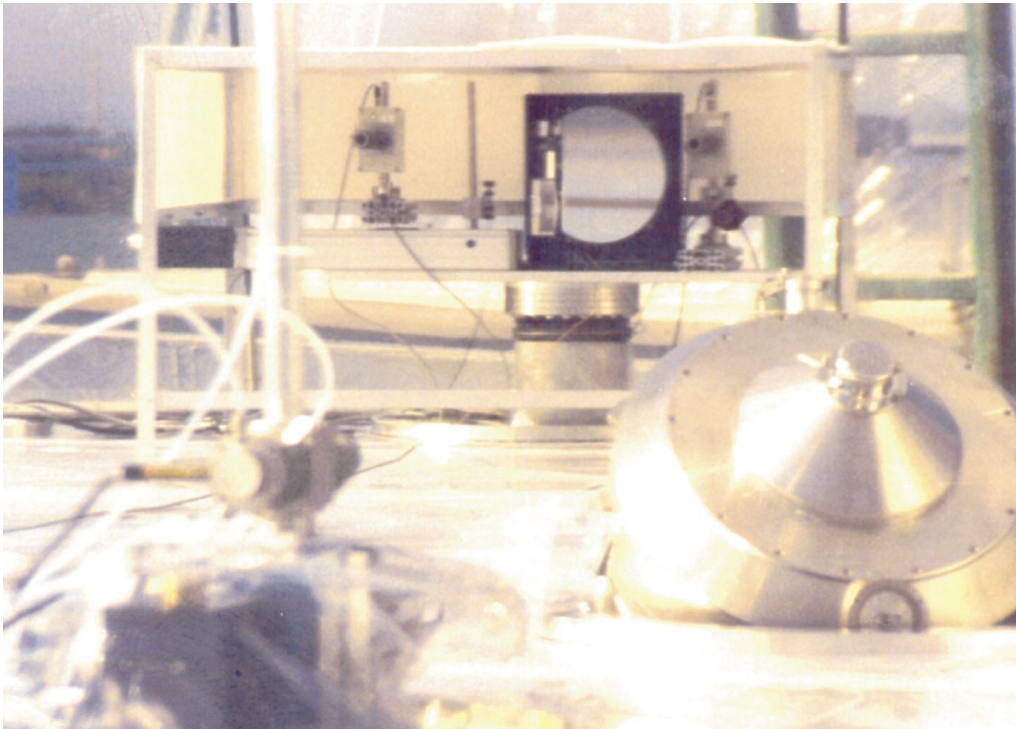


Figure A.2: Foto taken inside the EUPHORE chamber A. Foreground: (left) Fluorescence cell of the OH-LIF-system; (right) Matrix Isolation Electron-Spin-Resonance (MIESR) sampling-unit; Background: The improved field mirror of the DOAS-system (see Section 3.2.4).

In the following the Turbo-Basic-code (file: WHITE2.BAS) is listed, which was developed to control the auto-align of both objective mirrors of the White-system via the laser-alignment (see also Section 3.2.4):

```

10  REM Programm zur aktiven Laserjustage bei Whitesystem mit Mod Diodenlaser

50  rem SM initialisieren
51  OPEN "com1:9600,N,8,1,RS,CS,DS,CD" as #1
52  OPEN "PROT2311.dat" FOR APPEND AS #3: rem Protokollfile
53  write#3,date$,time$
54  PRINT#1,"@07":GOSUB 2000
55  Z=0 : X=0 : Y=0
58  OPEN "com2:9600,N,8,1,RS,CS,DS,CD" as #2
59  PRINT#2,"@07":GOSUB 3000

70  rem Justageparameter
75  wdh=5
76  minAh=1.2: minAv=1.2: maxAh=2: maxAv=2
77  IBh=1.5: IIBh=6: IIIBh=15: IVBh=50: VB1=100: VBr=100:minBv=1.5:maxBv=3:okB=3
78  wmin=15 : wmax=65 : wdia=55 : wext=310
79  wt=0
80  Iao=0: IIao=0: IIIao=0: VIao=0: rem gemessener Offset
81  Ibo=0: IIbo=0: IIIbo=0: IVbo=0: rem gemessener Offset
82  Iao=1050: IIao=1100: IIIao=1050: IVao=1150: rem gemessener Offset
83  Ibo=120: IIbo=20: IIIbo=250: IVbo=50: rem gemessener Offset
84  VertB=0: HorB=0: VertA=0: HorA=0
85  rem VertB=-1240: HorB=-440: VertA=-1490: HorA=-330

100 rem Start Justageschleife
101 A=0 : B=0 : rem goto 150
102 rem Justage von B
103 Z=Z+1
104 gosub 1000 : rem Auleseroutine

```

```

105 gosub 850 : rem Ausgabe der 4QD Werte
106 SummeB=IB+IIB+IIIB+IVB: rem stop
107 if inkey$><" then stop
108 gosub 4000 : rem Laserlichtcheck
109 rem goto 150 : rem B ueberspringen

110 IF (A>2 AND B>2) then goto 120
114 IF (linksB/rechtsB>VBr) then goto 291
115 IF (rechtsB/linksB>VBl) then goto 319
116 IF (linksB/rechtsB>IVBh) then goto 350
117 IF (linksB/rechtsB>IIIBh) then goto 340
118 IF (rechtsB/linksB>IVBh) then goto 371
119 IF (rechtsB/linksB>IIIBh) then goto 365
120 IF (linksB/rechtsB>IIBh) then goto 300
121 IF (linksB/rechtsB>IBh) then goto 310
122 IF (rechtsB/linksB>IIBh) then goto 325
123 IF (rechtsB/linksB>IBh) then goto 331
124 IF (obenB/untenB>maxBv AND rechtsB/linksB>maxBh) then goto 201
125 IF (untenB/obenB>maxBv AND rechtsB/linksB>maxBh) then goto 220
126 IF (linksB/rechtsB>maxBh AND obenB/untenB>maxBv) then goto 210
127 IF (linksB/rechtsB>maxBh AND untenB/obenB>maxBv) then goto 230
135 IF (obenB/untenB>maxBv) then goto 250
136 IF (obenB/untenB>minBv) then goto 260
137 IF (untenB/obenB>maxBv) then goto 270
138 IF (untenB/obenB>minBv) then goto 280

139 print ""
140 print "Sicherheitsabfrage RR:"
142 print "o/u_B : " obenB/untenB " u/o_B : " untenB/obenB
144 print "r/l_B : " rechtsB/linksB " l/r_B : " linksB/rechtsB

145 rem A ueberspringen
150 rem goto 193
151 rem Justage von A
153 rem cls
154 Z=Z+1
158 gosub 1000 : rem Auleseroutine
159 SummeA=IA+IIA+IIIA+IVA
160 GOSUB 850 : rem Ausgabe der 4QD Werte
162 gosub 5000 : rem Laserlichtcheck
163 if inkey$><" then stop
164 rem goto 193 : rem A ueberspringen

174 IF (obenA/untenA>maxAv AND rechtsA/linksA>maxAh) then goto 401
176 IF (untenA/obenA>maxAv AND rechtsA/linksA>maxAh) then goto 420
177 IF (linksA/rechtsA>maxAh AND obenA/untenA>maxAv) then goto 410
178 IF (linksA/rechtsA>maxAh AND untenA/obenA>maxAv) then goto 430
179 IF (obenA/untenA>maxAv) then goto 450
180 IF (obenA/untenA>minAv) then goto 460
181 IF (untenA/obenA>maxAv) then goto 470
182 IF (untenA/obenA>minAv) then goto 480
183 IF (linksA/rechtsA>maxAh) then goto 500
184 IF (linksA/rechtsA>minAh) then goto 510
185 IF (rechtsA/linksA>maxAh) then goto 520
186 IF (rechtsA/linksA>minAh) then goto 530

190 print "": print"Sicherheitsabfrage LR:"
191 print "o/u_A : " obenA/untenA " u/o_A : " untenA/obenA
192 print "r/l_A : " rechtsA/linksA " l/r_A : " linksA/rechtsA
193 print "Ende Justage"
194 FOR p=1 to wt : next p
195 if inkey$><" then stop
196 Z=0 : rem print" : print" Summe A: "IA+IIA+IIIA+IVA:print" Summe B: "IB+IIB+IIIB+IVB
199 goto 100

200 rem Diagonale Justage B
201 print Z
202 print" Justage RR ... diagonal 50 Schritte nach links-unten"
203 print#2,"@0A 0,3000,50,3000,50,3000,0,3000"
204 HorB=HorB+50 : VertB=VertB+50
205 write#3,date$,time$,0,0,50,50,HorA,VertA,HorB,VertB,IA,IIA,IIIA,IVA,SummeA, IB,IIB,IIIB,IVB,SummeB
206 for p=1 to wdia: next p : goto 100

210 print Z
211 print" Justage RR ... diagonal 50 Schritte nach rechts-unten"
212 print#2,"@0A 0,3000,-50,3000,50,3000,0,3000"
213 HorB=HorB-50 : VertB=VertB+50
214 write#3,date$,time$,0,0,-50,50,HorA,VertA,HorB,VertB,IA,IIA,IIIA,IVA,SummeA, IB,IIB,IIIB,IVB,SummeB
215 for p=1 to wdia: next p : goto 100

220 print Z
222 print" Justage RR ... diagonal 50 Schritte nach links-oben"
223 print#2,"@0A 0,3000,50,3000,-50,3000,0,3000"
224 HorB=HorB+50 : VertB=VertB-50
225 write#3,date$,time$,0,0,50,-50,HorA,VertA,HorB,VertB,IA,IIA,IIIA,IVA,SummeA, IB,IIB,IIIB,IVB,SummeB
226 for p=1 to wdia: next p : goto 100

230 print Z
232 print" Justage RR ... diagonal 50 Schritte nach rechts-oben"
234 print#2,"@0A 0,3000,-50,3000,-50,3000,0,3000"
235 HorB=HorB-50 : VertB=VertB-50
236 write#3,date$,time$,0,0,-50,-50,HorA,VertA,HorB,VertB,IA,IIA,IIIA,IVA,SummeA, IB,IIB,IIIB,IVB,SummeB

```

```

237     for p=1 to wdia: next p : goto 100

240 print "Vertikale Justage RR..."
250 print Z
252 print" Justage RR ... vertikal 30 Schritte nach unten"
253   print#2,"@0A 0,3000,0,3000,30,3000,0,3000"
254   VertB=VertB+30
255   write#3,date$,time$,0,0,0,30,HorA,VertA,HorB,VertB,IA,IIA,IIIA,IVA,SummeA, IB,IIB,IIIB,IVB,SummeB
256   for p=1 to wmax: next p : goto 100

260 print Z
262 print" Justage RR ... vertikal 10 Schritte nach unten"
263   print#2,"@0A 0,3000,0,3000,10,3000,0,3000"
264   VertB=VertB+10
265   write#3,date$,time$,0,0,0,10,HorA,VertA,HorB,VertB,IA,IIA,IIIA,IVA,SummeA, IB,IIB,IIIB,IVB,SummeB
266   for p=1 to wmin: next p : goto 100

270 print Z
272 print" Justage RR ... vertikal 30 Schritte nach oben"
273   print#2,"@0A 0,3000,0,3000,-30,3000,0,3000"
274   VertB=VertB-30
275   write#3,date$,time$,0,0,0,-30,HorA,VertA,HorB,VertB,IA,IIA,IIIA,IVA,SummeA, IB,IIB,IIIB,IVB,SummeB
276   for p=1 to wmax: next p : goto 100

280 print Z
282 print" Justage RR ... vertikal 10 Schritte nach oben"
283   print#2,"@0A 0,3000,0,3000,-10,3000,0,3000"
284   VertB=VertB-10
285   write#3,date$,time$,0,0,0,-10,HorA,VertA,HorB,VertB,IA,IIA,IIIA,IVA,SummeA, IB,IIB,IIIB,IVB,SummeB
286   for p=1 to wmin: next p : goto 100

290 print "Horizontale Justage RR..."
291 print Z
292 print" Justage RR ... horizontal 300 Schritte nach rechts"
293   print#2,"@0A 0,3000,-300,3000,0,3000,0,3000"
294   HorB=HorB-300
295   write#3,date$,time$,0,0,-300,0,HorA,VertA,HorB,VertB,IA,IIA,IIIA,IVA,SummeA, IB,IIB,IIIB,IVB,SummeB
296   A=A+1
297   for p=1 to wext: next p : goto 100

300 print Z
302 print" Justage RR ... horizontal 50 Schritte nach rechts"
303   print#2,"@0A 0,3000,-50,3000,0,3000,0,3000"
304   HorB=HorB-50
305   write#3,date$,time$,0,0,-50,0,HorA,VertA,HorB,VertB,IA,IIA,IIIA,IVA,SummeA, IB,IIB,IIIB,IVB,SummeB
306   for p=1 to wmax: next p : goto 100

310 print Z
312 print" Justage RR ... horizontal 10 Schritte nach rechts"
313   print#2,"@0A 0,3000,-10,3000,0,3000,0,3000"
314   HorB=HorB-10
315   write#3,date$,time$,0,0,-10,0,HorA,VertA,HorB,VertB,IA,IIA,IIIA,IVA,SummeA, IB,IIB,IIIB,IVB,SummeB
316   for p=1 to wmin: next p : goto 100

319 print Z
320 print" Justage RR ... horizontal 300 Schritte nach links"
321   print#2,"@0A 0,3000,300,3000,0,3000,0,3000"
322   HorB=HorB+300
323   write#3,date$,time$,0,0,300,0,HorA,VertA,HorB,VertB,IA,IIA,IIIA,IVA,SummeA, IB,IIB,IIIB,IVB,SummeB
324   B=B+1: for p=1 to wext: next p : goto 100

325 print Z
326 print" Justage RR ... horizontal 50 Schritte nach links"
327   print#2,"@0A 0,3000,50,3000,0,3000,0,3000"
328   HorB=HorB+50
329   write#3,date$,time$,0,0,50,0,HorA,VertA,HorB,VertB,IA,IIA,IIIA,IVA,SummeA, IB,IIB,IIIB,IVB,SummeB
330   for p=1 to wmax: next p : goto 100

331 print Z
332 print" Justage RR ... horizontal 10 Schritte nach links"
333   print#2,"@0A 0,3000,10,3000,0,3000,0,3000"
334   HorB=HorB+10
335   write#3,date$,time$,0,0,10,0,HorA,VertA,HorB,VertB,IA,IIA,IIIA,IVA,SummeA, IB,IIB,IIIB,IVB,SummeB
336   for p=1 to wmin: next p : goto 100

340 print Z
342 print" Justage RR ... horizontal 85 Schritte nach rechts"
343   print#2,"@0A 0,3000,-85,3000,0,3000,0,3000"
344   HorB=HorB-85
345   write#3,date$,time$,0,0,-85,0,HorA,VertA,HorB,VertB,IA,IIA,IIIA,IVA,SummeA, IB,IIB,IIIB,IVB,SummeB
346   for p=1 to wmax: next p : goto 100

350 print Z
352 print" Justage RR ... horizontal 120 Schritte nach rechts"
353   print#2,"@0A 0,3000,-120,3000,0,3000,0,3000"
354   HorB=HorB-120
355   write#3,date$,time$,0,0,-120,0,HorA,VertA,HorB,VertB,IA,IIA,IIIA,IVA,SummeA, IB,IIB,IIIB,IVB,SummeB
356   for p=1 to wmin: next p : goto 100

365 print Z
366 print" Justage RR ... horizontal 85 Schritte nach links"
367   print#2,"@0A 0,3000,85,3000,0,3000,0,3000"

```

```

368     HorB=HorB+85
369     write#3,date$,time$,0,0,85,0,HorA,VertA,HorB,VertB,IA,IIA,IIIA,IVA,SummeA, IB,IIB,IIIB,IVB,SummeB
370     for p=1 to wmax: next p : goto 100

371     print Z
372     print" Justage RR ... horizontal 120 Schritte nach links"
373     print#2,"@0A 0,3000,120,3000,0,3000,0,3000"
374     HorB=HorB+120
375     write#3,date$,time$,0,0,120,0,HorA,VertA,HorB,VertB,IA,IIA,IIIA,IVA,SummeA, IB,IIB,IIIB,IVB,SummeB
376     for p=1 to wmin: next p : goto 100

400     rem Diagonale Justage A
401     print Z
402     print" Justage LR ... diagonal 50 Schritte nach links-unten"
403     print#1,"@0A 0,3000,50,3000,50,3000,0,3000"
404     HorA=HorA+50: VertA=VertA+50
405     write#3,date$,time$,50,50,0,0,HorA,VertA,HorB,VertB,IA,IIA,IIIA,IVA,SummeA, IB,IIB,IIIB,IVB,SummeB
406     for p=1 to w: next p : goto 150

410     print Z
411     print" Justage LR ... diagonal 50 Schritte nach rechts-unten"
412     print#1,"@0A 0,3000,-50,3000,50,3000,0,3000"
413     HorA=HorA-50: VertA=VertA+50
414     write#3,date$,time$,-50,50,0,0,HorA,VertA,HorB,VertB,IA,IIA,IIIA,IVA,SummeA, IB,IIB,IIIB,IVB,SummeB
415     for p=1 to w: next p : goto 150

420     print Z
422     print" Justage LR ... diagonal 50 Schritte nach links-oben"
423     print#1,"@0A 0,3000,50,3000,-50,3000,0,3000"
424     HorA=HorA+50: VertA=VertA-50
425     write#3,date$,time$,50,-50,0,0,HorA,VertA,HorB,VertB,IA,IIA,IIIA,IVA,SummeA, IB,IIB,IIIB,IVB,SummeB
426     for p=1 to w: next p : goto 150

430     print Z
432     print" Justage LR ... diagonal 50 Schritte nach rechts-oben"
433     print#1,"@0A 0,3000,-50,3000,-50,3000,0,3000"
434     HorA=HorA-50: VertA=VertA-50
435     write#3,date$,time$,-50,-50,0,0,HorA,VertA,HorB,VertB,IA,IIA,IIIA,IVA,SummeA, IB,IIB,IIIB,IVB,SummeB
436     for p=1 to w: next p : goto 150

440     print "Vertikale Justage LR..."
450     print Z
452     print" Justage LR ... vertikal 30 Schritte nach unten"
453     print#1,"@0A 0,3000,0,3000,30,3000,0,3000"
454     VertA=VertA+30
455     write#3,date$,time$,0,30,0,0,HorA,VertA,HorB,VertB,IA,IIA,IIIA,IVA,SummeA, IB,IIB,IIIB,IVB,SummeB
456     for p=1 to w: next p : goto 150

460     print Z
462     print" Justage LR ... vertikal 10 Schritte nach unten"
463     print#1,"@0A 0,3000,0,3000,10,3000,0,3000"
464     VertA=VertA+10
465     write#3,date$,time$,0,10,0,0,HorA,VertA,HorB,VertB,IA,IIA,IIIA,IVA,SummeA, IB,IIB,IIIB,IVB,SummeB
466     for p=1 to w: next p : goto 150

470     print Z
472     print" Justage LR ... vertikal 30 Schritte nach oben"
473     print#1,"@0A 0,3000,0,3000,-30,3000,0,3000"
474     VertA=VertA-30
475     write#3,date$,time$,0,-30,0,0,HorA,VertA,HorB,VertB,IA,IIA,IIIA,IVA,SummeA, IB,IIB,IIIB,IVB,SummeB
476     for p=1 to w: next p : goto 150

480     print Z
482     print" Justage LR ... vertikal 10 Schritte nach oben"
483     print#1,"@0A 0,3000,0,3000,-10,3000,0,3000"
484     VertA=VertA-10
485     write#3,date$,time$,0,-10,0,0,HorA,VertA,HorB,VertB,IA,IIA,IIIA,IVA,SummeA, IB,IIB,IIIB,IVB,SummeB
486     for p=1 to w: next p : goto 150

490     print "Horizontale Justage LR..."
500     print Z
502     print" Justage LR ... horizontal 30 Schritte nach rechts"
503     print#1,"@0A 0,3000,-30,3000,0,3000,0,3000"
504     HorA=HorA-30
505     write#3,date$,time$,-30,0,0,0,HorA,VertA,HorB,VertB,IA,IIA,IIIA,IVA,SummeA, IB,IIB,IIIB,IVB,SummeB
506     for p=1 to w: next p : goto 150

510     print Z
512     print" Justage LR ... horizontal 10 Schritte nach rechts"
513     print#1,"@0A 0,3000,-10,3000,0,3000,0,3000"
514     HorA=HorA-10
515     write#3,date$,time$,-10,0,0,0,HorA,VertA,HorB,VertB,IA,IIA,IIIA,IVA,SummeA, IB,IIB,IIIB,IVB,SummeB
516     for p=1 to w: next p : goto 150

520     print Z
521     print" Justage LR ... horizontal 30 Schritte nach links"
522     print#1,"@0A 0,3000,30,3000,0,3000,0,3000"
523     HorA=HorA+30
524     write#3,date$,time$,30,0,0,0,HorA,VertA,HorB,VertB,IA,IIA,IIIA,IVA,SummeA, IB,IIB,IIIB,IVB,SummeB
525     for p=1 to w: next p : goto 150

```

```

530 print Z
532 print Justage LR ... horizontal 10 Schritte nach links"
533 print #1,"@0A 0,3000,10,3000,0,3000,0,3000"
534 HorA=HorA+10
535 write#3,date$,time$,10,0,0,0,HorA,VertA,HorB,VertB,IA,IIA,IIIA,IVA,SummeA, IB,IIB,IIIB,IVB,SummeB
536 for p=1 to w: next p : goto 150

840 STOP
850 REM Ausgabe der 4QD Werte
855 CLS
856 Print":print"
860 Print"QI_A : ",IA,"QII_A : ",IIA
861 Print"QIII_A : ",IIIA,"QIV_A : ",IVA
862 Print"
863 Print"QI_B : ",IB,"QII_B : ",IIB
864 Print"QIII_B : ",IIIB,"QIV_B : ",IVB
865 Print"
900 Print"Oben_A : ",obenA,"Unten_A : ",untenA
901 Print"Links_A : ",linksA,"Rechts_A : ",rechtsA
902 Print"
903 Print"Oben_B : ",obenB,"Unten_B : ",untenB
904 Print"Links_B : ",linksB,"Rechts_B : ",rechtsB
910 RETURN

1000 REM 4QD Auslesen bis 1410 von Detektor A
1005 IA=0 : IIA=0 : IIIA=0 : IVA=0
1006 IB=0 : IIB=0 : IIIB=0 : IVB=0
1010 FOR slope = 1 to wdh
1020 K=1
1021 DIN$="111101110001":GOTO 1070 : rem Kanal 1
1022 DIN$="111101110011":GOTO 1070 : rem Kanal 2
1023 DIN$="111101111001":GOTO 1070 : rem Kanal 3
1024 DIN$="111101111011":GOTO 1070 : rem Kanal 4
1025 DIN$="111101110101":GOTO 1070 : rem Kanal 5
1026 DIN$="111101110111":GOTO 1070 : rem Kanal 6
1027 DIN$="111101111101":GOTO 1070 : rem Kanal 7
1028 DIN$="111101111111":GOTO 1070 : rem Kanal 8
1070 B=512
1075 VOUT=0
1080 REF=5
1090 REM
1100 FOR I = 1 TO 12
1110 OUT &H3EC,(&HFE AND INP (&H3EC))
1120 IF MID$(DIN$, 13-I,1)="0" THEN OUT &H3EC, (&HFD AND INP (&H3EC)) ELSE OUT &H3EC, (&H2 OR
INP(&H3EC))
1130 OUT &H3EC, (&H1 OR INP (&H3EC))
1140 IF (INP (&H3EE) AND 16) = 16 THEN D = 0 ELSE D = 1
1150 VOUT=VOUT+(D*B) : B=B/2
1160 NEXT I
1170 REM
1200 OUT &H3EC, (&HFD AND INP (&H3EC))
1210 OUT &H3EC, (&H2 OR INP (&H3EC))
1220 REM
1230 FOR J=1 TO 20 : NEXT J : REM schneller Rechner
1240 REM
1250 REM PRINT VOUT
1260 VIN=INT((VOUT/1023)*REF*1000)
1261 IF K=1 THEN 1275
1262 IF K=2 THEN IB=IB+VIN
1263 IF K=3 THEN IVA=IVA+VIN
1264 IF K=4 THEN IIIA=IIIA+VIN
1265 IF K=5 THEN IIA=IIA+VIN
1266 IF K=6 THEN IA=IA+VIN
1267 IF K=7 THEN IIB=IIB+VIN
1268 IF K=8 THEN IIIB=IIIB+VIN
1269 IF K=9 THEN IVB=IVB+VIN
1272 IF K=9 THEN GOTO 1310
1275 K=K+1: ON K GOTO 1021,1022,1023,1024,1025,1026,1027,1028,1028
1310 rem FOR I= 1 to 10000: Next I:
1410 NEXT slope
1411 IA=INT(IA/wdh-Iao) : IIA=INT(IIA/wdh-IIao)
1412 IIIA=INT(IIIA/wdh-IIIAo) : IVA=INT(IVA/wdh-IVao)
1413 IB=INT(IB/wdh-Ibo) : IIB=INT(IIB/wdh-IIbo)
1414 IIIB=INT(IIIB/wdh-IIIBo) : IVB=INT(IVB/wdh-IVbo)
1415 obenA=IIIA+IIA:untenA=IA+IVA:linksA=IA+IIA:rechtsA=IVA+IIIA
1416 obenB=IB+IIB:untenB=IIIB+IVB:linksB=IB+IVB:rechtsB=IIB+IIIB
1420 RETURN

1990 rem Schrittmotorinitialisierung
2000 if loc(1)<1 then goto 2000: rem Fehlermeldung Karte SM
2010 a$=input$(1,1)
2020 if a$="0" then return
2030 print "Karte meldet Fehler: ";a$
2040 stop

3000 if loc(2)<1 then goto 3000: rem Fehlermeldung Karte SM
3010 a$=input$(1,2)
3020 if a$="0" then return
3030 print "Karte meldet Fehler: ";a$
3040 stop

4000 rem Check ob Laser gefunden sind

```

```
4010 print""
4020 X=X+1 : print "Auslesung B_Nr: "X,"SummeB: "SummeB HorB VertB
4030 print "Auslesung A_Nr: "Y,"SummeA: "SummeA HorA VertA
4100 IF (IB<100 AND IIB<100 AND IIIB<100 AND IVB<100) then goto 4120 else print "Laser RR gefunden!" : goto 4200
4120 print"Laser RR nicht gefunden!"
4200 IF (IA<100 AND IIA<100 AND IIIA<100 AND IVA<100) then goto 4220 else print "Laser LR gefunden!" : goto 4300
4220 print"Laser LR nicht gefunden!"
4300 IF (IB<100 AND IIB<100 AND IIIB<100 AND IVB<100) then goto 4320 else return
4320 print"" : print"Justage RR abgebrochen...!" : goto 150

5000 rem Check ob Laser gefunden sind
5010 print""
5015 print "Auslesung B_Nr: "X,"SummeB: "SummeB HorB VertB
5020 Y=Y+1 : print "Auslesung A_Nr: "Y,"SummeA: "SummeA HorA VertA
5100 IF (IB<100 AND IIB<100 AND IIIB<100 AND IVB<100) then goto 5120 else print "Laser RR gefunden!" : goto 5200
5120 print"Laser RR nicht gefunden!"
5200 IF (IA<100 AND IIA<100 AND IIIA<100 AND IVA<100) then goto 5220 else print "Laser LR gefunden!" : goto 5300
5220 print"Laser LR nicht gefunden!"
5300 IF (IA<100 AND IIA<100 AND IIIA<100 AND IVA<100) then goto 5320 else return
5320 print"" : print"Justage LR abgebrochen...!" : goto 193

10000 END
```


Acknowledgements

I want to thank,

Prof. Dr. Ulrich Platt for his engaged supervision of this PhD thesis and his confidence in me during my time abroad. He always promoted me and assured that this PhD thesis could be successful. Without his patronage and generous support this thesis would not have been possible.

Prof. Dr. Paul Crutzen for his interest and expert's opinion on this PhD thesis.

Prof. Dr. Karl-Heinz Becker for his far-sighted vision and effort to build the EUPHORE-facility. Having met him some years ago in Valencia inspired me to apply for the Marie Curie Fellowship.

Dr. Klaus Wirtz for his support and readiness to lively discuss on aspects of atmospheric chemistry during the Marie Curie grant. Dr. Millan Millan and my colleagues at CEAM-Institute are acknowledged for their valuable support and a good time during and after work. Special thanks to Mila.

Dr. Ian Barnes, Dr. Klaus Brockmann, Dr. Björn Klotz, Dr. Djuro Mihelcic, Romeo Olariu, Dr. Manfred Siese, Dr. Tim Wallington and Prof. Dr. Cornelius Zetzsch for helpful discussions as well as pleasant collaborations.

Jens Ücker for his help, support and friendship during our joint time in Valencia and afterwards. Dr. Thomas Wagner, Dr. Björn Alicke, Dr. Oliver Funk, Christoph v. Friedeburg and Johanna Symmons are acknowledged for proofreading this manuscript. I further thank all my colleagues in Heidelberg for their willingness to support whenever necessary.

my family for being an integral counterpart to my scientific life.

Menitoleta por su amor y la fe que tiene en mi y que me ha ayudado en escribir este libro.

the DG-XII, Commission of the European Communities for the Marie Curie Fellowship within the Environment and Climate program (Contract No. ERB 4001GT970196).

